Ferrite Nucleation on Non-metallic Inclusions in Steel

John Martin Gregg

1994

This work is dedicated to my parents.

'Mark you this Bassanio?
The devil can cite Scripture for his purpose.'
(William Shakespeare – The Merchant of Venice)

PREFACE

This dissertation is submitted as a PhD thesis in the University of Cambridge. The investigation described herein was carried out under the supervision of Dr. H. K. D. H. Bhadeshia in the Department of Materials Science and Metallurgy, University of Cambridge, between October 1991 and November 1994.

Except where acknowledgement and reference is specifically made to the contrary, this work is, to the best of my knowledge, original and has been carried out without collaboration. Neither this, nor any substantially similar dissertation has been, or is being submitted for any degree, diploma, or other qualification at any other university.

Marty Gregg

Marty Gregg
November 1994

ACKNOWLEDGEMENTS

I wish to thank Professor C. Humphreys for the provision of laboratory facilities in the Department of Materials Science and Metallurgy at the University of Cambridge. I would also like to thank Dr. H.K.D.H. Bhadeshia for his supervision and help during the course of this work.

My grateful thanks are also extended to the various members of the Phase Transformations Group, with whom I had the pleasure of working, and whose company contributed towards some of the happiest days of my life. As a result there are a great many people, from all over the world, who I miss very much indeed. I must also thank the technical staff in the department both for their help during the project and for their company.

This work has been jointly supported by The Department of Education for Northern Ireland and by ESAB Sweden.

ABSTRACT

Highly organised and aligned microstructures can often be observed in steel. Cleavage cracks, or deformation processes find propagation through such microstructures relatively easy. More chaotic microstructures can be expected to offer a greater resistance to crack propagation. This is why many recent steels, designed for toughness at low temperatures, contain high volume fractions of acicular ferrite. Acicular ferrite is bainite, but nucleates intragranularly from the surfaces of non–metallic inclusions within austenite grains. From these point sources, plates of acicular ferrite grow in many directions. This is in contrast to the common, but less desirable, microstructure in which plates of ferrite nucleating at austenite grain surfaces tend to align into packets which are susceptible to crack propagation.

A large number of experiments have been performed to elucidate the chemical nature of non–metallic inclusions which are particularly effective in producing acicular ferrite. Associated with these experiments, several mechanisms by which inclusions induce nucleation have been proposed. However, the non–metallic inclusions found in commercial alloys, on which most work has been performed, usually consist of many crystalline and amorphous phases, so that identification of the particular phase responsible for producing acicular ferrite nucleation is inherently difficult. These difficulties previously prompted Strangwood and Bhadeshia (1987) to conduct a series of controlled experiments in which pure ceramic phases were pressure bonded to steel in order to create interfaces which could be studied with confidence. Effective ceramic nucleants were observed to cause enhanced transformation in the vicinity of the interface when compared with reaction within the bulk of the steel. Because of the lack of adequate equipment, high hardenability steels were used, so that only allotriomorphic ferrite formation could be examined.

A large section of the work herein represents an extension of the above, in which experiments were performed using a low–alloy steel to study the bainite nucleation induced by various mineral compounds. Bainite and acicular ferrite appear to have the same transformation mechanism, so that results of nucleation efficacy should apply equally to acicular ferrite. It was found that the minerals tested could be categorised into three groups, according to their observed efficacy in inducing the nucleation of bainite. The dominant reason for the stimulation of bainite nucleation seemed to be a chemical interaction between mineral and steel. A noteable exception was TiO, which, within the limits of resolution, appeared to remain inert, and yet enhanced bainite

formation.

Despite the clarity of the pressure bonding experiments, there are potential difficulties in relating the results produced to systems where mineral inclusions form in the molten steel. For example the application of pressure in the solid–state does not necessarily lead to an intimate bond, on an atomic scale, between the chosen ceramic and steel. Further, the ceramic is bonded in the form of a powder, which may not fully densify during pressure bonding. Any differences in thermal expansivity between the steel and ceramic may not lead to the development of contraction stresses of the magnitudes expected when the liquid steel containing inclusions solidifies and cools. Therefore a further experimental technique was developed in which powdered mineral phases were added directly to the molten steel. These alloys were then studied from the point of view of the acicular ferrite microstructure. Results largely reiterated the implications of the bonding experiments, and showed chemical interaction, particularly involving oxygen, and carbon, as being paramount in producing high levels of acicular ferrite.

CONTENTS

CHAPTER 1

General Introduction and Literature Review

1.1 Phase Transformations in Steels

1.1.1 Allotropes of Iron

At atmospheric pressure, pure iron may exist in two forms, depending on the temperature. At low temperatures ($< 912\,^{\circ}C$), the atoms form a body-centred cubic (b.c.c.) structure known as ferrite (α), which is also stable at temperatures above $1394\,^{\circ}C$. Otherwise a face-centred cubic (f.c.c.) structure, called austenite (γ) exists at intermediate temperatures. Pure iron may also exist in a hexagonal close-packed (h.c.p.) form (ϵ), but this is only stable at high pressures ($\sim$130 kbar). Melting occurs at $1538\,^{\circ}C$.

1.1.2 The Effects of Alloying

Alloying elements are divided into two types. There are those which replace iron atoms in the lattice (substitutional alloying elements – *e.g.* Mn, Si, Cr), and those which reside in cavities between the iron atoms (interstitial alloying elements – *e.g.* C, N). All alloying additions affect the relative free energies of the f.c.c. and b.c.c. structures of iron. A conceptually convenient notion is to divide the alloying elements into those which tend to stabilise austenite (*e.g.* C, Mn, Ni), and those which tend to stabilise the ferrite (*e.g.* Mo, Cr, Si).

The transformations that occur during the cooling of steel depend critically on the chemical composition. The solubility of solutes is usually different in austenite (γ) and ferrite (α), so that their redistribution requires diffusion. Diffusional processes, in turn, require thermal activation which may be inadequate at low temperatures, thus prohibiting the achievement of equilibrium within the time scale of the experiment. The steel therefore often transforms into a metastable alternative which is kinetically favoured. The exact nature of the metastable transformation depends on the thermal energy available, and the relative stability of the transformation product. Transformation may proceed by either a reconstructive or a displacive mechanism. Reconstructive transformations involve the dissolution of the parent structure, before creation of the transformation product. This dissolution requires substitutional chemical bonds to be broken, and is thus associated with high activation energies. In displacive transformations, no breaking of bonds is required. Instead, the transformation product results from small relative atomic shifts. Atomic correspondence between parent and product phases is indicative of a displacive

transformation. Because atomic shifts are small, and there is no requirement for chemical bonds to be broken, the activation energies associated with displacive transformations are generally small.

1.1.3 Reconstructive Transformations in Steel

Allotriomorphic ferrite is the first phase to grow from austenite as it cools. It nucleates at, and grows preferentially along γ/γ grain boundaries. It grows by a reconstructive mechanism *i.e.* the pattern in which the atoms are arranged changes with the long-range uncorrelated migration of atoms, the diffusion occurring in such a way that strain is minimised. There is no atomic correspondence between the parent and product phases in the sense that nearest–neighbour relationships are not preserved.

The growth of allotriomorphic ferrite in binary Fe–C steels leads to the partitioning of carbon into austenite (where its solubility is higher) with the rate often being limited by the diffusion of carbon ahead of the transformation interface. During diffusion–controlled growth, the compositions at the interface of the α and γ are given, approximately, by a tie-line of the phase diagram. The tie-line concerned passes through the bulk composition of the Fe–C alloy. Such diffusion–controlled growth in Fe–C–X steels (where X represents a substitutional solute) is complicated in that redistribution of both substitutional and interstitial elements is required for growth to proceed. The diffusivities of substitutional elements are much lower than of interstitials, since atomic movement requires structural vacancy formation. If interactions between solutes are ignored, then the growth velocity (movement of the ferrite/austenite interface – V_{int}) must be such that it satisfies two flux equations simultaneously in a Fe–C–X alloy (Christian, 1965):

$$(c_1^{\gamma\alpha} - c_1^{\alpha\gamma})V_{int} = D_{11}\nabla c_1 \tag{1.1}$$

$$(c_2^{\gamma\alpha} - c_2^{\alpha\gamma})V_{int} = D_{22}\nabla c_2 \tag{1.2}$$

where c_1 and c_2 are the concentrations of carbon and substitutional element X respectively. D_{11} is the diffusivity of carbon, and D_{22}, the diffusivity of the substitutional solute. The superscript $\alpha\gamma$ denotes the concentration in α which is in equilibrium with γ, and a similar interpretation applies for the term $\gamma\alpha$ (Fig.1.1). Because $D_{11} >> D_{22}$, the equations cannot in general be satisfied simultaneously by a single value of V_{int}, whilst local equilibrium is maintained. In other words, the interface compositions cannot in general be fixed by a tie-line which passes through the bulk composition. Instead, another tie-line which enables the flux balance equations to be satisfied simultaneously has to be chosen. There are two solutions within the $\alpha + \gamma$ phase field. If the bulk carbon concentration is set to be close

to $c_1^{\gamma\alpha}$, then the flux of carbon is reduced to a value compatible with substitutional atom diffusion. This is called 'Partitioning Local Equilibrium' (PLE), because a tie-line in which $c_1^{\gamma\alpha} \simeq \overline{c}_1$ necessitates considerable partitioning of X.

Alternatively, if a tie-line is chosen such that $\overline{c}_2$ is allowed to approach $c_2^{\alpha\gamma}$, then the concentration gradient for X becomes very high allowing substitutional diffusion to keep pace with that of carbon. This is called 'Negligible Partitioning Local Equilibrium' (NPLE), because the ferrite has a concentration of X which is almost identical to $\overline{c}_2$.

At a large enough undercooling, the substitutional species cannot partition at all, so that local equilibrium breaks down. The carbon atoms can still diffuse such that a uniform chemical potential is achieved, subject to the constraint that the X/Fe ratio remains constant everywhere. This is called paraequilibrium.

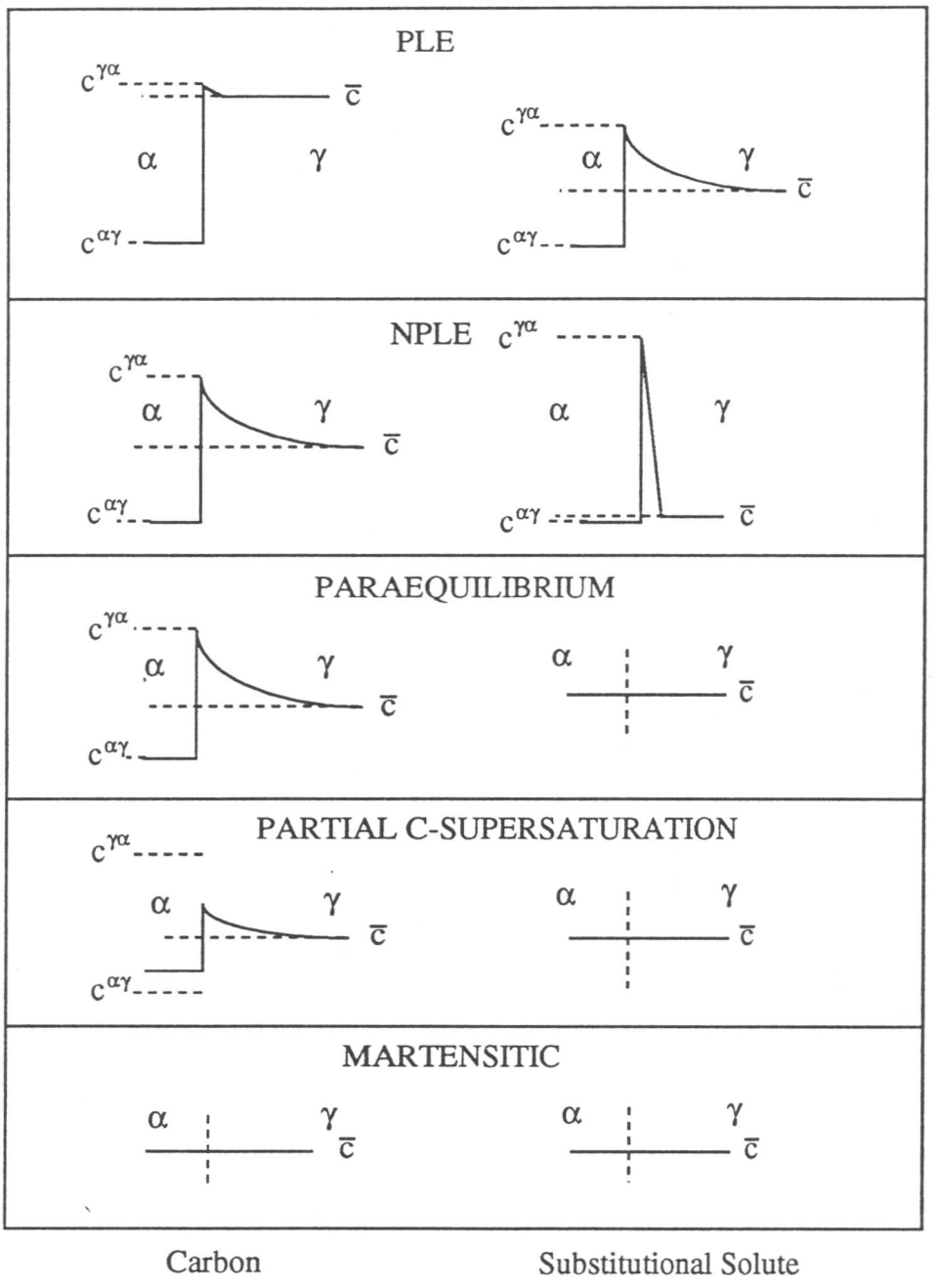

Figure 1.1 Schematic illustration of the growth modes possible for the ferrite–austenite interface (Bhadeshia, 1992).

1.1.4 Displacive Transformations in Steel

Displacive phase transformations involve a deformation of the parent crystal structure, in order to generate the product phase. Fig.1.2 shows the mechanism by which the transformation can be achieved without the need for near neighbour relationships to be disrupted.

The f.c.c. structure can be redefined using a body-centred tetragonal cell as shown in the figure. Representing the lattice vectors of the austenite cell as a_γ, b_γ and c_γ, and those of the tetragonal cell as a_{bct}, b_{bct} and c_{bct}:

$$a_{bct} = \tfrac{1}{2}(a_\gamma - b_\gamma)$$
$$b_{bct} = \tfrac{1}{2}(a_\gamma + b_\gamma)$$
$$c_{bct} = c_\gamma$$

Transformation from this b.c.t. cell to a b.c.c. cell would involve contraction along c_{bct} and equal expansions along a_{bct} and b_{bct}. This is known as the Bain Strain. The Bain Strain causes an excessive strain on transformation; the strain energy can be reduced with additional deformations which make the total strain (macroscopically) an invariant-plane strain (IPS), with a large shear component. An invariant–plane strain is that in which a plane remains undistorted, and unrotated after the operation of strain.

All of the plate-shaped forms of ferrite in steels grow with a shape deformation which is an IPS, with a large shear component.

1.1.4.1 Widmanstätten Ferrite

At rather small undercoolings, the first displacive transformation product to form is Widmanstätten ferrite (Fig.1.3). It has the appearance of thin wedges. This shape arises due to the tendency for the simultaneous growth of strain–compensating plates, which lie back-to-back, but are at a slight angle to one another. Such compensation reduces the strain energy associated with the transformation to about $50\,\mathrm{J\,mol^{-1}}$ (Bhadeshia, 1981).

The transformation mechanism involves growth under paraequilibrium conditions *i.e.* although the undercooling is sufficient to allow the ferrite to grow without the partitioning of substitutional solutes, the redistribution of interstitials is required if the transformation is to take place at all.

1.1.4.2 Bainite

At larger undercoolings, the growth of metastable ferrite of identical composition to the austenite becomes thermodynamically viable. Thus displacive transformation may occur without any diffusion. Bainite grows in this manner with the repeated nucleation and growth of platelets (sub-units) which form aggregates, known collectively as sheaves. Successive sub-units form, both at the tips of previously formed plates and at their sides.

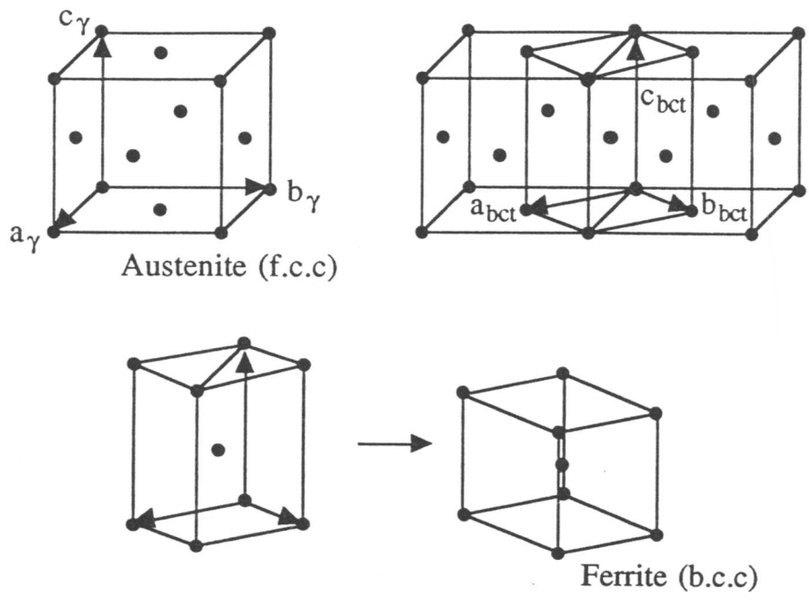

Figure 1.2 Bain Strain transformation from fcc to bcc lattices.

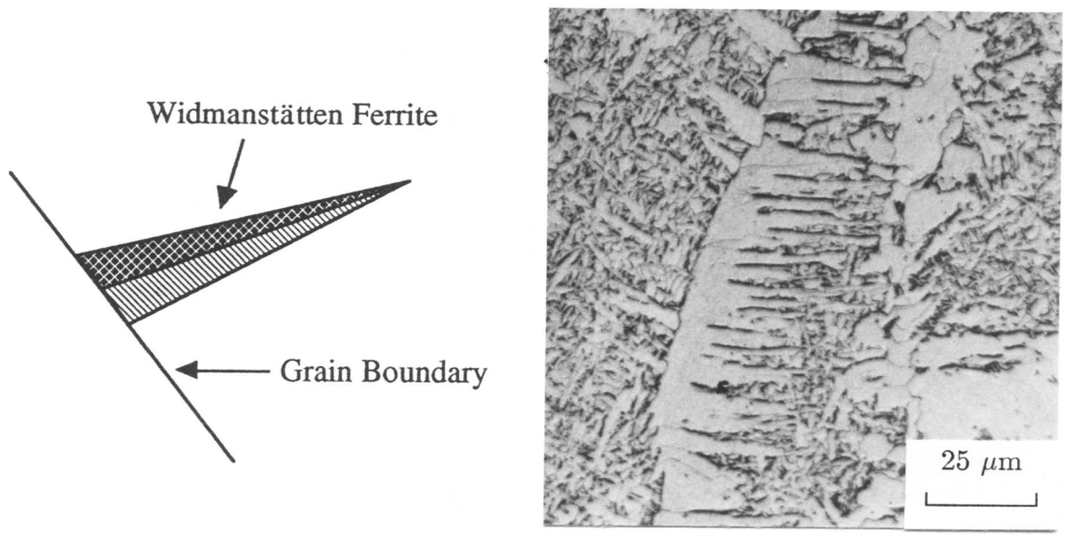

Figure 1.3 (a) Schematic of the morphology of Widmanstätten ferrite.
(b) Micrograph of the Widmanstätten ferrite microstructure.

The former site is more effective than the latter, thereby giving an overall plate–like appearance to the bainite sheaf. The reason why growth occurs in a series of discrete sub-units is because the large strain associated with the transformation, causes deformation and a high dislocation density, which ultimately stifles the movement of the transformation interface. Individual sub-units form fully supersaturated with carbon. The ferrite may then lower its free energy, either by rejecting the carbon into the surrounding untransformed austenite, or, if the temperature is low enough, by precipitating carbides within the bainite unit. These two possibilities lead to upper and lower bainite respectively (Fig.1.4).

The bainite transformation obeys what is called the 'incomplete reaction phenomenon'. During transformation, in most cases, bainite can partition carbon into untransformed austenite extremely rapidly. The remaining austenite therefore enriches in carbon, such that diffusionless growth eventually becomes impossible. The reaction stops when austenite and ferrite of the same composition have the same free energy. This thermodynamic point is known as T_o, and is a lower temperature than the equilibrium Ae_3 temperature which defines the $(\alpha + \gamma)/\gamma$ phase boundary. Since reaction stops when the austenite achieves a carbon concentration equal to that given by the T_o curve, rather than when its composition achieves the equilibrium Ae_3 value, the reaction is said to be incomplete. Experimentally, bainite is found to cease transformation before T_o (at T_o' – which takes the strain energy associated with the transformation into account). The observed incomplete reaction confirms that bainite grows with a full supersaturation of carbon (Fig.1.5).

1.1.4.3 Acicular Ferrite

Acicular ferrite is a 'basket weave' microstructure, frequently observed in weld deposits (Fig.1.6). The needle–like crystals appear to nucleate pre-dominantly on non–metallic inclusions which are more common in welds than in cast steels. It was originally thought that acicular ferrite was a form of intragranularly nucleated Widmanstätten ferrite (Ricks *et al.*, 1982), but most researchers now agree that it is, in fact, intragranularly–nucleated bainite. The transformation shows surface relief consistent with an IPS shape change (Strangwood and Bhadeshia, 1987), and demonstrates the incomplete reaction phenomenon, characteristic of bainite (Yang and Bhadeshia, 1987). Further, Sugden and Bhadeshia (1989) showed that upper and lower acicular ferrite could be produced, analogous to the upper and lower bainite described above.

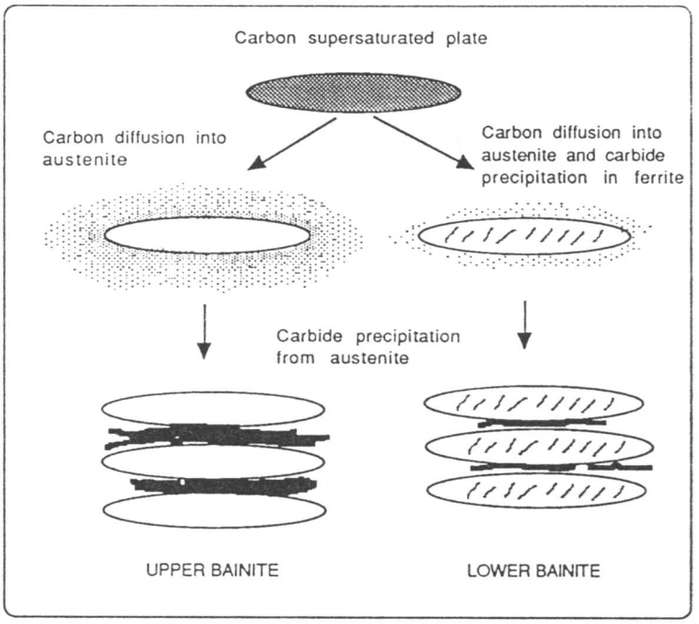

Figure 1.4 Schematic diagram showing the development of upper and lower bainite.

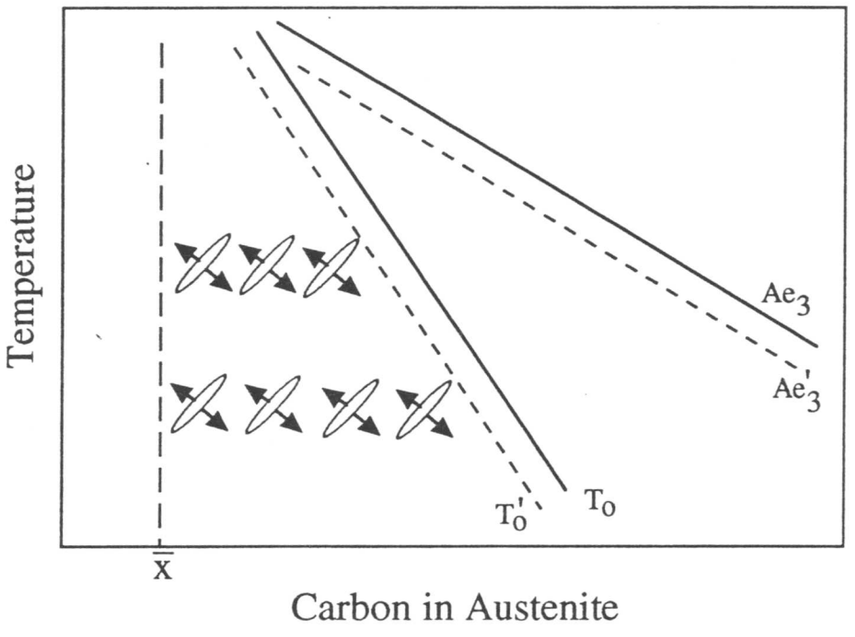

Figure 1.5 The bainite transformation ceases before the T_o line, and does not continue until the austenite is of a composition given by the Ae_3 boundary. This is clear evidence that bainite grows with a full saturation of carbon.

There is much interest in developing steel microstructures which contain very high volume fractions of acicular ferrite, as the disorganised, interlocking plates, present an extremely tortuous propagation path for any advancing cracks. Much crack energy may therefore be absorbed by this microstructure, so that toughness is maximised (Ishikawa and Haze, 1994).

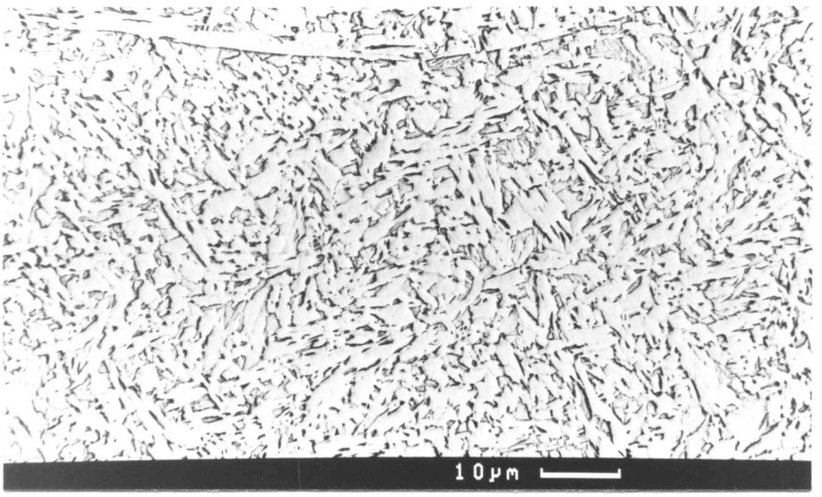

Figure 1.6 Micrograph showing the interlocking nature of the acicular ferrite microstructure.

1.1.5 Martensite

At the highest levels of austenite undercooling, transformation from f.c.c. to b.c.c. steel may occur without any diffusion. Hence, martensite growth rates are limited only by the speed of sound in the metal. The shape change associated with transformation is an invariant–plane strain. The growth of a plate is arrested at prior austenite grain boundaries. When transformation is constrained, the martensite adopts a curved habit plane with austenite, forming lenticular plates or laths. The orientation relationship between the austenite and martensite usually consists of close-packed planes and directions being parallel, or approximately so *e.g.* Kurdjumov–Sachs:

$$\{111\}_\gamma \parallel \{011\}_\alpha \text{ and } < 10\overline{1} >_\gamma \parallel < 11\overline{1} >_\alpha$$

Martensite can be extremely hard and brittle, and is to be avoided in weld deposits.

1.2 Importance of Inclusions

Large volume fractions of acicular ferrite are beneficial for the toughness properties of steel welds. This is because the chaotic, interlocking nature of the microstructure impedes the propagation of cracks. Acicular ferrite transforms in the same manner as bainite, save that nucleation occurs on non–metallic inclusions as opposed to austenite grain boundaries. Therefore, if no non–metallic inclusions are present, bainite rather than acicular ferrite may result. Parallel plates of bainite offer little resistance to crack propagation. Therefore, inclusion presence and potency as heterogeneous nucleation sites are critical to the development of tough, acicular ferrite–rich, welds. The research presented herein focusses on inclusions and their abilities to cause nucleation.

1.3 Inclusion description

1.3.1 Inclusion Composition

The chemical species present in weld inclusions have, in most cases, been identified with the aid of EDX (energy dispersive X–ray) analysis. Such analysis has shown the presence of the cations Mn, Al, Si, Ti, and Cu (Nb, V, Ca, and Fe to a lesser extent), and the presence of the anion S. Other anion species of interest are too light to be recorded using standard EDX, but, since the inclusions exist mainly as a result of oxidation of the weldpool, it can be safely assumed that oxygen is abundantly present in the inclusions. Nitrogen too, is present in many cases. Observation of nitrogen in compound form has often been made by measuring ammonia release when the weld metal is exposed to hot hydrogen gas (Mori *et al.*, 1981). The higher the temperature at which ammonia is released, the greater is the binding energy associated with the nitrogen. Dissolved nitrogen has a lower binding energy than that present in compound form.

It is easy to identify the elements present in weld inclusions, but much more difficult to pin down the formula for the mineral, or combination of minerals present. Properties of inclusions depend on these mineral formula rather than on the chemical species themselves. Mineral phases therefore need to be identified when attempting to interpret and rationalise the effects of inclusions on weld phase behaviour.

1.3.2 Inclusion Mineralogy

Pickering (1979) gave a comprehensive listing of the minerals found in inclusions in wrought steels. Of the sulphides, FeS_x, MnS and CaS are common. Oxides include (Fe,Mn)O, SiO_2, Al_2O_3, complex Cr oxides, TiO, Ti_2O_3, Ti_3O_5 and TiO_2 and even spinels, pyroxenes, olivines, garnets, feldspars and cordierites. Weld inclusion studies indicate that the range

of minerals found is somewhat narrower in weld metals than suggested, for wrought steels, by Pickering.

1.3.2.1 Titanium based minerals

Titanium-rich phases have been reported frequently to possess an f.c.c. (face-centred cubic) structure with a lattice parameter of between 4.2 and 4.4 Å. The structure and lattice parameter give a good indication of the phase involved, but the information is not sufficient to uniquely identify the phase without the chemical composition as well, since TiN, TiO and TiC all possess structures and lattice parameters consistent with that above. Consequently, there has been some debate as to the exact mineralogy of titanium-rich phases. Opinions are equally divided between TiN and TiO, although more recent investigations seem to favour TiO.

Barbaro *et al.* (1988) noted that, like the known shape of TiN, the titanium-rich phase found in weld inclusions was cuboidal. TiO usually forms as spheres. Thus, a cuboidal shape can be taken to indicate that the particle is likely to be TiN rather than TiO (Fig.1.7).

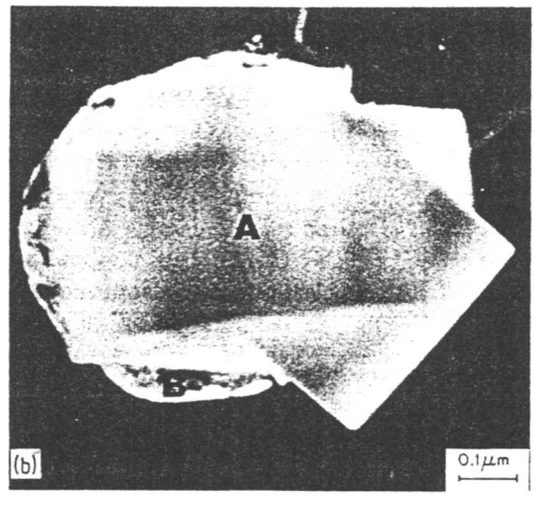

Figure 1.7 Weld inclusion showing angular, cubic morphology more typical of TiN than TiO - after Kayali *et al.* (1983)

Thewlis (1989) claimed, on the basis of X-ray analysis, to have found peaks characteristic of TiN and not of TiO, while Ito and Nakanishi (1976) and Watanabe and Kojima (1980) showed that the amount of insoluble titanium measured in a weld sample was proportional to the amount of insoluble nitrogen. This would obviously suggest the presence of TiN. However, Watanabe and Kojima (1980) also stated that relatively little titanium

is required to remove all the dissolved nitrogen present in the weld, leaving remanent titanium. They suggested that such remanent titanium would form TiO.

Mori *et al.* (1981) claimed that their XRD (X-ray diffraction) identified TiO and Ti_2O_3 (but not TiN). The concentration of free nitrogen in the weld metal did not correlate with titanium. The presence of boron, however, had a very potent effect indeed. Slight boron additions caused large drops in the free nitrogen, leading them to conclude that the most likely form of compound nitrogen would be boron nitride.

Chemical analysis (St.Laurent and L'Esperance, 1992) using EDX with a windowless detector has demonstrated large oxygen peaks associated with titanium–rich regions; little nitrogen was found, confirming the presence of titanium oxides. The analysis was on a weld containing high nitrogen and low oxygen concentrations, so that they were able to conclude that titanium in welds has a stronger affinity for oxygen than for nitrogen.

The presence of titanium oxide has therefore been directly established. However, this does not preclude TiN. It may be that both phases are present in the non–metallic inclusions found in welds, with the oxide dominating.

1.3.2.2 Aluminium based minerals

Aluminium may form a nitride in welds (Grong *et al.*, 1988), especially in flux-cored arc welding where the dominant gas in the weldpool is nitrogen and not oxygen. Various nitrogen fixing cations have been used to remove nitrogen, the most successful being aluminium (Husseen *et al.*, 1983; Grong *et al.*, 1988). Craig *et al.* (1978) failed to identify AlN in submerged arc welds, by correlating aluminium in the submerged arc weld metal with the amount of soluble nitrogen. X-ray analysis and TEM also did not reveal any AlN. Thus AlN is present in inclusions only when nitrogen is dominant in the weld atmosphere.

A glassy Al and Mn rich phase, suspected to be a silicate, has been frequently reported (Barbaro *et al.*, 1988; Maunder *et al.*, 1968; Kluken and Grong, 1989). Also a crystalline manganese/aluminium rich phase is sometimes observed (Mills *et al.*, 1987; Thewlis, 1989; Thewlis, 1993; Dowling *et al.*, 1986), with a f.c.c. structure and lattice parameter of between 8.15 and 8.3 Å. This is consistent with the mineral galaxite ($MnO.Al_2O_3$), a member of the spinel series. Galaxite has been identified as being particularly potent as a heterogeneous nucleation site for ferrite.

Aluminium oxidises before combining with any other cation. Alumina is therefore commonly found in weld non–metallic inclusions. The mineral may adopt many polymorphic forms, but the most frequently reported is the γ–form (f.c.c. $a \simeq 7.9\mathring{A}$) (Grong *et al.*, 1992; Thewlis, 1993; Saggese *et al.*, 1982).

1.3.2.3 Sulphides

Sulphur is usually in the form of manganese sulphide, copper sulphide, or a general (Mn,Cu)S. Cu_xS with $1.8 \leq x \leq 2$ has a cubic lattice with a = 5.4-5.9Å, and α-MnS has a f.c.c. structure with a = 5.2Å (Court and Pollard, 1989; Kayali *et al.*, 1983; Es-Souni *et al.*, 1990; Court and Pollard, 1985; Dowling *et al.*, 1986). Some doubt about the existence of copper sulphides in welds has been expressed by Kluken and Grong (1989), whose microanalysis experiments mapped manganese to be associated with sulphur, but a similar association was not found for copper. They suggested that the copper reported by others is due to contamination during the procedure of making extraction replicas. This is unlikely to be the case for all reported observations. Any contamination is unlikely to be in the form of crystalline copper sulphides as found by Dowling *et al.* (1986). In any case, Court and Pollard (1989) have observed copper/sulphur rich inclusions in both thin foil and extraction replica samples.

1.3.2.4 Other minerals

VN and VC exist in vanadium containing welds; even $BaZrO_3$ has been reported. BN and glassy $MnSiO_3$ have also been observed.

1.3.3 Inclusion Structure

The inclusions found in welds are usually multiphased and cored. Phases with high melting points precipitate first to form inclusion cores. Further subsequent layers are deposited with phases having successively lower melting points. The core should therefore be composed of the highly refractory oxides, surrounded by silicates, followed by sulphides (Fig 1.8).

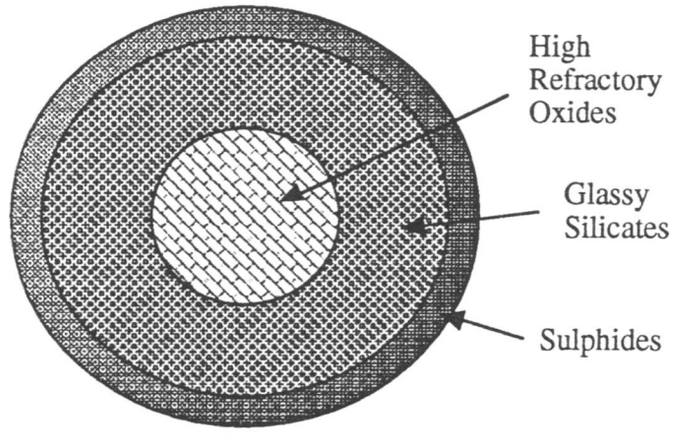

Figure 1.8 Idealised structure of a weld inclusion

Experiments show that structure is not as well defined as in Fig.1.8, but trends are evident: Es-Souni and Beaven (1990) found cores to be composed of either (Ti,Mn,Fe) silicates or galaxite. Kluken and Grong (1989), Kayali *et al.* (1983) and Thewlis (1990) all reported inclusion cores to be composed of manganese–aluminium silicates. Maunder and Charles (1968) found crystalline alumina cores, surrounded by glassy silicates, in an aluminium–rich alloy.

Many microanalysis experiments have demonstrated sulphide coatings on inclusions (Barrite *et al.*, 1981; Lathabai and Stout, 1985; Barbaro *et al.*, 1989; Kayali *et al.*, 1983).

Titanium–rich phases have been reported both in inclusion cores, and at the inclusion surface. The former occurs in the absence of more refractory oxides or silicates.

1.4 General Effects of Inclusions – The Role of Oxygen

Oxygen contamination of the molten weldpool is obviously unavoidable, and varies with the arc length and extent of shielding, together with factors such as the wind strength (Boniszewski, 1990). Oxygen content can therefore be difficult to control accurately, and even more difficult to predict. Consequently the bulk of the quantitative research has concentrated on the submerged arc process, where the welding arc is immersed in a flux which isolates the weld from the atmosphere. The constituents of the flux then become important in determining the weld chemistry.

The basicity index (B.I.) of a flux is defined as follows, where units are in wt %:

$$\text{B.I.} = \frac{\text{CaO} + \text{MgO} + \text{SrO} + \text{BaO} + \text{Na}_2\text{O} + \text{K}_2\text{O} + \text{Li}_2\text{O} + \frac{1}{2}(\text{MnO} + \text{FeO}) + \text{CaF}_2}{\text{SiO}_2 + \frac{1}{2}(\text{Al}_2\text{O}_3 + \text{TiO}_2 + \text{ZrO}_2)} \tag{1.3}$$

A lower basicity leads to a greater oxygen concentration in the weld (Cochrane and Keville, 1983; Indacochea and Olson, 1983; Cochrane *et al.*, 1986; Bailey and Pargeter, 1979). The basicity index thus offers a rather crude method for oxygen content prediction.

1.4.1 Modelling of Oxygen Incorporation in the Weld

Wegrzyn (1985) proposed that oxygen enters the weldpool in the form of molten FeO, which is not a significant constituent of normal welding flux. He suggested that molten iron can reduce some of the flux oxides, producing iron oxide, which could then be incorporated into the weld. However, iron oxide is less stable than any of the common flux oxides. The only way FeO can form in these circumstances is by the equilibrium partitioning of oxygen between the flux and the iron. Only SiO_2 and MnO have a low enough stability to be partially reduced by molten iron. Wegrzyn therefore suggested that the oxygen content of a weld can be rationalised by analysis of the SiO_2 and MnO content of the flux.

Christensen and Grong (1986) instead proposed that oxygen entered the molten weldpool purely by the dissolution of gaseous SiO into the metal droplets passing through the arc. There would be subsequent loss of dissolved Si and O from the weld on cooling, but the initial concentration should correlate with the final oxygen content. The calculated quantity of SiO that would be expected to dissolve in the weld at high temperatures was found to correlate with the basicity index. The solubility product of [Si][O], at high temperatures, behaved in exactly the same way with respect to the basicity index of the flux, as the final oxygen content of the weld (Fig 1.9).

Flux composition is, of course, not the only factor contributing to variation in weld oxygen content in submerged arc systems. The amount of time available to absorb oxygen

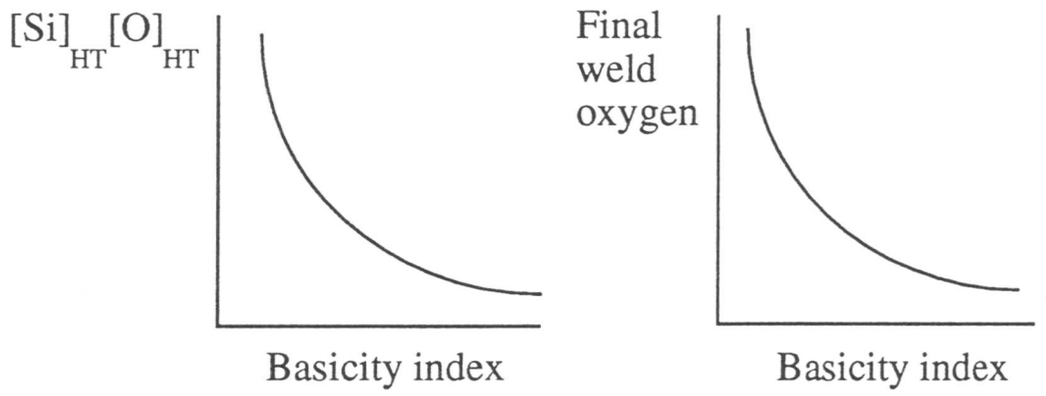

Figure 1.9 Schematic Plots indicating the similarity in the relationships between the final oxygen content with basicity index, and the $[Si]_{HT}[O]_{HT}$ concentration product with the basicity index, after Christensen and Grong (1986)

is also important, and depends on the cooling rate (in turn itself dependent on the heat input – Pargeter, 1981) and welding speed (Kawabata *et al.*, 1986).

The oxygen solubility decreases considerably to < 0.002wt% as the steel solidifies. In the absence of stronger reducing agents, the rejected oxygen will combine with carbon and form carbon monoxide bubbles, which are detrimental to the mechanical properties. Elements which prevent porosity are those which combine with rejected oxygen to form oxides which either float as slag (and are removed), or are retained as non-metallic inclusions in the solidified weld. The bulk of the inclusions present in the welds are therefore oxides, and the concentration of oxygen initially present in the molten weldpool will control their number and volume fraction.

1.4.2 Oxygen and Weld Microstructure

It is established that weld microstructure can be sensitive to oxygen. A low oxygen content (and hence low inclusion content) can be associated with a microstructure which is often predominantly bainitic. Medium concentrations favour the development of acicular ferrite, though excessive oxygen enhances the allotriomorphic ferrite or Widmanstätten ferrite fractions. This is because of the interaction of oxide inclusions with the development of microstructure. Inclusions have two main roles in the weld metal. Firstly, they are nucleation sites for ferrite, and secondly they may be of importance in pinning austenite grain boundaries.

If the inclusion population is small, then transformation nucleates predominantly on

the austenite grain boundaries. As the inclusion number density is increased, more sites become available for intragranular nucleation, leading to the formation of acicular ferrite, in appropriate circumstances. With excessive oxygen, grain boundary pinning causes a reduction in the austenite grain size, and a corresponding increase in the number density of grain boundary sites. The net result is that nucleation occurs more at grain boundary sites allowing allotriomorphic or Widmanstätten ferrite to dominate the microstructure.

These general observations are attributed to: Ito and Nakanishi (1976), Abson *et al.* (1978), Barrite and Edmonds (1981), Barrite *et al.* (1983), Kawabata *et al.* (1986), Watanabe and Kojima (1980), Bailey and Pargeter (1979), Ito *et al.* (1981), Terlinde *et al.* (1984).

The oxygen concentrations required to produce the different microstructures are dependent on many factors, but are roughly as follows:

$\leq$ 150ppm produces grain boundary dominated microstructure
$\sim$ 200-300ppm can produce a predominantly acicular ferrite microstructure
$\geq$ 350ppm produces grain boundary dominated microstructure.

Most of the papers mentioned above, also observed some austenite grain refinement, caused by large inclusion populations. However, it is important to distinguish between those experiments in which the weld specimens are reheated (Harrison and Farrar, 1981; Ferrante and Ferrar, 1982), from those made on the as–welded deposit. Grain growth during reheating is controlled by surface energy, whereas the austenite structure that evolves during welding is driven by transformation from δ–ferrite. Bhadeshia *et al.* (1986) found that in as–welded deposits the oxygen content had little effect on the size of the columnar austenite grains. However, Barrite *et al.* (1981), Liu and Olson (1986), Terlinde *et al.* (1984), Fleck *et al.* (1986) and North *et al.* (1990), presented contradictory evidence and the subject needs more investigation.

1.4.3 Inclusion Size and Shape

Opinions vary as to how oxygen affects the average size of weld inclusions. Kluken *et al.* (1988), Pargeter (1981), Lathabai and Stout (1985), Cochrane *et al.* (1986) and Mills *et al.* (1987) claim that an increase in the oxygen content is associated with coarser inclusions, while Tsuboi and Terashima (1983), and Lui and Olson (1986) claim the opposite.
Terlinde *et al.* (1984) felt that there was no significant variation in the average inclusion

size with oxygen.

However, inclusion size observations are limited by the resolution of techniques used, and it would seem that Liu and Olson offered the most rational interpretation of the oxygen effect on inclusion size. They suggested that the concentration of oxygen in the weldpool controls the nucleation frequency of oxide inclusions. High supersaturations lead to greater nucleation rates and a consequential drop in the mean inclusion size. Nevertheless, they were anxious about the many contrary results published. They suggested that their result was the product of a greater resolution of analysis than had previously been used. To test this hypothesis they then re-analysed their specimens, only noting the behaviour of the inclusions of diameter $\geq 0.2\,\mu$m (a size approximating to the resolution available in previous work). Their original observations included particles down to $0.08\,\mu$m in size. They found that the mean diameter of those particles $\geq 0.2\,\mu$m did indeed increase as the oxygen content increased. However, when those of smaller diameter were included in the statistical analysis, the overall mean diameter reduced on increasing oxygen (Fig 1.10).

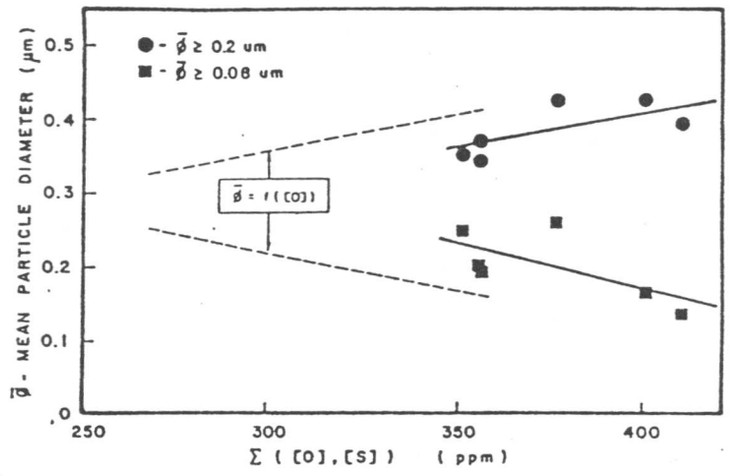

Figure 1.10 Plot showing the inclusion mean diameter results obtained by Liu and Olson (1986). When only those inclusions $\geq 0.2\,\mu m$ in size were considered, inclusion diameter was observed to increase with increased oxygen content in the weld. However, when all the inclusions observed were taken into consideration, the overall mean diameter of the inclusions was observed to decrease with increasing oxygen content.

Oxygen also affects the shape of the inclusions present. Low concentrations are usually associated with facetted inclusions, whereas high oxygen concentrations more often lead to a spherical or globular shape.

The general effects of oxygen are summarised in the flow chart presented below

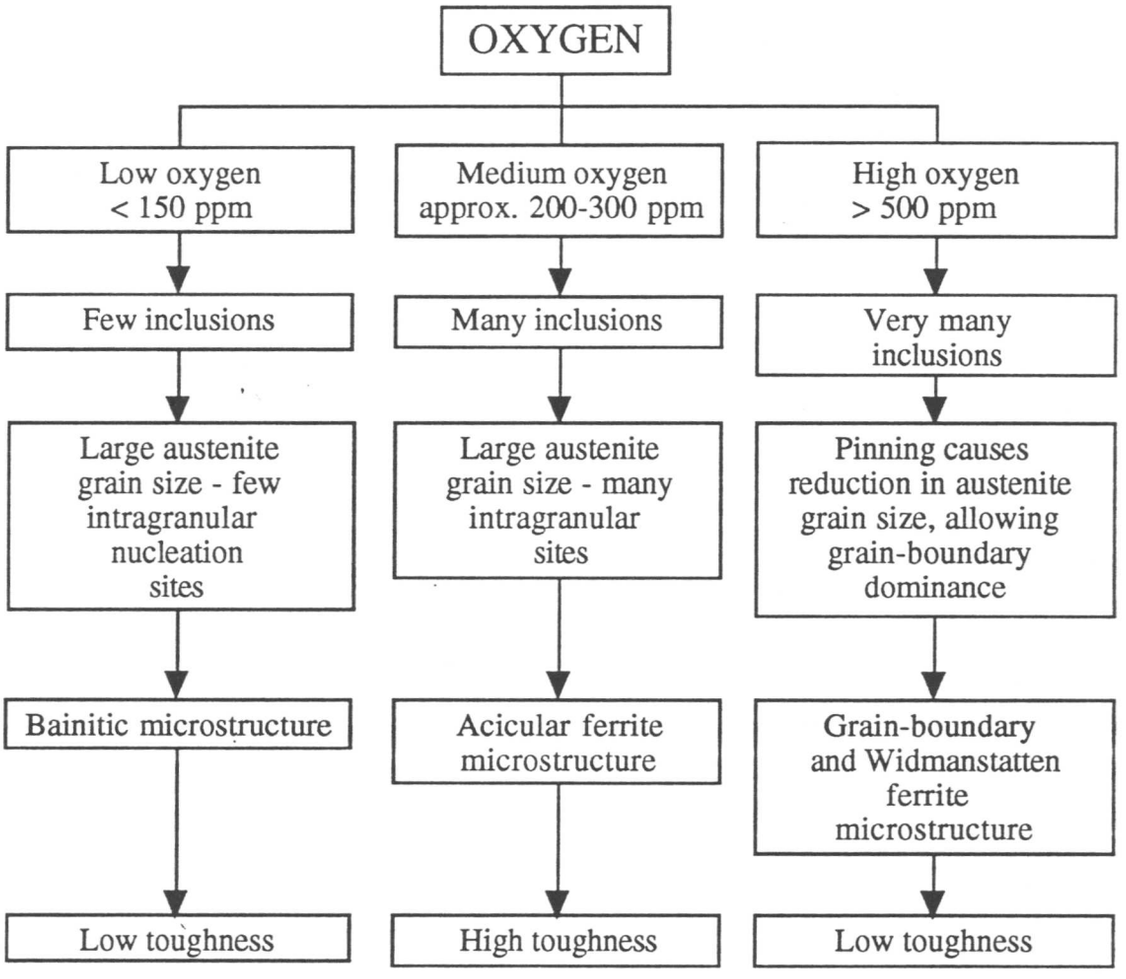

Figure 1.11 Flow chart summarising the effect of various oxygen levels on the microstructure and toughness of steel welds.

1.5 Role of Specific Minerals

The activity of inclusions in changing microstructure is dependent on their specific mineralogy.

1.5.1 The Titanium Phases

Titanium based inclusions seem to be particularly effective in nucleating ferrite. Bramfitt (1970) highlighted the importance of TiN and TiC in causing nucleation from the melt. This is not necessarily relevant to transformations in the solid state since solidification is unconstrained, whereas ferrite has to grow with a particular orientation relationship with austenite. Nevertheless in his experiments an alumina rod coated in particles of a pure phase, such as TiN, was lowered into a crucible of molten iron. The iron was allowed to cool at a constant rate, and the extent of undercooling required to cause its solidification was noted. TiN and TiC caused a marked decrease in the undercooling.

Willingham and Bailey (1975) tried to cause ferrite nucleation from the molten state in welds doped with inclusions. TiB_2 was found to cause a change from the columnar microstructure expected, to an equiaxed microstructure indicating that it had been responsible for ferrite nucleation.

The effect on the solid–state nucleation of ferrite seems almost as dramatic, although the exact chemistry of the phase still remains uncertain, as discussed previously. Numerous researchers have found that a microstructure initially poor in acicular ferrite, on addition of titania in the flux, or titanium in the welding wire, becomes acicular ferrite dominated. (Terashima and Hart, 1983; Pargeter, 1981; Saggese *et al.*, 1982; Bailey, 1983; Suzuki *et al.*, 1985; Cochrane *et al.*, 1986; Bailey, 1986; Es-Souni and Beaven, 1990; Thewlis, 1990; Es-Souni *et al.*, 1991; Fleck *et al.*, 1986; St.Laurent and L'Esperance, 1992). This has been attributed to the titanium phase becoming dominant in the weld inclusions.

However, Kayali *et al.* (1983) and Dowling *et al.* (1986) found that, although initial increases in titanium additions caused increased acicular ferrite, for high levels of titanium, the microstructure became bainite dominated. This effect was also noted by Horii *et al.* (1988). Liao and Liu (1992) made the same observation, but noted that the increases in titanium levels were associated with decreases in the austenite grain size. Decreased austenite grain size would be expected to favour grain boundary nucleated phases over intragranular phases, and would therefore explain the observed dominance of bainite over acicular ferrite.

That titanium additions are the sole factor in their apparent effectiveness in stimulating acicular ferrite has been questioned by Dowling *et al.* (1986). They found no correlation

between the overall Ti content in the inclusions and the volume fraction of acicular ferrite. They therefore suggested that although the titanium phase certainly seemed to contribute to acicular ferrite, its presence alone is not sufficient. Other workers have noted that, although titanium additions by themselves do cause some microstructural refinement, the effects are enhanced by the addition of boron (Watanabe and Kojima, 1980; Fleck *et al.*, 1986) or by the presence of galaxite in inclusions as a substrate for the titanium phase (Thewlis, 1990, 1993).

The question arises as to whether it is the titanium nitride or oxide which is the key to stimulating nucleation. In a classic experiment by Homma *et al.* (1987), a cast steel was doped with Ti_2O_3 particles, and another with TiN particles. The steel containing the oxide particles was found to be rich in acicular ferrite, whereas that with nitrides was devoid of any acicular ferrite. The obvious conclusion, then, was that titanium oxides are active in the nucleation of acicular ferrite, but the nitrides are not.

1.5.2 The Role of Alumina and Aluminium-Rich Phases

Some researchers claim that the presence of aluminium improves weld toughness, whereas others claim the exact opposite. The effect of aluminium addition is critically dependent on the levels of oxygen present.

Aluminium is the most powerful reducing agent commonly found in welds and therefore is likely to oxidise before any other element. If the oxygen concentration is low, and the aluminium concentration is high, then alumina dominates the inclusion population. Alumina seems not to be a potent nucleant for acicular ferrite, and hence causes low toughness and a mainly bainitic microstructure. Researchers who have examined the effect of aluminium at low oxygen levels have therefore found it detrimental to mechanical properties (Oldland and M^{c}Pherson, 1984; Suzuki *et al.*, 1985; Harrison, 1987; Horii, 1988; Thewlis, 1993).

At greater levels of oxygen, the aluminium concentration required to bind with all the available oxygen becomes prohibitively large. Any increase in aluminium should, therefore, have little effect on inclusion efficacy. However, alumina does not mix well with the weld-pool, the alumina–steel interface being of high energy (Kluken *et al.*, 1990). Alumina–rich particles then tend to coagulate more than alumina poor particles, attempting to reduce the overall inclusion–steel interfacial area. In an aluminium–rich weld, the inclusions are therefore fewer and larger than in a corresponding aluminium–poor weld (Terashima and Hart, 1983; Thewlis, 1989; Liao and Liu, 1992). The effectiveness of inclusions, as pinning sites, is directly proportional to their volume fraction, and inversely proportional to their

diameter. The larger inclusions, associated with high aluminium levels, are not effective in pinning grain boundaries. This is beneficial since the number density of grain boundary nucleation sites is reduced. Thus at high oxygen levels, aluminium has been observed to be beneficial to the development of an intragranular microstructure (Saggese *et al.*, 1982; Cochrane *et al.*, 1986).

Devillers *et al.* (1983) summarised the aluminium effect. They found that the toughness maximum, commonly observed with increasing oxygen content, shifted to higher oxygen levels with increasing aluminium in the welds. (*i.e.* for a given constant oxygen concentration below that of the maximum toughness (low oxygen), increasing aluminium caused a reduction in toughness. For a given constant oxygen concentration greater than that of maximum toughness, increasing aluminium caused an increase in toughness.) Aluminium is obviously critical in determining the extent to which acicular ferrite may form, and its effect must be considered in relation to the oxygen content in the weld. Because of the complexity of the aluminium effect, a flow diagram is presented below which summarises the interpretation given (Fig 1.12).

Despite the apparent low efficacy of alumina in nucleating ferrite in the solid state, it does seem that it may nucleate ferrite from the melt. Kluken *et al.* (1990), believed that alumina is an active nucleating agent for the solidification of ferrite from the melt. They found a progressive refinement of grain structure in welds as the fraction of alumina in the weld inclusions was increased. This refinement continued until the inclusions were virtually 100% alumina, and then ceased. They also claimed that alumina nucleated austenite in the solid state.

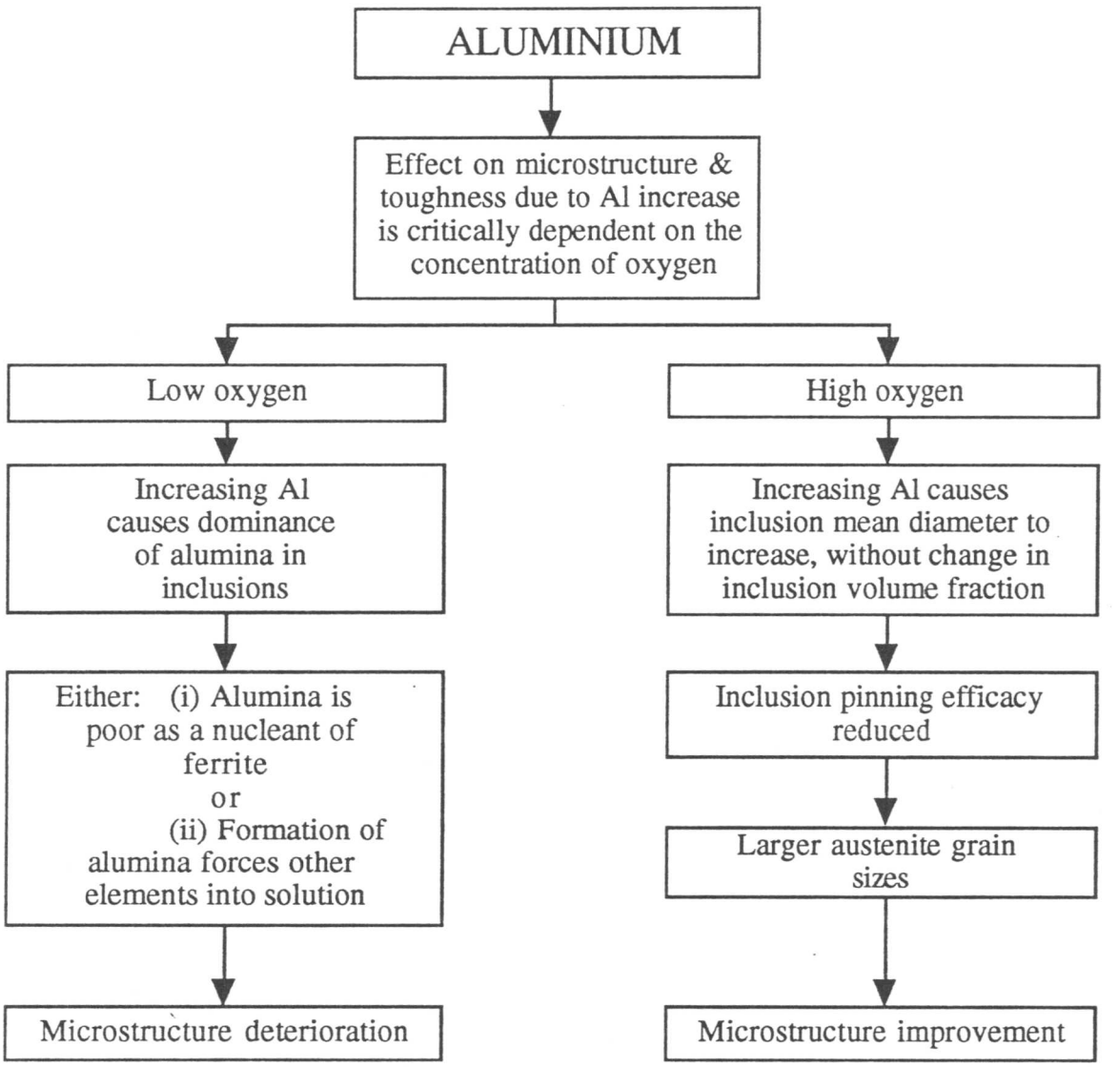

Figure 1.12 Flow chart summarising the possible effects of aluminium on the microstructure of steel welds.

There have been several suggestions that galaxite has a particularly important role in the nucleation of acicular ferrite. Thewlis (1990) examined the effects of various concentrations of Ti and B on weld microstructure. In low Ti/B welds the presence of galaxite caused a significant increase in the start temperature for the austenite to ferrite transition and was thus concluded to be effective in promoting ferrite nucleation. In high Ti/B welds the presence of TiO/TiN as surfaces on galaxite substrates caused a marked increase in the transformation temperature and rapidity. This may have been attributed to the TiO/TiN effect alone, but when the TiO/TiN surfaces were present on $MnSiO_3$ substrates the kinetic effect in assisting the austenite to ferrite transition was not so great. Best results in assisting the transformation were thus obtained when both TiO/TiN and galaxite were present.

Dowling *et al.* (1986) examined the overall content of TiX (where X=O,N or C) in the sample welds, and found that, although the phase seemed to aid the formation of acicular ferrite, the correlation between overall content and acicular ferrite volume fraction was poor. Correlation between the galaxite present and the volume fraction of acicular ferrite was, however, very good, and led to the suggestion that galaxite was extremely important as a nucleating phase.

1.5.3 The Effect of Boron

Fleck *et al.* (1986) systemmatically varied the composition of welds, and observed the volume fraction of acicular ferrite produced. Without additions of Mo, Ti or B, the volume fraction of acicular ferrite was found to be 0.26. Mo additions alone did not alter this value, but when Ti was also added, 0.5 acicular ferrite was produced. Further addition of boron, however, increased the acicular ferrite yield to 0.85.

Dowling *et al.* (1986) suggested two possible reasons for the observed effect of boron:
(i) That boron oxides or nitrides may be particularly active in causing ferrite nucleation (Ito *et al.*, 1982).
(ii) That boron may segregate to austenite grain boundaries in the steel, so reducing the energy yield on destruction of the boundaries, when ferrite nuclei are produced.

Certainly BN precipitation may occur (Mori *et al.*, 1981; Thewlis, 1989; Horii *et al.* 1988; Kawataba *et al.*, 1986). However, most research indicates that the precipitation o boron–rich particles is detrimental to acicular ferrite production, because of the remova of boron from solution (Oh *et al.*, 1991; Watanabe and Kojima, 1980; Thewlis, 1993) Yamamoto *et al.* (1993) have observed the segregation of boron to austenite grain bound aries, and such segregation has been found to considerably reduce levels of grain boundar

ferrite (Bailey, 1986; Thewlis, 1993), so allowing maximum development of acicular ferrite.

1.5.4 The Sulphides

Sulphur in solution, and in the form of sulphides is not beneficial to weld toughness. Few researchers have reported an increase in the acicular ferrite content with the presence of sulphide phases in inclusions (Ochi *et al.*, 1988). In fact the opposite is true. Abson *et al.* (1978) laser reheated welds in order to examine the microstructural effects caused by a reduction in the weld oxygen levels. They found a large reduction in the volume fraction of acicular ferrite. However, they also noted that although oxygen levels had been reduced the volume fraction of inclusions had changed little, due to an influx of sulphur. Consequently the sulphides did not stimulate acicular ferrite. Cochrane (1986) claimed that an increase in MnS reduces acicular ferrite content, and Dowling *et al.* (1986) claimed a similar effect for Cu_xS. It is therefore safe to conclude that there is no evidence that either MnS or Cu_xS are useful in causing the formation of acicular ferrite.

1.5.5 Phosphorus

Phosphorus is not desirable in welds because it causes embrittlement. However, Kluken *et al.* (1990) have claimed that phosphorus, segregated to grain boundaries, inhibits the nucleation of grain boundary ferrite, and thus promotes the formation of acicular ferrite in a similar way to boron.

In contradiction, Narayen and Goldstein (1983) observed in Fe-Ni-P alloys that grain boundary ferrite could only be produced if phosphorus remained at grain boundaries.

1.6 Importance of Inclusion Size

Several workers have claimed that the size distribution of the inclusions in welds is crucial in determining the nucleating potential of the inclusion population (Barbaro *et al.*, 1989; Jang and Indacochea, 1987). Jang and Indacochea (1987) claimed that inclusions $<0.3\mu$m in diameter would cause grain boundary pinning, and not ferrite nucleation. Inclusions $>0.3\mu$m but $<0.6\mu$m in diameter would be effective in causing intragranular nucleation, while larger ones would nucleate blocky ferrite only, and not the desired acicular ferrite. These claims are largely unsubstantiated.

Experiments by Terishima and Hart (1980) showed that the size of the inclusion population varied in the same manner on addition of aluminium and on addition of titanium. Aluminium additions, however, were associated with reductions in acicular ferrite, while titanium additions were associated with acicular ferrite increases. St. Laurent and L'Esperance (1992) examined two series of welds. One series had systemmatic variations in titanium content, while the other varied in sulphur content. They found that when variations in the levels of titanium occurred, the size, and number density, of the inclusions was secondary in importance to inclusion chemistry, in determining the extent of intragranular nucleation. They did demonstrate a slight size effect, but this was only observed when titanium additions were kept constant. Inclusion mineralogy seems therefore to be the most critical factor influencing acicular ferrite production – size and number density of inclusions being less important.

1.7 Mechanisms of Inclusion Effects

The important effects of inclusions are their ability to nucleate ferrite and to pin grain boundaries. Pinning is well understood, however the mechanisms by which inclusions stimulate nucleation are not. This section is therefore devoted to nucleation problems.

There are five main theories, each of which is discussed below:

1.7.1 Lattice Matching

According to the lattice matching theory, a nucleating agent may be effective in promoting nucleation when the atomic surface structures in low–index crystallographic planes of both the substrate (s) and the nucleated solid (n) are similar. Structural similarity across the interface plane reduces the energy barrier to nucleation. The extent of the differences between two structures across a potential interface is usually calculated according to a method given by Bramfitt (1970):

$$\delta^{(hkl)_s}_{(hkl)_n} = \frac{1}{3}\sum_{l=1}^{3}\left(\frac{d_{[uvw]^l_s}cos\theta - d_{[uvw]^l_n}}{d_{[uvw]^l_n}}\right) \times 100$$

$\delta^{(hkl)_s}_{(hkl)_n}$ = lattice mismatch between two planes
$(hkl)_s$ = low index plane of the substrate
$(hkl)_n$ = low index plane of nucleated solid
$[uvw]_s$ = low index direction in $(hkl)_s$
$[uvw]_n$ = low index direction in $(hkl)_n$
$d_{[uvw]_s}$ = interatomic spacing along $[uvw]_s$
$d_{[uvw]_n}$ = interatomic spacing along $[uvw]_n$
θ = the angle between $[uvw]_s$ and $[uvw]_n$

This method compares the interatomic spacings across the interface resolved along three different directions in the interface plane. The differences between interatomic spacings are normalised and averaged over the three directions. The 'disregistry' is then expressed as a percentage. Results of disregistry analysis are shown in Table.1.1 (after Mills *et al.*, 1987).

As can be seen from the table, minerals such as TiN, TiO, γ-Al_2O_3, or galaxite can offer surfaces of low disregistry with ferrite. Indeed, direct observation of lattice matching involving some of these phases has been made by Grong *et al.* (1992) (Table.1.2).

There are, however, several criticisms of the lattice matching theory. Firstly, the crystallography of acicular ferrite is constrained by the crystallography of the austenite

Parallelism (ferrite‖substrate)		Extent of disregistry (%)						
Planar	Directional	TiO	γ-Al_2O_3	Galaxite	TiN	BN	CuS	MnS
{100} ‖ {100}	< 100 >‖< 110 >	3.0	3.2	1.8	4.6	10.7	37.4	29.0
{110} ‖ {100}	< 100 >‖< 110 >	22.0	16.7	20.5	23.9	12.9	62.7	52.7
{100} ‖ {110}	< 100 >‖< 110 >	24.4	19.0	22.8	26.3	14.9	65.9	55.7
{110} ‖ {110}	< 100 >‖< 110 >	37.4	33.3	35.6	39.5	33.3	83.2	72.0
{111} ‖ {110}	< 110 >‖< 100 >	14.6	9.8	13.2	16.4	6.5	52.8	43.5
{100} ‖ {111}	< 100 >‖< 110 >	34.5	28.5	32.8	36.5	23.7	79.3	68.3
{110} ‖ {111}	< 100 >‖< 110 >	15.9	11.0	14.4	17.6	7.5	54.5	45.0
{111} ‖ {111}	< 110 >‖< 110 >	27.2	31.5	28.0	26.0	36.9	2.8	8.8
{111} ‖ {100}	< 110 >‖< 110 >	20.8	23.6	20.9	20.6	29.6	16.5	17.6

Table 1.1 Summary of the extent of lattice disregistry between various minerals and ferrite, calculated according to Bramfitt (1970). After Mills *et al.* (1987).

from which displacive transformation occurs. Nucleating substrates must therefore be of specific orientations if they are to produce nucleation. It has never been established that a randomly oriented population of non–metallic inclusions could provide enough suitable nucleation surfaces to create acicular ferrite. Secondly, some inclusion phases such as γ-Al_2O_3 offer reasonably good lattice matching, and yet experimentally are found to be associated with poor yields of acicular ferrite (Oldland and M^{c}Pherson, 1984; Suzuki *et al.*, 1985; Harrison, 1987; Horii, 1988; Thewlis, 1993).

1.7.2 Inert Surface

This theory suggests that any surface may assist nucleation (*e.g.* Barbaro *et al.*, 1988). However, since some inclusion surfaces have been shown to be more efficient in causing ferrite nucleation than others (*e.g.* TiO/TiN), the model seems inconsistent with experimental data.

1.7.3 Inclusion–caused Mn depletion

As discussed earlier, many inclusions have been observed to possess surface coatings of MnS. This MnS is likely to precipitate from the steel at a fairly late stage in the cooling of

Inclusion phase	Parallel planes & directions	
	Mineral	Ferrite
γ-Al_2O_3	(100)	(011)
	$[01\bar{1}]$	$[5\bar{3}3]$
$MnAl_2O_4$	(200)	(110)
$MnAl_2O_4$	(011)	(010)
	$[0\bar{1}1]$	[001]
TiN	$(\bar{1}10)$	(100)
	(112)	(011)
	$[11\bar{1}]$	$[0\bar{1}1]$
TiN	$(10\bar{1})$	$(\bar{1}03)$
	(320)	(112)
	$[2\bar{3}2]$	$[3\bar{5}1]$
TiN	(110)	$(\bar{1}33)$
	(221)	(200)

Table 1.2 Summary of orientation relationships experimentally established by Grong *et al.* (1992).

the weld. The resulting depletion in the adjacent matrix may stimulate nucleation, since manganese is an austenite stabiliser.

Evidence for such manganese depletion, based on EDX examination, has been sought by several workers (notably Barrite *et al.*, 1981; Barbaro *et al.*, 1988). Depletion zones have not been found (Fig.1.13), but the techniques used may not have had sufficient resolution, and some (notably Yamamoto *et al.*, 1993) still advocate this nucleation mechanism.

1.7.4 Inclusion–caused carbon depletion

It has been suggested by Es-Souni and Beaven (1990), and Es-Souni *et al.* (1991) that the nucleation properties associated with the titanium–rich phase TiX are actually due to carbon absorption by TiN forming a member of the Ti(C,N) solid solution. Diffusion of carbon into inclusions would result in a carbon–depleted zone in adjacent matrix which may stimulate nucleation, since carbon stabilises austenite.

Ochi *et al.* (1988) examined microalloying effects on Mn, S, V and N containing steels.

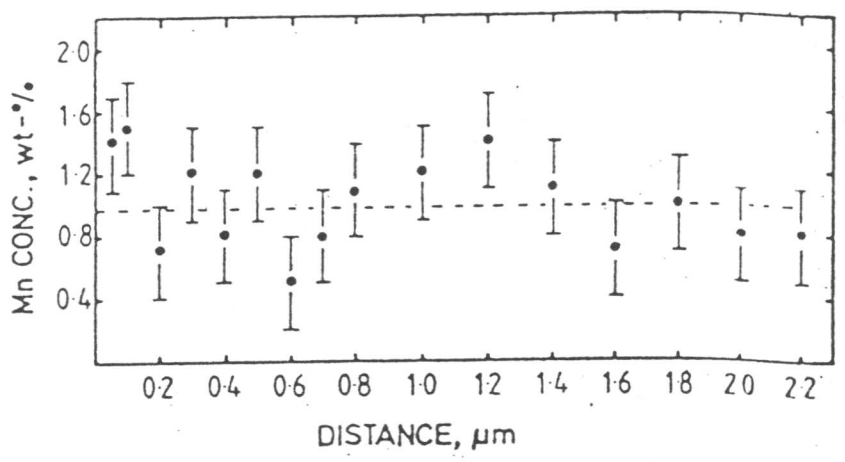

Figure 1.13 Mn concentration profile away from an inclusion which possessed a manganese sulphide coating (after Barrite *et al.*, 1981). No locally depleted zone surrounds the inclusion, within the limits of resolution.

They found intragranular ferrite to be associated with the precipitation of V_8C_7 particles. Such carbide precipitation could well have caused local carbon depletion, but such analysis may only be speculative. This, indeed, is the problem in investigating the likelihood of carbon depletion inducing nucleation, since, so far, no actual carbon profiles have been measured. Additionally, intragranular bainite formation will cause carbon rejection from the ferrite, so that the profile present at the time of transformation cannot be preserved.

1.7.5 Tessellated Stresses

Tessellated stresses arise when two materials, with different physical properties are present together in a mechanical mixture. In steel welds, the inclusions have lower thermal expansivity than austenite, so that stresses are induced during cooling in both the inclusions and the surrounding steel. It has been suggested that such tessellated stresses may be responsible for causing a greater drive to form ferrite adjacent to inclusions than elsewhere in the weld, since transformation from austenite may allow stress relief (Barrite and Edmonds, 1981; and Barrite, 1983).

For reference Table 1.3 shows the expansion coefficients of various mineral types.

Mineral	Coeff. of thermal expansion /K^{-1}	Temp. range of measurement /K	Reference
SnO_2	4 x 10^{-6}	273–1073	[1]
	3.76 x 10^{-6}	295–923	[1]
NbC	7 x 10^{-6}	–	[2]
Al_2O_3	8.0 x 10^{-6}	293–1853	[1]
	8.4 x 10^{-6}	293–1273	[1]
	7.5 x 10^{-6}	1273–1573	[1]
	a-axis: 7.1 x 10^{-6}	373	[1]
	a-axis: 9.7 x 10^{-6}	773	[1]
	a-axis: 14.2 x 10^{-6}	1273	[1]
	c-axis: 6.0 x 10^{-6}	373	[1]
	c-axis: 8.9 x 10^{-6}	773	[1]
	c-axis: 13.8 x 10^{-6}	1273	[1]
$MnAl_2O_4$	8 x 10^{-6}	273–1073	[3]
$SrTiO_3$	8.9 x 10^{-6}	273–1080	[4]
TiN	9.4 x 10^{-6}	273–1073	[3]
TiO_2	9.5 x 10^{-6}	273–1080	[4]
	7.8 x 10^{-6}	293–873	[1]
	8.19 x 10^{-6}	273–773	[1]
$CaTiO_3$	1.2 x 10^{-5}	273–1700	[4]
TiO	1.4 x 10^{-5}	273–1400	[4]
MnS	1.8 x 10^{-5}	273–1073	[3]
Austenite	2.3 x 10^{-5}		[3]

Table 1.3 The coefficient of thermal expansion of a selection of minerals. References [1,2,3,4] are as follows: [1] – Samsonov (1973), [2] – Barantseva (1974), [3] – Brooksbank and Andrews (1972), [4] – Goldsmith *et al.* (1961).

1.8 Summary

Cooling steel may undergo a variety of solid–state phase transformations, both reconstructive and displacive. The products of each transformation vary in size and shape. Such microstructural variations affect the physical and mechanical properties of the final steel.

Acicular ferrite is a transformation product which is of great benefit to steel toughness. It is composed of fine interlocking plates, which nucleate heterogeneously on non–metallic inclusions. Therefore, for acicular ferrite production, inclusions are desirable. However, cracks frequently initiate at inclusions so that, although necessary for acicular ferrite to occur, the presence of too many inclusions could be detrimental for mechanical properties. It is therefore desirable to produce acicular ferrite with the minimum number of inclusions.

Some inclusion types are more potent at causing nucleation than others. For example, alumina–rich inclusions are relatively ineffective nucleants, in contrast to titanium–rich inclusions. Obviously the inclusion population should be designed so that its nucleation potency is high. However, the research to date has failed to fully identify the phases of exceptional potency. Also the dominant mechanism of nucleation is not well understood.

The reason for uncertainty is because of the complex nature of real inclusions and real weld systems. Ideally, inclusion–induced nucleation should be investigated in much less complicated systems, with pure single phase mineral powders. Such has been the aim of this project.

CHAPTER 2

Experimental Methods

2.1 Materials

2.1.1 Alloys

The compositions of the alloys used are shown in Table 2.1. Alloy A5763 was used for most of the experiments. Its relatively high silicon content supressed the formation of cementite during the bainite transformation. The carbides could, themselves interfere with the experiments by stimulating heterogeneous nucleation. This would interfere with the aim of studying nucleation from pure mineral phases. The manganese and carbon concentrations in A5763 gave sufficiently high hardenability to allow bainite to form without interference from higher temperature reactions, such as the allotriomorphic ferrite transformation. The alloys A5763 and A5762 were received in the form of 10 mm diameter rods. IC373 (a duplex stainless steel) was received in sheet form, ~ 4 mm in thickness.

Alloy	C	Si	Mn	Cr	Ni	Mo	B	O (ppm)	N (ppm)
A5763	0.204	1.95	1.54	0.00	0.01	0.00	0.0016	8	7
A5762	0.3	0.15	<0.02	—	—	4.20	—	—	—
IC373	0.026	0.5	0.67	25.9	5.1	3.65	—	—	1420

Table 2.1 Chemical compositions (wt %) of the alloys used. Oxygen and nitrogen concentrations are shown in ppm by weight.

2.1.2 Mineral Powders

Mineral powders were obtained from commercial chemical synthesis companies. The mineral types used, their minimum purities, and the chemical suppliers used are summarised in Table 2.2. Mineral particle sizes were not often stipulated, and were not measured during the course of this work.

Mineral type	Minimum purity	Commercial supplier
TiO_2	unknown	unknown
PbO_2	$\geq$99%	Johnson Matthey
MnO_2	$\geq$99%	Ventron
SnO_2	$\geq$99.9%	Johnson Matthey
MoO_3	$\geq$99.5%	Johnson Matthey
WO_3	$\geq$99%	Johnson Matthey
V_2O_5	$\geq$99%	Johnson Matthey
KNO_3	$\geq$99%	BDH
TiO	$\geq$99%	Ventron
Ti_2O_3	$\geq$99%	Johnson Matthey
Cr_2O_3	$\geq$99%	Johnson Matthey
V_2O_3	$\geq$99%	Aldrich
TiN	$\geq$99%	Johnson Matthey
$CaTiO_3$	$\geq$99%	Johnson Matthey
$SrTiO_3$	$\geq$99%	Johnson Matthey
α-Al_2O_3	$\geq$99%	Fisons
γ-Al_2O_3	$\geq$99.99%	Johnson Matthey
NbC	$\geq$97%	Aldrich
MnS	$\geq$99.9%	Johnson Matthey

Table 2.2 Summary of information for the various chemical powders used.

2.2 Thermal and Mechanical Processing

2.2.1 Furnace Treatment

An electrical resistance heated furnace was employed for any long term heat treatments, or for specimens not suitable for the thermomechanical simulator (described below). For furnace heat treatments, samples were first sealed in silica tubes under partial pressure of argon ($\sim$ 150 mm Hg) to minimise decarburisation or oxidation. The quartz tubes were then placed on ceramic boats inside the furnaces, to prevent any contamination by contact with the base of the furnace.

2.2.2 Thermomechanical Simulator

Most heat treatments required considerably more control than was possible using furnaces; mechanical stress was often required to allow intimate ceramic–steel bonding. Accurate thermal and mechanical control was made possible by the use of a thermomechanical simulator (Thermecmastor, manufactured by Fuji Electronic Industrial Co. Ltd.). This equipment is computer–controlled, with computer data collection of strains (measured in two orthogonal directions), stress and temperature. The sample is heated by an RF-induction heating coil, in an environmental chamber. Standard thermal and mechanical treatment involved spot–welding a Pt / Pt–13 wt.% Rh thermocouple to the steel specimen and placing it between the two ram–heads within the specimen chamber. The ram–heads were then lowered so that the specimen was held in place, surrounded by the RF-induction heating coil. The environment chamber was then evacuated to a pressure of $\sim 2 \times 10^{-2}$ Pa before commencing the experiment.

Controlled quench rates of up to $50^{\circ}\mathrm{C\,s^{-1}}$ (between 1200°C and $\sim$ 100°C) were possible using He cooling gas. N_2 could also be used as a gas coolant, but could not give cooling rates as high as He. The Thermecmastor also allowed a rapid water–quench, water being directed at the specimen from small jet–holes in the RF–coil. Water quenching produced cooling rates of upto $\sim$ $400^{\circ}\mathrm{C\,s^{-1}}$.

The standard steel specimen size required by the machine for compressive or unloaded testing, was a cylinder, 8 mm in diameter and 12 mm long. In some cases, specimens of these dimensions were impossible to obtain, but this did not seriously impair treatment in the Thermecmastor.

2.3 Analysis Techniques

2.3.1 Microstructural Observations

Specimens were prepared for general microstructural observation, using both optical and scanning electron microscopy (SEM), by sectioning using a Struers Accutom–2 high speed precision saw. Sectioned specimens were then hot–mounted in conductive bakelite, ground on SiC paper (1200 grit–size), and polished using 6 μm diamond paste. The low–alloy steels A5763 and A5762 were etched in 2% Nital (nitric acid in methanol), while the duplex stainless steel IC373 was etched in a solution containing 50 ml methanol, 30 ml HCl and 12.5 g $CuCl_2$.

Grain–boundary etching was carried out on A5763, and was successful with a picric acid based solution: 40 g picric acid, 990 ml distilled water and 2 ml liquid detergent (*Fairy*

liquid). The etchant was heated to ~50°C and clear grain boundary definition was obtained after ≃45 s etching.

Optical micrographs were taken on an Olympus microscope, with camera attached, using Ilford PanF film. SEM microstructural investigation was carried out on a CamScan S2 microscope, and micrographs were taken using Ilford FP4 films.

2.3.2 Transmission Electron Microscopy

2.3.2.1 Thin-foil Preparation

The majority of thin foils were prepared as follows: a slice of the specimen ≃200 μm thick was cut using a Struers Accutom–2 high speed precision saw. It was then mounted on a brass block and ground on fine SiC paper (1200 or 800 grit) to ≃75 μm thickness. Undistorted 3 mm discs were punched from the ground slice using a specialised foil–punch. The discs were then jet–polished to electron transparency at ≃50 V with the polishing solution being cooled to -5°C using liquid nitrogen. The polishing solution contained 5% perchloric acid, 20% glycerol and 75% industrial methylated spirits.

However, certain specific Transmission Electron Microscope (TEM) investigations were also undertaken on the steel–mineral interface area produced on pressure bonding, for which cross-sectional thin-foils were prepared. Slices were cut in the same way as described above, and ground down to ≃100 μm before punching discs such that the mineral–steel interface lay as a diameter of the foil. The discs were then ground to 50 μm thickness. A concave dimple was made in the centre of the foil, so that the interface area would thin preferentially during ion–beam milling.

Two methods of dimpling were tried:
(i) Chemical dimpling – performed using a solution of 40% perchloric acid, 35% glycerol and 25% ethanol, gravity fed with a voltage applied to the region being dimpled.
(ii) Mechanical dimpling – performed on a mechine with diamond paste abrasive.
Both methods were successful in producing a smooth hollow ≃25 μm deep in the interface area. Ion–beam milling was then performed to achieve electron transparency in the region of interest.

2.3.2.2 Extraction Replica Preparation

Replicas allow chemical analysis, diffraction analysis and the general investigation of non–metallic particles without interference from the steel matrix. Magnetic foil–electron beam interactions on the TEM are also avoided. The replica was amorphous, and so did not seriously impede the taking of crystalline particle diffraction patterns.

Carbon extraction replicas were prepared from surfaces etched slightly deeper than is usual for optical microscopy, to allow easy particle removal from the steel. A carbon coating of 200–300Å (a blue–brown colour) was evaporated onto the sample in a vacuum of 10^{-5} torr. The deposited film was scored using a razor blade, and then removed by electrolytic etching in a solution containing 5% HCl in methanol at +2.5 V. The detachment of the film from the metal could be observed as blistering occurred. The film was then washed in industrial methylated spirits and floated–off on the surface of distilled water. Sections of floating film were collected on 400 square mesh copper grids for examination using TEM.

2.3.2.3 Diffraction Patterns

For ease of interpretation, diffraction patterns from crystalline inclusions in steels were taken along simple crystallographic zone axes. Rotation of the specimen relative to the electron beam, in order to sample such zones, involved tilting about two perpendicular axes in the plane of the specimen. Frequently, diffraction from non-zero-layer spots could be seen in the form of rings (Fig 2.1). Tilting so that these rings centred on the straight–through beam ensured that the beam direction lay along a prominant zone in the crystal.

To identify the mineral the spacings of two prominant lattice vectors on the diffraction photograph were measured. These reciprocal vectors were converted to interplanar spacings, using the Bragg equation:

$$2d \sin\theta = \lambda \tag{2.1}$$

where

θ = Bragg angle

d = interplanar spacing

λ = wavelength of the incident radiation.

From Fig 2.2, it can be seen that

$$\tan 2\theta = \frac{X}{L} \tag{2.2}$$

where

X = measured reciprocal lattice vector from the diffraction pattern

L = camera length

Therefore

$$\theta = \frac{1}{2}\arctan\left(\frac{X}{L}\right) \tag{2.3}$$

and from (2.1)

$$d = \frac{\lambda}{2\sin\left(\frac{1}{2}\arctan\left(\frac{X}{L}\right)\right)} \tag{2.4}$$

λ is given by the following expression which is corrected for relativistic effects (Hirsch *et al.*, 1965):

$$\lambda = \frac{h}{2meV\left(\frac{1+eV}{2mc^2}\right)} \tag{2.5}$$

For 120 kV λ= 0.0335 Å

For 100 kV λ= 0.037 Å

In this way d may be evaluated for two reflecting planes in the crystal. These spacings were compared to Powder Diffraction File (PDF) cards of the most likely suspected mineral phases. When a match was obtained, the expected angle between the reciprocal vectors was calculated and compared with that measured. This information, along with chemical analysis generally allowed phase identification.

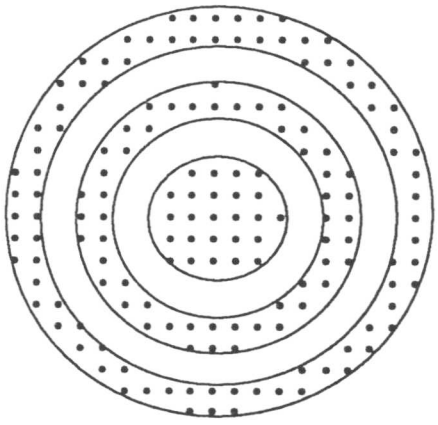

Figure 2.1 Non–zero layer diffraction planes were sometimes observed as rings of spots surrounding the central zero layer plane. Alignment of the specimen relative to the beam such that the beam lay parallel to a prominent crystal zone was achieved by tilting until the rings were centred on the straight–through beam.

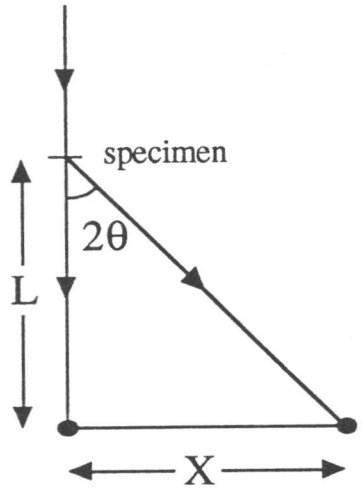

Figure 2.2 Schematic diagram showing the diffraction geometry on TEM.

2.3.3 Energy Dispersive X–ray Analysis

Chemical analysis of particles examined using TEM involved the use of a LINK series 860 energy dispersive X–ray spectrometer, attached to a Phillips 400T 120 kV TEM. X–ray spectra were recorded at a specimen tilt of 35°, and live times of 100 s were used as long as individual count rates were good. The dead time was not allowed to exceed 25% . The data were analysed using the LINK RTS2–FLS software. This arrangement involved use of a beryllium–windowed detector which prevented detection of the soft characteristic X–rays of elements lighter than sodium. For chemical analysis involving examination of lighter elements, an Energy Dispersive X–ray (EDX) system with a windowless detector, attached to a Jeol 2000FX TEM was employed.

EDX analysis was also used to examine matrix steel chemistry using a system attached to a CamScan S4 SEM microscope. For maximum X–ray detection the specimen under examination was polished, lightly etched, and was tilted to 45° relative to the electron beam. Again dead times were not allowed to exceed 25% .

2.3.4 X–ray Powder Diffraction

X–ray powder diffraction of mineral powders was carried out using one of two diffractometers – a Rigaku GFX–RAD3C and a Philips PW1710. Both systems used a copper target and Ni–filter, producing CuK_{α} radiation.

CHAPTER 3

Titanium-Rich Mineral Phases and the Nucleation of Bainite

3.1 Introduction

As already described in Chapter 1, a great number of investigations have been carried out on the non–metallic inclusions in steel welds. Such studies have largely tried to elucidate the chemical nature of non–metallic inclusions which are particularly effective in the nucleation of acicular ferrite (thought to lead to an improvement in toughness). They have also tried to identify possible mechanisms by which inclusion–caused nucleation may occur. Unfortunately, inclusions in welds tend to consist of a conglomeration of many crystalline and amorphous phases (Barrite *et al.*, 1981; Dowling *et al.*, 1986; Barbaro *et al.*, 1988), so that identification of the particular component responsible for stimulating acicular ferrite production is inherently difficult.

A major part of the present investigation therefore involved the pressure–bonding of pure ceramics to steel, so that the resulting interface could be studied without ambiguity. Similar experiments have been performed previously by Strangwood and Bhadeshia (1988). However, because of the lack of adequate equipment, high hardenability steels were used, so that only allotriomorphic ferrite formation was examined.

3.2 The Experimental Technique

An intimate bond between the mineral and steel was achieved by dusting pure mineral powder on top of a cylinder of steel of diameter 8 mm and depth 6 mm, placing an identical steel cylinder on top of the mineral layer, and compressing the composite specimen in the thermomechanical simulator (described in Chapter 2) – Fig.3.1. The optimum values of bonding pressure and temperature were determined by trial and error; a compressive stress of ~8 MPa for 10 mins at 1200°C was found to work well. For stresses significantly lower than this optimum value, adequate mineral–steel bonding was not achieved, while significantly higher stresses caused unnecessary deformation of the specimen.

In some of the initial experiments, a countersunk region 3 mm in diameter and 2 mm in depth was machined in the lower steel cylinder, to house the mineral powder. This was later deemed unnecessary, as it involved machining, and also created less intimate bonds between the steel and mineral. Having formed the required ceramic/steel interface, the transformation behaviour of steel adjacent to the mineral could be compared with that in the steel away from the interface. Any differences in the reactions at these two locations could be interpreted to reveal inclusion–stimulated phenomena.

Acicular ferrite appears to be intragranularly nucleated bainite (Sugden and Bhadeshia, 1989; Yang and Bhadeshia, 1987; Strangwood and Bhadeshia, 1987; Kluken *et al.*, 1990). Its morphology, which consists of plates radiating from 'point' nucleation sites, is different from that of the parallel ferrite plates associated with bainite. This is because the latter grows from austenite grain surfaces rather than point sites. A planar ceramic/steel interface is therefore expected to give a conventional bainitic microstructure, rather than one which looks like acicular ferrite. It is assumed that, since bainite and acicular ferrite form by the same transformation mechanism, a mineral which is effective in stimulating bainite should also be useful as a nucleant for acicular ferrite.

In order to design the experiments, it was necessary to determine the bainite–start temperature (B_S) of the alloy used (A5763). This was estimated using a computer program designed to calculate TTT behaviour from steel composition (Bhadeshia, 1982). A more accurate value was obtained by isothermal transformation experiments at temperatures close to the calculated start temperature, after austenitisation at 1200°C for 10 mins (using the thermomechanical simulator). Microstructural observations showed that bainite was produced during transformation at temperatures up to ~540°C, with Widmanstätten ferrite occurring at higher temperatures (Fig.3.2). B_S was therefore identified experimentally to be close to ~540°C, which compares with the calculated value of 560°C.

The heat treatment involved austenitisation of the steel–mineral specimen at 1200°C for 10 mins during which a compressive load of 400 N (~8 MPa) was applied to achieve bonding, as described above. This load was then removed, and the specimen gas–quenched (using nitrogen or helium) at ~ 40°C/s to 510°C (safely within the bainite region). It was held at this temperature for 25 seconds, before further gas–quenching to room temperature. During the quench, any untransformed austenite decomposed to martensite. The bonded specimens were then sectioned in a plane normal to that of the ceramic/steel interface using a Struers Accutom–2 precision high speed saw, and prepared for metallographic examination.

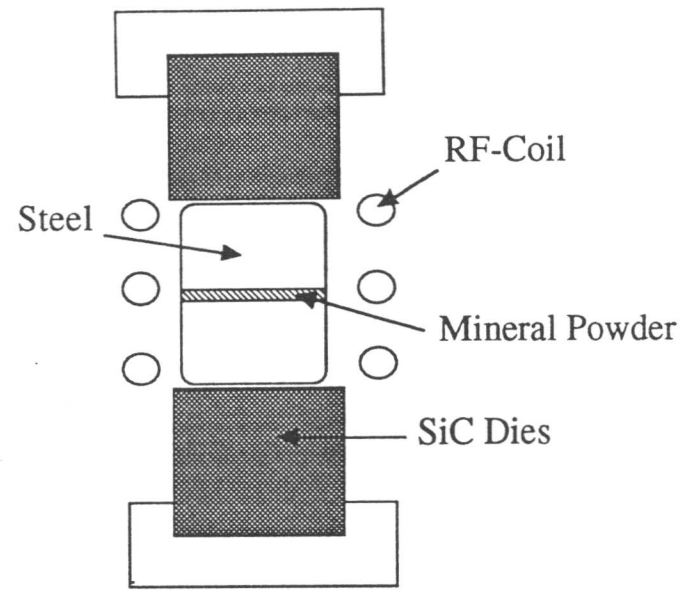

Figure 3.1 The steel–mineral arrangement used in the bonding experiments

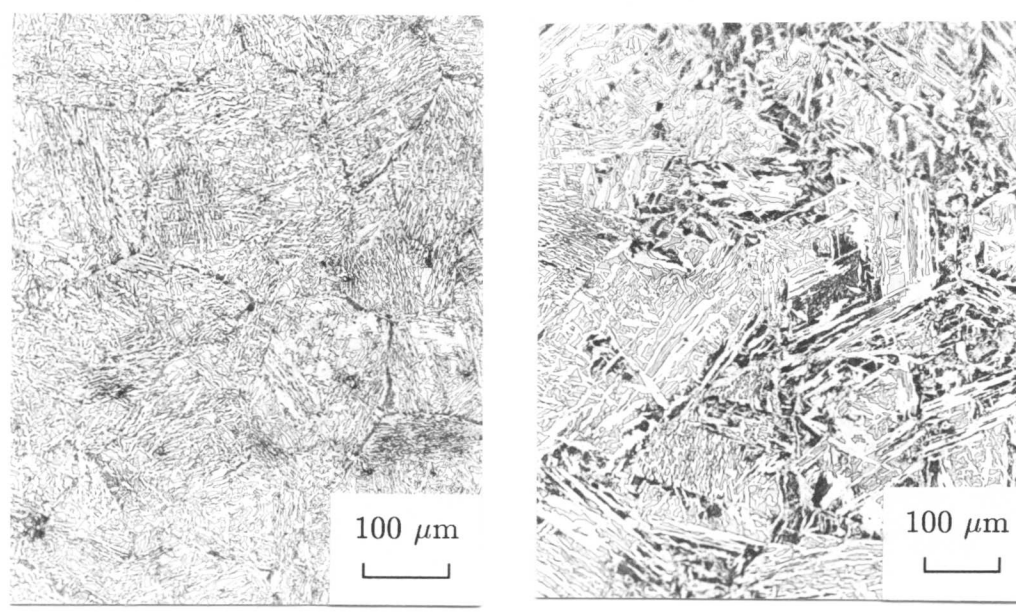

Figure 3.2 **(a)** Optical micrograph of the microstructure produced due to isothermal treatment of A5763 at 520°C. It is dominantly bainitic.

(b) Optical micrograph of the microstructure produced due to isothermal treatment of A5763 at 560°C. Much coarser Widmanstätten plates have formed.

3.3 Testing Titanium–Rich Mineral Phases

As discussed in Chapter 1, a large number of experiments have indicated that inclusions rich in titanium are most effective in acicular ferrite production (*e.g.* Terashima and Hart, 1983; Dowling *et al.*, 1986; Homma *et al.*, 1987; Es-Souni *et al.*, 1991). Despite the frequency of observation of this titanium effect, identification of the specific titanium–rich compound responsible is rare. This is because elements such as C, N, or O are either undetectable, or their concentrations cannot be estimated with sufficient accuracy to determine the stoichiometry with titanium. Minerals such as TiN, TiO and TiC have similar structures and lattice parameters, such that the bulk of diffraction data obtained experimentally cannot distinguish between them. The obvious importance of titanium–rich minerals in the production of acicular ferrite, and the confusion over the exact compounds responsible for nucleation, prompted the testing of TiO_2, Ti_2O_3, TiO and TiN for their nucleation potency in a series of pressure bonding experiments.

3.3.1 Results and Discussion

Each of the various combinations of mineral and steel were found to be quite different in their response to heat–treatment and are discussed separately:

3.3.1.1 Titanium Dioxide: TiO_2

Figure 3.3 reveals that the steel near the TiO_2 layer shows a lot more bainite than the bulk of the steel away from the ceramic/steel interface. It would therefore appear to be very potent in nucleating bainite. Closer examination showed that the bainite does not emanate directly from the TiO_2–steel interface. The presence of TiO_2 causes the production of a zone of allotriomorphic ferrite ~15–20 μm thick (Fig 3.4) which contains amorphous spherical particles approximately 0.5 μm in diameter (Fig 3.5, 3.6). These were found, using microanalysis, to consist almost entirely of silicon and oxygen. A typical EDX trace of these particles taken on TEM is shown in Fig 3.7. Such spherical particles are probably amorphous silica. Detailed investigation revealed that silicon was not the only possible cation constituent, iron and manganese were also present. However, as can be seen from Fig.3.8, silicon was dominant as the cation constituent. Cross-sectional TEM revealed that some of the particles were considerably larger than 0.5 μm , and were not spherical (Fig.3.9). Further that although the cores of the particles were amorphous, their surfaces appeared to be microcrystalline (Fig.3.10).

The presence of these particles clearly shows that oxygen has diffused over a distance of some 20 μm from the TiO_2 into the steel. Similar effects were not found at the surfaces of the steel which were not in contact with the ceramic, confirming that the observed

phenomenon was induced by the ceramic (Fig 3.11).

In order to show that it is the property of TiO_2 to cause oxidation which in turn induces the ferrite, silica and bainite production, another oxygen producing mineral was tested in the bonding experiments – KNO_3 (a mineral which decomposes to give oxygen at 400°C – Sidgewick, 1950; Irving Sax, 1968). The decomposition of KNO_3 produced bainite nucleation as can be seen in Fig 3.12, 3.13. The particles observable in the figure are composed predominantly of silica – their high Si-content was observed using SEM EDX (Fig 3.14). These particles are contained within a ferrite layer (Fig 3.15). Thus the decomposition of KNO_3, and consequential exposure of the steel to oxygen, produced the same salient 'reaction zone' features displayed at the TiO_2–steel interface.

Furthermore, exposure of the steel to water vapour at 1200°C also caused a 'reaction zone' adjacent to the free surface (Fig 3.16). Oxidation can therefore duplicate the effects on the steel found adjacent to TiO_2. It seems therefore that it is the ability of TiO_2 to cause local oxidation in Alloy A5763 which is responsible for the nucleation observed. The effects on steel hardenability due to oxygen entry were investigated in detail, and will be discussed in Chapter 4.

3.3.1.2 Titanium Sesquioxide: Ti_2O_3

The characteristics of Ti_2O_3 as a stimulant for bainite nucleation were found to be similar to those of titanium dioxide (Fig 3.17). However, the presence of Ti_2O_3 did not produce the layer of allotriomorphic ferrite or any silica particles. Furthermore, SEM microanalysis revealed that the presence of Ti_2O_3 caused the long–range depletion of Mn in the steel local to the mineral layer; Fig 3.18 illustrates a typical concentration profile, which was verified on four separate occasions.

Figure 3.19 shows that the oxide is in fact a sink for manganese. Manganese presence in steel is known to stabilise austenite over ferrite, and so its depletion in the alloy adjacent to the Ti_2O_3 was clearly responsible for the enhanced bainite production observed. Exactly why Ti_2O_3 should have absorbed manganese was not obvious. It was thought that a chemical reaction was occurring which favoured the production of a manganese–rich mineral within the Ti_2O_3 layer.

3.3.1.2.1 Furnacing Ti_2O_3 with chippings of A5763

In order to investigate this possibility, some Ti_2O_3 powder was mixed with fine chippings of A5763. A reference X–ray powder diffraction trace was then taken from this mixture. It was sealed in a silica tube under partial pressure of argon, and subjected to a furnace treatment of 3 hrs at 1200°C. It was hoped that this treatment would induce enough reac-

tion that changes in mineralogy could be readily observed in the powder diffraction trace. X–ray powder diffraction of the post–furnaced mixture was performed and compared to the pre–furnace trace. Fig.3.20 shows that clear differences in the powder diffraction traces occurred due to the heat treatment. Interpretation of these traces was not straightforward, but certain conclusions could be made:

(i) That the peaks corresponding to Ti_2O_3 in the pre–furnaced mixture disappear after heat treatment.

(ii) New peaks emerge which correspond very well with Ti_3O_5.

(iii) Other peaks emerge, not associated with Ti_3O_5. Exactly what these peaks correspond to is not known, however, they do match reasonably with a manganese–titanium intermetallic.

Analysis of the mineral powder after furnace treatment with the steel chippings under TEM confirmed the general observations made from X–ray analysis. Fig.3.21 shows a diffraction pattern taken from the mineral. It indexes not as Ti_2O_3, but as Ti_3O_5. TEM EDX performed on the powder shows a consistent level of manganese is indeed present (Fig.3.22). However, TEM investigation was unable to elucidate the mineralogical nature of any manganese–rich regions.

In summary, then, the results from the furnace treatment of Ti_2O_3 with steel chippings confirmed that manganese absorption into the mineral had occurred. Also, that this manganese absorption was associated with a transformation of the titanium oxide from Ti_2O_3 to Ti_3O_5. Such transformation involves a loss of titanium. The creation of γ–$Mn_{1-2}Ti$ intermetallic, although thought unlikely, was consistent with the changes observed in the titanium oxide.

3.3.1.2.2 Analogues of Ti_2O_3

To see if analogous behaviour could be observed in other minerals, V_2O_3 and Cr_2O_3 were tested in the bond experiment. These oxides were selected because they are structurally the same as Ti_2O_3. Also the cations are adjacent in the transition element region of the periodic table. This meant that behavioural similarities were likely. Futher, vanadium, chromium and titanium may form a variety of oxides, with differing stoichiometry. For all three cation types, if the stoichiometry of the oxides was the same, then they were structurally similar (see Table 3.1). So, great similarities between Cr_2O_3, V_2O_3 and Ti_2O_3 were apparent. Fig.3.23 and Fig.3.24 show the results of the bonding experiments. Both Cr_2O_3 and V_2O_3 caused the nucleation of bainite, as expected. However, nucleation has not occurred directly from the mineral–steel interface. Instead a layer of ferrite has formed.

No silica particles were obvious within this layer, so it was thought that the ferrite may have formed because of considerable reductions in manganese concentrations. This may have been so, but SEM EDX line profile analysis perpendicular to the Cr_2O_3 and V_2O_3 revealed that outside the ferrite layer, no manganese depletion was apparent (Fig.3.25 and Fig.3.26). Thus bainite transformation has occurred in alloy of bulk manganese concentration. Therefore, despite the apparent similarities between Ti_2O_3, V_2O_3 and Cr_2O_3, only Ti_2O_3 seemed to react with the steel to cause manganese depletions. The reason for this was not clear.

In summary Ti_2O_3, when tested in the bond experiment, caused the accelerated formation of bainite in local steel. Unlike TiO_2, no reaction zone was associated. It was found that nucleation was induced due to a tendency of Ti_2O_3 to absorb manganese, so reducing the hardenability of the local alloy. Manganese absorption may be related to a change in the oxide from Ti_2O_3 to Ti_3O_5.

Mineral Type	System	Space Group	Structural Type	Lattice Constants /Å		
				a	b	c
TiO_2	Tetrag.	$P4_2/m\ 2_1/m\ 2/m$	TiO_2	4.59	4.59	2.96
VO_2	Monocl.	$P2_1/b$	TiO_2	5.74	4.52	5.38
CrO_2	Tetrag.	$P4_2/n\ 2_1/c\ 2/m$	TiO_2	4.42	4.42	2.92
Ti_2O_3	Hex.	$R\bar{3}c$	α-Al_2O_3	5.16	5.16	13.57
V_2O_3	Hex.	$R\bar{3}c$	α-Al_2O_3	5.43	5.43	–
Cr_2O_3	Hex.	$R\bar{3}c$	α-Al_2O_3	4.95	4.95	13.67
Ti_3O_5	Monocl.	–	–	9.76	3.80	9.45
V_3O_5	Monocl.	–	–	9.98	5.04	9.84

Table 3.1 Summary of some of the structural information for the oxides of titanium, vanadium and chromium. Note the similarities between oxides of the same stoichiometries (after Samsonov, 1973).

3.3.1.3 Titanium Nitride: TiN

The TiN–steel interface can be seen in Fig 3.27. Under an optical microscope it seems that this interface does not enhance the nucleation of bainite in the steel adjacent to it. SEM examination confirms that little, if any extra inducement for transformation occurs adjacent to TiN than elsewhere in the steel. Certainly, the level of bainite production caused by the TiN–steel interface is meagre when compared with that caused by TiO_2 and Ti_2O_3–steel interfaces. It would therefore seem that TiN is not an active nucleant for the production of acicular ferrite in real steel systems. This is contrary to the suggestions of Barbaro *et al.* (1988), Watanabe and Kojima (1980), Kluken and Grong (1989), and Grong *et al.* (1992).

3.3.1.4 Titanium Monoxide: TiO

The TiO–steel combination is similar to the Ti_2O_3–steel interface, in that it induces the nucleation of bainite in the adjacent steel (Fig 3.28). There is also an absence of the layer of allotriomorphic ferrite and SiO_x particles that occurred with TiO_2. However, unlike the Ti_2O_3, SEM EDX indicates that the presence of TiO does not radically affect the substitutional solute concentration in the adjacent steel (Fig 3.29). Slight manganese depletion is apparent, although it is within the levels of scatter typical of the EDX analysis technique. Nevertheless, an attempt to exaggerate any depletion was undertaken, by furnace treating a TiO–bonded specimen at 1200°C for 6 hrs. Fig.3.29 also shows the substitutional element concentration profile measured after this treatment. Again, slight manganese depletion was evident, but had not been exaggerated. TiO–caused manganese depletion was therefore not established. The lack of reaction zone implied that nucleation of bainite was not due to oxygen impregnation of the steel either. Therefore, it seemed that a different nucleation mechanism was in operation. The observation that TiO does cause bainite nucleation is in agreement with earlier work (Bailey, 1983; Mori *et al.*, 1981; St.Laurent and L'Esperance, 1992) where it is argued that TiO is effective as a nucleant because it has a good lattice match with ferrite. In the present context, however, TiN also offers a good lattice match for ferrite, and yet does not appear to enhance bainite nucleation.

The true mechanism by which TiO causes the nucleation of bainite, when pressure bonded to steel, is therefore still under consideration and obviously requires further investigation with a much wider range of minerals.

3.4 Summary and Conclusions

Using a pressure bonding technique to create interfaces between pure powdered minerals and steel, nucleation potency of various titanium–rich minerals was investigated. It has been demonstrated that TiO_2, Ti_2O_3 and TiO are all effective in enhancing the formation of bainite in the adjacent steel. The mechanism by which each compound stimulates ferrite nucleation is found to be different in detail:

- TiO_2 appears to induce transformation by oxidising the steel at elevated temperatures. Exactly how the oxidation process causes nucleation will be discussed in detail in Chapter 4.

- Ti_2O_3 appears to act as a sink for Mn and hence causes a reduction of Mn levels in the steel which surrounds it. Mn is known to retard the transformation of steel to ferrite, and so any depletion in the steel has the opposite effect.

- TiO is found not to be reactive in the sense discussed above, nor does it act as a sink for elements such as manganese. It nevertheless enhances the nucleation of bainite although the mechanism by which this happens is not clear since its lattice match with ferrite is similar to that of TiN, which does not stimulate bainite formation.

In contrast to these titanium oxides, TiN appears to show little efficacy in inducing bainite transformation in adjacent steel.
On the basis of these results it would seem that it is titanium oxides and not nitrides which are important in causing the formation of acicular ferrite in welded and wrought steels. The mechanisms by which such oxides cause nucleation seem to be dependent on their stoichiometry.

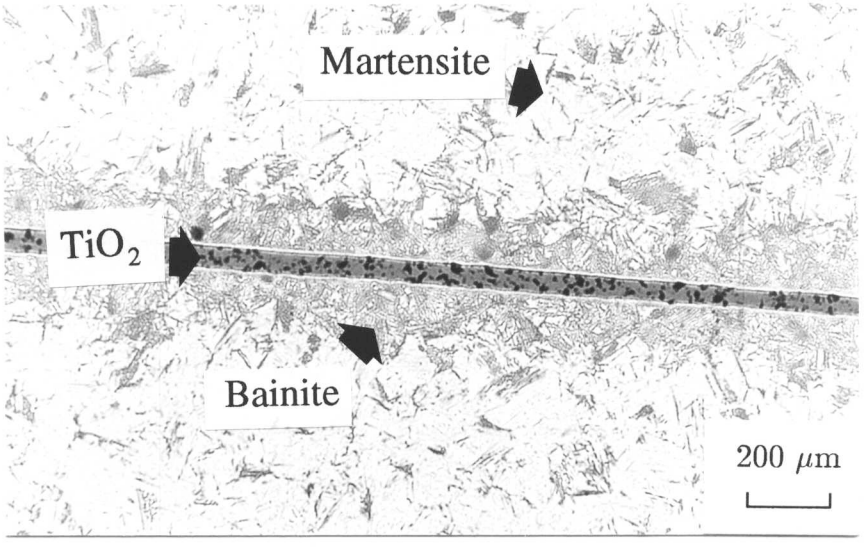

Figure 3.3 Optical photomicrograph of the TiO_2–steel interface region. There is clearly more bainite present adjacent to the mineral than elsewhere in the steel

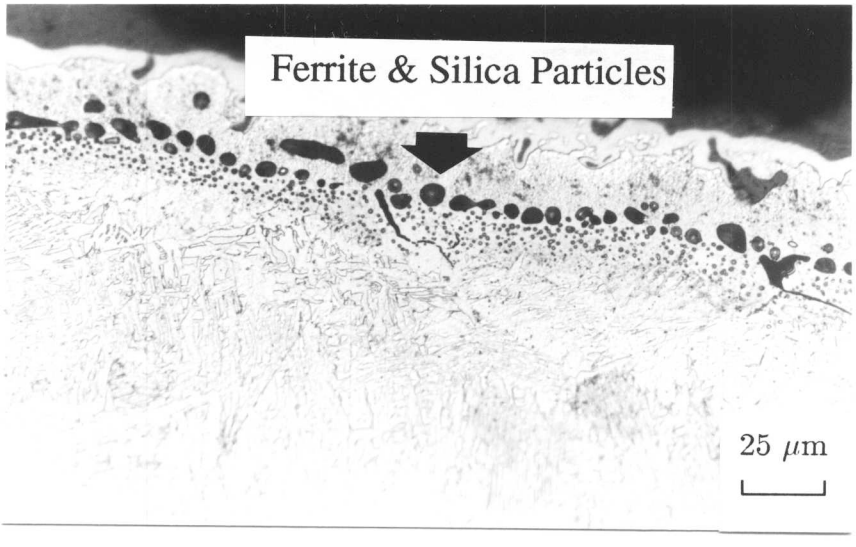

Figure 3.4 Optical photomicrograph of the ferrite and SiO_x particles produced adjacent to the TiO_2

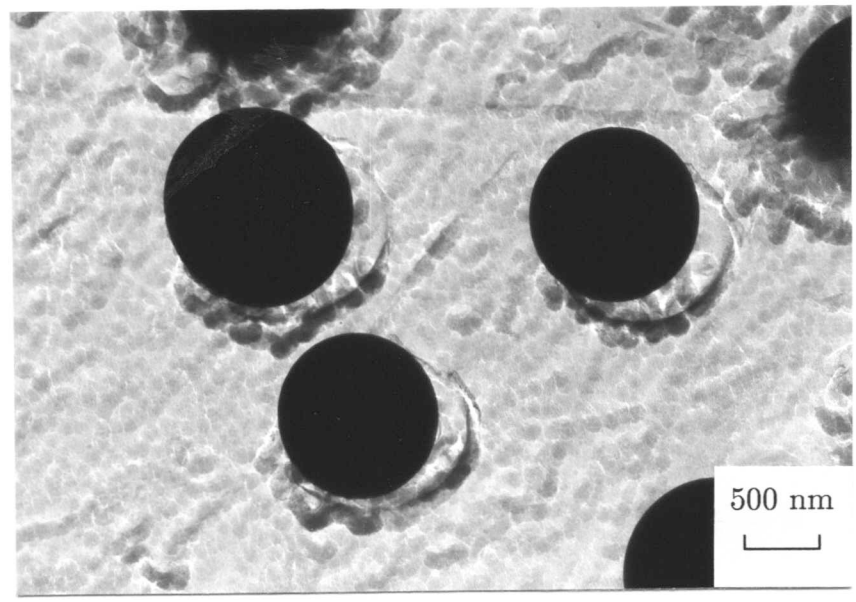

Figure 3.5 TEM photomicrograph of typical silica particles

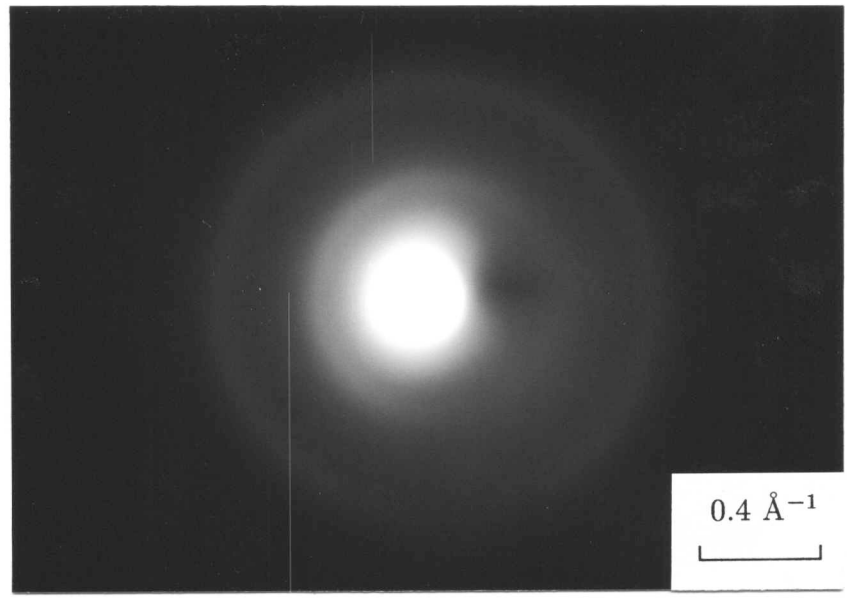

Figure 3.6 Diffraction produced from a silica particle illustrating its amorphous nature

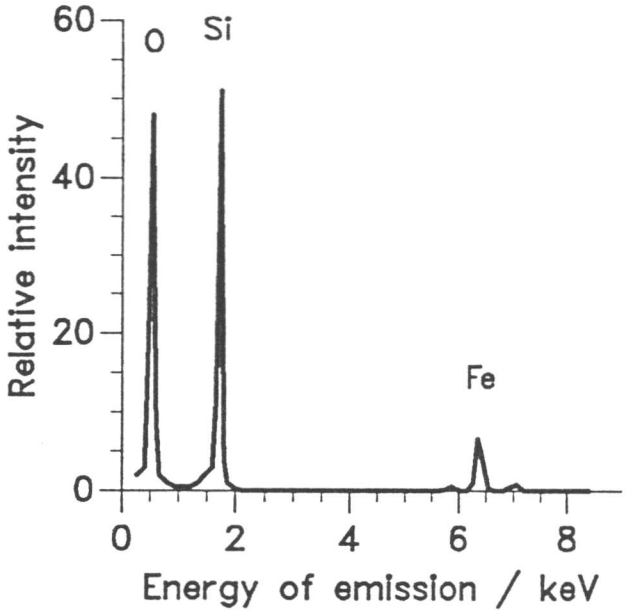

Figure 3.7 TEM EDX trace (using thin-windowed detector) of the particles present in the ferrite layer produced adjacent to the TiO_2

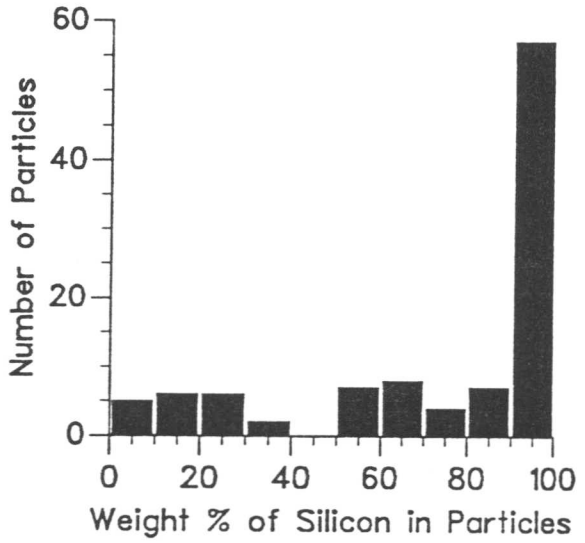

Figure 3.8 TEM EDX microanalysis of the cation constituent of the particles in the reaction zone. Although iron and manganese were observed present, silicon dominates as the cation species.

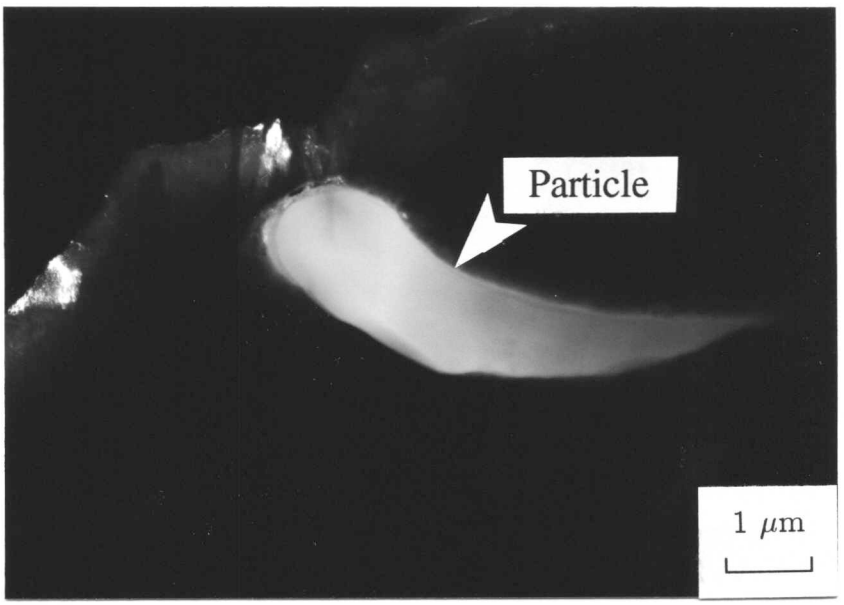

Figure 3.9 Cross-sectional thin-foil examination of the reaction zone shows that the particles need not be at all spherical in shape. They may also be somewhat larger than $0.5\,\mu m$ in diameter.

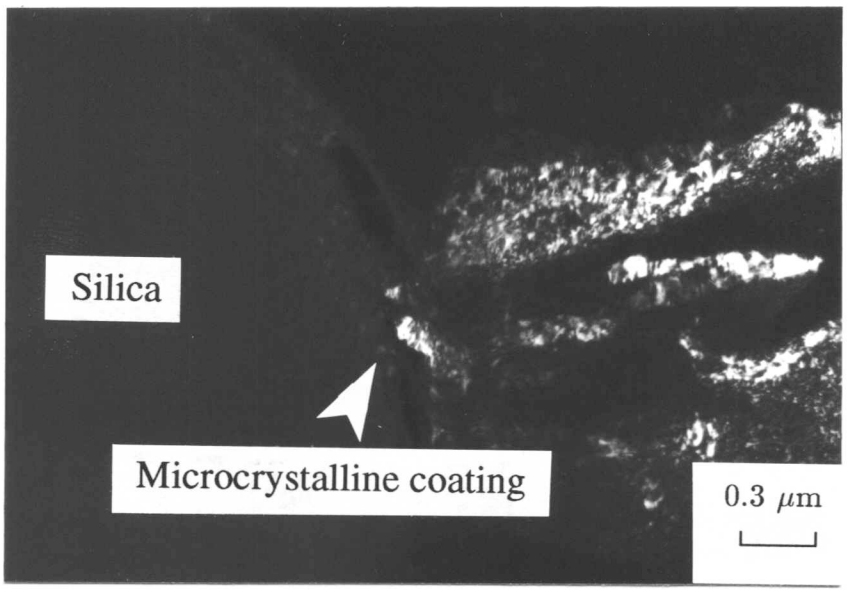

Figure 3.10 Cross-sectional thin-foil examination of the particles showed them to possess microcrystalline surface coatings.

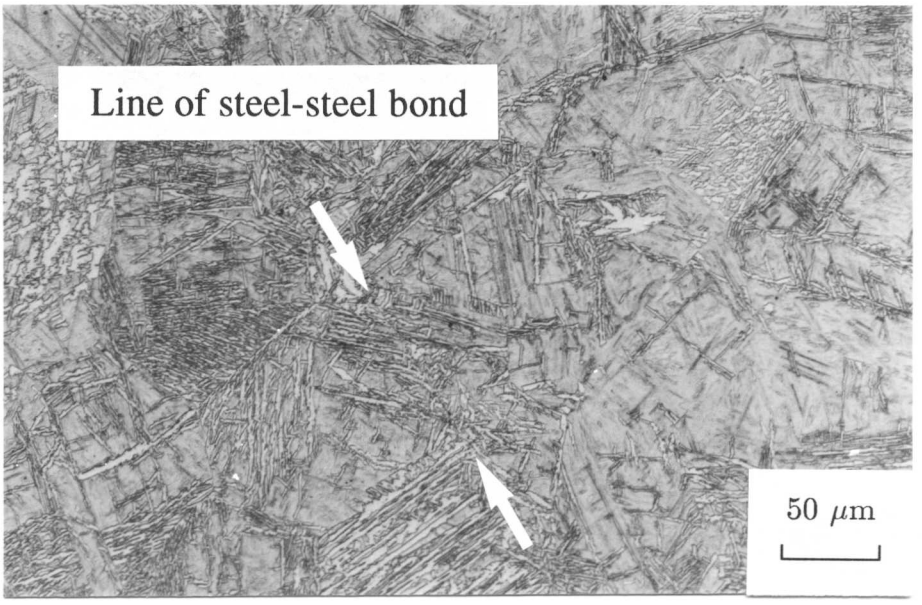

Figure 3.11 Optical photomicrograph of a steel–steel interface produced by pressure bonding. As can be seen, no 'reaction zone' is produced

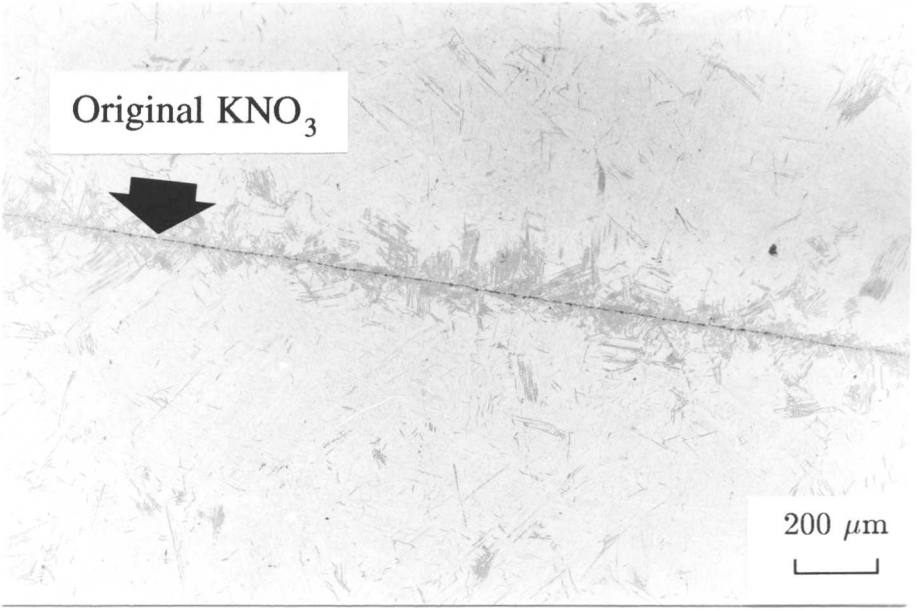

Figure 3.12 Optical micrograph of the interface region between A5763 and KNO_3. Bainite nucleation is clearly evident

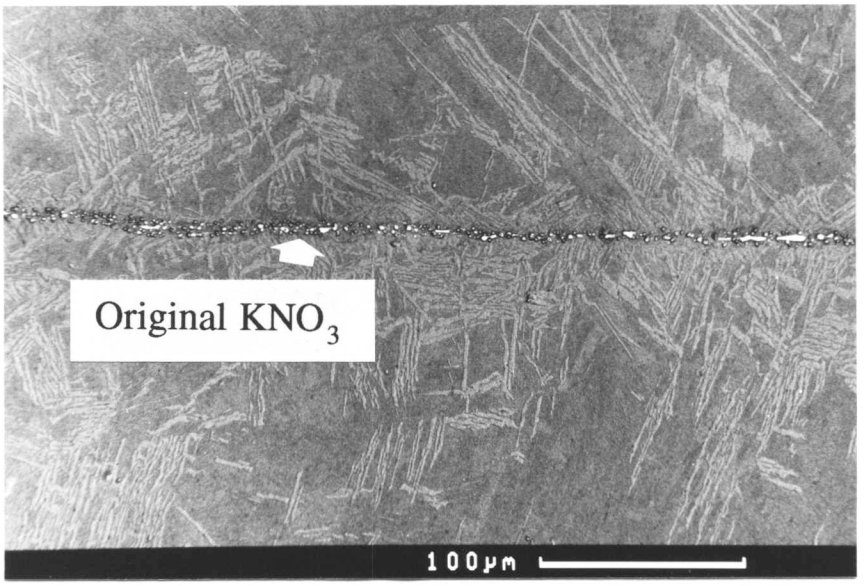

Figure 3.13 SEM photomicrograph of the KNO_3–A5763 interface showing the bainite produced local to the KNO_3. The observable particles are predominantly silica

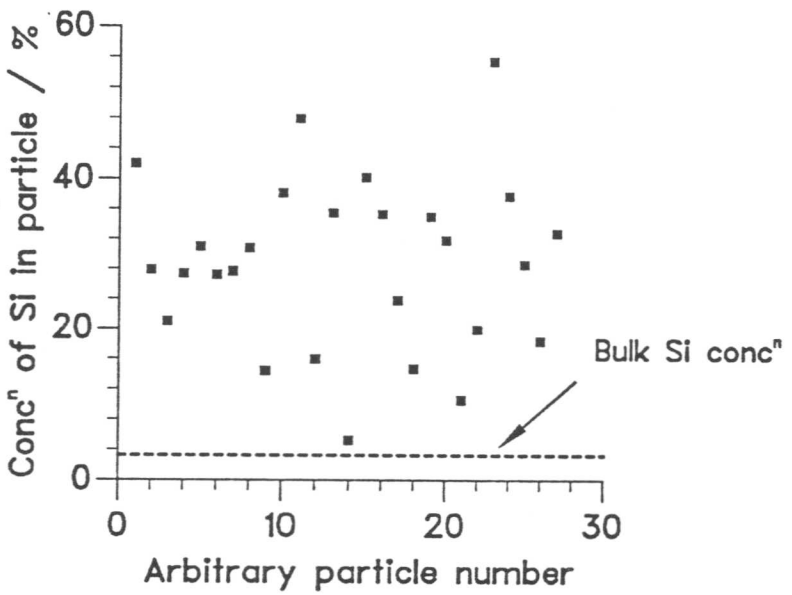

Figure 3.14 SEM EDX results taken from particles in KNO_3–steel specimen. As can be seen, they are highly enriched in Si

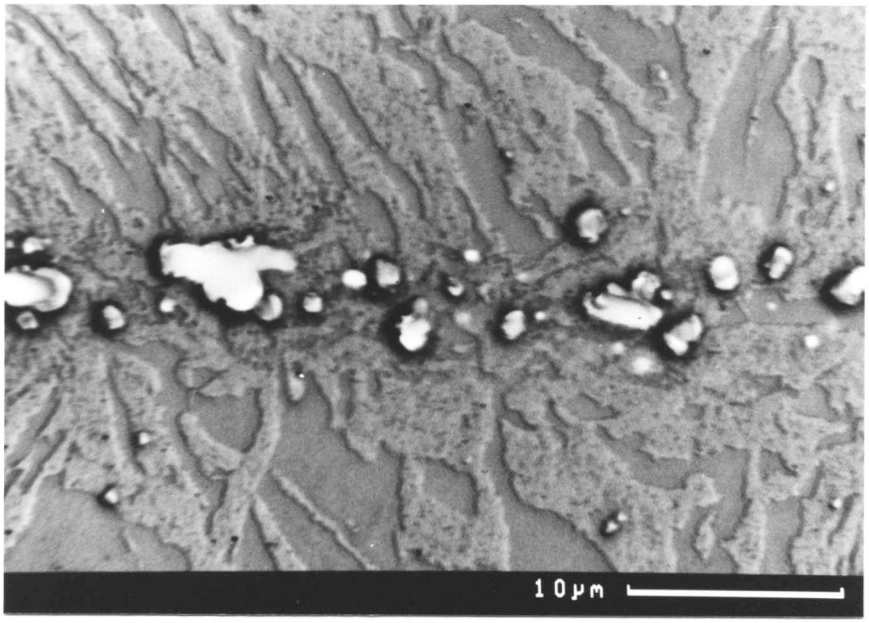

Figure 3.15 SEM photomicrograph illustrating the ferrite layer which surrounds the Si–rich particles produced by the KNO_3

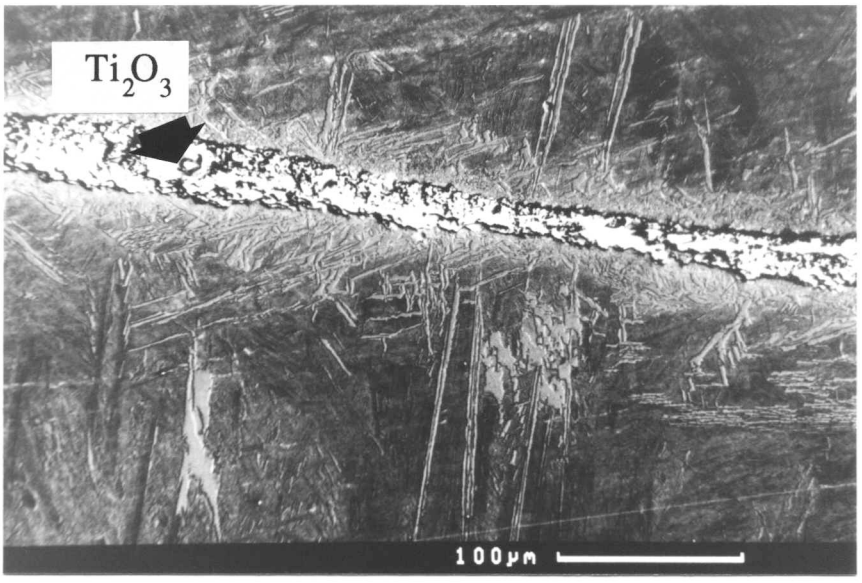

Figure 3.16 SEM photomicrograph of the interface region between Ti_2O_3 and the steel. Bainite production is enhanced by the interface, but without the production of a ferrite and particle layer

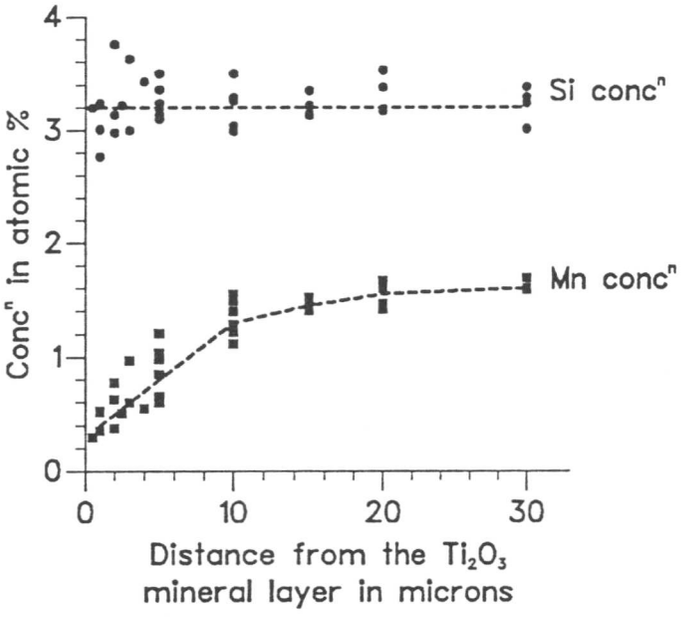

Figure 3.17 SEM EDX concentration profile showing the relative depletion of Mn caused by the Ti_2O_3 mineral layer

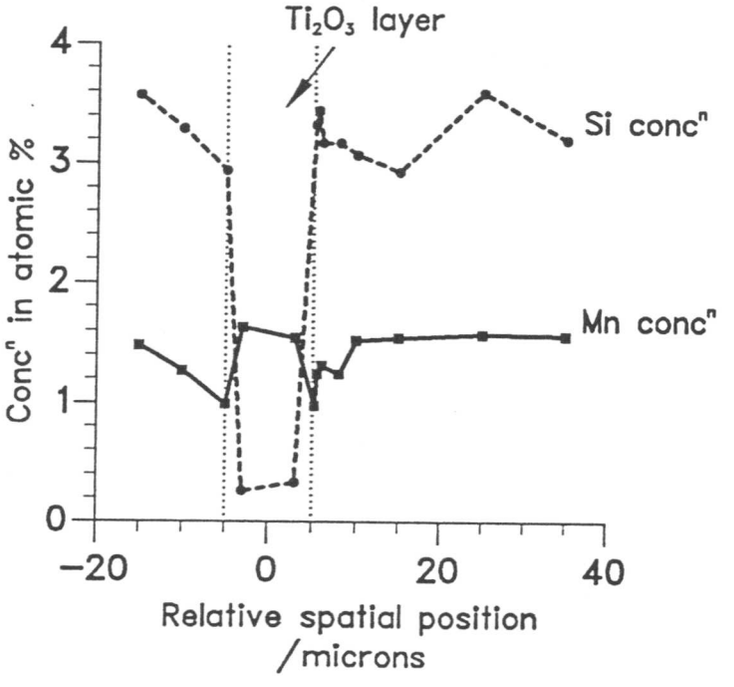

Figure 3.18 SEM EDX concentration profile across the Ti_2O_3 layer showing the presence of Mn within this layer

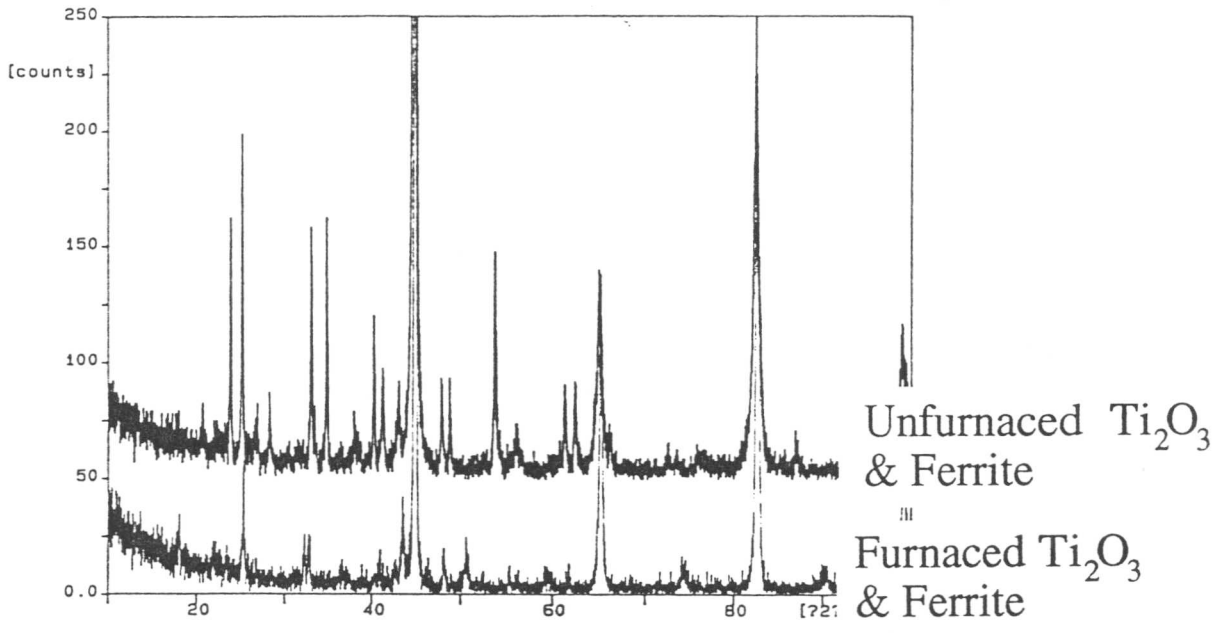

Figure 3.19 X–ray powder diffraction showed that mineralogical changes did occur in Ti_2O_3 due to furnace treatment with steel chippings.

Figure 3.20 Diffraction pattern taken from the mineral powder after furnace treatment with steel chippings. This pattern indexes as Ti_3O_5 and not Ti_2O_3.

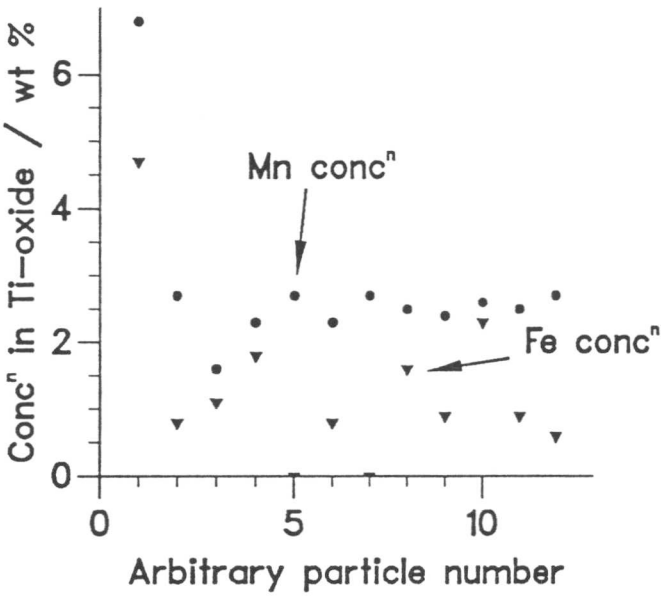

Figure 3.21 EDX performed on particles examined on TEM showed consistent levels of manganese associated with the Ti_3O_5.

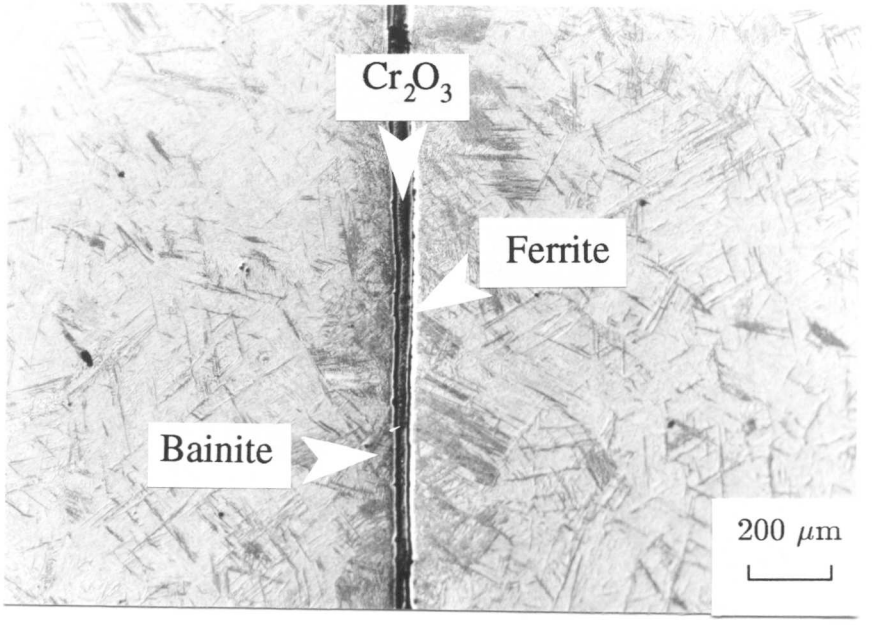

Figure 3.22 Optical micrograph of the interface region between steel and Cr_2O_3. Clearly nucleation of bainite has been induced, but with an associated band of ferrite, reminiscent of a reaction zone.

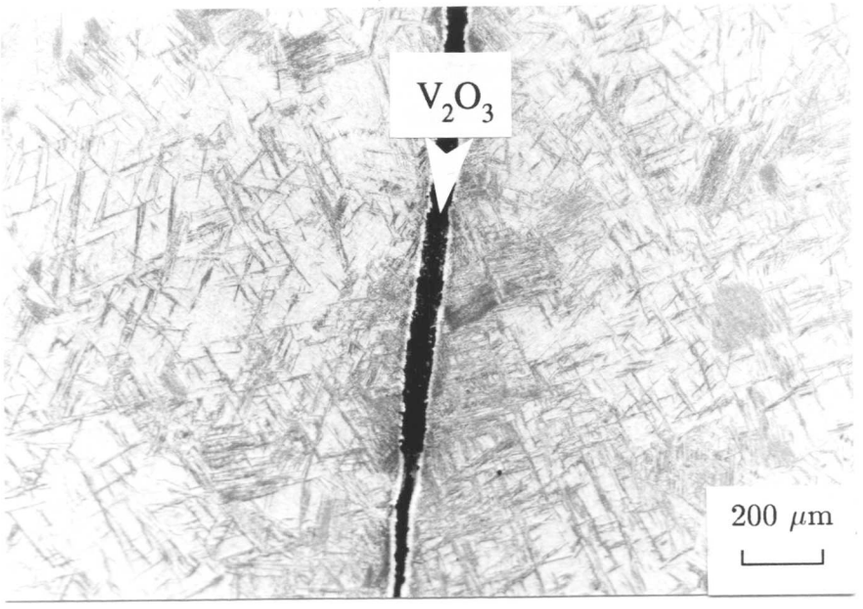

Figure 3.23 Optical micrograph of the interface region between V_2O_3 and steel. Bainite nucleation has been produced, but it is associated with a band of ferrite.

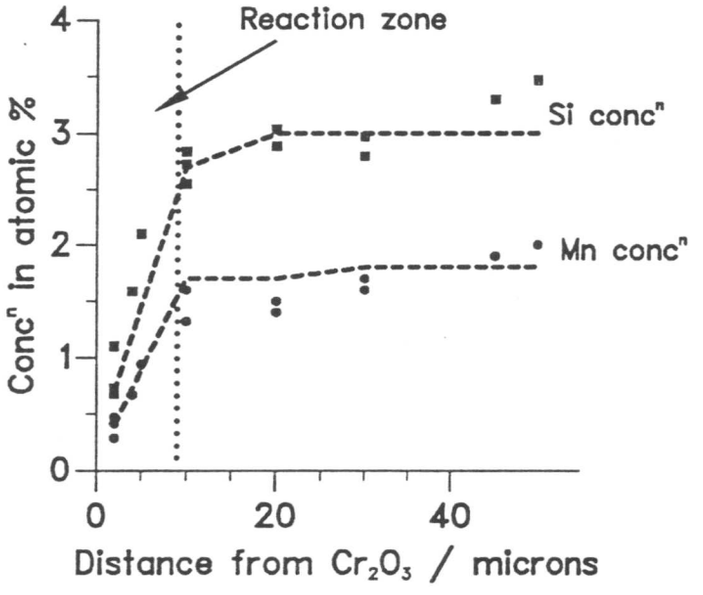

Figure 3.24 SEM EDX line profile of substitutional elements adjacent to Cr_2O_3.

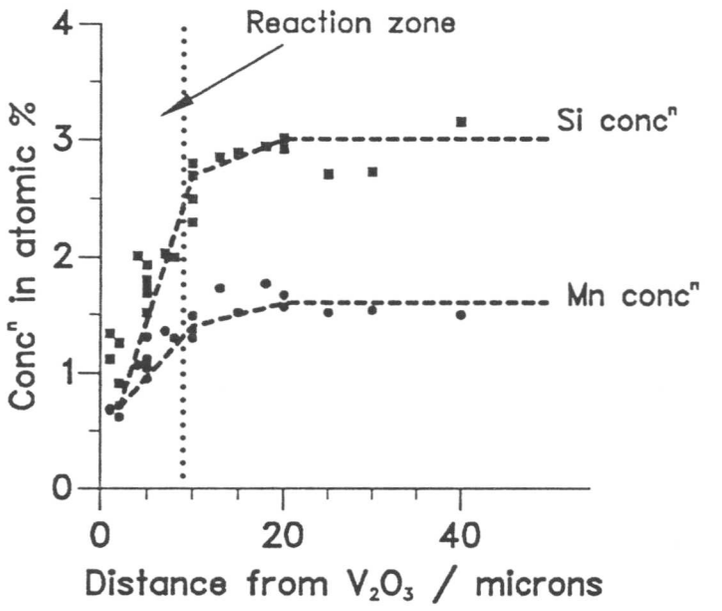

Figure 3.25 SEM EDX line profile of substitutional elements adjacent to V_2O_3.

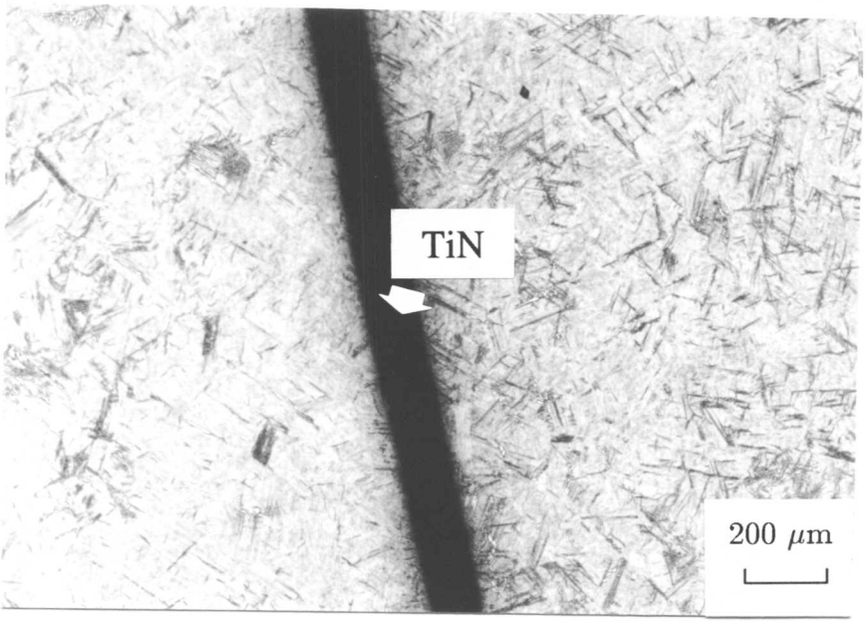

Figure 3.26 Optical photomicrograph of the interface region between TiN and the steel. There is little if any extra inducement to form bainite adjacent to the TiN than elsewhere

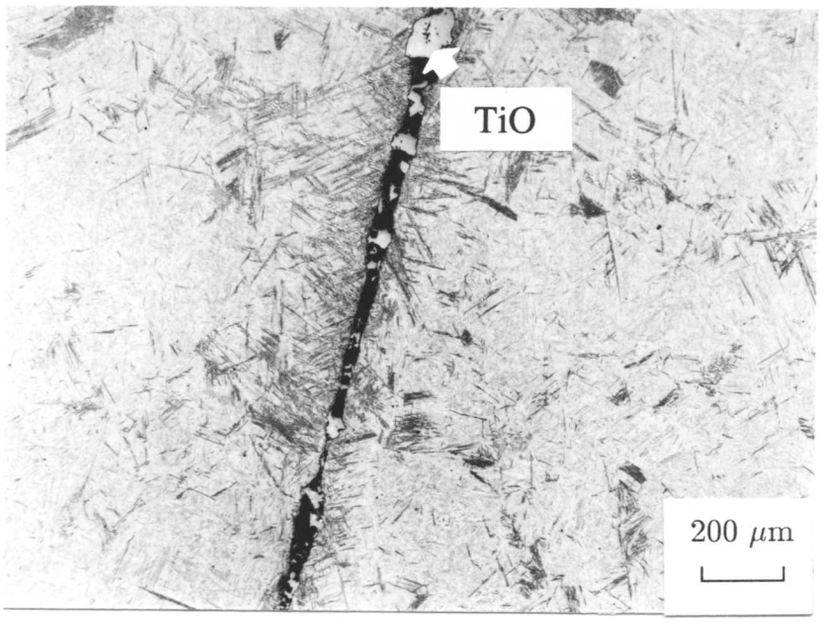

Figure 3.27 Optical photomicrograph of the interface between TiO and the steel. Bainite nucleation adjacent to the mineral layer is evident, and no ferrite and particle layer has been produced

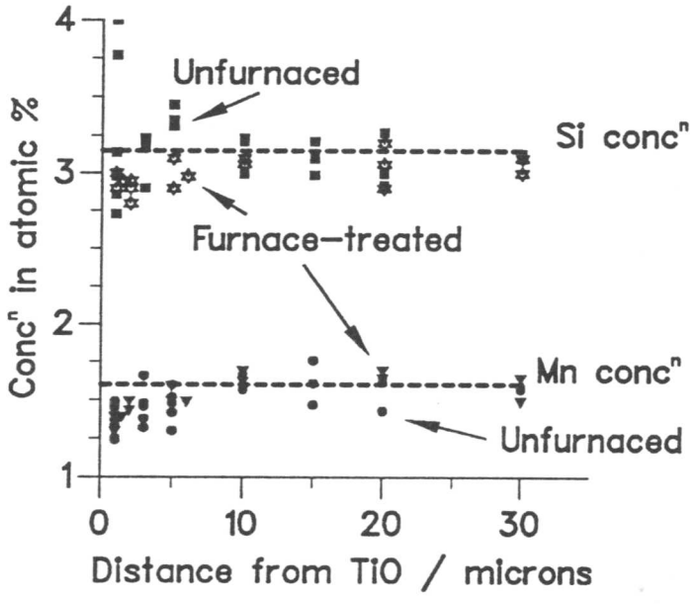

Figure 3.28 SEM EDX line profile of the substitutional elements away from the TiO–steel interface. No obvious chemical variation exists between steel adjacent to, and away from, the interface. Also plotted is the concentration profile measured after heat treatment at 1200°C for 6 hrs.

CHAPTER 4

Bainite Nucleation from Mineral Surfaces

4.1 Introduction

In the previous chapter, the potency of nucleation of titanium–rich minerals was investigated by the examination of mineral–steel interfaces, produced by pressure bonding. The nucleation behaviour exhibited was different for each titanium mineral. However, results from a large number of pressure bonding experiments indicate that an overall pattern of behaviour is present. Minerals examined appear to fall naturally into 3 categories, depending on their effects on the steel. These are as follows:

GROUP I: minerals which appear to react with the steel in a way which induces the nucleation of bainite. These include TiO_2, PbO_2, SnO_2, MnO_2, WO_3, MoO_3, V_2O_5 and KNO_3.

GROUP II: minerals which cause the nucleation of bainite but without any obvious reaction. These include TiO and Ti_2O_3.

GROUP III: minerals which do not stimulate the production of bainite. These include TiN, $MnAl_2O_4$, γ-Al_2O_3, α-Al_2O_3, NbC, $CaTiO_3$, $SrTiO_3$ and MnS.

4.2 GROUP I

Fig.4.1 illustrates the profuse nucleation produced adjacent to a group I mineral which is, in the case illustrated, TiO_2. The steel away from the ceramic has transformed to a much smaller extent than in the vicinity of the ceramic. As described in the previous chapter, bainite nucleation from TiO_2 does not occur directly from the mineral surface. There is, instead, a layer of ferrite in contact with the oxide, which contains particles found largely to be amorphous silica. This layer extends for $\simeq 15 - 20\,\mu$m normal to the ceramic/steel interface, beyond which a thick layer ($\simeq$100 μm) of bainite is observable. The creation of this ferrite and silica zone (or reaction zone), and the production of bainite are features which are common to all minerals assigned to group I. Structural and behavioural analogues to TiO_2 (SnO_2, PbO_2 and MnO_2 – Table 4.1) were all found to exhibit this group I behaviour (Fig.4.2).

The presence of silica particles within the steel and the fact that reaction zone features may be duplicated by the decomposition of KNO_3, or exposure of steel to water vapour (as described in Chapter 3) clearly indicates that group I features are associated with oxygen entry into steel.

In order further to demonstrate the importance of oxygen liberation in determining the ability of a mineral to nucleate ferrite, a series of bonding experiments was performed using members of the perovskite mineral group. These minerals were chosen for investigation because it is possible within the same structural group, to find those which have the ability to liberate oxygen, and others which do not. Normal perovskites (ABO_3 – Fig.4.3) have a similar crystal structure to the defect–perovskites (BO_3 – Fig.4.4) save for the addition of the large A-atom. The absence of the A-atom in defect–perovskites allows local relaxations in the structure which allow further oxygen loss. Consequently, the defect perovskites are capable of producing many more oxygen vacancies than normal perovskites.

Fig.4.5 shows that defect–perovskites cause classic group I effects on adjacent steel, whereas normal perovskites (Fig.4.6) seem inert. In spite of structural similarities, only the defect–perovskites were found to be capable of stimulating the formation of bainite. It follows that any mineral capable of liberating oxygen should stimulate the formation of bainite by the 'Group I mechanism'. Exactly how oxygen absorption into the local steel causes the drive to form ferrite, however, required investigation.

Mineral	System	Space Group	Lattice Parameters /Å
TiO_2	Tetragonal	P $4_2/m$ $2_1/n$ $2/m$	a=4.594 c=2.958
SnO_2	Tetragonal	P $4_2/m$ $2_1/n$ $2/m$	a=4.737 c=3.185
β–MnO_2	Tetragonal (TiO_2 structure)	—	a=4.398 c=2.867
β–PbO_2	Tetragonal	P $4/m$ $2/m$ $2/m$	a=4.93 c=3.37

Table 4.1 Crystal structure data for TiO_2 and its analogues (Samsonov, 1973).

4.2.1 Effects of Oxygen on the Steel

4.2.1.1 Effects on Substitutional Alloy Chemistry

Line profiles of substitutional element concentrations were taken perpendicular to the mineral–steel interfaces of group I minerals in order to investigate the effects that oxygen may have on steel hardenability. A typical SEM EDX profile is shown in Fig.4.7. As can be seen, there is an apparent depletion of manganese and silicon within the reaction zone. The depletion of silicon is likely to be due to the formation of the silica particles within this zone. The depletion of manganese is likely to be due to its expulsion from the growing

allotriomorphic ferrite. For this to be so, a peak in the manganese concentration beyond the ferrite/bainite interface would be expected. This cannot be observed. However, it should be noted that the SEM EDX system samples an area of the order of 5 μm in diameter, so that a peak in manganese may not be observable if situated close to a trough, since peak and trough will be sampled, for the most part, simultaneously. It is suspected that the lack of observation of such a manganese–peak is due to the poor resolution of the SEM EDX system. Apart from this substantial depletion within the reaction zone, the oxygen presence seems to have had no other effect.

Although the silicon and manganese depletion may be explained by the precipitation of silica particles, and the formation of the ferrite layer, it may be that the oxygen presence affected the substitutional elements in the austenite prior to the formation of the ferrite. Indeed, such oxygen effects may have been responsible for the formation of the ferrite layer.

4.2.1.1.1 Water–Quench Experiment

In order to investigate this possibility, TiO_2 was bonded to A5763 and then water–quenched from 1200°C to room temperature. It was hoped that such rapid quenching would prevent the formation of any ferrite, so allowing observation of the effects on substitutional element concentrations produced due to oxygen penetration alone. As can be seen from Fig.4.8, the formation of the reaction zone was not totally supressed, even at the cooling rates produced by water–quenching (300–400°C/s).

The extent of growth of the reaction zone was, however, reduced to 4–5μm. EDX analysis showed that the manganese and silicon depletion was again present, but was again strictly associated with the reaction zone (Fig.4.9). Such strict association of depletion of substitutional elements with reaction zone is important:

Both the water–quench experiment and bonding experiments, involving partial transformation, share the austenitising treatment of 10 mins at 1200°C. It is likely that the majority of the oxygen diffusion into the steel occurs during this time, since partial transformation is induced at significantly lower temperatures (510°C) and for only 25 s. It is reasonable, therefore, to assume that the oxygen diffusion profile away from the TiO_2 is similar in water–quench and in partial transformation experiments. The presence of silica particles ~15–20 μm away from the TiO_2 in the partially transformed specimens indicates that significant oxygen concentrations have been produced up to 20 μm away from the mineral–steel interface. Since a similar oxygen diffusion profile should be present in the water–quench experiments, effects of oxygen within the steel, independent of the reaction zone may be examined between 5 and 20 μm away from the TiO_2–steel interface. As can be

seen from Fig.4.10, measurements of substitutional element concentrations at $\sim$10 μm away from the TiO_2, independent of the reaction zone, show no variation from the concentrations in the bulk steel, despite the oxygen presence. It may therefore be concluded, that oxygen presence alone does not affect the substitutional element concentrations prior to transformation.

4.2.1.1.2 Bond Experiment with Low Silicon Alloy

This lack of oxygen interaction with substitutional elements was further validated by an experiment performed to demonstrate that silica formation was not necessary for the production of bainite. This experiment was conducted using a low–silicon steel (A5762 – see Chapter 2). The B_S temperature of this alloy was estimated in the same way as for A5763, using computer calculation, accompanied by a series of isothermal experiments. For this alloy, the true molybdenum concentration was too high for the range of the computer model used, and so an estimated B_S was calculated on the basis of 1.5wt% molybdenum. This gave B_S $\sim$570°C. Experimentally, it was found to be $\sim$510°C in the 4.2wt% molybdenum alloy. Partial transformation of the bonded TiO_2–A5762 specimens was performed at 480°C for 55 s.

For this alloy, no reaction zone was found, nor was any layer of allotriomorphic ferrite formed at the ceramic/steel interface. The oxide, nevertheless, stimulated the formation of bainite (Fig.4.11). A line profile of the concentrations of silicon and molybdenum produced adjacent to the TiO_2 layer in A5762 is shown in Fig.4.12. Because of the lack of any reaction zone in this alloy, the effects produced by oxidation alone may be observed. Clearly, there is very little, if any, effect on the substitutional elements due to the presence of oxygen. Further, since bainite production was induced without the precipitation of silica, these particles were clearly not responsible for the nucleation observed in the silicon–rich alloy, A5763.

4.2.1.1.3 Summary of the Effects of Oxygen on Substitutional Elements

Both the water–quench experiment, and the partial transformation experiment conducted using A5762, indicate that oxygen presence alone in the steel, although responsible for causing nucleation, has no observable effect on the substitutional element concentrations.

4.2.1.2 Effects on Interstitial Alloy Chemistry

Any effects on carbon levels in the steel due to the presence of oxygen could not be directly measured using standard SEM EDX techniques, since the levels of carbon were small, and the Be–window covering the detector on the EDX system would not allow penetration and

detection of the soft X–rays associated with electron bombardment of carbon. However, the strong interactions normally associated with carbon and oxygen suggested that alterations in carbon levels in solution would occur. Any decarburisation would stabilise ferrite over austenite, so that accelerated ferrite transformation would be expected in the affected area. Decarburisation would explain the nucleation effects observed. If this were the case, then oxygen–releasing minerals would not only be expected to accelerate transformations from austenite to ferrite, but also to inhibit transformations from ferrite to austenite. If the ferrite–austenite transformation was examined in bonding experiments, then we would expect to observe greater transformation to austenite in the bulk material than adjacent to the oxygen–releasing mineral.

4.2.1.2.1 Duplex Stainless Steel

Examination of this predicted transformation inhibition was undertaken using a duplex stainless steel (see Chapter 2), ferritic at high temperatures, but which is partly austenitic at low temperatures. WO_3 powder was sandwiched between two blocks of this duplex stainless steel, and was subjected to the following treatment in the thermomechanical simulator:

The steel was ferritised at 1350°C for 5 mins during which a compressive load of 500N was applied (~8 MPa) manually, to achieve bonding between steel and ceramic. The composite specimen was gas–quenched to 1000°C and held for 5 mins before gas–quenching to room temperature (quench rates of ~40°C/s were achieved).

Fig.4.13 clearly shows that the extent of transformation to austenite in the region adjacent to WO_3 was greatly reduced, and the microstructure refined, as compared with transformation in the bulk alloy. Such a result is consistent with the decarburisation hypothesis. Other interstitial–oxygen interactions may have occurred, for example between nitrogen and oxygen in the duplex stainless steel, to cause the same effects on transformation. Nevertheless, it would appear that oxygen does interact with interstitial elements in such a way as to stabilise ferrite over austenite.

4.2.1.2.2 Furnace Homogenisation of Carbon Profile

It has been shown that group I minerals, which release oxygen on heating, cause oxygen impregnation of local steel. This has no apparent effect on the concentration of substitutional elements in the alloy, but may effect the concentrations of interstitial elements. Oxygen interaction with carbon, to cause local carbon depletion is consistent with the experimental observations described above.

If local chemical depletion was responsible for the production of bainite adjacent to

group I minerals, then extended high temperature treatment of bonded specimens would be expected to equilibrate the system by:

(i) allowing the group I mineral to release all the oxygen possible.

(ii) homogenising the chemical profiles within the steel.

Homogenisation in chemistry would mean that the drive to form bainite would be uniform across the bonded specimen. Hence, the mineral layer would be expected to be rendered ineffective in causing nucleation. The examination of such an effect was undertaken by preparing a series of 6 bonded specimens containing TiO_2. These specimens were held at 1200°C for varying times before allowing partial transformation below B_S. For holding times $\geq$6 hrs, the bonded specimens were sealed in silica tubes under partial pressure of argon, and heat treated in high temperature furnaces, rather than in the thermomechanical simulator.

Results showed that there is a very real dependence of the extent of the bainite zone on time held at 1200°C. Fig.4.14 shows the mean bainite thickness produced adjacent to the TiO_2 as a function of austenitisation time. As can be seen, the thickness drops dramatically for extended austenitisation times, consistent with homogenisation of chemistry within the steel. Very short austenitisation times also produced reduced thicknesses of bainite. This was presumably because the full extent of oxygen diffusion into the steel could not occur in such a short period.

Clearly, this type of behaviour is entirely consistent with oxygen–caused local carbon depletion profiles being responsible for the observed nucleation.

4.2.1.2.3 Direct Measurement of Carbon Profile

Experimental evidence points to oxygen impregnation of the steel affecting the local levels of carbon in solution. However, conventional EDX analysis could not determine the concentrations of carbon. In the Harwell Laboratories, Oxfordshire, though, carbon concentration profiles could be measured by using Nuclear Reaction Analysis. A bonded specimen was prepared containing TiO_2 and was water–quenched from 1200°C to minimise redistribution of carbon on cooling. This specimen was metallographically prepared and sent to the Harwell Laboratories for analysis. The results of this analysis can be seen in Fig.4.15. As can be seen from the figure, the levels of carbon in the steel are strongly affected by the presence of oxygen, adjacent to the TiO_2 layer. However, in contrast to expectations, the carbon concentration increased, rather than decreased, with proximity to the interface. Nevertheless, bainite and ferrite production were accelerated in the apparently carbon–enriched region.

Carbon enrichment and increased stability of ferrite over austenite are not compatable observations. However, this assumes that carbon is present in solution. This may not be so. One explanation for the apparent contradiction is that carbon has precipitated out of solution, either by clustering in voids or dislocations produced as a result of oxygen presence, or by combining with oxygen to form microvoids of carbon–oxide gases. Removal of carbon by precipitation would cause local regions depleted of carbon, and would hence reduce the hardenability of the alloy. Such an hypothesis is extremely difficult to test, and is, therefore, only tentatively suggested.

4.2.2 Summary

To summarise, group I minerals are those which are capable of liberating oxygen, which in turn is thought to cause a reduction in the levels of carbon in solution in adjacent steel. It is this decarburisation which stimulates the nucleation of bainite. There are some associated effects such as the formation of a reaction zone, which are of secondary importance in the mechanism by which nucleation is stimulated.

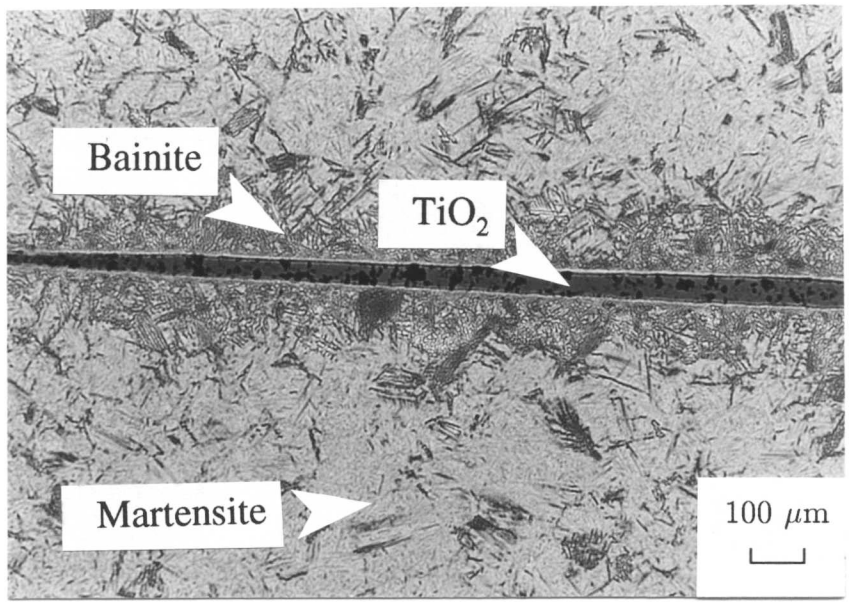

Figure 4.1 Profuse bainite nucleation in the interface region between A5763 and TiO_2. Such levels of nucleation are typical of group I minerals.

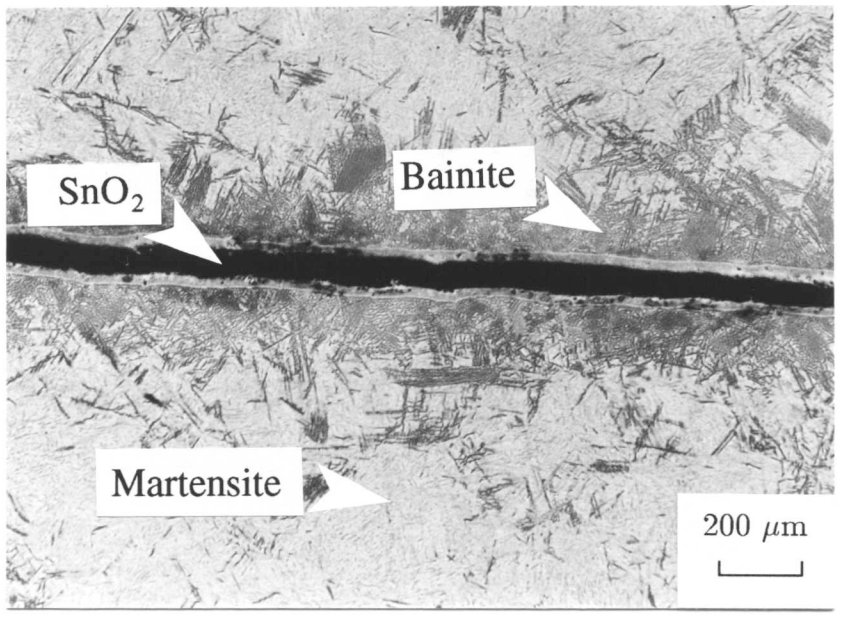

Figure 4.2 Analogues of TiO_2 also induce large amounts of transformation – here bainite production is induced by SnO_2.

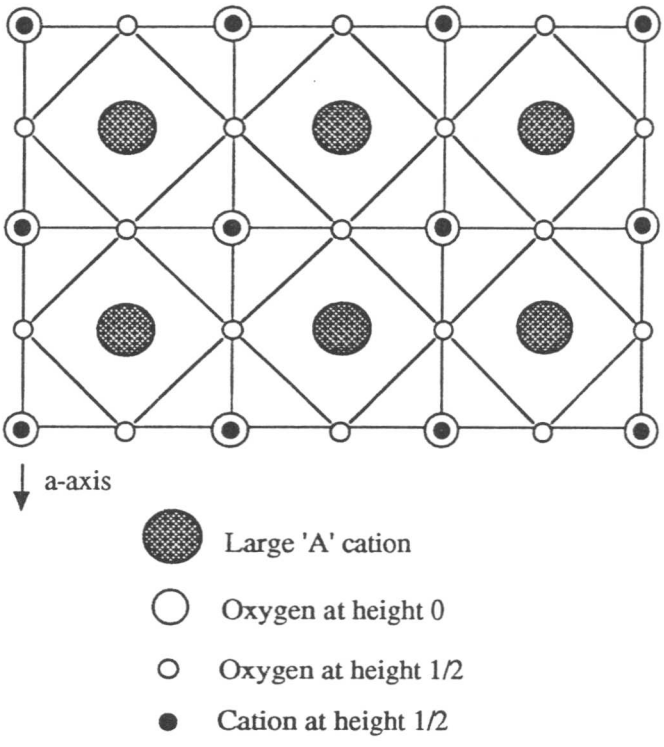

Figure 4.3 Idealised structure of the normal perovskites (viewed down [001]).

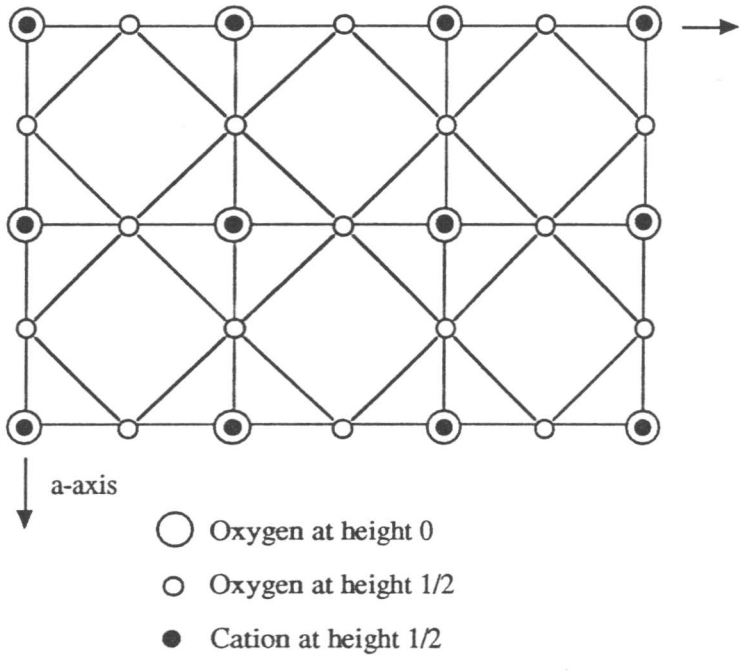

Figure 4.4 Idealised structure of the defect perovskite mineral family (viewed down [001]) – similar to the normal perovskites, save for the absence of the large 'A' atom.

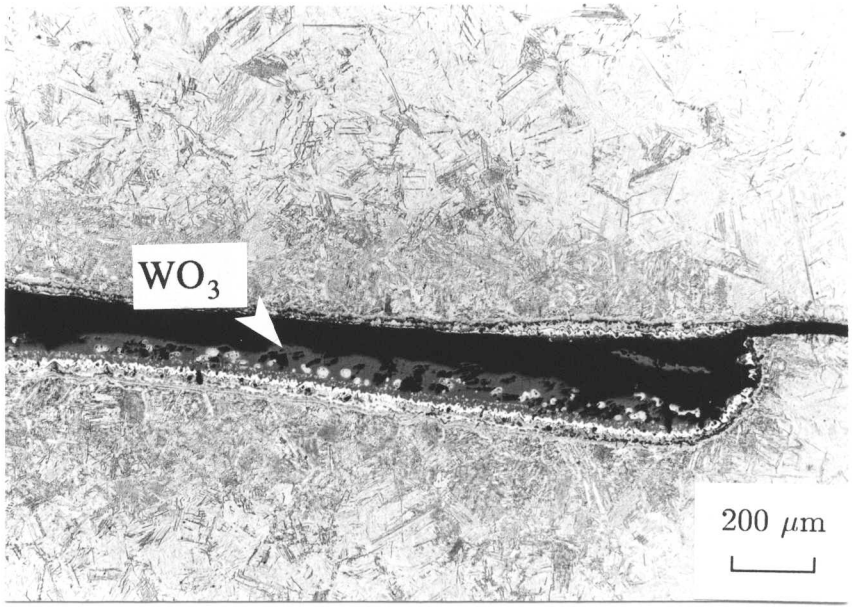

Figure 4.5 Defect perovskites cause profuse nucleation of bainite, and obvious reaction zone areas.

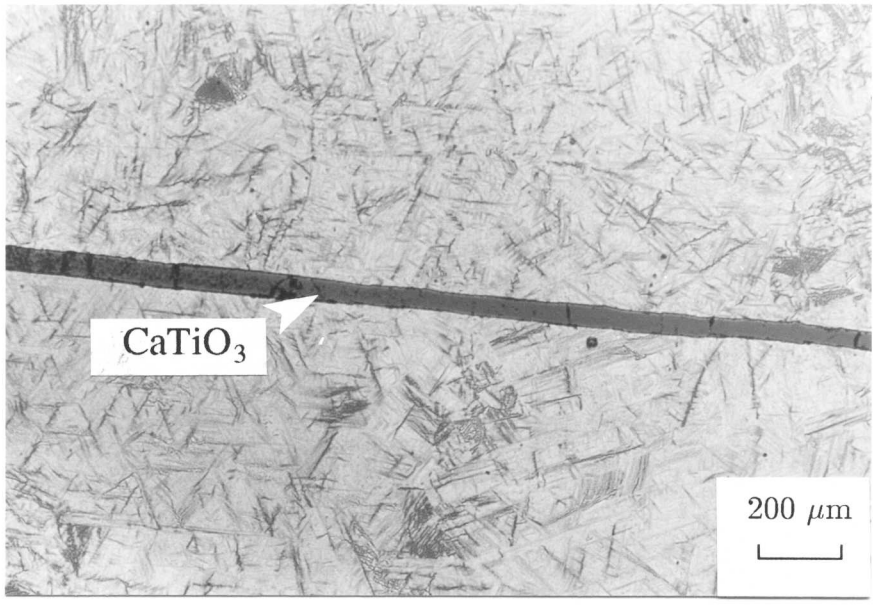

Figure 4.6 Normal perovskites do not enhance nucleation of bainite in the local steel.

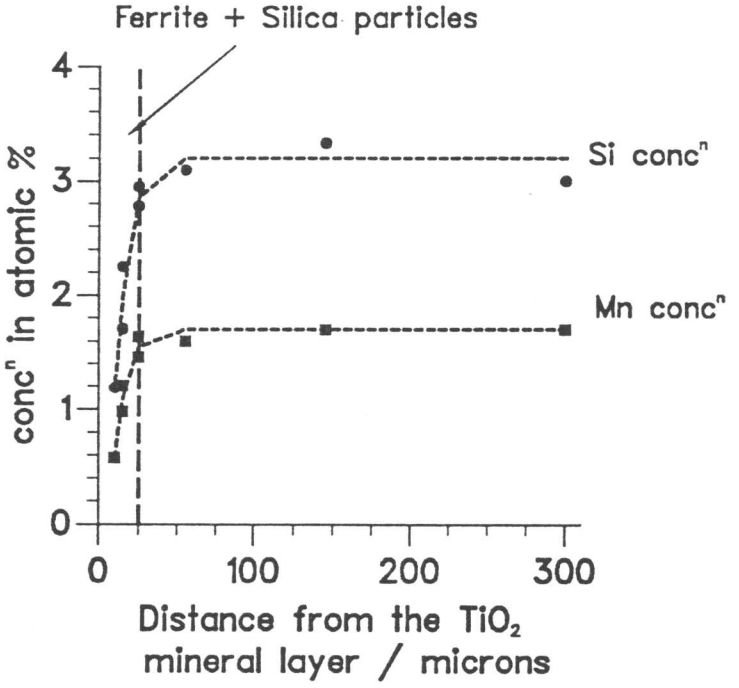

Figure 4.7 Line profile of the concentrations of substitutional elements measured perpendicular to the interface between a group I mineral and A5763, using SEM EDX. Depletion of manganese and silicon has occurred, but the region of depletion is confined to the reaction zone.

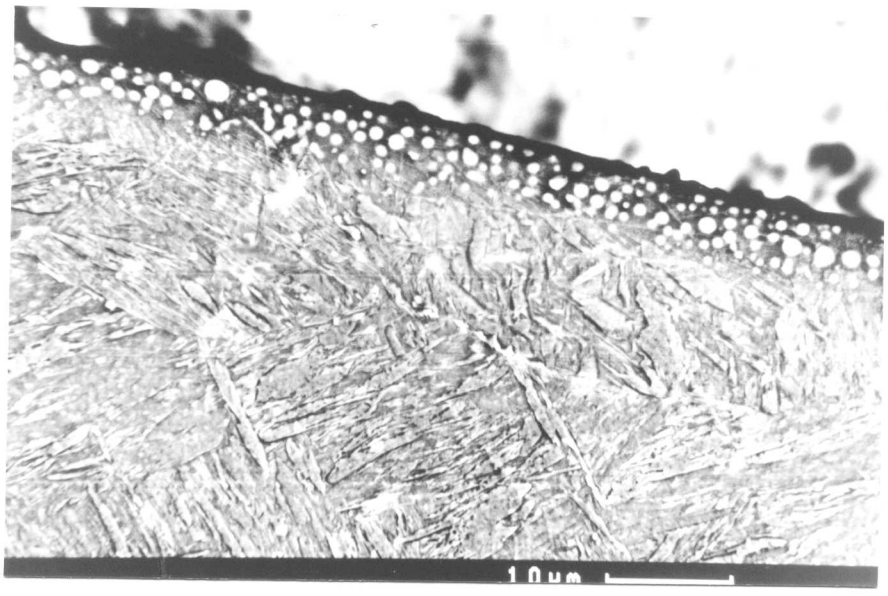

Figure 4.8 SEM micrograph of the TiO_2–steel interface after water–quenching from 1200°C. The rapid quench has not been successful in preventing the formation of the reaction zone, but has reduced its extent to $\sim 5\mu$m.

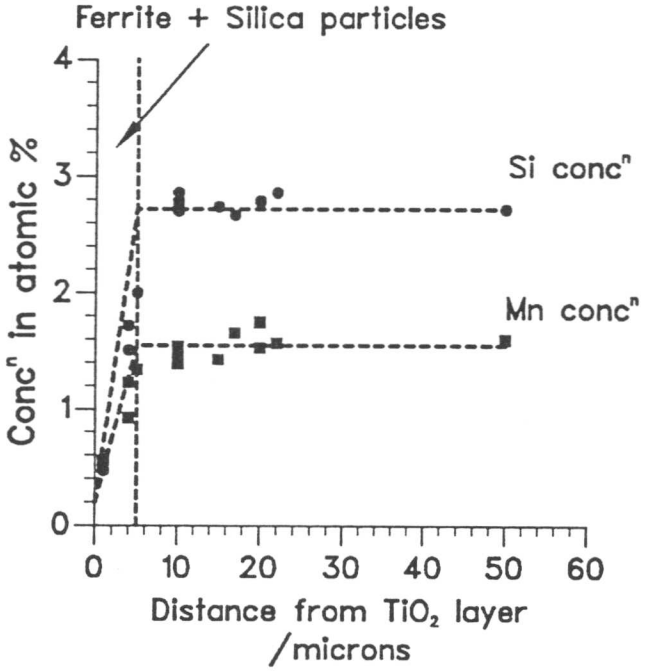

Figure 4.9 SEM EDX line profile taken perpendicular to the TiO_2–steel interface in the water–quench experiment. Depletion in silicon and manganese is still restricted to the reaction zone.

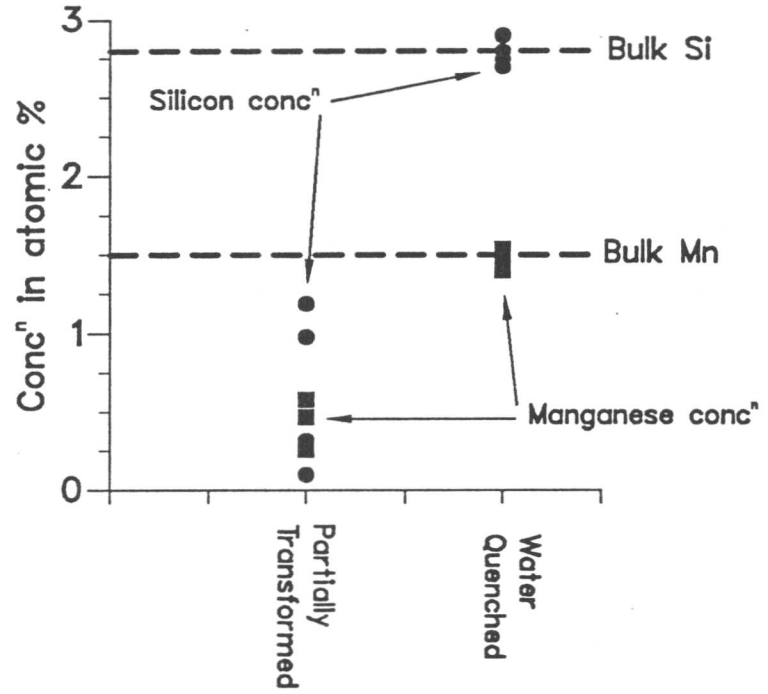

Figure 4.10 EDX microanalysis 10 μm away from TiO_2–steel interface for the water–quench and a partially transformed specimen. Oxygen is present at this distance from the interface, but, independent of the reaction zone, has no effect on the concentrations of substitutional elements.

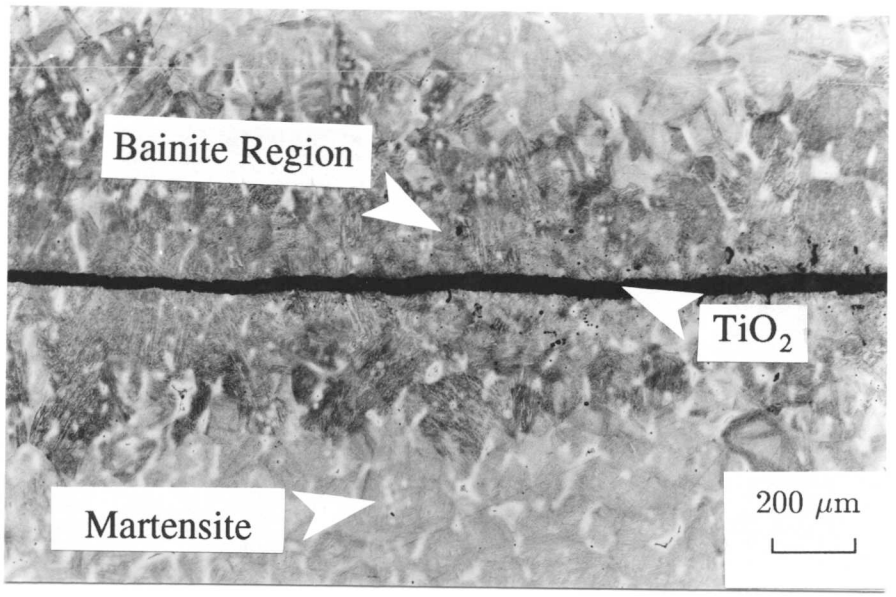

Figure 4.11 Optical micrograph of the TiO_2–A5762 interface. A thick bainitic region was produced adjacent to the mineral.

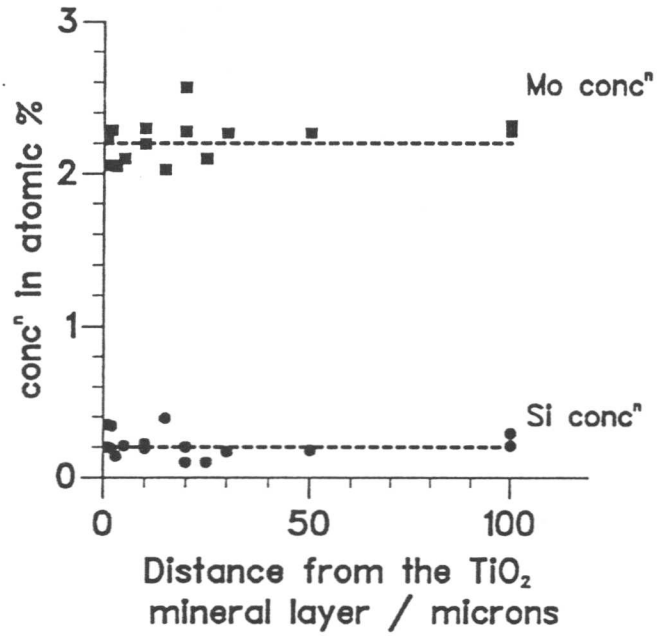

Figure 4.12 SEM EDX line profile taken perpendicular to the TiO_2–A5762 interface. No alteration from the bulk chemistry has occurred adjacent to the mineral layer.

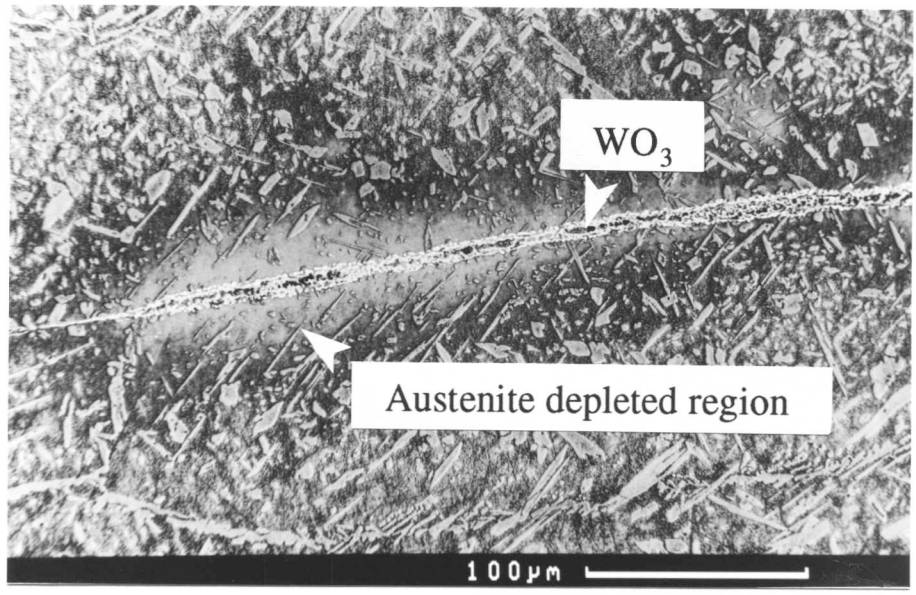

Figure 4.13 SEM micrograph of the interface region between WO_3 and the duplex stainless steel. Obvious reduction in the extent of transformation from ferrite to austenite has occurred adjacent to the WO_3. The microstructure is also more refined than the austenite in the bulk steel.

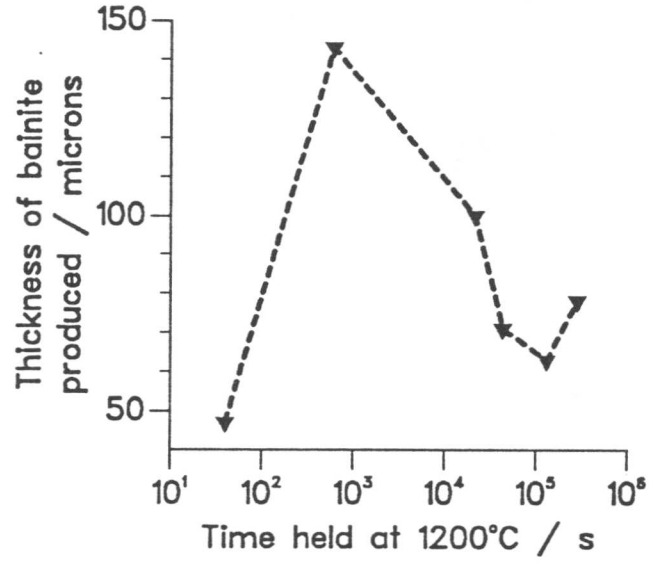

Figure 4.14 Plot showing the thickness of the bainite–rich zone produced adjacent to TiO_2 as a function of the time held at 1200°C before partial transformation.

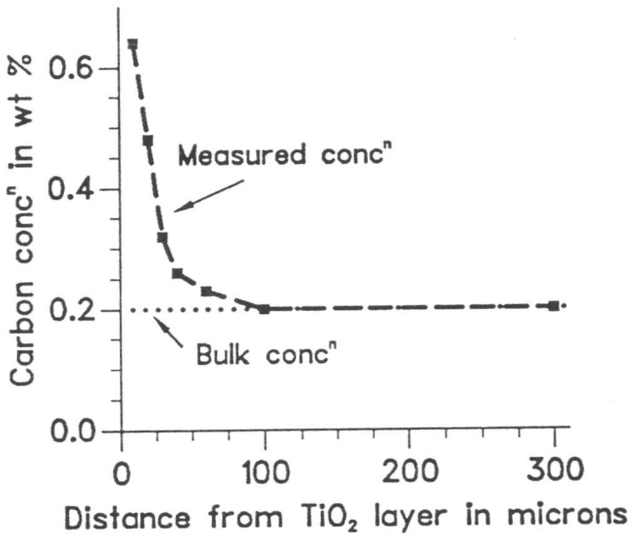

Figure 4.15 Line profile of the carbon concentration away from TiO_2 in a water quenched specimen, as measured by the Harwell Laboratories.

4.3 Group II

It has already been shown that TiO and Ti_2O_3 appear to stimulate bainite nucleation from their surfaces (for detailed investigation see Chapter 3). However, this nucleation potency is not associated with the production of a reaction zone. These minerals would therefore be classed differently from those of group I, and are instead assigned to 'Group II'. The lack of reaction zone does not preclude any oxygen–steel interaction, but it indicates that such interaction is unlikely to be the dominant reason for their nucleation potency. Indeed, investigations showed that Ti_2O_3 appears to act as a sink for manganese (Chapter 3). The mechanism by which TiO causes nucleation remains unknown.

4.4 Group III

This group of minerals was found to remain inert, both chemically and in their ability to stimulate bainite nucleation. TiN was found to belong to this group of minerals, as described in Chapter 3. However, a variety of other minerals were also found to be inert and are each discussed briefly below:

4.4.1 α-Al_2O_3

Fig.4.16 shows the steel/α-Al_2O_3interface, and the lack of acceleration of the bainite transformation. α-Al_2O_3 is not often cited as a major constituent of real non–metallic inclusions. Alumina has more often been observed in its γ–form.

4.4.2 γ-Al_2O_3

γ-Al_2O_3 is a commonly suspected phase in real non–metallic inclusions. It was therefore important to test its nucleation potency. However, γ-Al_2O_3 is a metastable aluminium

oxide and has a tendency to invert to α-Al_2O_3 when held above ~1000°C (Rooksby, 1951).

Since the austenitising and bonding procedure used in the bonding experiments involved a 10 min isothermal hold at 1200°C, it was possible that by the time the steel was partially transformed at 510°C, the γ-Al_2O_3 would all have transformed to α-Al_2O_3. However, this was not necessarily so, as the γ-Al_2O_3 to α-Al_2O_3 transition is described as slow. In order to see if full transformation from the γ–form to the α–form would occur during the bonding treatment, powdered γ-Al_2O_3 was heat–treated in a furnace for 15 mins at 1200°C. The powder was then X–rayed on a powder diffractometer, to observe the extent of transformation. Fig.4.17 shows that α-Al_2O_3 was strongly present in the post–furnaced powder. However, not all the powder had transformed. Some γ-Al_2O_3 remained, and so it was thought likely that some γ-Al_2O_3 would still be present in the bonding experiment after the bonding treatment. Results show that the α-Al_2O_3–γ-Al_2O_3 mixture did not cause enhanced nucleation adjacent to the mineral–steel interface. It was therefore concluded that γ-Al_2O_3 did not show any nucleation potency.

4.4.3 $MnAl_2O_4$

Another phase commonly observed in real–weld inclusions is $MnAl_2O_4$ (or galaxite). Powdered galaxite was not, however, commercially available, and so the first stage in testing its potency of nucleation was to synthesise some of the mineral. $MnAl_2O_4$ production was achieved by sintering α-Al_2O_3 and MnO in the stoichiometric ratio 1:1. Sintering was conducted in a ceramic boat of compressed Al_2O_3, since this was deemed preferrable to other ceramic materials, which may have contaminated the galaxite. Sintering for 26 hrs at 1300°C was sufficient to produce galaxite, as verified by X–ray powder diffraction (Fig.4.18). However, as can be seen from the figure, excess α-Al_2O_3 was present after the heat treatment. It was thought that this excess alumina was due to sintering being performed in an alumina boat. Fig.4.19 shows the X–ray powder trace obtained when sintering was performed in a platinum cricible – the excess alumina was considerably reduced.

However, the presence of excess alumina was not considered to be problematic in interpreting any potency produced by $MnAl_2O_4$, since previous experiments had shown alumina to be ineffective in the nucleation of bainite. Fig.4.20 shows that the mixture of galaxite and α-Al_2O_3 did not cause the accelerated production of bainite adjacent to the mineral–steel interface. It was therefore concluded that $MnAl_2O_4$ was not an effective nucleating mineral.

4.4.4 NbC

Another mineral phase found in real steels is NbC. As can be seen in Fig.4.21, it does not enhance the formation of bainite.

4.4.5 MnS

A very common mineral in non–metallic inclusions in real welds and cast steels is MnS. When tested in the bonding experiments, it did show a slight tendency to nucleate bainite. This tendency was minimal (Fig.4.22) and was often not observed at all. MnS was therefore classified as a non–nucleating mineral, and assigned to group III.

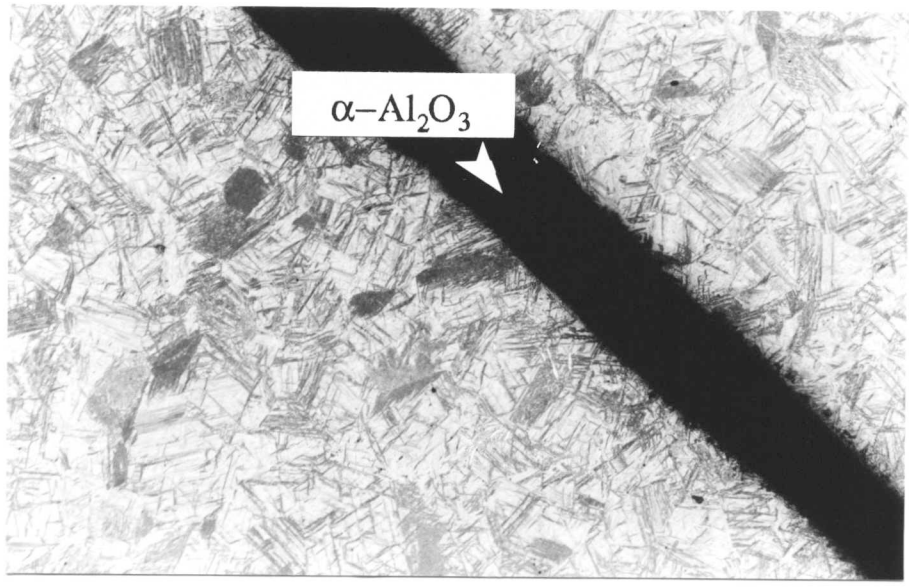

Figure 4.16 Optical micrograph of the interface region between α-Al_2O_3 and steel. No acceleration of bainite transformation has occurred adjacent to the interface.

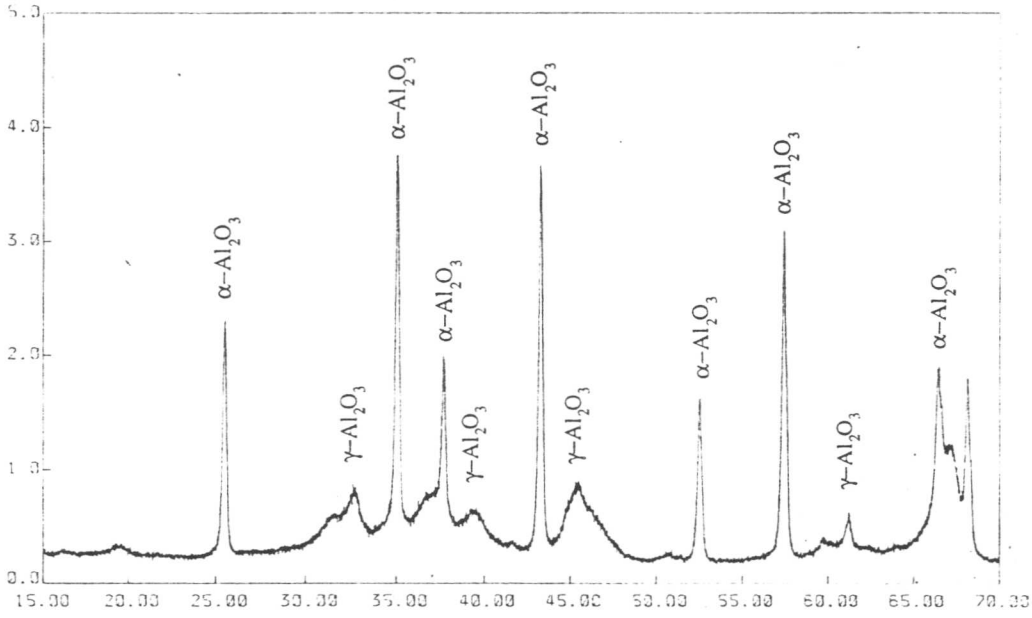

Figure 4.17 X–ray diffraction trace of the powder produced after heat treating γ-Al_2O_3 at 1200°C for 15 mins. α-Al_2O_3 is strongly evident, but γ-Al_2O_3 has not totally disappeared.

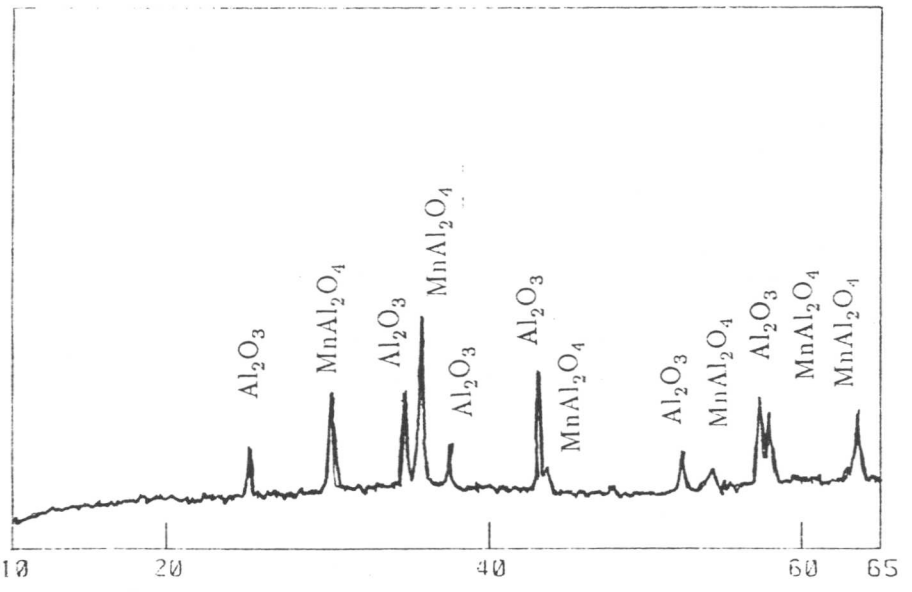

Figure 4.18 X–ray diffraction trace produced due to the post–sintered mixture of MnO and α-Al_2O_3. Galaxite has been produced, but excess alumina was apparent.

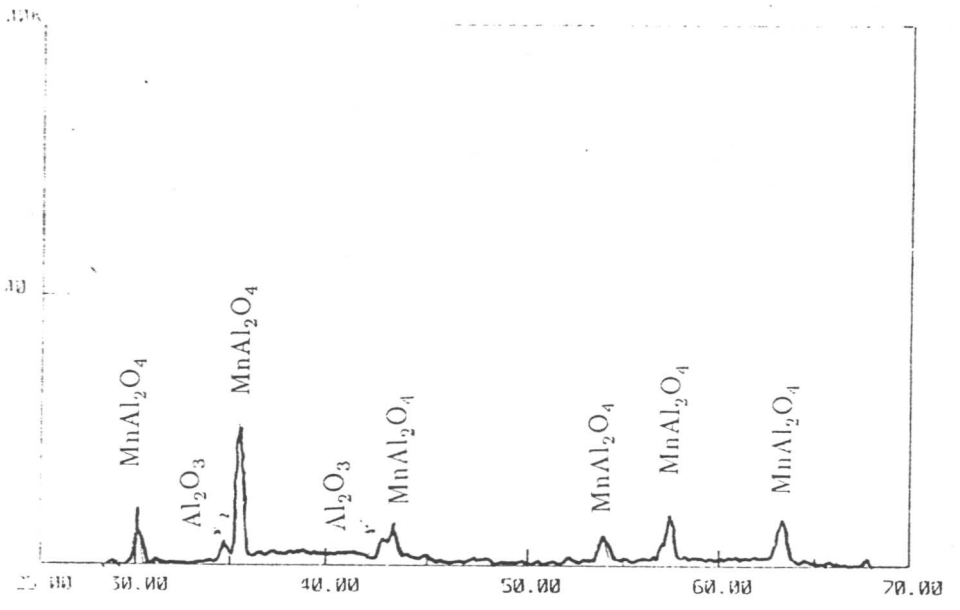

Figure 4.19 X–ray diffraction trace produced after sintering α-$Al_2O_3$and MnO in a platinum crucible. The excess alumina has been considerably reduced.

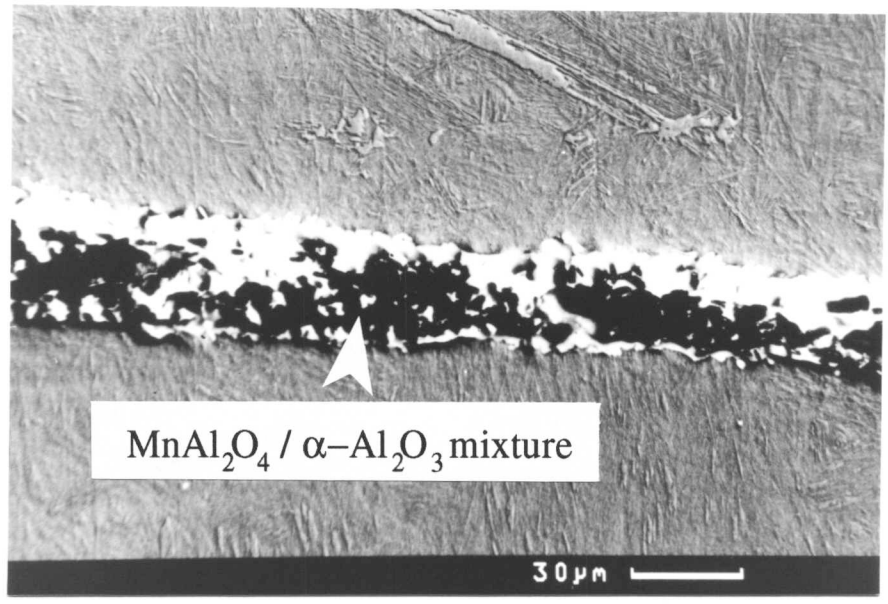

Figure 4.20 SEM micrograph showing the lack of nucleation induced by the galaxite/alumina mixture.

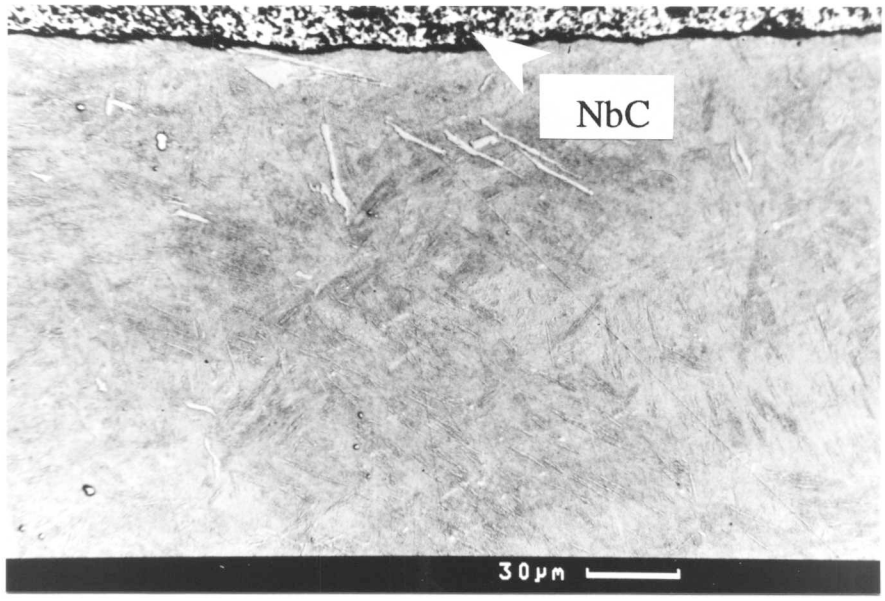

Figure 4.21 SEM micrograph of the NbC–steel interface region. Nucleation from the interface has not occurred.

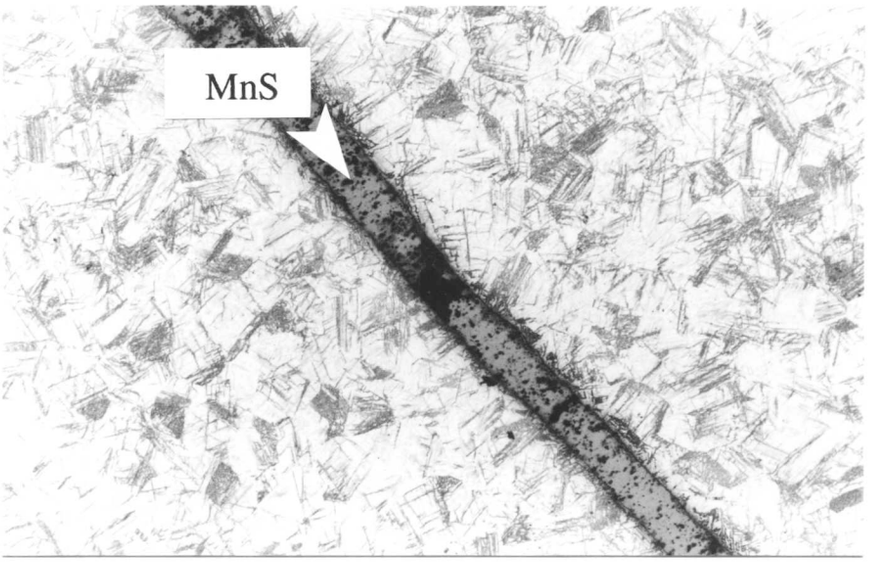

Figure 4.22 Optical micrograph of the MnS–steel interface area. Slight nucleation was observed, but was considerably less than in group I, or group II minerals.

4.5 Summary of Results, and Conclusions

Extensive bonding experiments have revealed that minerals may be assigned to one of three groups, depending on their effects on the steel:

(i) Group I: The minerals in group I induce accelerated bainite transformation adjacent to the mineral–steel interface. They also cause the formation of a reaction zone – a region of ferrite, containing amorphous silica particles. This behaviour is caused by the ability of all group I minerals to release oxygen at elevated temperatures. Oxygen enters the steel, and affects the local carbon concentrations such that the steel hardenability is reduced.

(ii) Group II: The minerals in group II induce accelerated bainite transformation adjacent to the mineral–steel interface, but do not cause reaction zone formation. Instead, bainite nucleates directly from the mineral–steel interface. Only two minerals were associated with this group – TiO and Ti_2O_3. The mechanism of nucleation due to Ti_2O_3 was found to be a depletion of manganese in local steel, so reducing hardenability.

(iii) Group III: The minerals in group III did not induce any acceleration of transformation adjacent to the mineral–steel interface.

A summary of the minerals assigned to each group is shown in Table 4.2.

Effective: Group I	Effective: Group II	Ineffective: Group III
TiO_2, SnO_2	Ti_2O_3	TiN, NbC
MnO_2, PbO_2	TiO	$CaTiO_3$, $SrTiO_3$
WO_3, MoO_3		α-Al_2O_3, γ-Al_2O_3
KNO_3, V_2O_5		$MnAl_2O_4$

Table 4.2 Summary table of the minerals tested in the bond experiments, assigned to groups according to their effects on steel.

The bonding experiments clearly showed that some mineral types could induce nucleation, while others could not. The testing of pure mineral phases, rather than complex real inclusions, has shown unequivocably the minerals capable of causing nucleation. Moreover, the bonding experiments have elucidated two mechanisms for nucleation:

(i) Oxygen–caused effects on carbon concentrations locally around the mineral.

(ii) Manganese depletion locally around the mineral.

These two mechanisms of nucleation by inclusions have already been proposed (Carbon--depletion – Es-Souni and Beaven, 1990; Es-Souni *et al.*, 1991; Manganese–depletion –

Yamamoto *et al.*, 1993; Farrar and Watson, 1979), but here they have been clearly shown in operation.

Lattice matching is a popular explanation for the apparent nucleation potency of the TiX phase (X=C, N or O) in welds (Grong *et al.*, 1992). However, the present experiments indicate that TiO acts as a potent nucleant while TiN does not. Both minerals have a similar lattice match with ferrite (Bramfitt, 1970; Mills *et al.*, 1987). Therefore, the bonding results suggest that a consideration of lattice matching alone cannot distinguish effective from ineffective nucleants.

Differences in thermal expansion coefficients of inclusion and steel cause strains around an inclusion during cooling. It has been suggested that ferrite transformation adjacent to the inclusion may relieve this strain (Barrite and Edmonds, 1981). Table 4.3 shows the thermal expansion coefficients of some of the minerals tested. There is clearly no direct correlation between the expansion coefficient difference and bainite nucleation potency, as measured here.

Although many of the mineral phases utilised in the experiments are unlikely to occur in commercial steels, a number of compounds which do occur have been tested. Specifically TiO, TiN, Ti_2O_3, γ-Al_2O_3, NbC, $MnAl_2O_4$ and MnS. The results show that of these minerals, only TiO and Ti_2O_3 are potent nucleators. Inclusions rich in both TiO and Ti_2O_3 should help maximise yields of acicular ferrite in welds where alloy design ensures that grain boundary nucleated phases do not overwhelm intragranularly nucleated phases.

However, some reservation as to the applicability of the bond experiment results to the production of acicular ferrite in real welds may exist. Because of such reservations, the further experiments described in Chapter 5 were undertaken.

Mineral	Coeff. of thermal expansion /K^{-1}	Temp. range of measurement /K	Reference
SnO_2	4 x 10^{-6}	273–1073	[1]
	3.76 x 10^{-6}	295–923	[1]
NbC	7 x 10^{-6}	–	[2]
Al_2O_3	8.0 x 10^{-6}	293–1853	[1]
	8.4 x 10^{-6}	293–1273	[1]
	7.5 x 10^{-6}	1273–1573	[1]
	a-axis: 7.1 x 10^{-6}	373	[1]
	a-axis: 9.7 x 10^{-6}	773	[1]
	a-axis: 14.2 x 10^{-6}	1273	[1]
	c-axis: 6.0 x 10^{-6}	373	[1]
	c-axis: 8.9 x 10^{-6}	773	[1]
	c-axis: 13.8 x 10^{-6}	1273	[1]
$MnAl_2O_4$	8 x 10^{-6}	273–1073	[3]
$SrTiO_3$	8.9 x 10^{-6}	273–1080	[4]
TiN	9.4 x 10^{-6}	273–1073	[3]
TiO_2	9.5 x 10^{-6}	273–1080	[4]
	7.8 x 10^{-6}	293–873	[1]
	8.19 x 10^{-6}	273–773	[1]
$CaTiO_3$	1.2 x 10^{-5}	273–1700	[4]
TiO	1.4 x 10^{-5}	273–1400	[4]
MnS	1.8 x 10^{-5}	273–1073	[3]
Austenite	2.3 x 10^{-5}		[3]

Table 4.3 The coefficient of thermal expansion of a selection of minerals. References [1,2,3,4] are as follows: [1] – Samsonov (1973), [2] – Barantseva (1974), [3] – Brooksbank and Andrews (1972), [4] – Goldsmith *et al.* (1961).

CHAPTER 5

Acicular Ferrite Nucleation on Minerals Added to Molten Steel

5.1 Introduction

The bonding experiments performed to date have both indicated mineral phases capable of inducing bainite nucleation, and revealed the mechanisms by which such nucleation occurs (Chapters 3 and 4). However, the pressure bonding of steel and mineral powder may not create the conditions required for some nucleation mechanisms to operate. For example, the application of pressure in the solid–state does not necessarily lead to an intimate bond, on an atomic scale, between the chosen mineral and steel. Such lack of intimacy may preclude epitaxial relationships across the interface. Therefore minerals which cause nucleation by offering surface epitaxy with acicular ferrite may not be effective. This is not expected to be a problem when the mineral is added directly to the melt.

A second difficulty is that the ceramic is bonded in the form of powder, which does not fully densify during pressure bonding. Any difference in thermal expansivity between the steel and ceramic may not lead to the development of contraction stresses of the magnitudes expected when liquid steel, containing inclusions, solidifies and cools.

A further objection to the application of bonding results to the likely efficacies of various mineral types in producing acicular ferrite microstructures, is that the bond experiments investigated the production of bainite, and not acicular ferrite. Evidence suggests that bainite and acicular ferrite transform in the same manner (Yang and Bhadeshia, 1987; Sugden and Bhadeshia, 1989). Nevertheless, a direct investigation into the effects of pure mineral inclusions on the production of acicular ferrite specifically, would yield less equivocable results. It was therefore decided to attempt to investigate the nucleation properties of minerals introduced to molten steel.

5.2 Experimental Technique

A potential difficulty with experiments in which minerals are added to liquid steel is that they may react, and change their character. Consequently, a number of different techniques was attempted, with the aim of rapid melting and cooling in order to reduce the opportunity for reaction. Melting using a Nd-Yag pulsed laser (0.5kW average power) proved ineffective; the laser was traversed across a slit in a steel sample, the slit being filled with the desired mineral. The small depth of melting, and considerable spatter made it impossible to exercise effective control.

Melting of 60 g mixtures of steel and mineral in an argon arc furnace led to the strong clustering of mineral particles (Fig.5.1), and to excessive solidification–induced chemical segregation. Such segregation has large effects on transformation behaviour, which can mask the role of the mineral addition. An attempt was made to homogenise the solidified sample by heat–treatment. However, many of the minerals investigated in Chapters 3 and 4 were found to stimulate bainite nucleation by oxidising and decarburising adjacent steel. The effectiveness of nucleation produced by this mechanism was found to diminish dramatically after heat treatment at 1200°C for time periods in excess of 6 hr (Fig.5.2). Therefore, it was likely that homogenising the steels would affect the nucleating capabilities of the mineral inclusions added.

All of these problems were avoided by melting using the RF–induction coil in the Thermecmastor (described in Chapter 2). A countersunk region of 2 mm diameter and 3 mm depth was drilled in a cylinder of A5763, of diameter 8 mm, and depth 6 mm. This was filled with powdered mineral, as shown in Fig.5.3. The sample was contained in an alumina crucible, and was heated manually to melting, and held in the molten state for five seconds before allowing the melt to solidify. The arrangement was then gas–quenched, using He, to room temperature. The relatively rapid solidification and cooling resulted in a specimen with no visible signs of chemical segregation. Furthermore, the mineral particles were found to be evenly distributed throughout the sample, presumably because of the electromagnetic stirring of the melt in the RF–field.

A number of mineral powders were used in the experiments: TiO_2, Ti_2O_3, TiN, MnS, ($MnAl_2O_4$ + α-Al_2O_3), γ-Al_2O_3 and WO_3.

5.3 Characterisation of Inclusions

Electron diffraction and microanalytical experiments (using energy dispersive X-ray analysis, EDX) were conducted on the solidified samples, in order to establish whether or not the particles added to the melt had been successfully incorporated into the solid state. These experiments were all conducted on particles extracted on carbon replicas.

It should be noted that relatively small particles ($\simeq 0.1\,\mu$m), of apparently consistent mineralogy, could be found present in all the replicas examined, irrespective of the mineral powder deliberately added (Table 5.1). These particles showed no EDX signal above background levels. They also all produced electron diffraction data consistent with a f.c.c. mineral of lattice parameter a$\sim$3.6Å (Fig.5.4).

Mineral Added to Melt	d_{hkl} Observed	Observed Angular Relationships			
		2.1Å:2.1Å	2.1Å:1.8Å	2.1Å:1.3Å	1.3Å:1.3Å
TiO_2	2.1Å	72°	55°	60°	58°
	1.8Å				
	1.3Å				
Ti_2O_3	2.1Å	72°	55°		
	1.8Å				
	1.3Å				
γ-Al_2O_3	2.1Å	71°	54°	90°	60°
	1.8Å				
	1.3Å				
$MnAl_2O_4$	2.1Å	70°	54°	90°	90°
& α-Al_2O_3	1.8Å				
	1.3Å				
WO_3	2.1Å	70°		90°	90°
	1.8Å				

Table 5.1 Shows the interplanar spacings and interplanar angles found from the small crystallites present in all the melts produced. The spacings and angles are largely the same irrespective of the powder added.

5.3.1 TiN Additions

Fig.5.5a shows the classic facetted cubic shape of the added TiN particles. The particles examined were titanium–rich, and gave diffraction patterns (Fig.5.5b) consistent with f.c.c TiN (a=4.2Å). Table 5.2 summarises the electron diffraction information obtained. Taking the evidence as a whole, the particles appear to have been transferred successfully into the solid steel.

5.3.2 MnS Additions

Particles typical of those produced due to MnS powder additions to the steel melt are shown in Fig.5.6. Such particles EDX as containing manganese and sulphur, and the diffraction data (Table 5.3) is consistent with a cubic form of MnS (with space group F43m and lattice parameter a=5.612Å).

Observed		Observed	Likely	Likely		Calculated		Calculated
d_1	d_2	$d_1 \hat{} d_2$	Phase	$(hkl)_1$	$(hkl)_2$	d_1	d_2	$d_1 \hat{} d_2$
2.0Å	2.3Å	55°	TiN	(200)	(111)	2.1Å	2.4Å	54.7°
2.0Å	2.0Å	90°	TiN	(200)	(020)	2.1Å	2.1Å	90°
2.3Å	2.3Å	71°	TiN	(111)	$(1\bar{1}1)$	2.4Å	2.4Å	70.5°
2.0Å	2.3Å	56°	TiN	(200)	(111)	2.1Å	2.4Å	54.7°
1.4Å	2.3Å	90°	TiN	(220)	$(1\bar{1}1)$	1.5Å	2.4Å	90°

Table 5.2 Electron diffraction patterns from added particles in the TiN inoculated sample. The data index well to TiN.

Observed		Observed	Likely	Likely		Calculated		Calculated
d_1	d_2	$d_1 \hat{} d_2$	Phase	$(hkl)_1$	$(hkl)_2$	d_1	d_2	$d_1 \hat{} d_2$
3.2Å	3.2Å	71°	MnS	(111)	$(1\bar{1}1)$	3.2Å	3.2Å	70.5°
1.4Å	1.4Å	60°	MnS	(331)	$(3\bar{1}3)$	1.3Å	1.3Å	60°
1.2Å	1.4Å	90°	MnS	$(11\bar{5})$	(331)	1.1Å	1.3Å	90°
1.4Å	1.4Å	60°	MnS	(331)	$(3\bar{1}3)$	1.3Å	1.3Å	60°
3.4Å	3.4Å	71°	MnS	(111)	$(1\bar{1}1)$	3.2Å	3.2Å	70.5°

Table 5.3 Electron diffraction patterns from added particles in the MnS inoculated sample. The data index well to MnS.

5.3.3 γ-Al_2O_3 Additions

Fig.5.7 shows a particle which was typical of those found in the γ-Al_2O_3 inoculated specimen. Such particles EDX as aluminium–rich, and diffraction data, on the whole, is consistent with γ-Al_2O_3. This is surprising, since it was expected that the subjection of the particles to temperatures significantly above 1000°C would cause an inversion from the metastable γ–form to the stable α–form (Rooksby, 1951). Clearly the melting process used does not have sufficient kinetic strength to induce the transformation.

Observed		Observed	Likely	Likely		Calculated		Calculated
d_1	d_2	$d_1 \hat{} d_2$	Phase	$(hkl)_1$	$(hkl)_2$	d_1	d_2	$d_1 \hat{} d_2$
2.9Å	2.5Å	64.5°	γ-Al_2O_3	(220)	(113)	2.8Å	2.4Å	64.8°
4.7Å	4.7Å	70°	γ-Al_2O_3	(111)	$(1\bar{1}1)$	4.56Å	4.56Å	70.5°
5.2Å	3.8Å	77°	Other Al_2O_3					
2.9Å	2.4Å	90°	γ-Al_2O_3	(220)	$(1\bar{1}3)$	2.8Å	2.4Å	90°

Table 5.4 Electron diffraction patterns from added particles in the γ-Al_2O_3–inoculated sample. The data index well to γ-Al_2O_3.

5.3.4 ($MnAl_2O_4$ & α-Al_2O_3) Additions

Galaxite ($MnAl_2O_4$) was prepared by heating together a mixture of alumina and manganese oxide, as described in Chapter 4. The formation of galaxite was confirmed by X–ray diffraction, but some α-Al_2O_3 could not be avoided from the alumina crucible used. It was a mixture of galaxite and α-Al_2O_3 that was, therefore, added to the melt. The galaxite was found to be polycrystalline, and clear electron diffraction patterns proved very difficult to obtain. Microanalysis did confirm that the particles contained both manganese and aluminium, so it is assumed that galaxite is retained in the solidified melt.

5.3.5 WO_3 Additions

This experiment was unsuccessful, in that tungsten oxides could not be found in the solidified steel, presumably because the oxide sublimes readily.

5.3.6 Ti_2O_3 Additions

Particles typically produced by the addition of Ti_2O_3 to molten steel are shown in Fig.5.8. Such particles, when microanalysed, were composed dominantly of titanium. However, diffraction data suggests that, in the smaller titanium–rich particles, and in the surfaces of the larger particles, the oxide is present as TiO, and not Ti_2O_3 (Fig.5.8b). In some cases Ti_3O_5 was found. Results from the bonding experiments suggested that oxygen loss, or absorption of manganese, associated with titanium oxide mineralogical changes, were responsible for their apparent nucleation potency. It seems that similar mineralogical changes have also occurred here. The diffraction data are summarised in Table 5.5.

Observed		Observed	Likely	Likely		Calculated		Calculated
d_1	d_2	$d_1 \hat{} d_2$	Phase	$(hkl)_1$	$(hkl)_2$	d_1	d_2	$d_1 \hat{} d_2$
1.3Å	2.2Å	71°	TiO	(311)	(020)	1.3Å	2.14Å	72.5°
2.5Å	1.5Å	90°	TiO	(111)	$(2\bar{2}0)$	2.48Å	1.53Å	90°
3.5Å	3.8Å	88.5°	Ti_3O_5	(111)	$(\bar{2}02)$	3.3Å	3.5Å	89.8°
1.6Å	1.6Å	61°	Complex Ti-Oxide					
2.5Å	2.5Å	70.5°	TiO	(111)	$(1\bar{1}1)$	2.48Å	2.48Å	70.5°

Table 5.5 Diffraction data from the steel inoculated with Ti_2O_3. All the cases reveal mineralogy changes.

5.3.7 TiO_2 Additions

The morphology of the particles resulting from TiO_2 additions is illustrated in Fig.5.9. Microanalysis showed them to be titanium based. However, the diffraction patterns did not index as any form of TiO_2. Some patterns are consistent with TiO (Fig.5.9b), but the majority of the patterns taken are more likely to correspond to some of the many complex deoxidation products, intermediate between TiO_2 and TiO. This kind of deoxidation was entirely expected from the work described in Chapters 3 and 4.

Observed		Observed	Likely	Likely		Calculated		Calculated
d_1	d_2	$d_1 \hat{} d_2$	Phase	$(hkl)_1$	$(hkl)_2$	d_1	d_2	$d_1 \hat{} d_2$
2.0Å	1.75Å	55°	Complex Ti-oxide					
2.5Å	2.55Å	68.3°	TiO	(111)	$(1\bar{1}1)$	2.48Å	2.48Å	71°
2.4Å	3.1Å	68°	Complex Ti-oxide					
2.4Å	3.1Å	69°	Complex Ti-Oxide					
4.4Å	4.4Å	90°	Complex Ti-oxide					

Table 5.6 Data from steel inoculated with TiO_2. The observed changes from TiO_2 are suspected to involve oxygen loss.

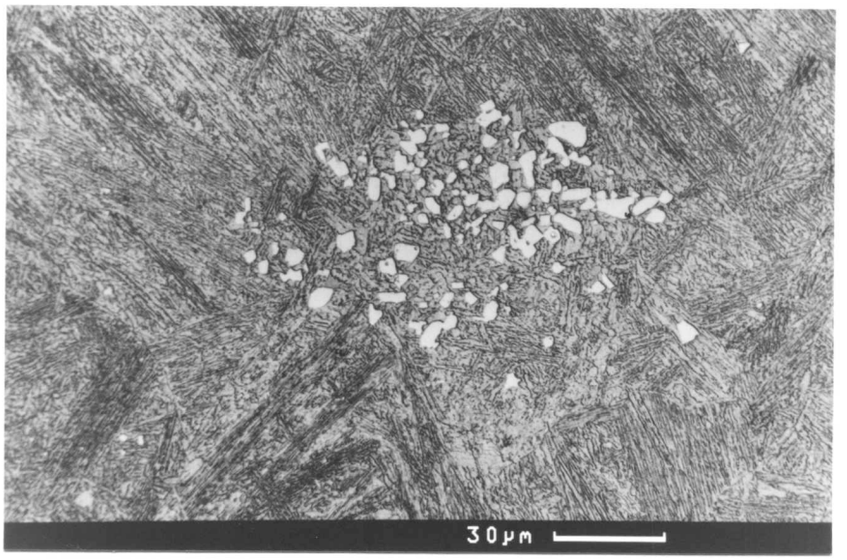

Figure 5.1 SEM micrograph of the particle clustering which occurred after arc melting. This case illustrates TiN–clusters.

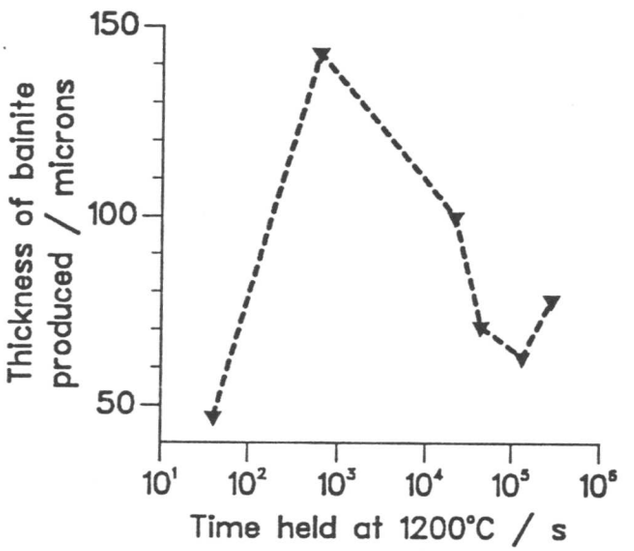

Figure 5.2 Plot showing the variation in the thickness of the bainite layer adjacent to TiO_2 with the time held at 1200°C before partial transformation.

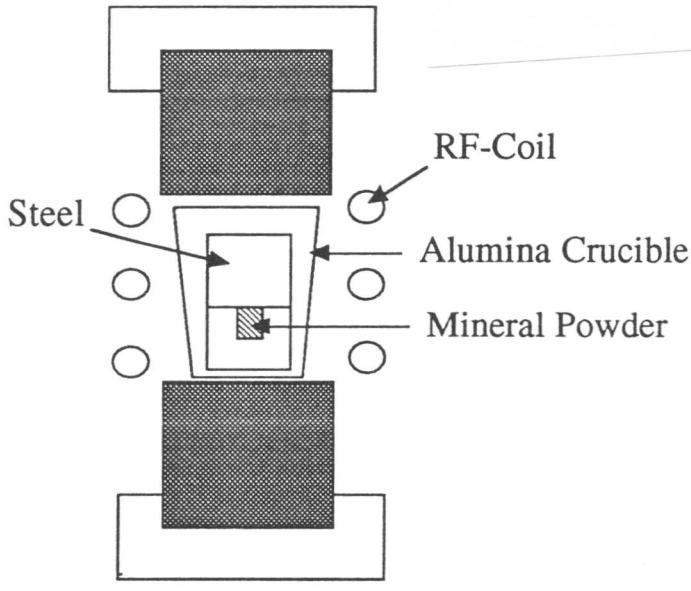

Figure 5.3 Experimental arrangement for RF-induction coil melts, using the thermomechanical simulator.

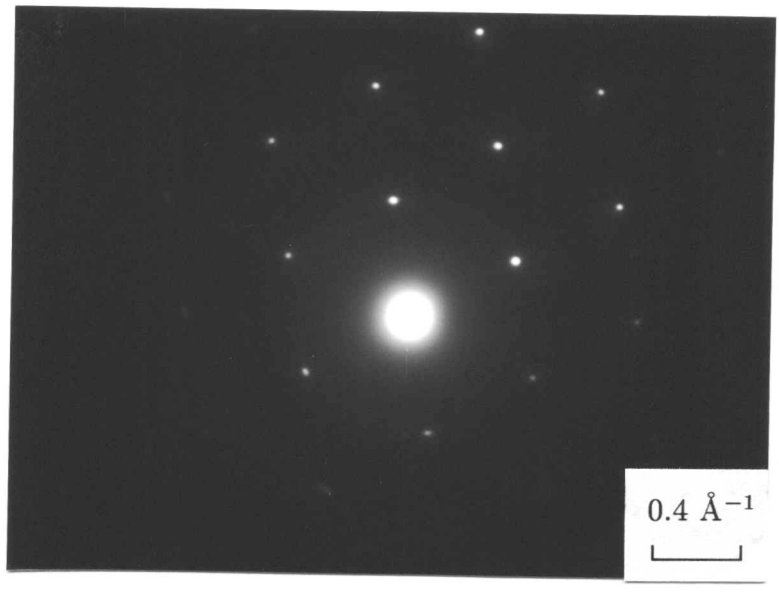

Figure 5.4 Diffraction pattern from the small crystallites present in all the inoculated alloys produced. Diffraction data was consistent with a f.c.c. crystal, a$\sim$3.6Å. On this basis the pattern shown indexes as (111):(1$\bar{1}$1)

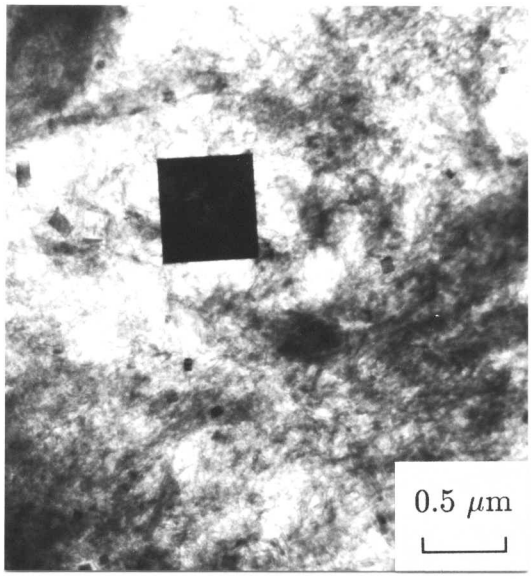

(a)

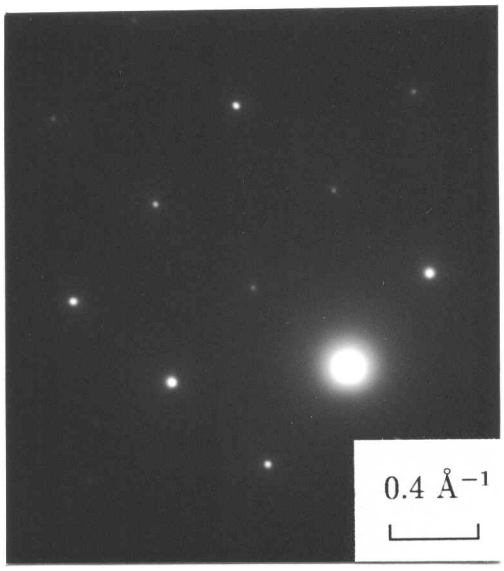

(b)

Figure 5.5 **(a)** Bright field TEM image of a typical particle present in the melt to which TiN powder had been added. The cubic morphology of these particles and their Ti-rich composition suggests that they are TiN.

(b) Diffraction pattern from the particle is consistent with (200):(020) of TiN.

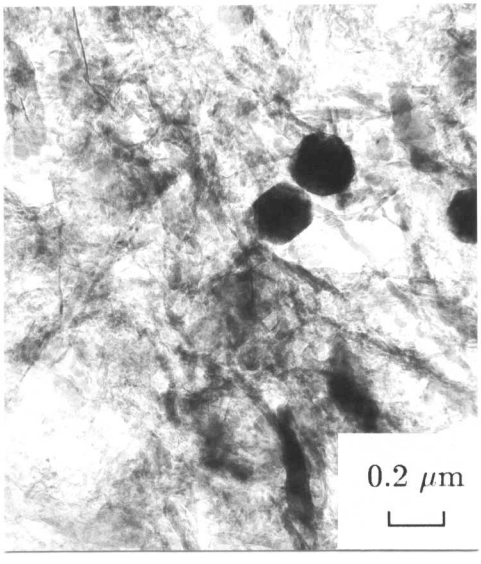

(a)

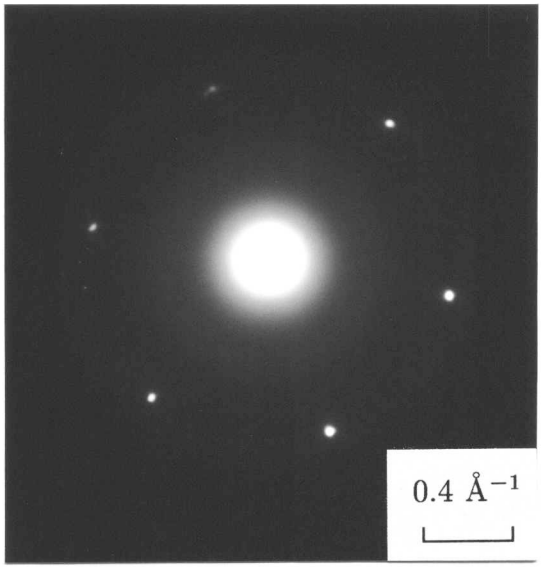

(b)

Figure 5.6 **(a)** Bright field TEM image of particles typically found in the melt to which MnS had been added.

(b) EDX analysis indicates that these particles contain manganese and sulphur, and the diffraction patterns taken confirm the MnS mineralogy.

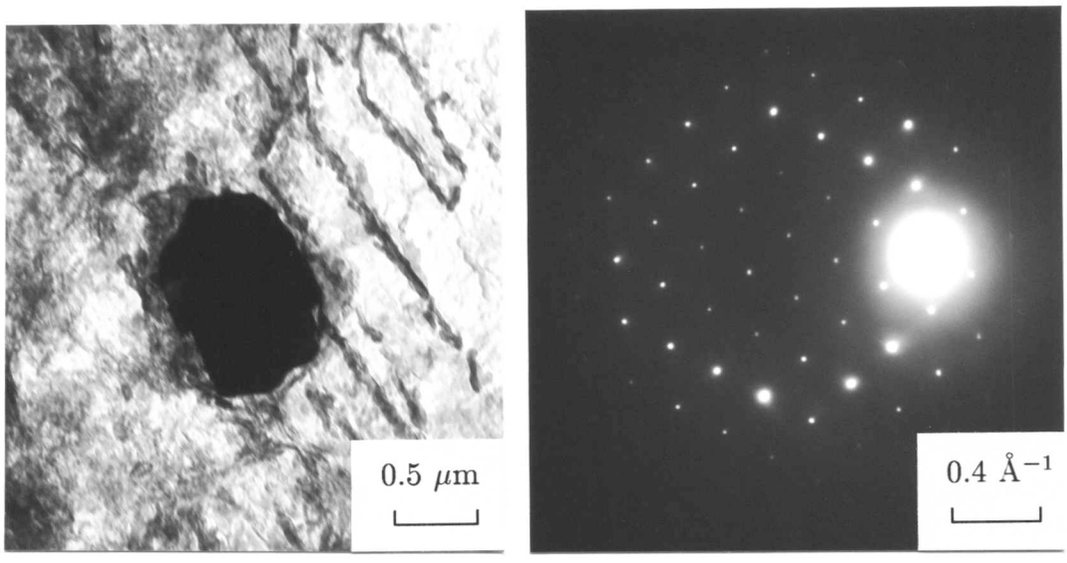

(a) (b)

Figure 5.7 **(a)** Bright field TEM image of a particle in an extraction replica taken from γ-Al_2O_3 additions to steel.

(b) Diffraction patterns taken indicate that the particles have remained in the γ–form, and have not transformed to the stable α–form.

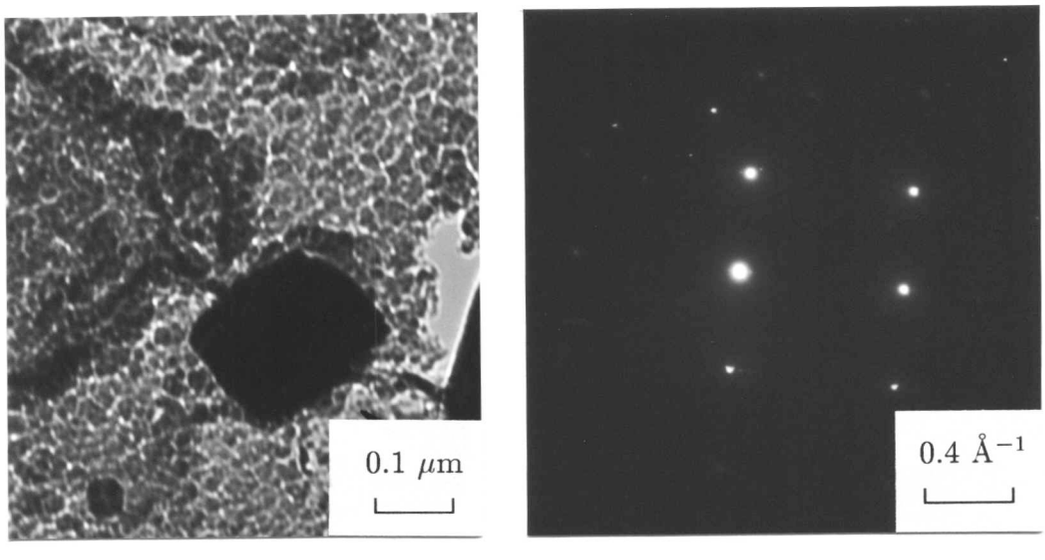

(a) (b)

Figure 5.8 **(a)** Bright field TEM image of a particle present after the addition of Ti_2O_3 to the molten steel.

(b) This diffraction pattern was taken from one of the thinner particles. It does not index as Ti_2O_3, but as TiO.

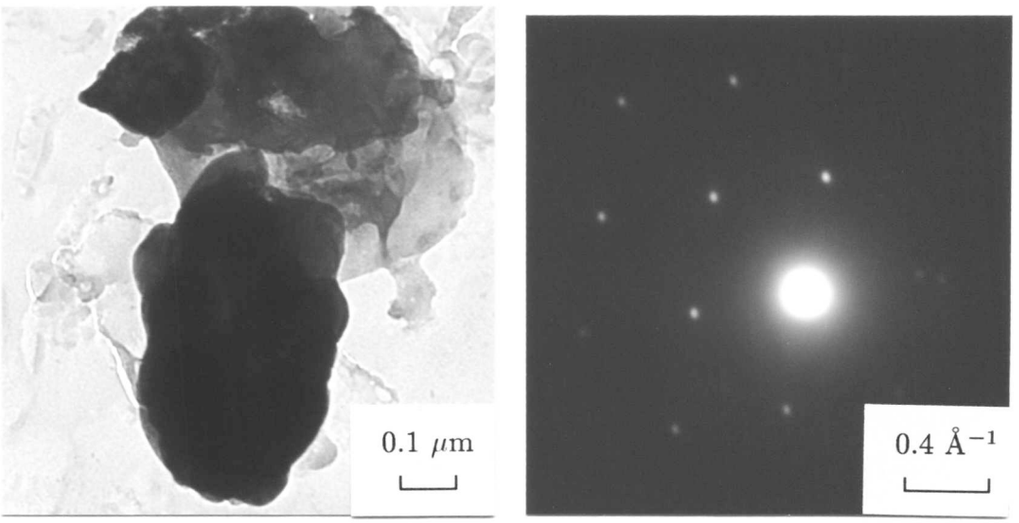

Figure 5.9 **(a)** Bright field TEM image of a particle present after the addition of TiO_2 to the molten steel.

(b) This diffraction pattern from one such particle indexes as TiO, however, most diffraction patterns were probably from complex intermediate structures produced due to deoxidation of TiO_2.

5.4 Partial Transformation Experiments

Having characterised the particles in the inoculated alloys, it remained to establish the activity of the incorporated inclusions with respect to the nucleation of ferrite. A ranking experiment was designed in which the alloys were partially transformed below the bainite–start temperature, B_S. The thermal processing was the same as for the bonding experiments, but no stress was applied (*i.e.* 1200°C for 10 mins; gas-quench at 40°C s^{-1} to 510°C; isothermal hold for 25 s, before gas-quenching to room temperature.) More effective inclusions are expected to lead to a greater degree of transformation given the same transformation time and temperature. It was also hoped to directly observe the intragranular nucleation of ferrite from inclusion surfaces.

5.4.1 Results

As can be seen from the series of micrographs shown in Figures 5.10–5.16, quite different microstructures are obtained from the different mineral additions. The extent of transformation observed in the steel containing γ-Al_2O_3 particles (Fig.5.11) is much less than in the steel to which TiO_2 additions were made (Fig.5.15). The differences were measured by point counting on a series of random SEM photographs (Table 5.7).

Mineral Addition	% Transformed	Estimated Error /%
WO_3	20	±2.9
γ-Al_2O_3	52	±2.9
TiN	65	±2.9
($MnAl_2O_4$ & α-Al_2O_3)	68	±2.9
MnS	71	±2.9
TiO_2	80	±2.9
Ti_2O_3	84	±2.9

Table 5.7 Point counting results illustrating the extent of transformation induced by various mineral additions to the steel, given the same transformation time.

The observed variation in transformation kinetics due to different mineral additions again indicates that all mineral types are not equal in their abilities to nucleate ferritic

phases. The results also show a strong correlation with the work described in Chapters 3 and 4. In all cases titanium oxides are particularly potent in causing nucleation.

5.5 Bainite *vs* Acicular Ferrite

The experiments described above indicate the relative potencies of the different inclusions in terms of transformation kinetics. A further series of experiments was designed to see how acicular ferrite (nucleated intragranularly on inclusions) competes against bainite (nucleated at the austenite grain boundaries).

A new set of samples was made by adding γ-Al_2O_3, ($MnAl_2O_4$ & α-Al_2O_3), TiO_2, Ti_2O_3, TiN and MnS to the steel melt as described earlier. These alloys were austenitised for 15 mins at 1200°C before gas–quenching at $50°C\,s^{-1}$ to 510°C. They were held at 510°C for 5 mins to allow full transformation to occur, before gas–quenching to room temperature. All heat treatments were performed on the thermomechanical simulator.

To meaningfully compare the levels of acicular ferrite and bainite requires a control of the austenite grain size. Smaller grain size favours bainite at the expense of acicular ferrite (Yang and Bhadeshia, 1987; Rees and Bhadeshia, 1994). In fact, the austenite grain size was similar for all samples except that containing TiN powder, which had significantly smaller size. Hence the TiN–containing alloy was reaustenitised at 1300°C instead of 1200°C, in order to achieve a greater grain size, before fully transforming at 510°C. Table 5.8 shows the grain size data for all the samples.

Mineral Addition	Mean Linear Intercept / μm	Estimated Error / μm	Austenitising Temp. /°C
TiO_2	167	±11.5	1200
Ti_2O_3	111	±6.2	1200
γ-Al_2O_3	117	±6.3	1200
($MnAl_2O_4$ & α-Al_2O_3)	173	±12.1	1200
MnS	139	±8.7	1200
TiN	105	±6.6	1300
Control	128	±8.0	1200

Table 5.8 Prior austenite grain sizes of the steels to which various mineral additions have been made, after austenitisation and full transformation below B_S.

Eight random photgraphs were taken using scanning electron microscopy, at magnifications of 500 and 1000. Areas which could be identified as obviously bainitic were traced out onto acetate, and measured by point counting to quantitatively define the fraction of bainite. All microstructural areas not obviously bainitic were therfore classified here as acicular. This method has unquantifiable errors, since the acicular ferrite content is likely to be somewhat overestimated. Nevertheless, it is the best that could be done given the fine scale of the microstructures.

5.5.1 Results

Figures 5.17–5.22 illustrate microstructures which are representative. Alloys containing ($MnAl_2O_4$ & α-Al_2O_3), γ-Al_2O_3 and MnS are obviously quite bainitic (Figures 5.17–5.19), whereas additions of TiN, Ti_2O_3 and TiO_2 have produced much more highly refined microstructures (Fig.5.20–5.22). Amongst the titanium mineral additions there is also an increase in refinement from TiN to Ti_2O_3 to TiO_2. TiO_2 additions have been particularly effective in producing the fine interlocking acicular ferrite microstructure (Fig.5.22) (note that the mineralogy of TiO_2 is likely to have changed on addition to the melt). The microstructural results are shown in Table 5.9, which confirms the trends illustrated in the figures.

Mineral Addition	Area Fraction α_b	Inferred Area Fraction $\alpha_{acic.}$
Control	0.67	0.33
$MnAl_2O_4$ & α-Al_2O_3	0.60	0.40
MnS	0.56	0.44
γ-Al_2O_3	0.42	0.58
TiN	0.37	0.64
Ti_2O_3	0.23	0.77
TiO_2	0.09	0.91

Table 5.9 Microstructural point counting results showing the area fractions of bainite and acicular ferrite produced due to the addition of various mineral powders to molten steel.

The results are in reasonable accordance with the mineral efficacies inferred from

analysis of the partial transformation experiments. The titanium oxide additions are particularly effective in causing intragranular nucleation. TiN too, seemed to be reasonably effective.

The results are also largely consistent with those from pressure bonding. This suggests that the mechanisms of nucleation identified in the pressure bonding experiments, apply also in these melt experiments. TEM analysis has shown that deoxidation of the titanium oxides has occurred as a result of addition to the molten alloy, and since this was capable of inducing nucleation in the bonding experiments, it seems likely as the nucleating mechanism operating here. Manganese–absorption has been shown to occur as a result of reactions between steel and Ti_2O_3, and this may also be contributory to nucleation.

5.6 Removal of Grain Boundary Sites

The problems associated with distinguishing inter- from intra- granular nucleation of bainite plates has already been discussed. In the previously described set of experiments, only areas which were obviously bainitic were classified as grain boundary nucleated. Clearly, other regions of sheaves, not obviously bainitic, may also have nucleated from grain boundaries. Hence, some degree of uncertainty as to the exact levels of intragranular nucleation induced by the various powder additions exists. In order to combat this uncertainty, another series of particle additions to molten steel was produced. With these alloys the intention was to decorate the prior austenite grain boundaries with allotriomorphic ferrite, before partially transforming the remaining austenite below B_S. Decoration of austenite grain boundaries with allotriomorphic ferrite largely prevents the production of bainite – only variants with favourable orientation with both matrix austenite, and grain boundary ferrite may form. Thus virtually all transformation produced below B_S in the alloys could be said to have nucleated intragranularly. If given the same levels of partial transformation, then the density of the acicular ferrite produced for each powder addition would be indicative of the specific mineral's efficacy in causing nucleation.

Heat treatments of the alloys were again performed in the thermomechanical simulator. They were austenitised at 1250°C for 5 min, then gas–quenched at $50°C\,s^{-1}$ to 700°C, and held for 80 s to produce allotriomorphic ferrite at the grain boundaries, before gas–quenching to room temperature at $20°C\,s^{-1}$ (so allowing some level of transformation on cooling). This heat treatment was devised by trials performed on undoped alloy A5763. The aim was to produce complete covering of prior austenite grain boundaries and find a cooling rate which was likely to show good contrast in levels of transformation induced between effective nucleants and ineffective nucleants.

5.6.1 Results

Although the intention was to analyse the variation in mineral potential in nucleating acicular ferrite, this was not achieved. Instead, the microstructures produced gave a greater indication as to the various mineral efficacies for nucleating idiomorphic ferrite. During the isothermal hold, designed to cause allotriomorphic ferrite decoration of grain boundaries, some inclusion types caused the nucleation of idiomorphs. Interestingly, the minerals most potent in this respect did not seem to be those most potent in acicular ferrite production, indicated from the previous experiments.

Specifically MnS, TiN, TiO and Ti_2O_3 all produced dominantly idiomorphic ferrite microstructures (Fig.5.23–5.26). Ti_2O_3, however, also caused significant production of acicular ferrite between idiomorphs (Fig.5.26). TiO_2 (previously observed to be extremely potent in the production of acicular ferrite), V_2O_3, SnO_2, γ-Al_2O_3 and ($MnAl_2O_4$ & α-Al_2O_3) did not nucleate idiomorphs to nearly the same extent as MnS, TiN, TiO and Ti_2O_3 (Fig.5.27–5.31).

5.6.2 Brief Discussion

These results imply that the effective nucleation of intragranular allotriomorphic ferrite is dependent on different inclusion properties to that of effective acicular ferrite nucleation. TiO and TiN are considered to offer good lattice matching with ferrite, and were both observed to nucleate idiomorphs. However, $MnAl_2O_4$ and γ-Al_2O_3 are also suspected to offer potential epitaxial relationships with ferrite, but did not induce idiomorphic nucleation.

TiO_2, V_2O_3 and SnO_2 were all observed to be effective as nucleants in the context of the pressure bonding experiments, and yet appeared not to produce significant levels of idiomorphic ferrite. It is therefore believed that the mechanism by which non–metallic inclusions stimulate the nucleation of acicular ferrite (which is a displacive transformation) is different from that which stimulates ferrite which grows by a reconstructive mechanism. This may be responsible for the different effects observed for acicular ferrite and idiomorphic ferrite, but the details remain to be resolved in future work.

5.7 Note on Inert Surface Mechanism

One suggested mechanism by which inclusions cause nucleation, as mentioned previously, is that they merely offer an inert surface from which heterogeneous nucleation may occur. In general, this mechanism is dismissed since such a wide variation in the apparent nucleation efficacies of various mineral types exists. This level of potency variation is not consistent with the inert surface theory. However, during investigation of nucleation induced by

particles added to molten steel, a great many instances of direct nucleation from individual mineral particles were observed. Such observations of direct particle–caused nucleation were not restricted to mineralogies judged to be particularly potent. Instead it seemed that any particle type, irrespective of mineralogy, could cause intragranular nucleation under certain circumstances (Fig.5.32, 5.33).

The implication, therefore, is that the presence of any mineral surface can induce nucleation of acicular ferrite to some degree. An inert surface mechanism seems therefore contributory to mineral–caused nucleation, although other mechanisms may operate for inclusions of specific potent mineralogies.

5.8 Conclusions

(i) All mineral types are not equal in their abilities to nucleate acicular ferrite. TiO_2 and Ti_2O_3 additions are extremely potent; TiN seems to show moderate efficacy, while $MnAl_2O_4$ & α-Al_2O_3, γ-Al_2O_3 and MnS seem relatively poor as nucleants.

(ii) That TiO_2 and Ti_2O_3 additions should show the greatest potency in nucleating acicular ferrite is consistent with results from the pressure bonding experiments. It would seem reasonable to assume that in both types of experiment, nucleation is induced due to the operation of the same mechanism. Therefore, acicular ferrite nucleation has been induced by mineral–caused local depletion zones of either carbon or manganese.

(iii) That TiN shows moderate efficacy in the melt experiments, but not in the bond experiments, indicates that the contact between mineral and molten steel is necessary for the nucleation mechanism to operate. This would be consistent with TiN offering an epitaxial relationship with the ferrite lattice.

(iv) The factors governing the nucleation of acicular ferrite are different from those which govern the nucleation of idiomorphic ferrite.

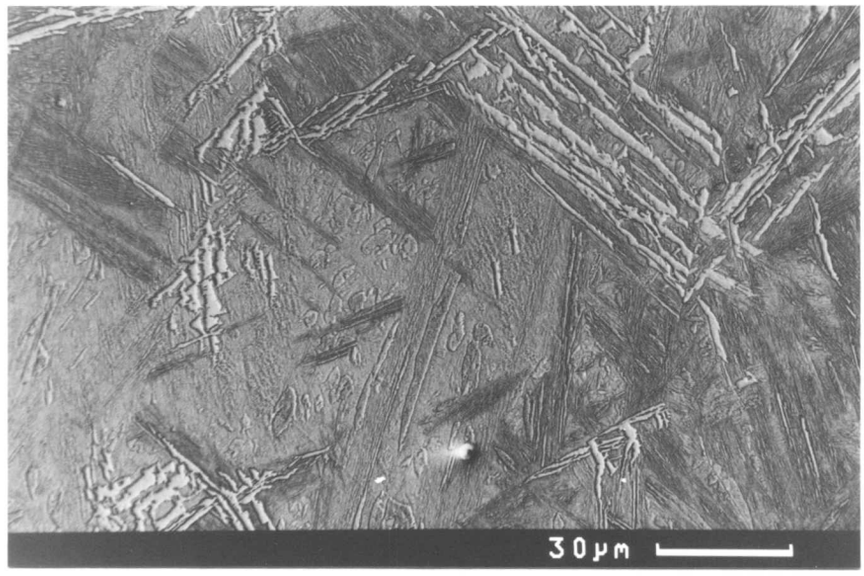

Figure 5.10 SEM micrograph of the extent of transformation induced due to additions of WO_3 to molten steel. It is suspected that WO_3 completely decomposes during the melting of the steel sample.

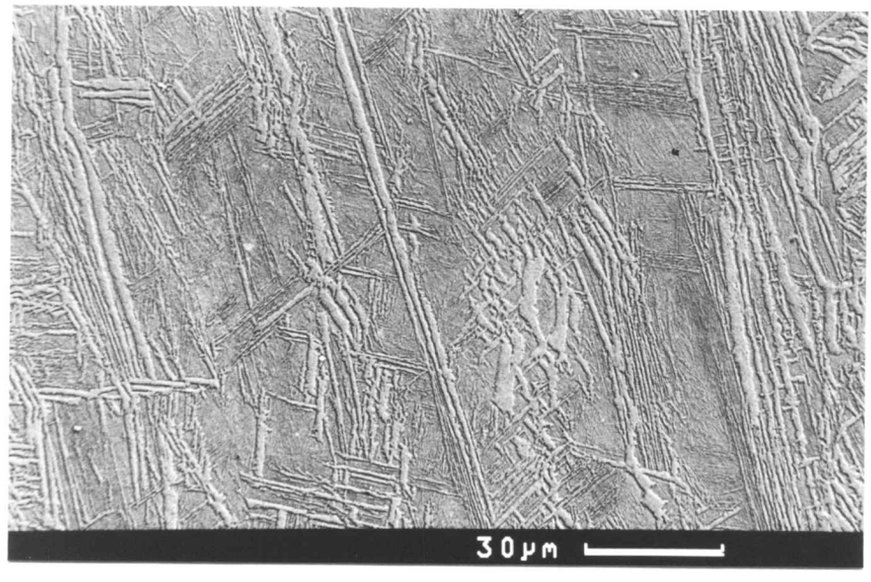

Figure 5.11 SEM micrograph of the extent of transformation due to γ-Al_2O_3 additions to the steel.

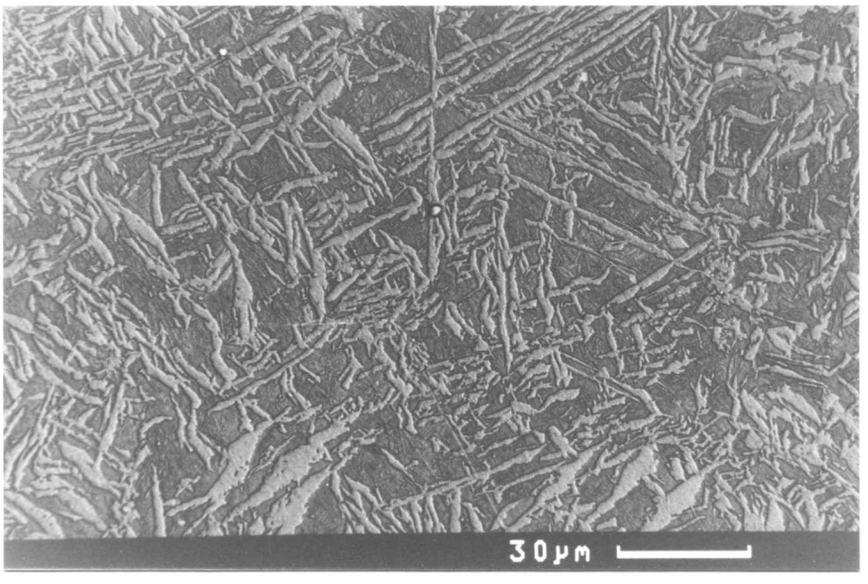

Figure 5.12 SEM micrograph of the extent of transformation induced due to partial transformation of steel containing TiN additions.

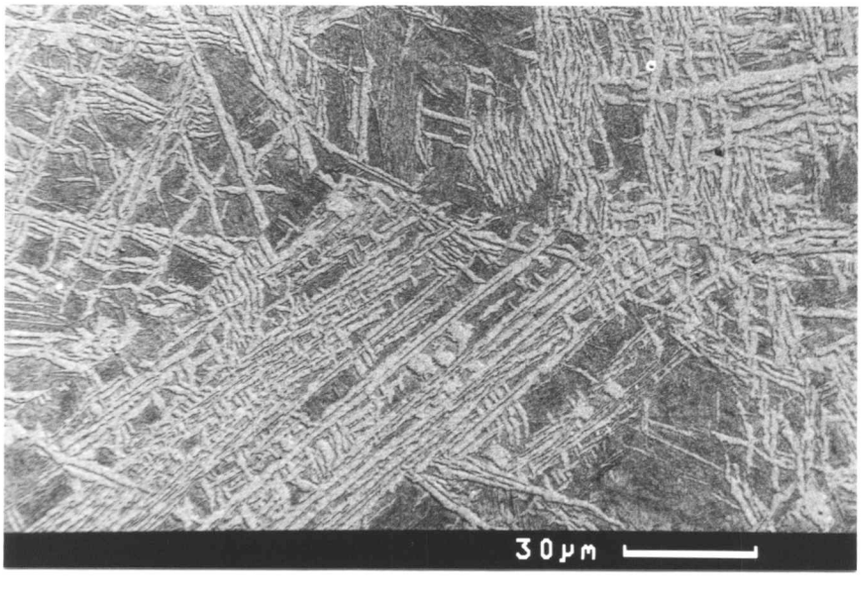

Figure 5.13 SEM micrograph of transformation induced in steel to which $MnAl_2O_4$ & α-Al_2O_3 additions have been made.

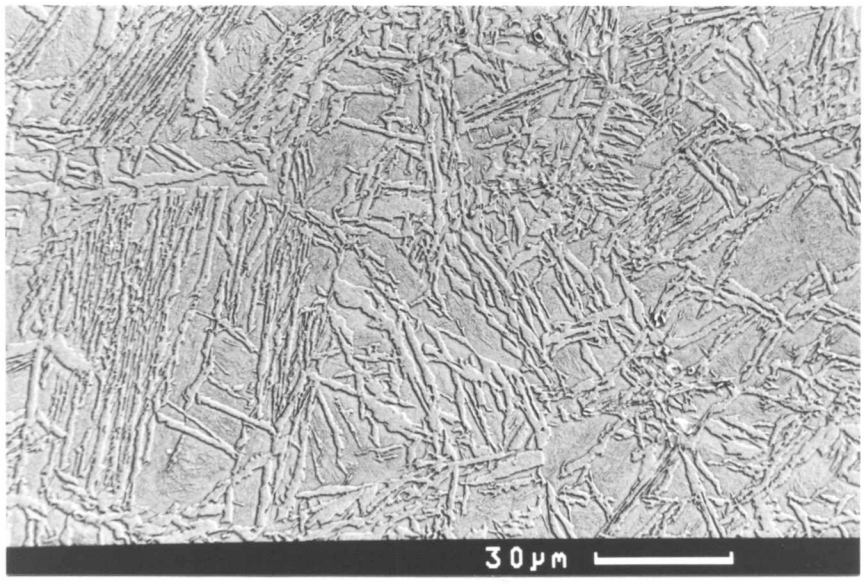

Figure 5.14 SEM micrograph of the microstructure produced on partial transformation of steel to which MnS particles had been added.

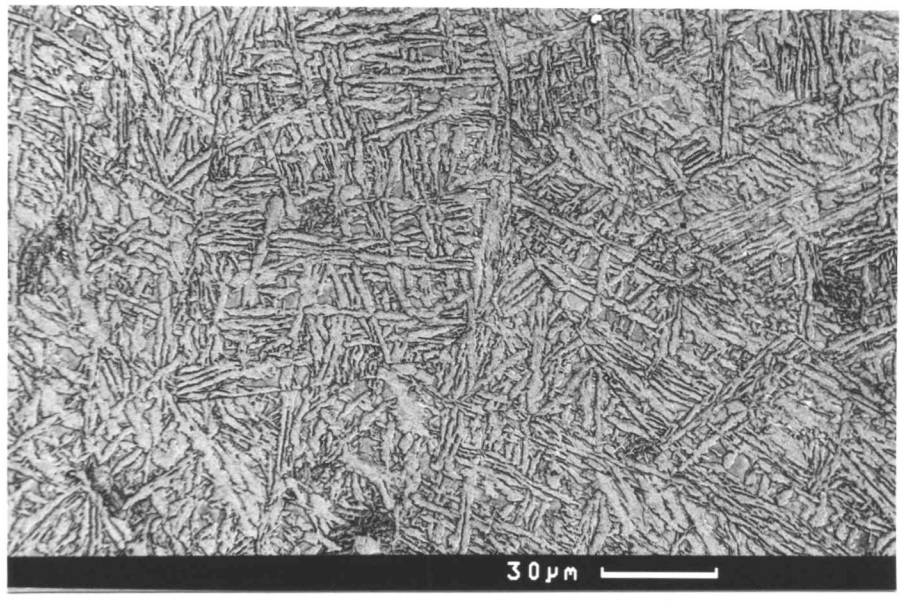

Figure 5.15 SEM micrograph of the microstructure produced on partial transformation of steel to which TiO_2 particles had been added.

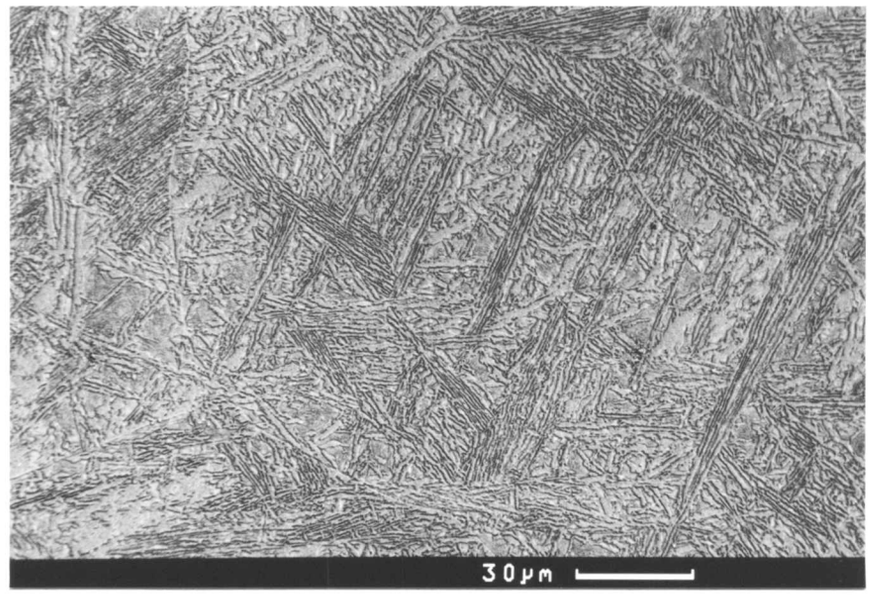

Figure 5.16 SEM micrograph of the microstructure produced on partial transformation of steel to which Ti_2O_3 particles had been added.

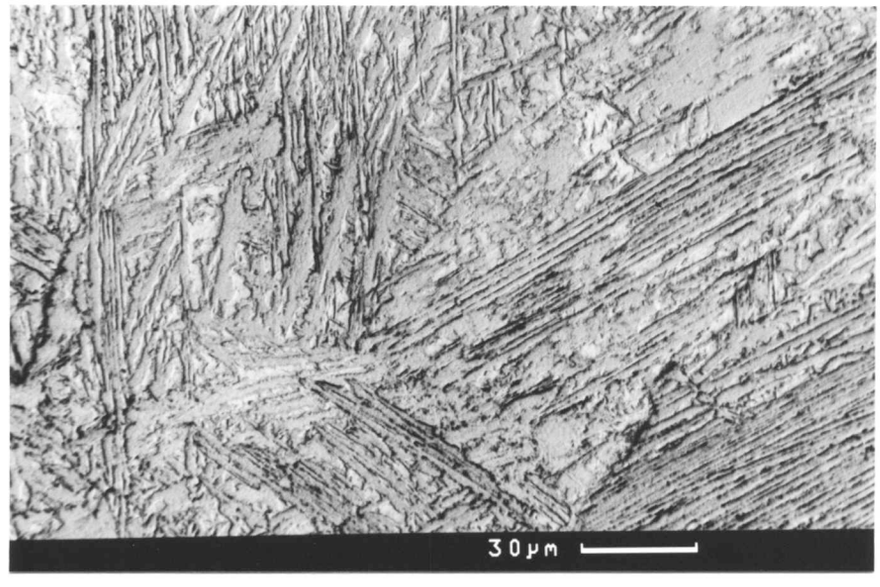

Figure 5.17 Full transformation of steel to which $MnAl_2O_4$ & α-Al_2O_3 additions have been made. The microstructure is reasonably bainite–rich.

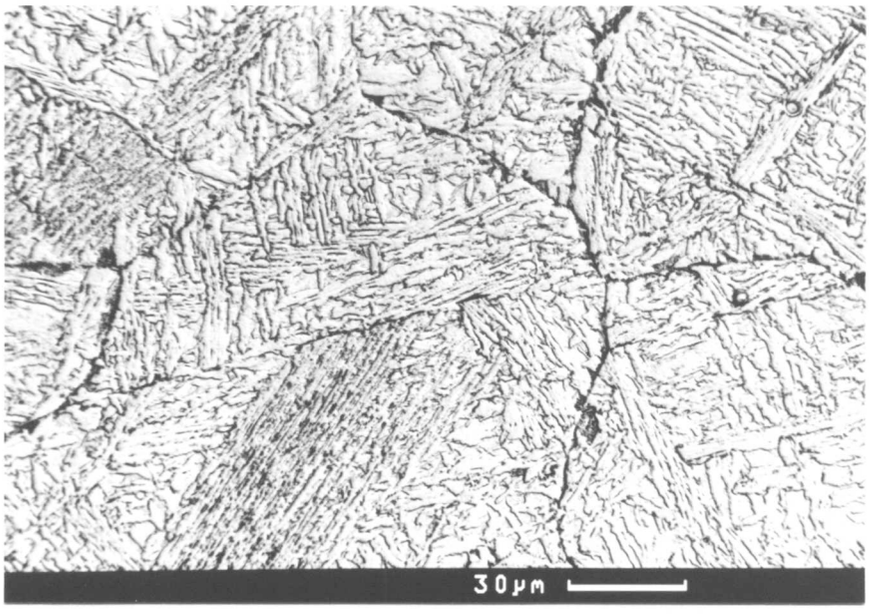

Figure 5.18 Full transformation of alloy containing MnS particles. The microstructure is reasonably bainitic.

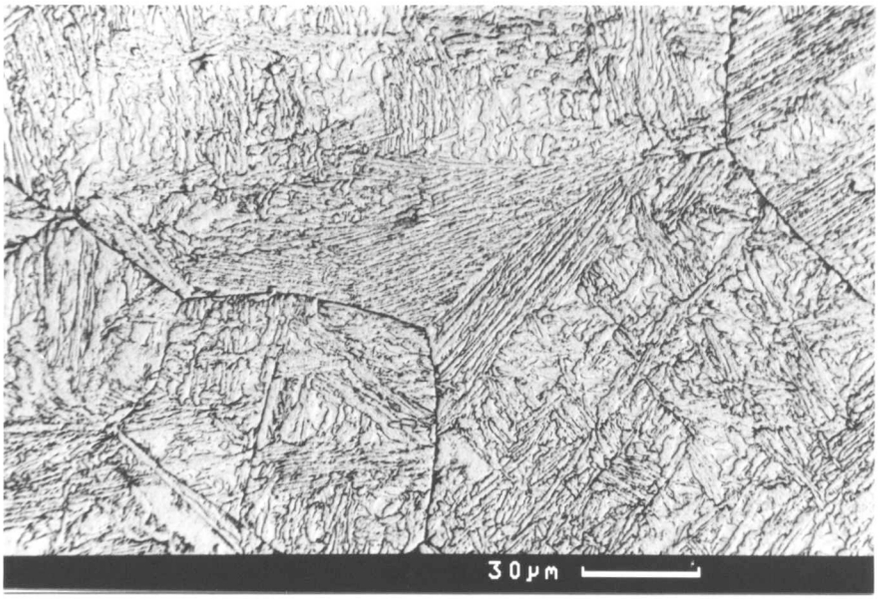

Figure 5.19 Full transformation of alloy containing γ-Al_2O_3 particles. Again the microstructure is reasonably bainitic.

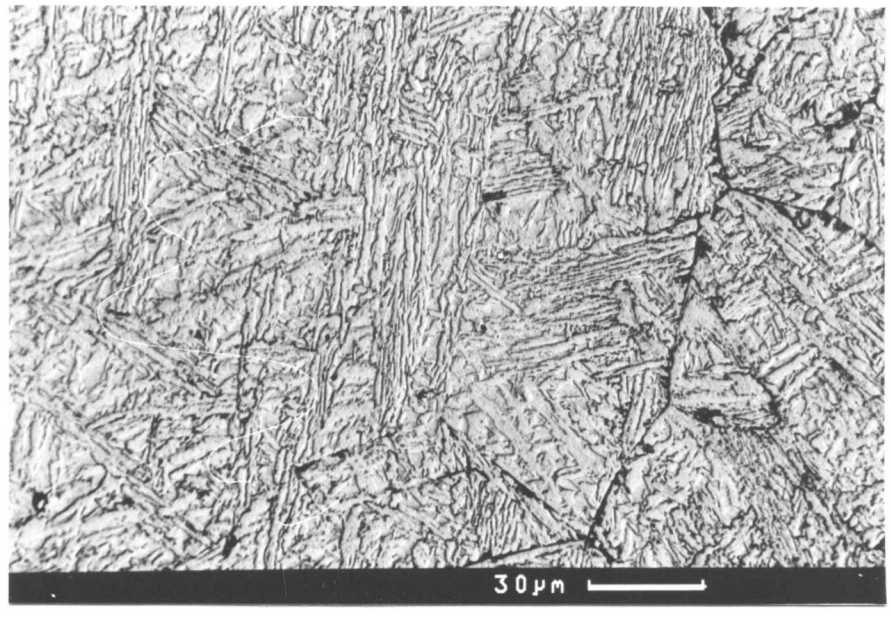

Figure 5.20 Full transformation of steel containing TiN particles. Levels of acicular ferrite are higher here than in the previously illustrated microstructures.

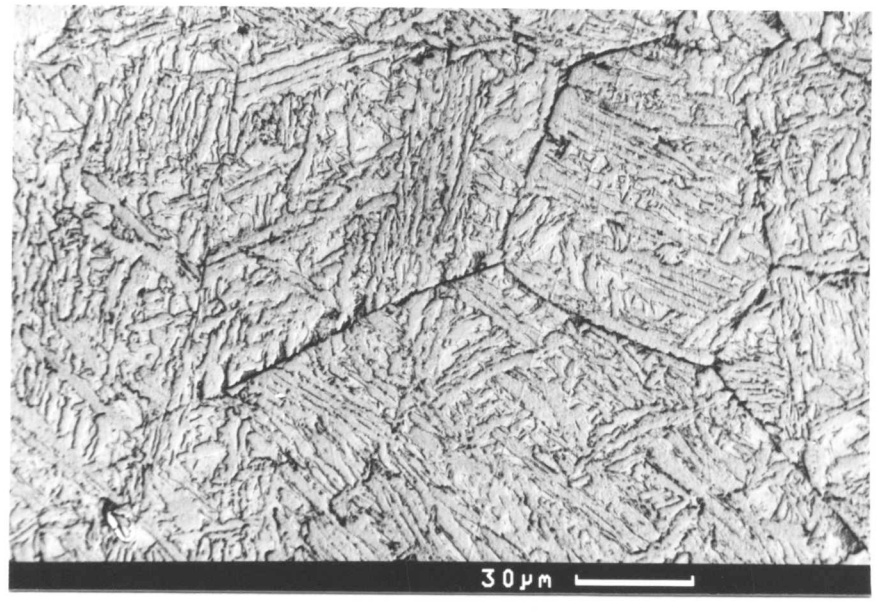

Figure 5.21 Full transformation of steel to which Ti_2O_3 powder additions have been made. A reasonable amount of acicular ferrite is present.

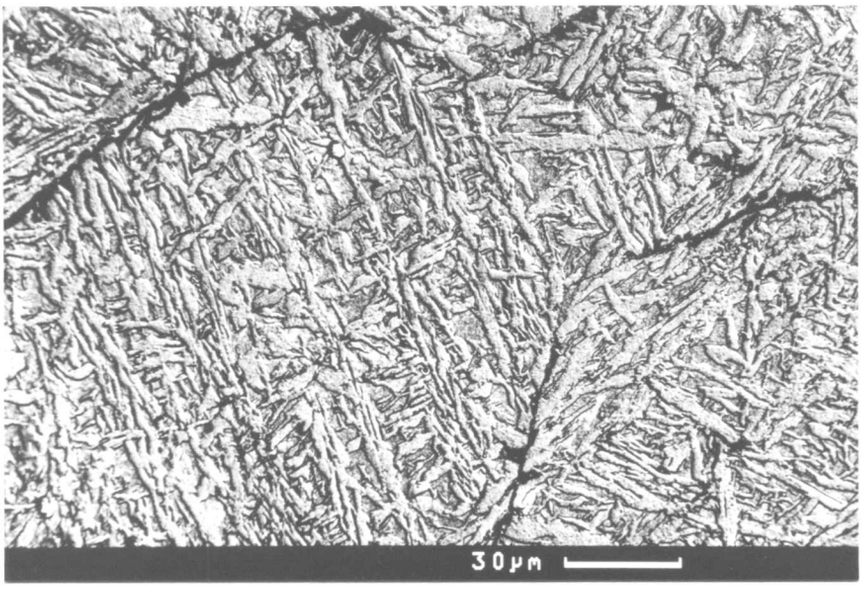

Figure 5.22 Full transformation of steel to which TiO_2 additions have been made. As can be seen, the microstructure is extremely acicular.

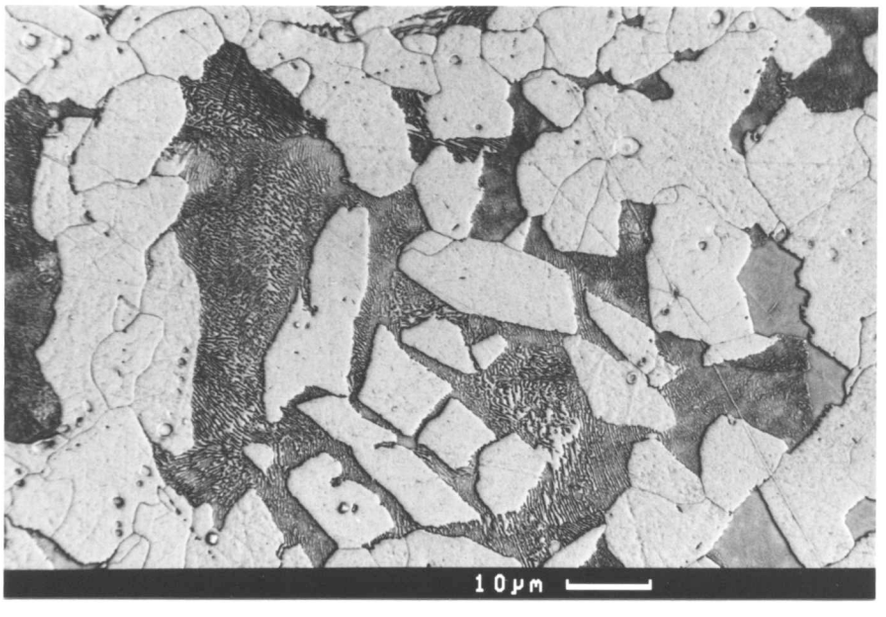

Figure 5.23 SEM micrograph showing the microstructure induced when grain boundary decoration with allotriomorphic ferrite was attempted in steel containing MnS particles. Much idiomorphic ferrite has been produced.

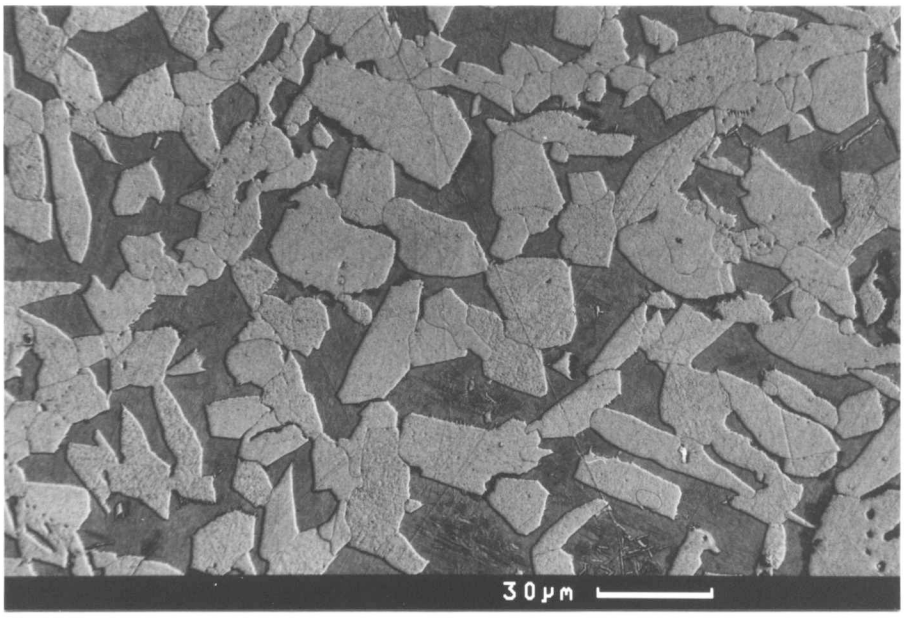

Figure 5.24 Idiomorphs induced by the presence of TiN particles.

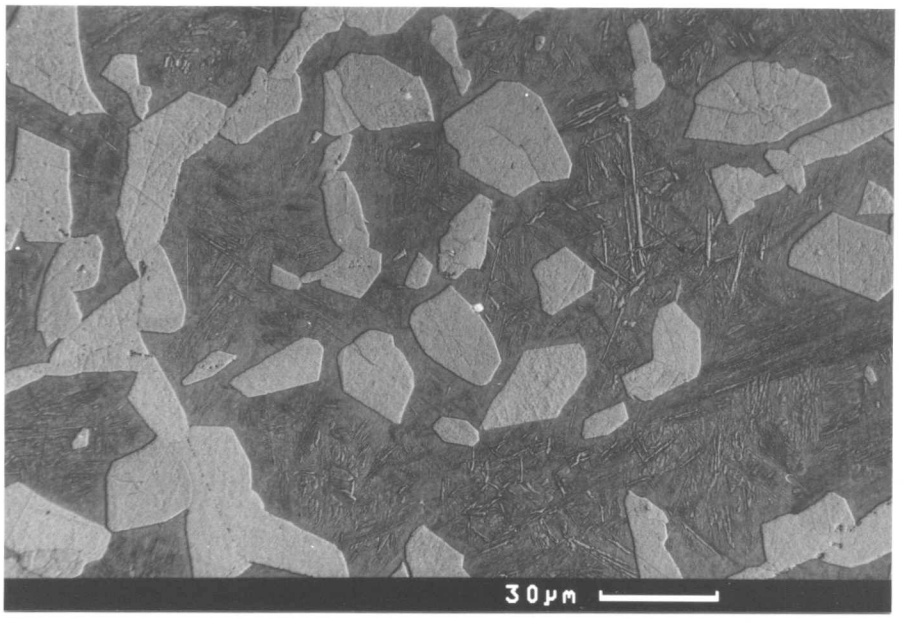

Figure 5.25 Idiomorphs induced by the addition of TiO to the molten steel.

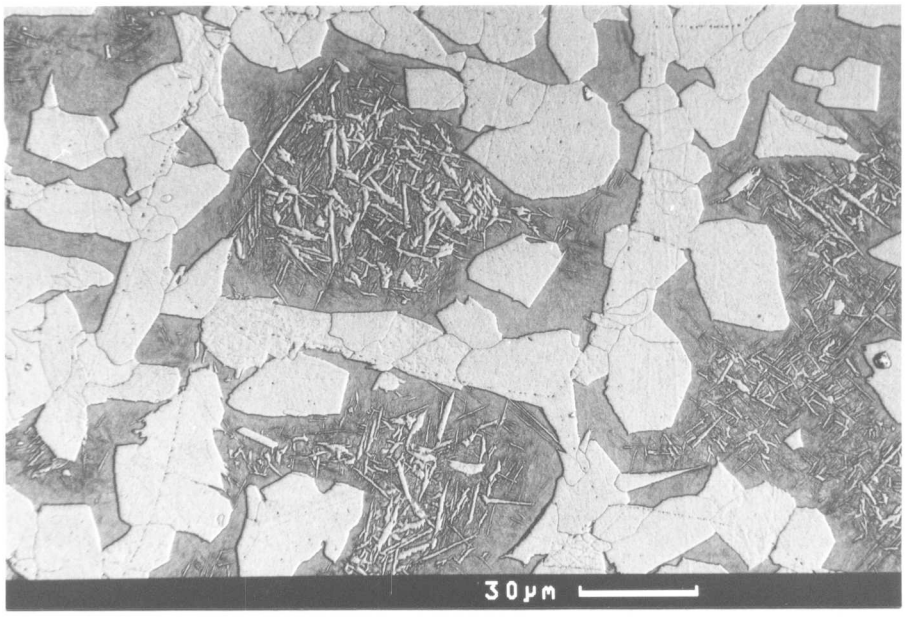

Figure 5.26 Idiomorphic ferrite produced by the addition of Ti_2O_3 to the molten steel.

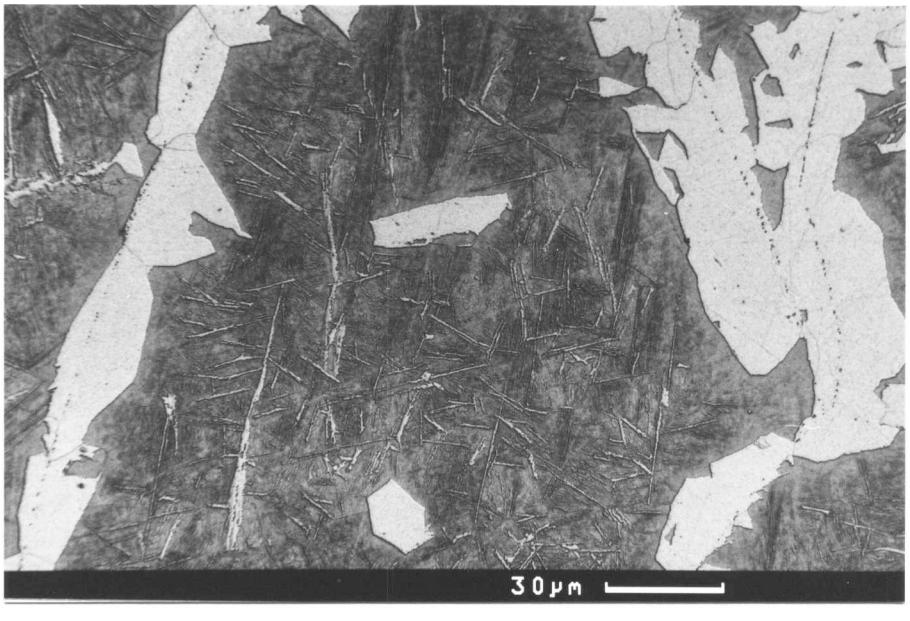

Figure 5.27 Addition of V_2O_3 does not induce formation of idiomorphs.

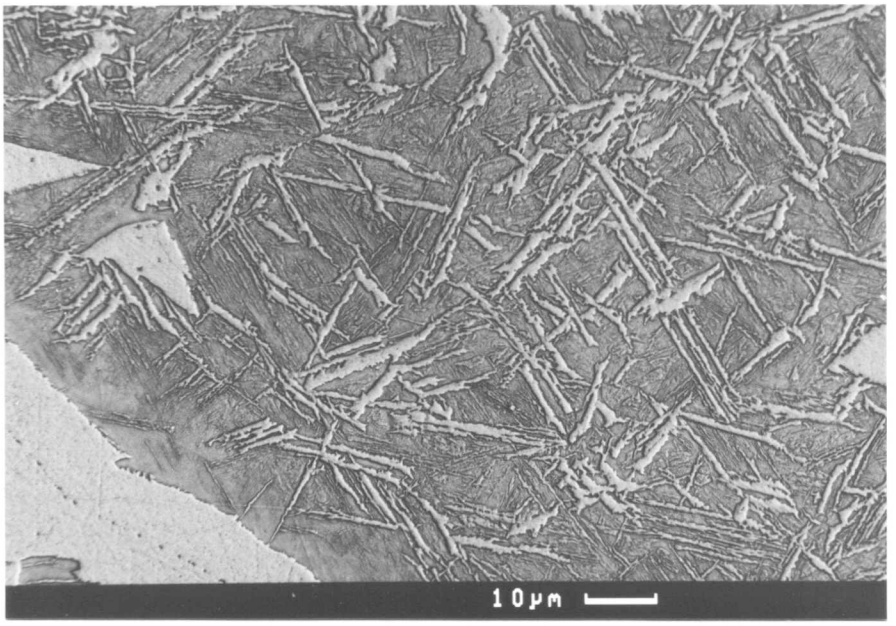

Figure 5.28 Addition of SnO_2 particles does not induce idiomorph formation.

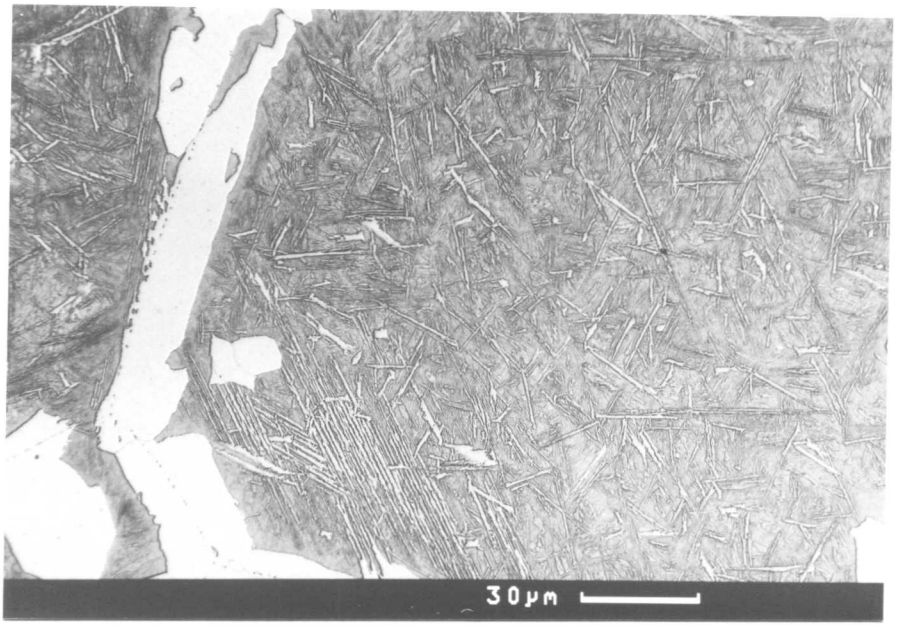

Figure 5.29 TiO_2 addition to the molten steel does not, in this instance, induce formation of idiomorphic ferrite.

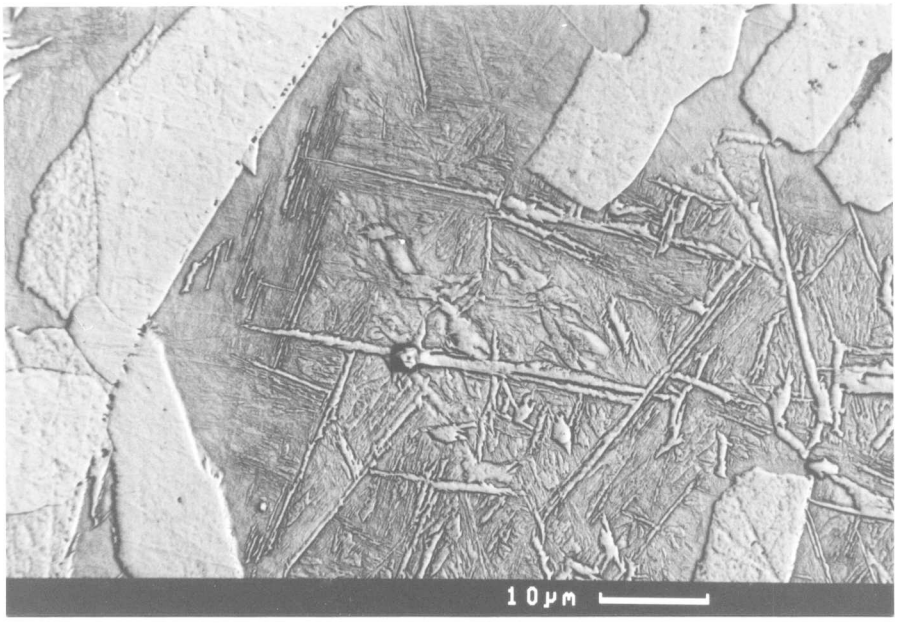

Figure 5.30 γ-Al_2O_3 addition to the molten steel does not induce significant formation of idiomorphic ferrite.

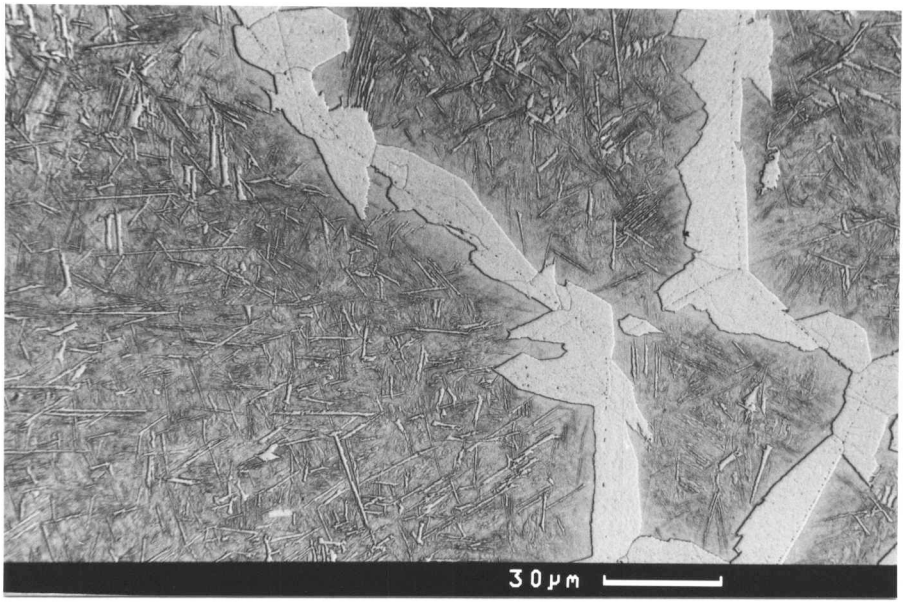

Figure 5.31 $MnAl_2O_4$ & α-Al_2O_3 additions do not induce significant formation of idiomorphs.

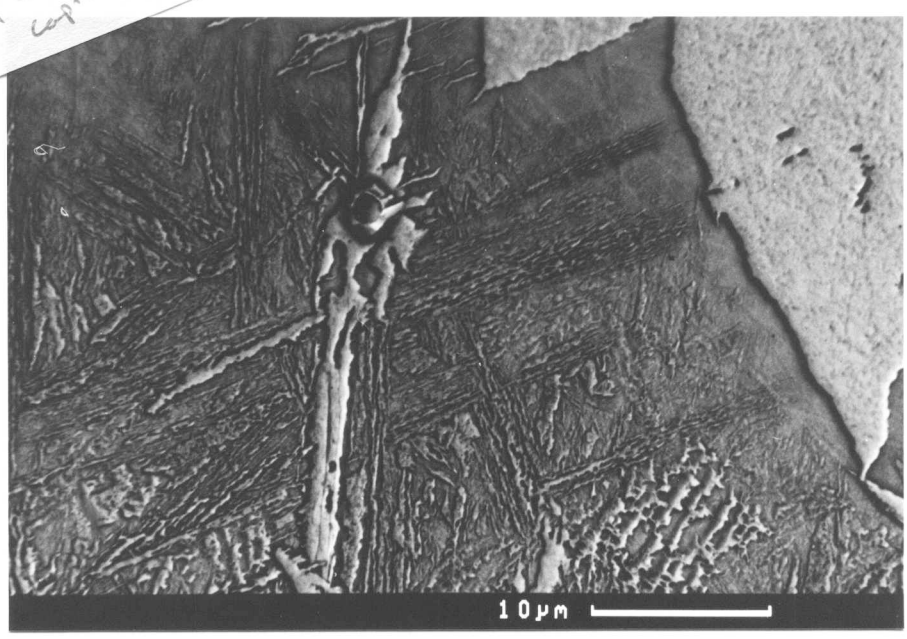

Figure 5.32 Direct observation of nucleation on a particle in the SnO_2–inoculated steel.

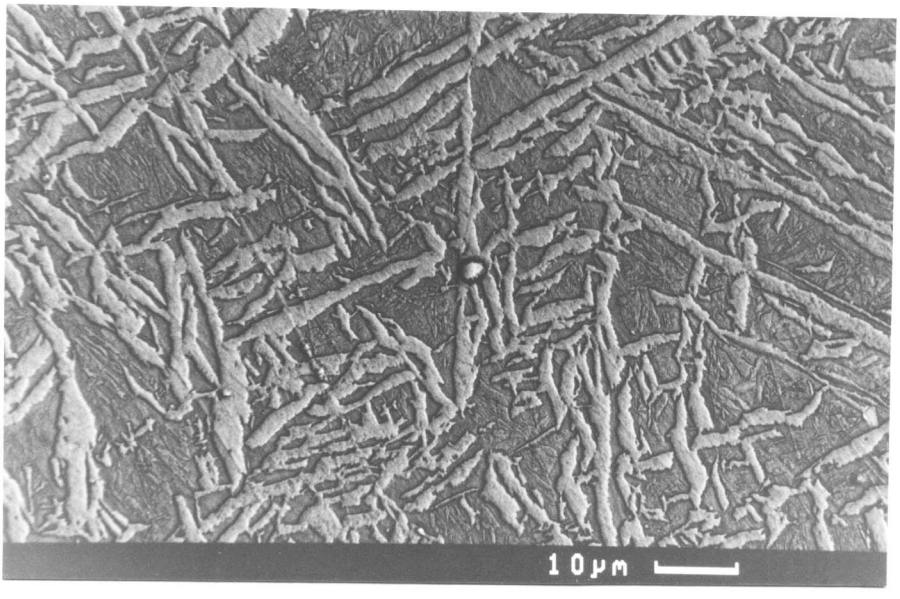

Figure 5.33 Direct observation of nucleation on TiN particle.

CHAPTER 6

Additions of Mineral Powders to Steel Welds

6.1 Introduction

Results from the pressure bonding experiments (Chapters 3 and 4) and from the inoculation of steel melts with mineral powders (Chapter 5), showed that titanium–rich compounds were particularly potent in the nucleation of ferritic phases. The bonding experiments also showed that WO_3 was extremely potent in causing nucleation. On the basis of these results, and as an extension of the research, attempts were made to add titanium–rich and tungsten–rich compounds to submerged arc steel welds via powders introduced into the flux. The aim was to investigate the effects that such additions would have on weld microstructures.

6.2 Experimental

Two series of experimental 0.5 m long submerged arc welds were produced, with weld geometry as shown in Fig.6.1. The welding conditions for all the welds are summarised in Table 6.1. The first series of welds (B–D) involved variations in titanium and the second (E–G) in tungsten. A control weld (A) was also made for comparison purposes, without any deliberate mineral addition (Table 6.2). The welding wire used was ESAB AB Autrod 12.22. The exact weld chemistries formed by various powder additions are discussed in the following sections.

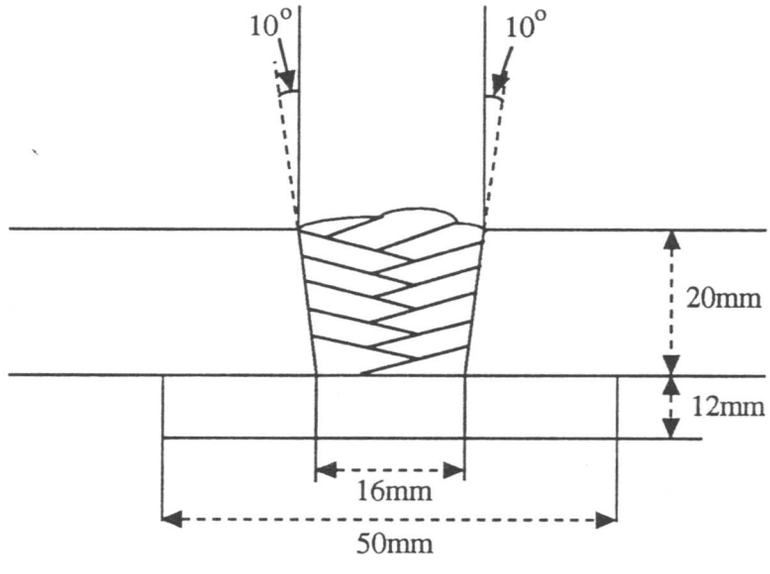

Figure 6.1 Geometry of the experimental welds produced

Weld	Flux used	ϕ /mm	Interpass Temp. /°C	Current Type	Voltage /Volts	Current /Amps	Speed /m/h
A	Basic Flux	4.0	175 ± 25	DC+	29	580	33
B	Basic Flux + TiO_2 powder	4.0	175 ± 25	DC+	29	580	33
C	Basic Flux + FeTi powder	4.0	175 ± 25	DC+	29	580	33
D	Basic Flux + Ti powder	4.0	175 ± 25	DC+	31	580	33
E	Basic Flux + WO_3 powder	4.0	175 ± 25	DC+	29	580	33
F	Basic Flux + W powder	4.0	175 ± 25	DC+	29	580	33
G	Basic Flux + FeW powder	4.0	175 ± 25	DC+	29	580	33

Table 6.1 Welding conditions for experimental submerged arc welds.

FeSi	SiMn	SiO_2	Al_2O_3	MgO	AlSi	CaF_2
1.7	2	5	15.9	43.6	5	26.8

Table 6.2 Composition of the basic flux to which powder additions were made. Concentrations shown are in wt%

6.3 Titanium–Rich Additions

Weld A was produced using the unmodified flux (Table 6.2). Titanium was introduced differently in each of the other welds in the titanium series, but, in each case the powder added constituted 4 wt% of the flux composition. Additions were as follows: flux rich in TiO_2 powder was used to produce Weld B; FeTi powder was added to the flux to produce Weld C; Ti–powder was added to the flux for Weld D. The weld compositions thus achieved are shown in Table 6.3. The titanium concentration increases across the series A→D, without significant variations in the C, Si or Mn concentrations.

6.3.1 As–Deposited Microstructure

The welds were sectioned perpendicular to the welding direction and the top bead isolated for metallographic examination. Because of the fine scale, the microstructures had to be characterised using scanning electron microscopy. Figures 6.2–6.5 show that an increase in the titanium concentration seems to lead to a corresponding increase in the acicular

Weld	C	Si	Mn	Al	Ti	O	N
A	0.075	0.36	1.26	0.012	0.003	280	48
B	0.082	0.49	1.29	0.015	0.019	218	64
C	0.090	0.70	1.34	0.028	0.081	204	90
D	0.091	0.73	1.28	0.030	0.124	134	64

Table 6.3 Composition of the titanium series welds. Concentrations are given in wt.%, with O and N given in parts per million by weight.

ferrite content. At the same time, the amount of grain boundary allotriomorphic ferrite and Widmanstätten ferrite was observed to decrease, eventually with complete elimination from the microstructure.

Variations in Widmanstätten ferrite are expected with changes in the frequency of intragranular nucleation events. Widmanstätten ferrite grows from the austenite grain surfaces and its growth can be stifled by impingement with intraganularly nucleated acicular ferrite. If the latter forms more rapidly, then the fraction of Widmanstätten ferrite is expected to decrease. Thus the reduction of Widmanstätten ferrite may be explained by an increase in the nucleation potency of the inclusions, as titanium levels are increased. It is more surprising that the amount of allotriomorphic ferrite is reduced since its growth starts from a significantly higher temperature than acicular ferrite (Bhadeshia *et al.*, 1985). It is possible that, in addition to any nucleation effect due to increased levels of titanium–rich phases in the inclusions, some of the titanium is retained in solution, enhancing hardenability, which in turn is reflected in the reduced allotriomorphic ferrite content.

Kluken and Grong (1989) have developed methods to estimate the constitution of inclusions in steel welds, by sequentially distributing the oxygen and nitrogen, beginning with the most potent oxidisers *etc.* . The method has been stated explicitly in (Bhadeshia and Svensson, 1993) and is used here to estimate the likely constituents of the non–metallic inclusions present in the weld series, and also to examine the likelihood that excess titanium may be present in solution in the high titanium welds. The results of the analysis are presented in Table 6.4.

As can be seen from the table, according to calculations, the levels of titanium present in welds C and D were such that excess titanium would indeed be present in solution. Despite being a ferrite stabiliser (Massalki, 1986), titanium in solution has been observed to cause a dramatic increase in steel hardenability (Widgery, 1976).

Weld	Allocation of Oxygen /ppmwt				Allocation of Titanium /ppmwt		
	Al_2O_3	Ti_2O_3	MnO	SiO_2	TiN	Ti_2O_3	Ti in solution
A	107	15	80	78	0	30	0
B	121	95	1	1	0	190	0
C	173	31	0	0	308	63	439
D	181	0	0	0	219	0	1021

Table 6.4 Calculated allocation of titanium and oxygen to mineral groups in non–metallic inclusions

Despite this hardenability effect, it should be noted that areas of bainite could readily be observed in Weld C, but not in Weld D. Bainite and acicular ferrite compete directly as transformation products – their mechanism of transformation being the same, save that bainite nucleates from planar grain boundaries, and acicular ferrite nucleates from point sources within grains. The reduction of bainite in Weld D implies that intragranular nucleation has been enhanced over grain boundary nucleation. It seems, from metallographic observations alone, that the role of titanium is therefore two–fold:

(i) Its presence in solution increases the hardenability of the weld metal.

(ii) It causes greater levels of intragranular over grain boundary nucleation – probably attributable to changes in the nucleation potency of non–metallic inclusions.

6.3.2 Examination of Inclusions

Carbon extraction replicas were prepared for each of the welds in this titanium–series. These replicas allowed examination of the weld inclusions and analysis of their chemical, mineralogical, and morphological information.

As expected, EDX microanalysis revealed that increased titanium led to inclusions richer in Ti (Fig.6.6). More profound chemical differences were also identified. Figures 6.7–6.9 show that for Welds A & B (the titanium–poor welds) the levels of silicon, aluminium and manganese were reasonably constant in all inclusions examined (*i.e.* there were specific peaks in the distributions of chemical concentrations). As the level of titanium increased, the manganese and silicon concentrations dropped, and the distribution of aluminium within the inclusions became more homogeneous.

The change from specific concentrations of aluminium in the low titanium welds to a more homogeneous concentration distribution implies a change in the state of aluminium in the non–metallic inclusions. This change, accompanied by the removal of silicon and

manganese, is consistent with a mineralogical change from manganese–aluminium oxide, or manganese–aluminium silicate–rich inclusions, to those containing varying levels of alumina as a phase component in the inclusion. The likelihood of such mineralogical changes is supported by the calculated results shown in Table 6.4.

Diffraction patterns taken from crystalline inclusions revealed the presence of MnS (only in Ti–poor welds – Fig.6.10), Al_2O_3 (apparently in several forms, in all welds – Fig.6.12, Fig.6.13), TiX (where X=C, N, or O, in all welds – Fig.6.11), $MnAl_2O_4$ (in Weld D only, Fig.6.14) and a sulphide phase suspected to be a copper sulphide (in all welds, Fig.6.15). Crystalline silicate was never observed, presumably because the silicate was present in its glassy form.

Information from specific diffraction patterns is summarised in Table 6.5. The mineralogies present are largely the same across the weld series. However, the relative amounts of each mineral phase varies – as inferred from chemical changes, and also from qualitative morphological observations:
Often, inclusions which were demonstrated to contain a lot of Ti by microanalysis, showed angular, cuboidal shapes consistent with TiN. The number of such cuboidal inclusions increased across the weld series, but showed a dramatic jump between Weld B and Weld C (Figures 6.16 and 6.17). This sudden increase in levels of TiN is supported by the calculated results in Table 6.4.

6.3.3 Thin–foil Examination

Although the levels of titanium in the weld metals were quite low, an attempt to demonstrate the presence of titanium in solution in the matrix steel was made, by preparing thin–foils for matrix microanalysis. Unfortunately, the concentration of Ti was below the resolution of the EDX system employed. However, three cases of detectable titanium levels in matrix steel were recorded – all for the titanium–rich weld, Weld D.

Weld	Observed			Likely Phase	Likely		Calculated		
	d_1	d_2	d_1 ^ d_2		$(hkl)_1$	$(hkl)_2$	d_1	d_2	d_1 ^ d_2
Weld A	2.7Å	1.6Å	72°	MnS	(311)	(020)	2.6Å	1.6Å	72°
Weld A	2.4Å	1.45Å	88°	γ-Al_2O_3	(311)	$(11\bar{5})$	2.4Å	1.5Å	87°
Weld A	2.3Å	2.0Å	54°	TiX	(111)	(200)	2.4Å	2.1Å	54.7°
Weld B	1.9Å	1.2Å	90°	Cu_xS					
Weld B	2.4Å	2.35Å	60°	α-Al_2O_3	(110)	$(2\bar{1}0)$	2.4Å	2.4Å	60°
Weld B	1.3Å	1.3Å	60°	TiX	(311)	$(1\bar{1}3)$	1.28Å	1.28Å	63°
Weld B	3.7Å	3.7Å	68°	Form of Al_2O_3					
Weld B	2.7Å	8.5Å	78°	Complex Ti-oxide					
Weld B	2.0Å	2.0Å	82°	Form of Al_2O_3					
Weld C	2.6Å	2.6Å	70°	TiX	(111)	$(1\bar{1}1)$	2.4Å	2.4Å	70.5°
Weld C	2.2Å	2.2Å	90°	TiX	(020)	(200)	2.1Å	2.1Å	90°
Weld C	2.3Å	1.4Å	90°	Cu_xS					
Weld C	2.6Å	2.6Å	65°	α-Al_2O_3	(104)	(014)	2.6Å	2.6Å	60°
Weld C	2.7Å	4.2Å	86°	γ-Al_2O_3	(111)	$(2\bar{2}0)$	2.8Å	4.56Å	90°
Weld C	3.6Å	3.6Å	88°	α-Al_2O_3	(012)	$(10\bar{2})$	3.5Å	3.5Å	86°
Weld C	3.0Å	3.0Å	90°	$MnAl_2O_4$	(220)	$(2\bar{2}0)$	2.9Å	2.9Å	90°
Weld D	4.8Å	4.7Å	70°	γ-Al_2O_3	(111)	$(1\bar{1}1)$	4.56Å	4.56Å	70.5°
Weld D	2.1Å	2.1Å	70.5°	Cu_xS					
Weld D	2.9Å	3.1Å	90°	$MnAl_2O_4$	(220)	$(2\bar{2}0)$	2.9Å	2.9Å	90°
Weld D	2.5Å	1.5Å	90°	TiX	(111)	$(2\bar{2}0)$	2.4Å	1.5Å	90°
Weld D	2.1Å	2.1Å	70°	Cu_xS					

Table 6.5 Summary of the data obtained from diffraction patterns taken from particles in the titanium series of welds.

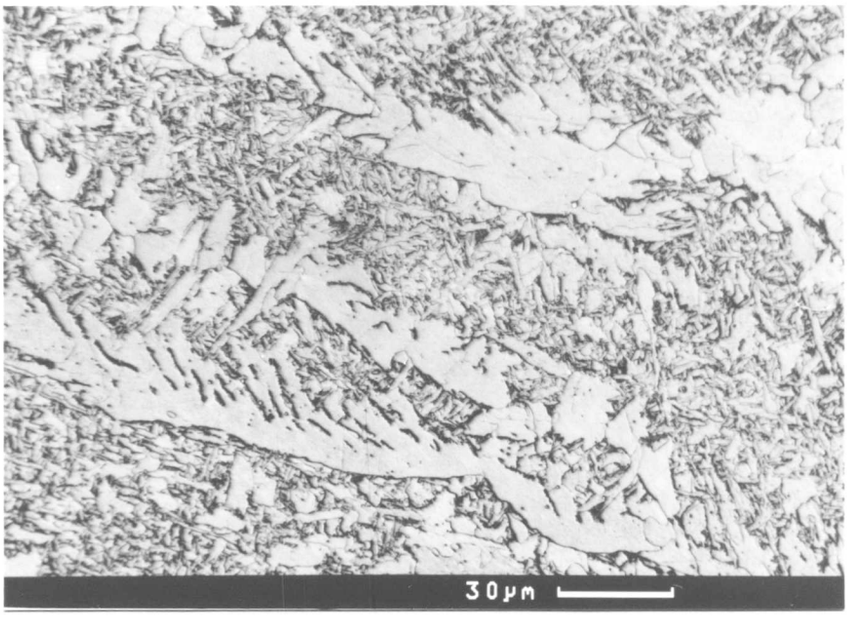

Figure 6.2 SEM micrograph of the as–deposited microstructure in Weld A (low titanium weld).

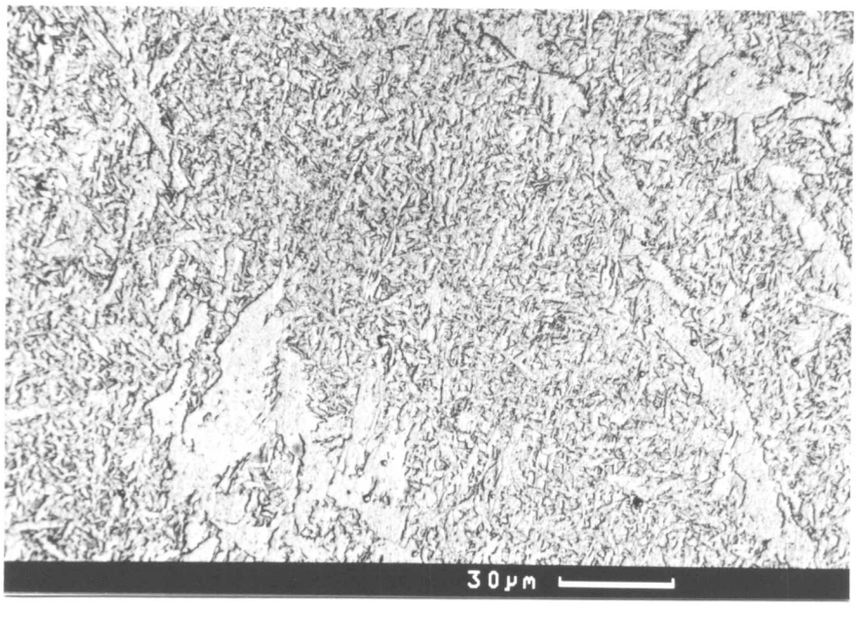

Figure 6.3 SEM micrograph of the as–deposited microstructure in Weld B.

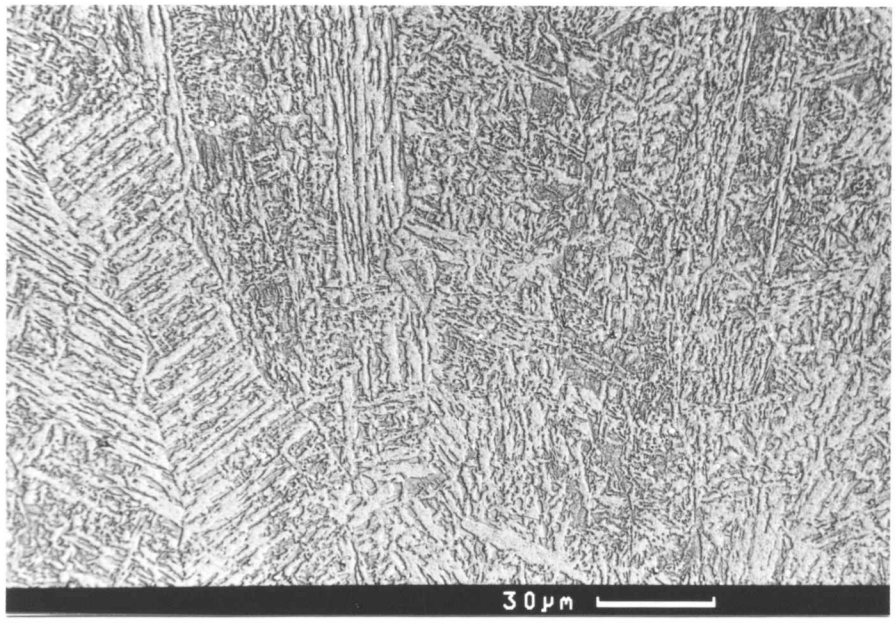

Figure 6.4 SEM micrograph of the as–deposited microstructure in Weld C.

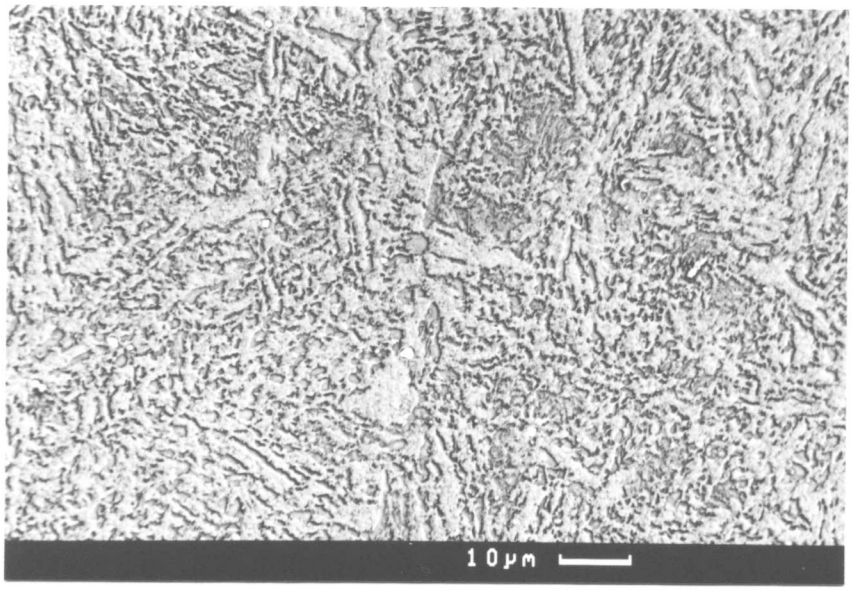

Figure 6.5 SEM micrograph of the as–deposited microstructure in Weld D (titanium–rich weld).

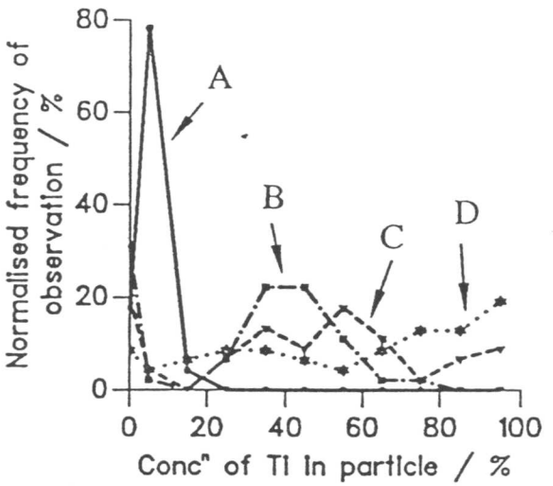

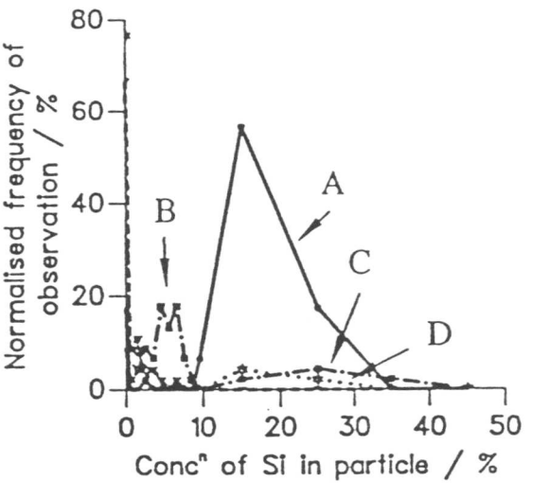

Figure 6.6 (left) Titanium concentration distribution in inclusions across the titanium–weld series. Concentrations are in wt% .
Figure 6.7 (right) Silicon concentration distribution in inclusions across the titanium–weld series. Concentrations are in wt% .

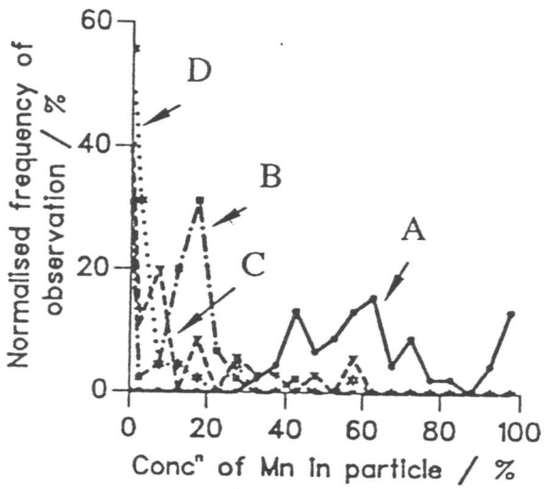

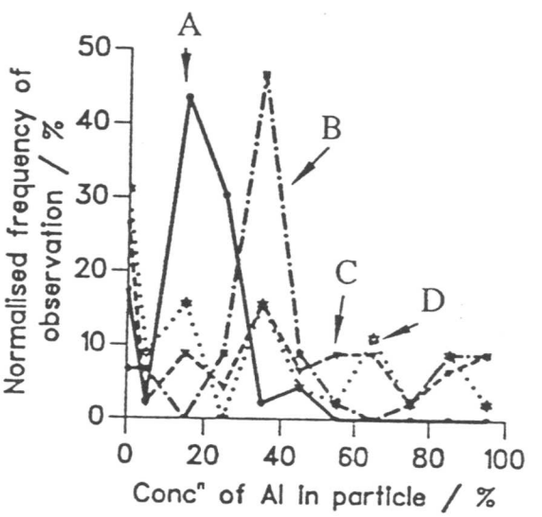

Figure 6.8 (left) Manganese concentration distribution in inclusions across the titanium–weld series. Concentrations are in wt% .
Figure 6.9 (right) Aluminium concentration distribution in inclusions across the titanium–weld series. Concentrations are in wt% .

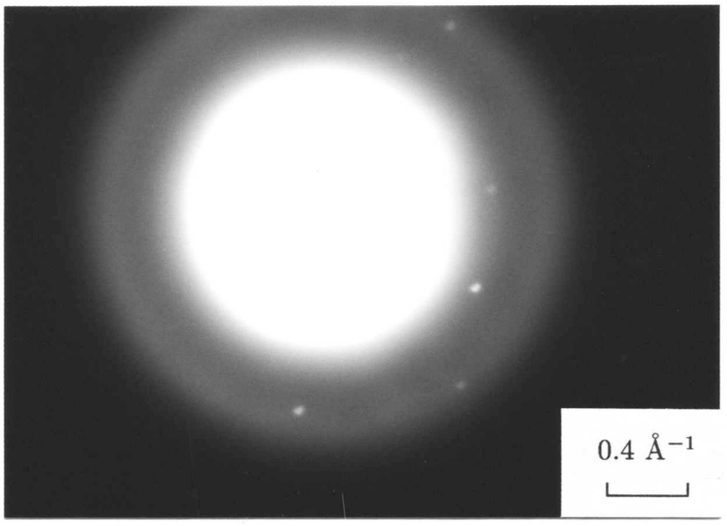

Figure 6.10 Diffraction pattern from part of an inclusion in Weld A. It is consistent with MnS. This phase does not appear in the more titanium–rich welds.

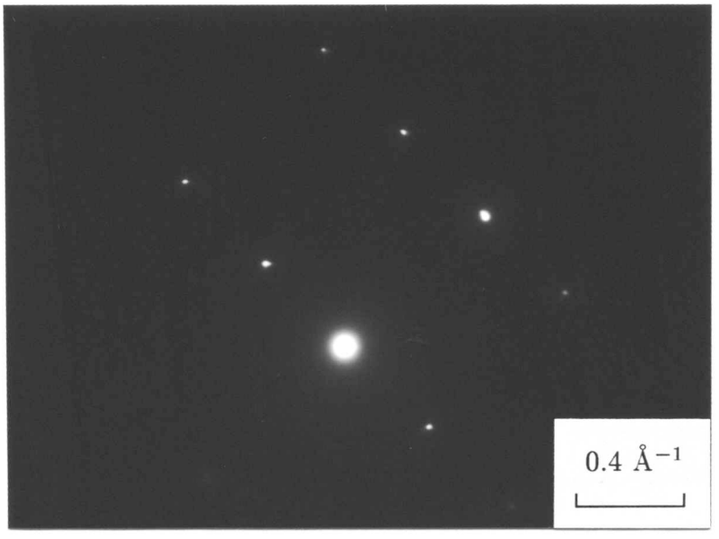

Figure 6.11 Diffraction patterns consistent with TiX were found in all the welds, but become more common with increases in titanium addition.

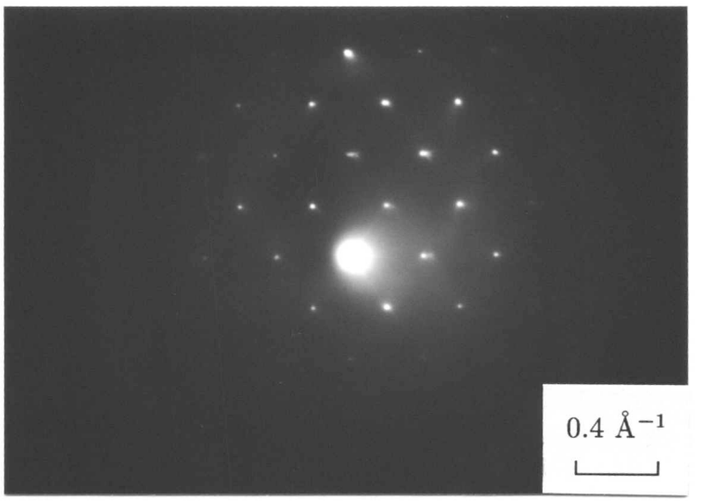

Figure 6.12 Different alumina types were distinguished in particles across the titanium–weld series. This pattern is consistent with γ-Al_2O_3.

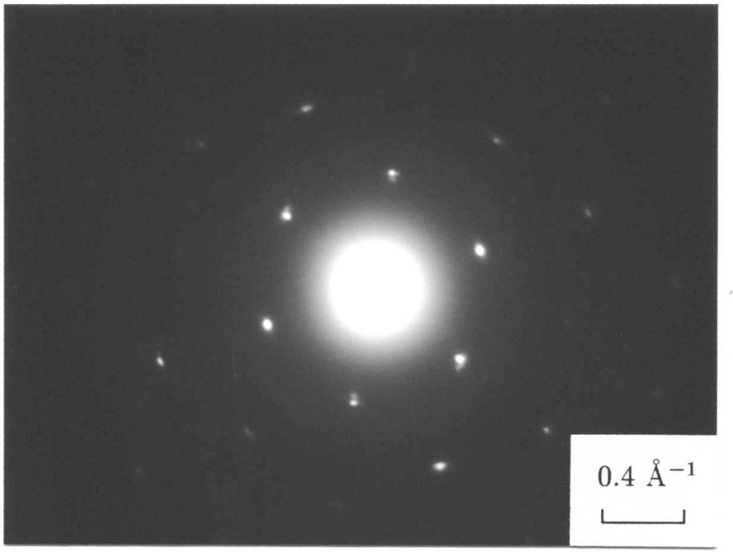

Figure 6.13 This diffraction pattern is consistent with α-Al_2O_3.

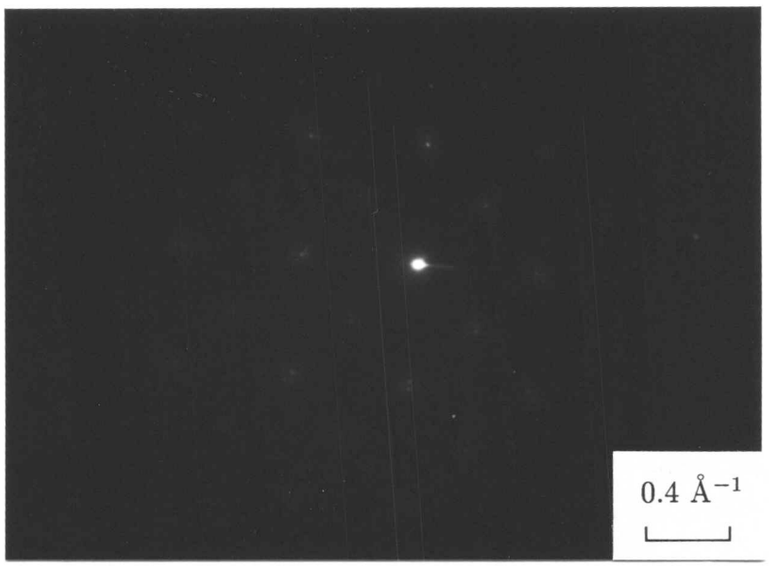

Figure 6.14 Several diffraction patterns were found which corresponded well with $MnAl_2O_4$. Here some super–periodicity is illustrated by the numerous satellite spots.

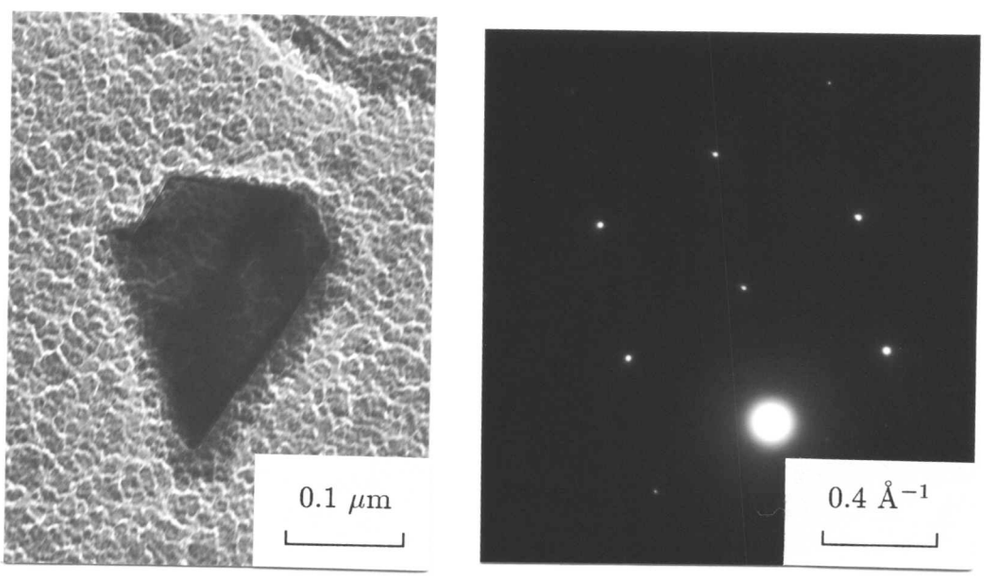

(a) (b)

Figure 6.15 **(a)** A sulphur–rich phase was frequently observed, which did not contain significant levels of manganese. It was suspected that this phase was a copper sulphide of some kind.

(b) Diffraction patterns from this sulphide phase were consistent with an f.c.c. mineral, a$\sim$3.6Å.

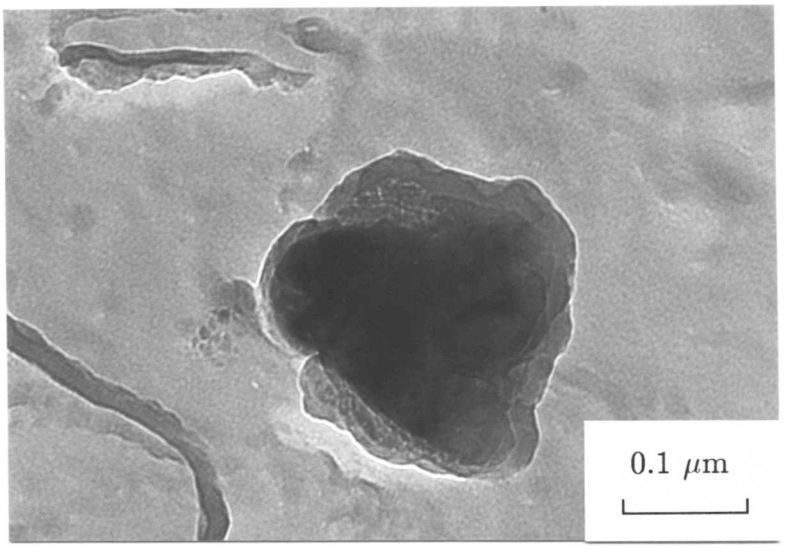

Figure 6.16 TEM micrograph showing the morphology typical of inclusions in Weld B. They are well rounded.

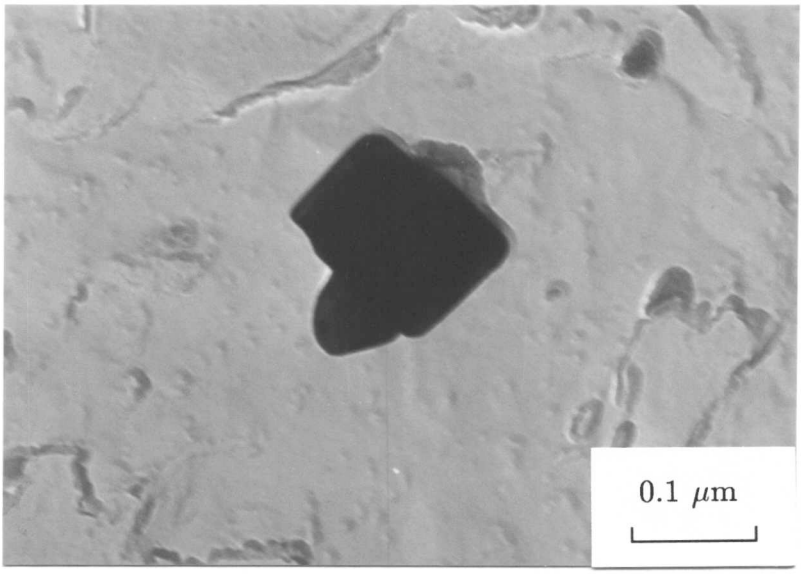

Figure 6.17 TEM micrograph showing more angular inclusions frequently observed in Weld C and Weld D.

6.4 Tungsten–Containing Welds

Welds A, E, F and G contained systematic variations in tungsten. As already stated, Weld A was prepared using the unmodified flux (Table 6.2). Weld E was produced by addition of WO_3 powder to the flux; additions of W powder produced Weld F; FeW powder was added to the flux to produce Weld G. The compositions of the welds are shown in Table 6.6.

Weld no.	C	Si	Mn	W	Al	Ti	O	N
Weld A	0.075	0.36	1.26	0.014	0.012	0.003	280	48
Weld E	0.064	0.22	1.01	0.683	0.011	0.002	401	53
Weld F	0.075	0.41	1.24	1.479	0.014	0.004	314	81
Weld G	0.072	0.40	1.22	1.693	0.032	0.004	313	73

Table 6.6 Compositions of the tungsten weld series. Concentrations are given in wt.%, and O and N in parts per million by weight.

6.4.1 As–Deposited Microstructure

A cross–section of the top bead was examined using optical microscopy (Figures 6.18–6.21), which illustrates a continuous reduction in the amount of grain boundary nucleated phases with increasing tungsten content. The low tungsten welds, Weld A and Weld E, show considerable quantitites of allotriomorphic and Widmanstätten ferrite. In weld Weld F, the thickness of the allotriomorphic ferrite layers is greatly reduced, although Widmanstätten ferrite can still be seen.

The as–deposited microstructures show an increasing dominance of intragranular phases over grain boundary nucleated phases, with increasing tungsten. However, the reduction in allotriomorphic ferrite again implies hardenability changes as well as possible alterations in the inclusion potency.

The greater refinement of the as–deposited microstructure may therefore have occurred for two reasons:

(i) increased nucleation efficacy of inclusions which changed in chemistry/mineralogy as tungsten was added.

(ii) increased hardenability of the alloy due to tungsten present in solution.

6.4.2 Examination of Inclusions

Carbon extraction replicas were prepared from each of the top weld beads to characterise the inclusions. TEM EDX analysis was performed in order to investigate variations in the levels of tungsten present, as well as other potential chemical, and hence mineralogical differences between the inclusion populations. The work revealed the following:

(i) Tungsten was not detected in any of the one hundred and forty–seven particles examined. The experiments have not resulted in the incorporation of tungsten oxide in the welds. The tungsten is present in solid solution in the ferrite.
(ii) The chemical composition of the inclusions did not change much for the different welds (Figures 6.22–6.25). Some minor variations were found (*e.g.* manganese levels decrease while aluminium levels increase as the additions of tungsten increase), but were judged not to be of much consequence.

Diffraction patterns were taken when possible, during the collection of EDX microanalysis data. These showed the presence of γ-Al_2O_3 (Fig.6.26), TiX (where X=C, N or O, Fig.6.27), MnS (Fig.6.28), and a phase which indexed as f.c.c. with a$\sim$3.6Å (as in the melt experiments, Chapter 5). No obviously crystalline silicon–rich areas could be observed, presumably because of the presence of glass silicate.

Although the spatial and size distributions of the inclusions across the weld series were not measured quantitatively, no significant differences seemed apparent. Fig.6.29 a,b are from the high and low tungsten welds, and show that the inclusion sizes and spatial distributions are qualitatively similar. Further, no obvious inclusion morphological differences are apparent.

6.4.3 Hardenability Effect of Tungsten

Since different concentrations of tungsten present in the experimental welds produced no significant effects on the non–metallic inclusion populations, it is suspected that microstructural alterations have been produced due to the effects of tungsten in solution.

In order to demonstrate the hardenability effect of tungsten, standard thermomechanical specimens (cylinders of diameter 8 mm, and height 12 mm) were machined from weld metal of the low and high tungsten extremes of the weld series. These were austenitised at 1000°C for 5 mins before gas–quenching to room temperature. Radial dilatational information was recorded during the quench to determine the transformation kinetics.

Two different cooling rates were used to study transformations – 10 and 50°C s^{-1}. As the dilatational curves in Fig.6.30 a,b indicate, the onset of transformation was retarded

in the high tungsten samples. The onset temperatures for the two weld metals can be seen in Fig.6.31 a,b (high W ~690°C, low W ~720°C at 10 °C s^{-1}; high W ~530°C, low W ~580°C at 50°C s^{-1}). The hardenability of the alloy is clearly increased by tungsten in solution.

Optical micrographs of the microstructures produced by these gas–quench experiments are shown in Figures 6.32 and 6.33. There is more martensite in the high tungsten alloy, as would be expected from its greater hardenability.

6.5 Conclusions

Variations in levels of titanium and tungsten in experimental submerged arc welds have been achieved by the addition of various powders to a standard welding flux. Increasing titanium has caused a general increase in intragranular as opposed to grain-boundary phases in the as–deposited weld microstructure. The microstructural changes have arisen due to an apparent dual effect of titanium:

(i) Increases in titanium have caused increases in Ti–rich minerals in the non–metallic inclusions. This has been associated with an increased efficacy for nucleating acicular ferrite.

(ii) For large levels of titanium, such as in Weld C and Weld D, much of the titanium remains in solution. This seems to cause increased alloy hardenability.

Increasing tungsten has also caused a general increase in acicular ferrite. However, tungsten is not involved as a cation in the non–metallic inclusions. Instead, microstructural refinement has occurred due to hardenability effects of tungsten in solution.

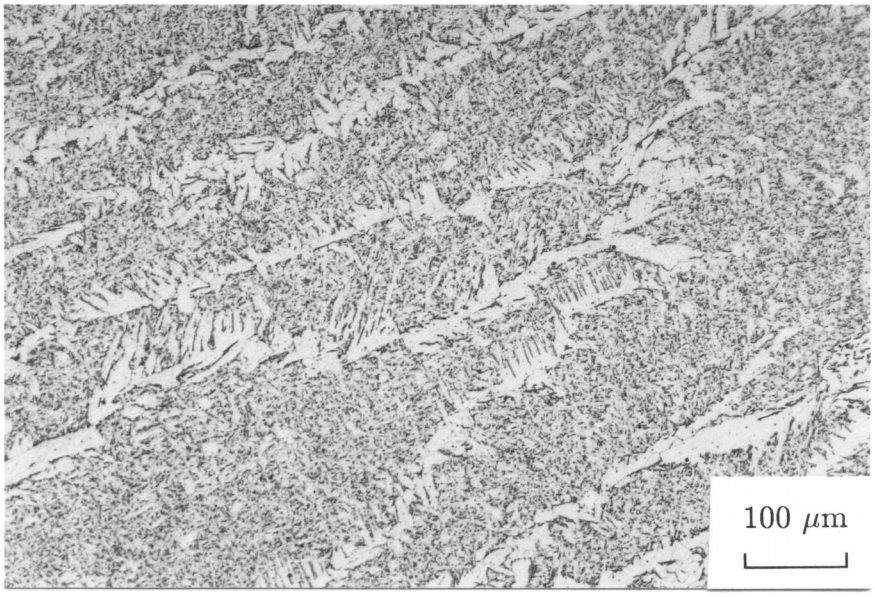

Figure 6.18 Optical micrograph of the as–deposited microstructure of Weld A (the lowest tungsten addition).

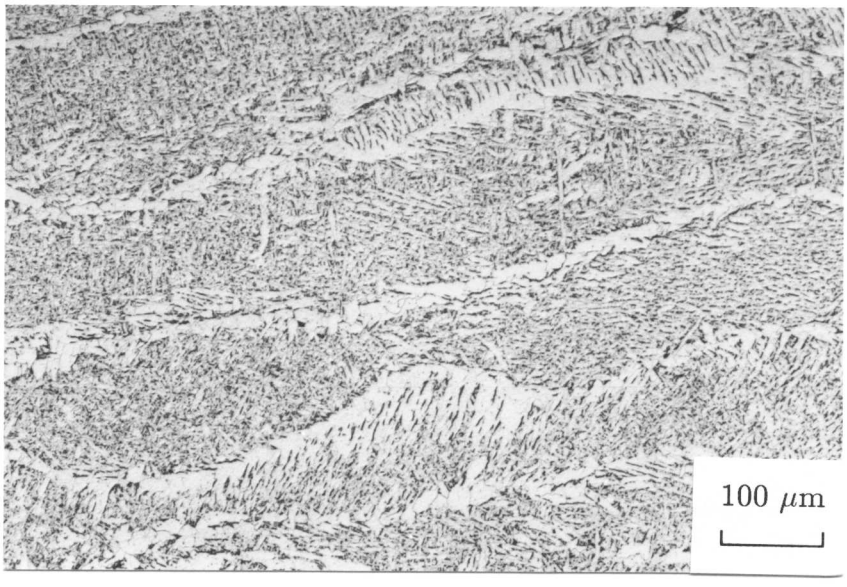

Figure 6.19 Optical micrograph of the as–deposited microstructure of weld Weld E.

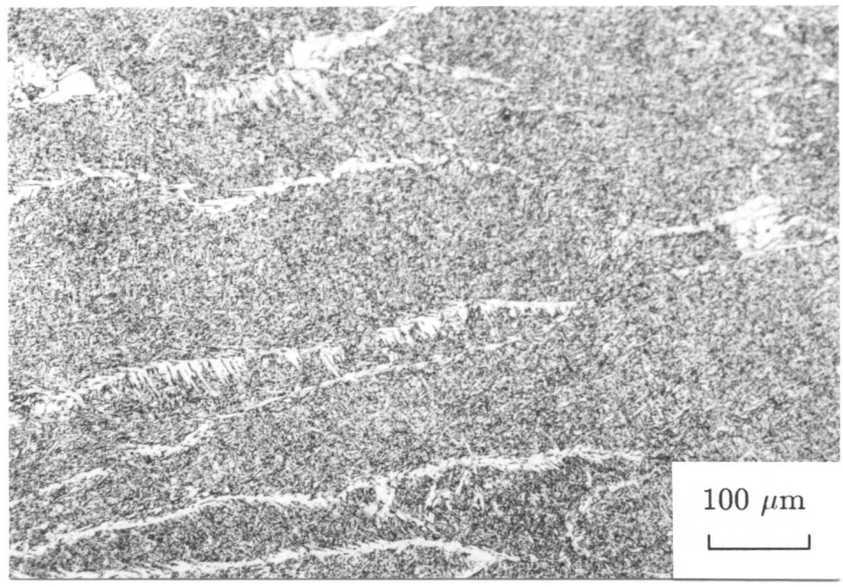

Figure 6.20 Optical micrograph of the as–deposited microstructure of weld Weld F.

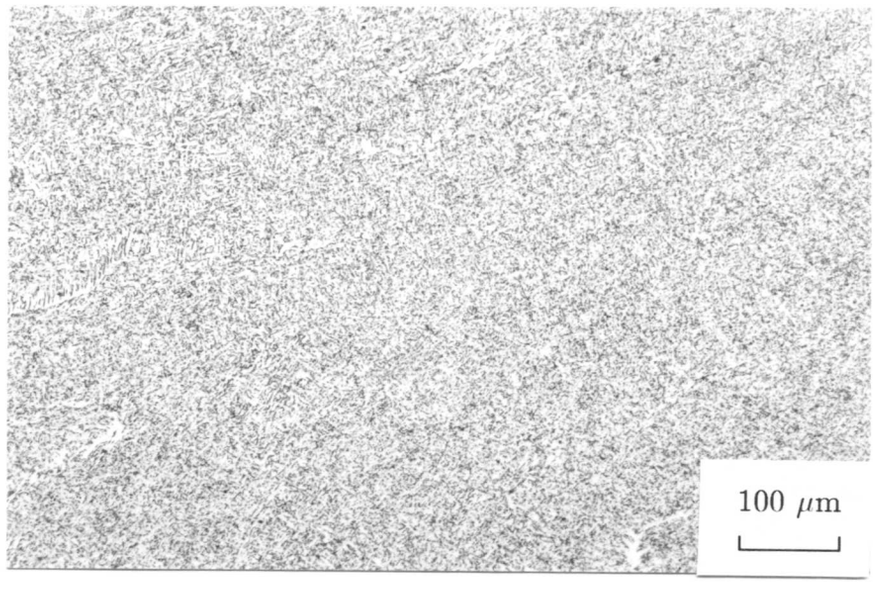

Figure 6.21 Optical micrograph of the as–deposited microstructure of weld Weld G (the most tungsten rich of the weld series).

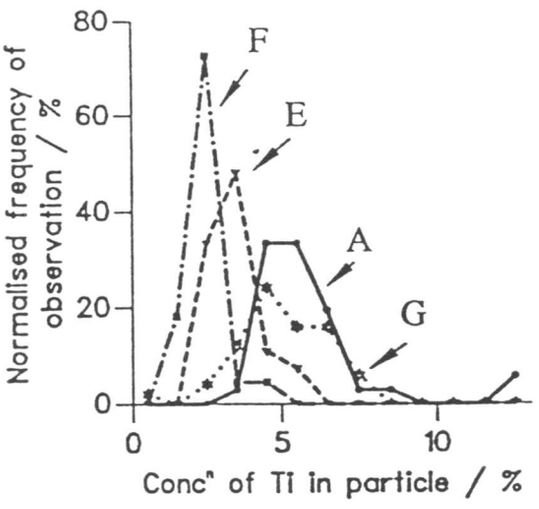

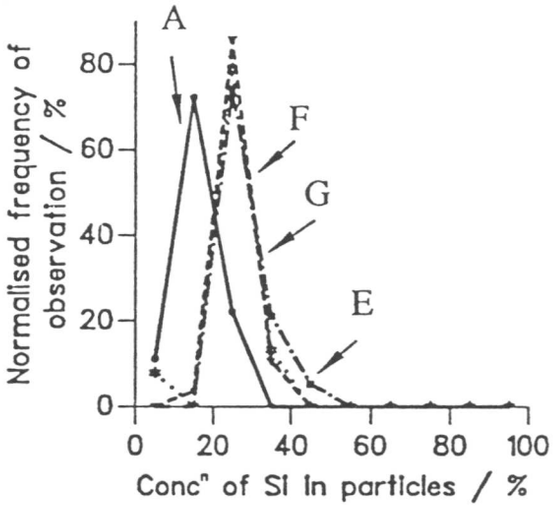

Figure 6.22 (left) Titanium concentration distributions in the inclusions across the tungsten–weld series. Concentrations are in wt% .
Figure 6.23 (right) Silicon concentration distributions in the inclusions across the tungsten–weld series. Concentrations are in wt% .

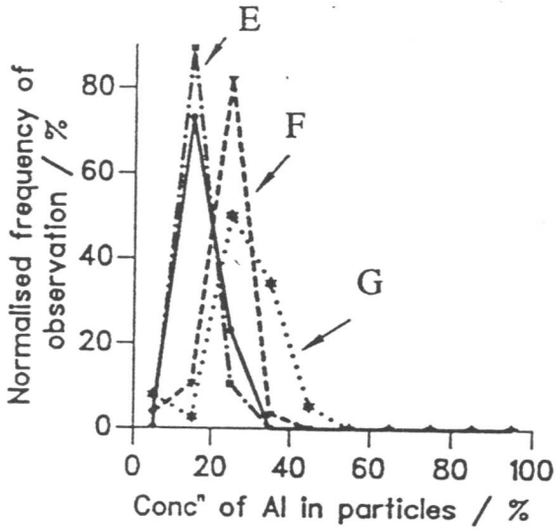

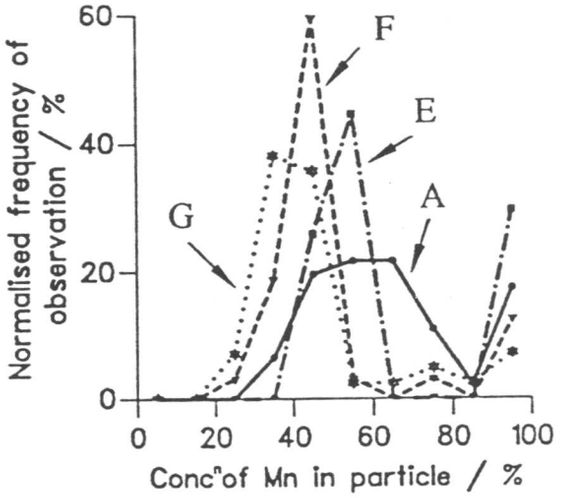

Figure 6.24 (left) Aluminium concentration distributions in the inclusions across the tungsten–weld series. Concentrations are in wt% .
Figure 6.25 (right) Manganese concentration distributions in the inclusions across the tungsten–weld series. Concentrations are in wt% .

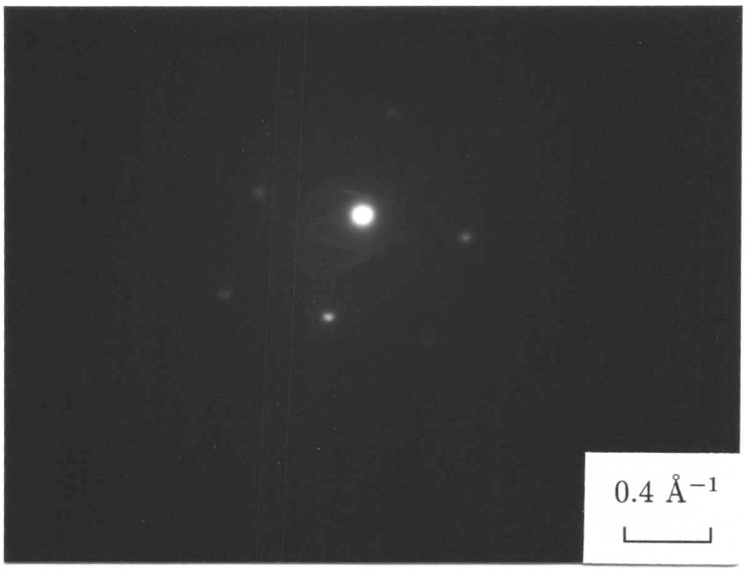

Figure 6.26 Diffraction patterns taken from strongly diffracting inclusions, found during EDX analysis, showed the presence of various minerals. This pattern illustrates the presence of γ-Al_2O_3.

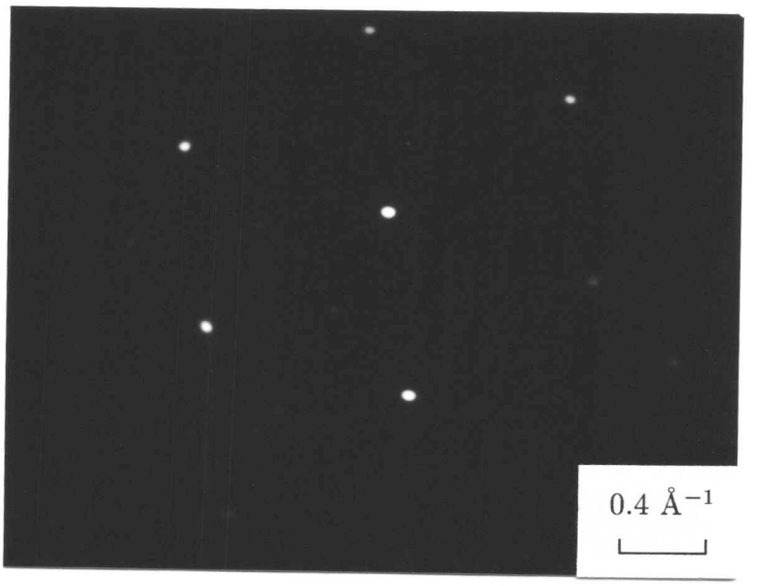

Figure 6.27 Diffraction patterns consistent with a TiX phase were obtained.

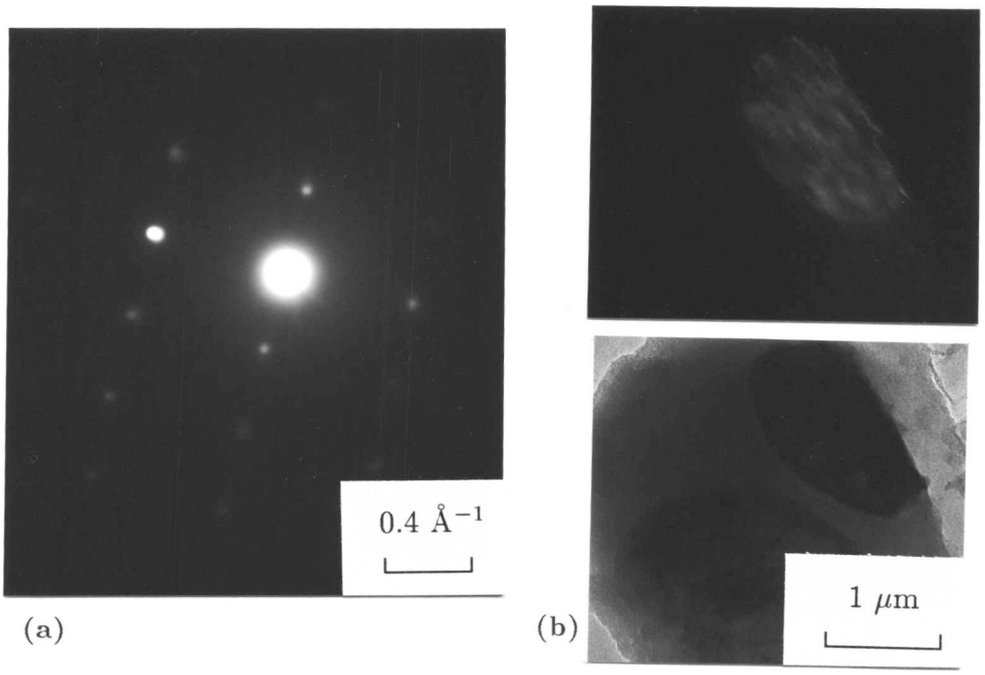

Figure 6.28 **(a)** Diffraction consistent with MnS was obtained in inclusions across the weld series.

(b) Dark and bright field micrographs of the MnS regions within one inclusion. This illustrates the inhomogeneous, multicrystalline nature of real weld inclusions.

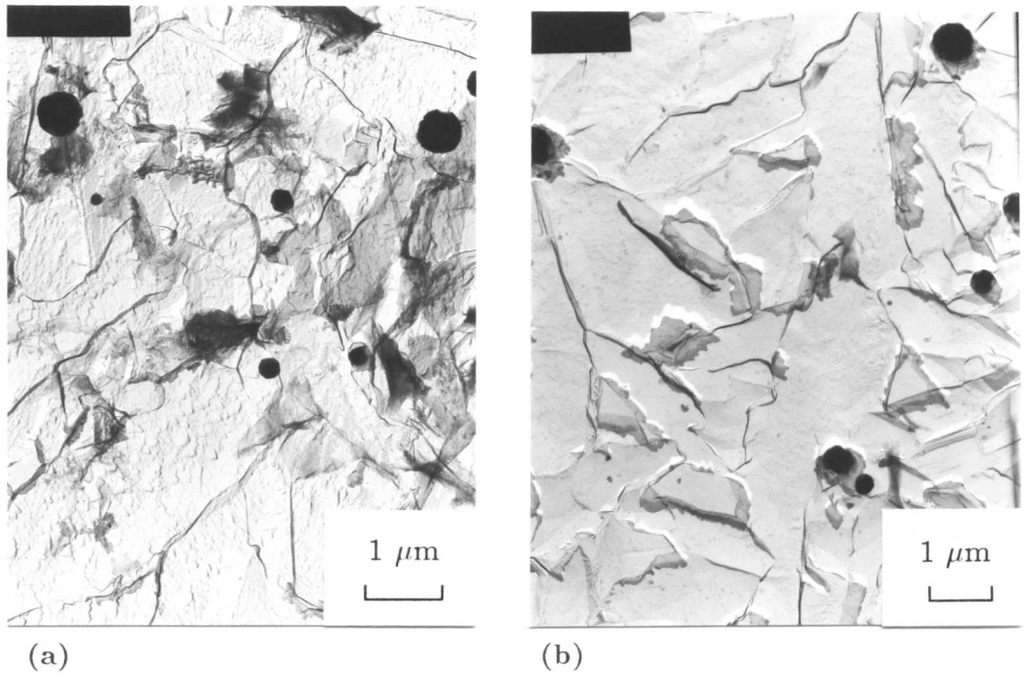

Figure 6.29 **(a)** TEM bright field micrograph showing the qualitative size and distribution of inclusions in Weld A.

(b) TEM bright field micrograph showing the qualitative size and distribution of inclusions in weld Weld G.

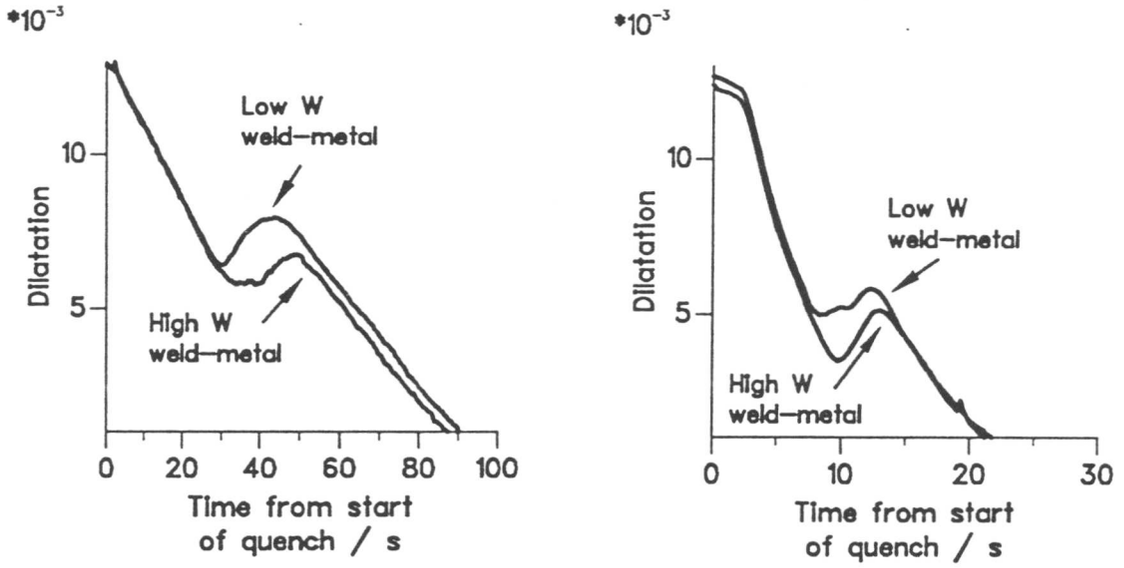

(a) (b)

Figure 6.30 (a) Dilatation curves obtained during the gas–quenching of weld metal Weld A and Weld G (low and high tungsten respectively) at $10°C\,s^{-1}$.

(b) Dilatation curves obtained for gas–quenching at $50°C\,s^{-1}$.

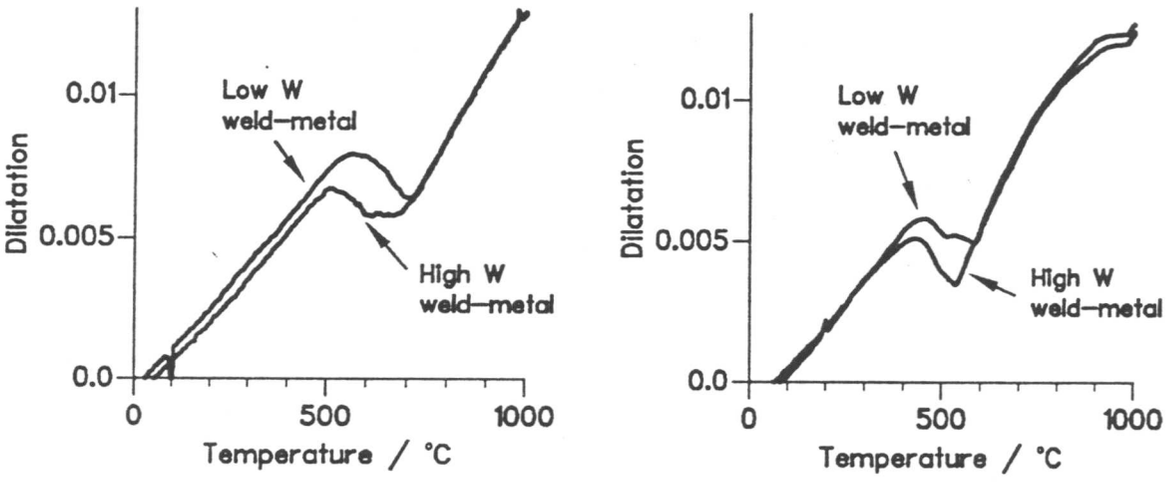

(a) (b)

Figure 6.31 (a) Dilatation curves obtained during gas–quenching at $10°C\,s^{-1}$, illustrating the differences in temperatures at which tranformation was initially observed.

(b) Dilatation curves showing the onset temperatures of transformation during gas–quench of $50°C\,s^{-1}$.

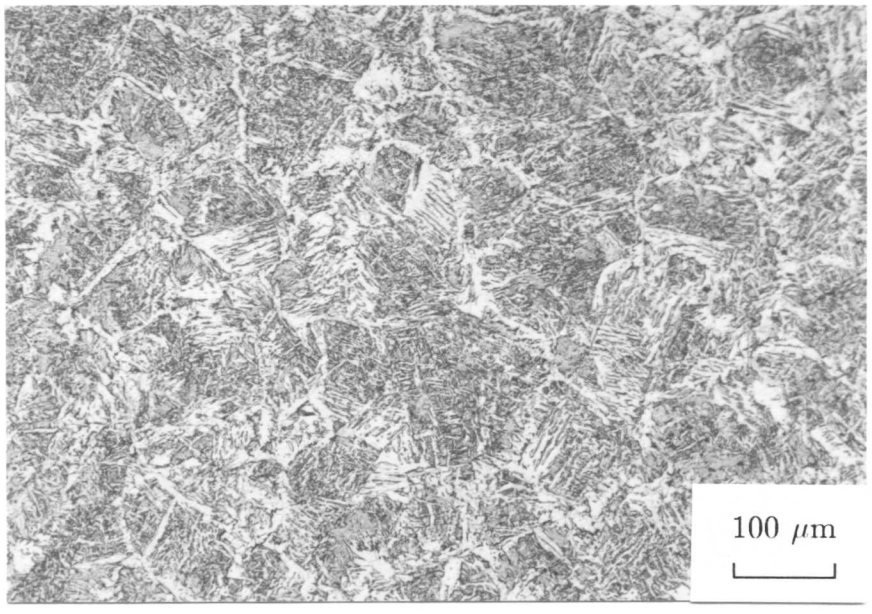

Figure 6.32 Optical micrograph of the microstructure of the low tungsten weld (Weld A) after quenching at $50°C\,s^{-1}$ from 1000°C.

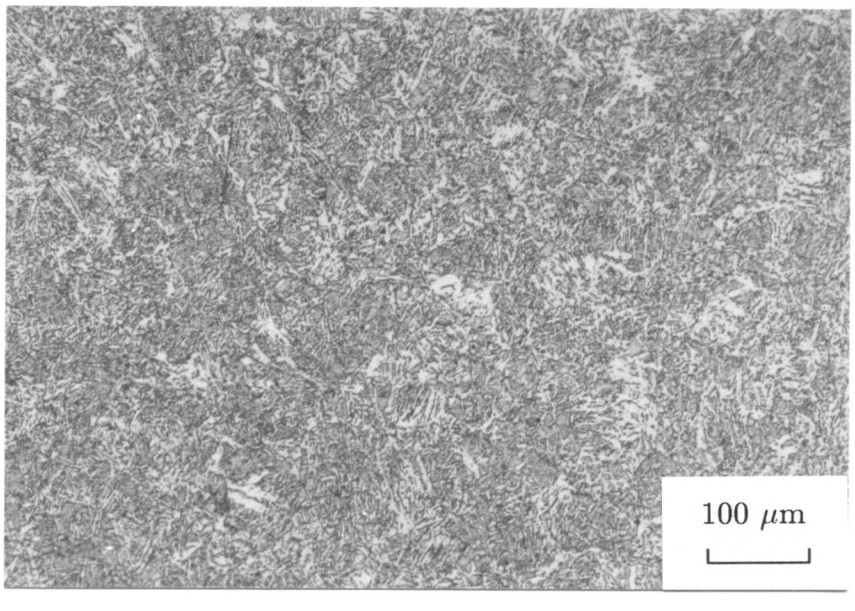

Figure 6.33 Optical micrograph of the microstructure of the high tungsten weld (Weld G) after quenching at $50°C\,s^{-1}$ from 1000°C. There is more martensite apparent in the high tungsten alloy, illustrating its greater hardenability.

APPENDIX 1
A Model for the Investigation of Epitaxy

1.1 Introduction

The experiments described in Chapters 3–5 identified two dominant mechanisms of heterogeneous nucleation of bainite or acicular ferrite on non–metallic inclusions:
(i) Localised oxidation with associated depletion of carbon in adjacent regions.
(ii) Localised depletion of manganese.

Such chemical effects being responsible for stimulating nucleation have been discussed previously (Farrar and Watson, 1979; Es-Souni and Beaven, 1990; Es-Souni *et al.*, 1991). Most research, however, suggests that mineral particles induce nucleation because of their crystallographic similarity with the b.c.c. ferrite lattice (Mori *et al.*, 1981; Saggese *et al.*, 1982; Thewlis, 1990; Grong *et al.*, 1992). This lattice matching theory is investigated here. Although progress in the investigation has been made, the results obtained were limited by the crude nature of the developed model. Hence this section is presented as an appendix.

1.2 Lattice Matching

The usual analysis of lattice matching follows Bramfitt (1970):

$$\delta^{(hkl)_s}_{(hkl)_n} = \frac{1}{3}\sum_{l=1}^{3}\left(\frac{d_{[uvw]^l_s}\,cos\theta - d_{[uvw]^l_n}}{d_{[uvw]^l_n}}\right) \times 100$$

$\delta^{(hkl)_s}_{(hkl)_n}$ = lattice mismatch between two planes
$(hkl)_s$ = low index plane of the substrate
$(hkl)_n$ = low index plane of nucleated solid
$[uvw]_s$ = low index direction in $(hkl)_s$
$[uvw]_n$ = low index direction in $(hkl)_n$
$d_{[uvw]_s}$ = interatomic spacing along $[uvw]_s$
$d_{[uvw]_n}$ = interatomic spacing along $[uvw]_n$
θ = the angle between $[uvw]_s$ and $[uvw]_n$
Subscripts 's' and 'n' denote reference to substrate and nucleated solid respectively.

Misfit values for some of the minerals discussed in Chapters 3–5 have been calculated using the Bramfitt analysis by Mills *et al.* (1987), and are shown in Table 1.1. Of these minerals only TiO was herein observed to cause significant ferrite nucleation. Although the Bramfitt analysis does predict a good lattice match between $\{100\}_{\mathrm{TiO}}$ and $\{100\}_{\alpha}$, it also predicts good matching for galaxite, γ-Al_2O_3 and TiN for the same relative orientation with ferrite. These three minerals were not observed to cause significantly enhanced nucleation experimentally in the pressure bonding experiments, and were not amongst the most potent nucleants when introduced into steel melts. Thus Bramfitt analysis does not seem to properly discriminate between nucleant and non–nucleant minerals. This suggests that lattice matching is not responsible for any of the nucleation observed.

However, it may be the case that new ideas are needed to examine the lattice matching concept. A model was therefore developed to re-evaluate interfacial epitaxy between mineral surfaces. Although this model clearly possesses shortcomings, it is conceptually interesting.

Parallelism (ferrite‖substrate)		Extent of disregistry (%)			
Planar	Directional	TiO	γ-Al_2O_3	Galaxite	TiN
$\{100\} \parallel \{100\}$	$<100> \parallel <110>$	3.0	3.2	1.8	4.6
$\{110\} \parallel \{100\}$	$<100> \parallel <110>$	22.0	16.7	20.5	23.9
$\{100\} \parallel \{110\}$	$<100> \parallel <110>$	24.4	19.0	22.8	26.3
$\{110\} \parallel \{110\}$	$<100> \parallel <110>$	37.4	33.3	35.6	39.5
$\{111\} \parallel \{110\}$	$<110> \parallel <100>$	14.6	9.8	13.2	16.4
$\{100\} \parallel \{111\}$	$<100> \parallel <110>$	34.5	28.5	32.8	36.5
$\{110\} \parallel \{111\}$	$<100> \parallel <110>$	15.9	11.0	14.4	17.6
$\{111\} \parallel \{111\}$	$<110> \parallel <110>$	27.2	31.5	28.0	26.0
$\{111\} \parallel \{100\}$	$<110> \parallel <110>$	20.8	23.6	20.9	20.6

Table 1.1 Bramfitt-type misfit values for four of the minerals tested experimentally for their nucleation potency (after Mills *et al.* , 1987).

1.3 Details of the Model

1.3.1 Data Input

The information required includes the lattice type, lattice parameters, structural motif, atomic type and Miller indices of the planes in contact at the interface, for both the substances involved in the analysis. The analysis is restricted to orthonormal lattices. This is not a serious constraint, because hexagonal and trigonal minerals can be considered using their orthorhombic representations. Only monoclinic and triclinic minerals are excluded.

1.3.2 Planes of Interest

Having specified the Miller indices of the interface plane for each of the two minerals under consideration, the program must isolate all atoms which lie on this plane. It does this by first generating a miniature crystal, using the unit cell information supplied by the user. It then sections this small group of cells along the proposed interface plane, and identifies the atoms whose co-ordinates exactly lie on this plane. Atoms which lie on the plane, and their x, y and z co-ordinates are held in memory, and the rest of the crystal is discarded. Expressing atomic co-ordinates in terms of x, y and z now becomes cumbersome, since all the atoms of interest are co-planar. A series of subroutines transforms the co-ordinate system, so that atomic positions are described in two dimensions, with an atom at the origin.

In a perfect crystal, all the structural information of that crystal is contained within the description of one unit cell. Similarly, for a plane within a crystal, all the structural information is contained within a 2-dimensional unit mesh. The next stage in the program is to define this unit mesh for the selected planes of the interface. All lattice points are labelled in the program. The lattice points which lie at the corners of the unit mesh are defined by selecting the two lattice points nearest to the origin (itself a lattice point), whose position vectors were non–parallel. These two non–parallel position vectors were simply summed to give the position vector of the fourth corner of the unit mesh.

All other atoms on the plane of interest, are then considered, and if their co-ordinate positions lie within the unit mesh defined above, they are held in memory, others being discarded. In this way, all the atoms contained within one unit mesh are isolated, and the unit mesh completely defined.

1.3.3 Topography of the Atomic Surfaces

Once the positions of all the atoms within the unit mesh had been defined, the relief of the atomic surface needed to be modelled. In order to do this, the radii of the various atoms are

required, and were represented by the ionic radii. The use of ionic radii is a limitation in the program, particularly for highly covalent mineral structures. For austenite and ferrite, the metallic radius of iron was considered. Physical protrusion of the atomic surface above the base plane was calculated for each x, y position in the unit mesh. The x, y positions considered were discrete so that the mesh was effectively divided into a large number of pixels. Initially the atomic shape was modelled as conical. Although unconventional, it was felt that conical protrusions may tessellate more cleanly than hemispherical ones, yielding clear results after meshing analysis.

At this point in the programming, it was important to check that the atomic surfaces had been modelled reasonably, so that any results from epitaxy analysis could be viewed with a certain amount of confidence. To this end, the information describing the unit mesh and its atomic topography was presented graphically (Fig.1.1–Fig.1.4). As can be seen from the figures, the modelling of the atomic surface within one mesh could be achieved, this being varified for a wide range of minerals.

The next area of the model required a direct comparison between the two atomic surfaces across the user–proposed interface plane, in order to quantify the degree of epitaxy possible. The method used involved comparing the atomic topography of one surface with the topography of the hollows in the other surface. Direct comparison therefore involved inverting one of the surface topographies – in effect creating a relief which corresponded to a mould of the original surface. Such an inverted surface is shown in Fig.1.5 and Fig.1.6. The inverted and non-inverted surfaces from the two minerals of interest were then directly compared by calculating the difference function between the heights of atoms and depths of hollows. The value of this difference function obviously varied, depending on the relative position and orientation of the two surfaces. In order to find a minimum difference function, and therefore the best epitaxial fit in terms of atom relief, the two surfaces were moved and rotated systematically relative to each other, and after each relative movement, the difference function was calculated. The value of the minimum difference obtained overall was retained in memory, and displayed as the end result of the program. The lower this minimum value, the better the epitaxial fit was expected to be.

It should be noted that relative movement of one atomic surface with the other, involved high resolution in terms of non–rotational shift. However, only relative rotations of 90° were considered. This was used initially for simplicity, but represented a serious flaw in the model.

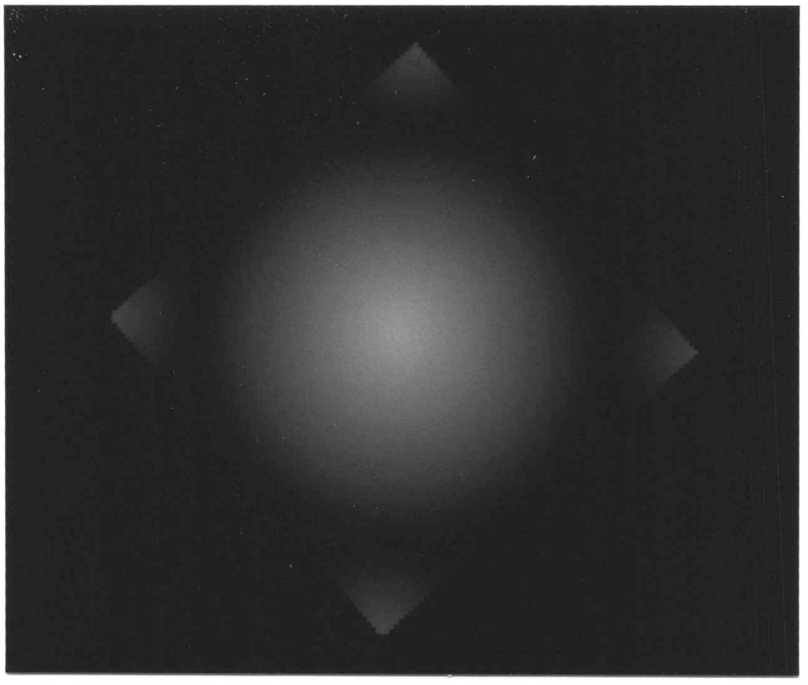

Figure 1.1 Photograph of the graphical output representing the surface topography of a unit mesh of the {100} section of MnS

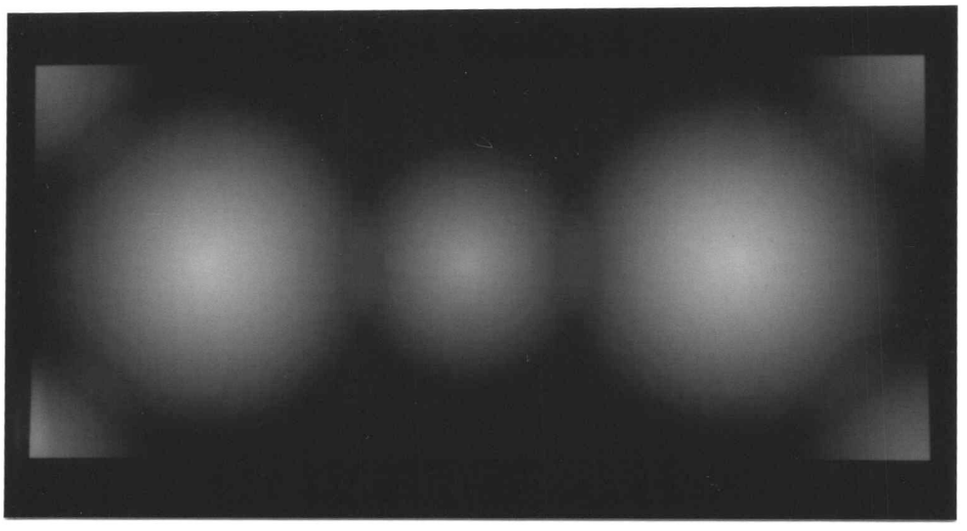

Figure 1.2 Photograph of the graphical output representing the surface topography of a unit mesh of the (110) section of TiO_2

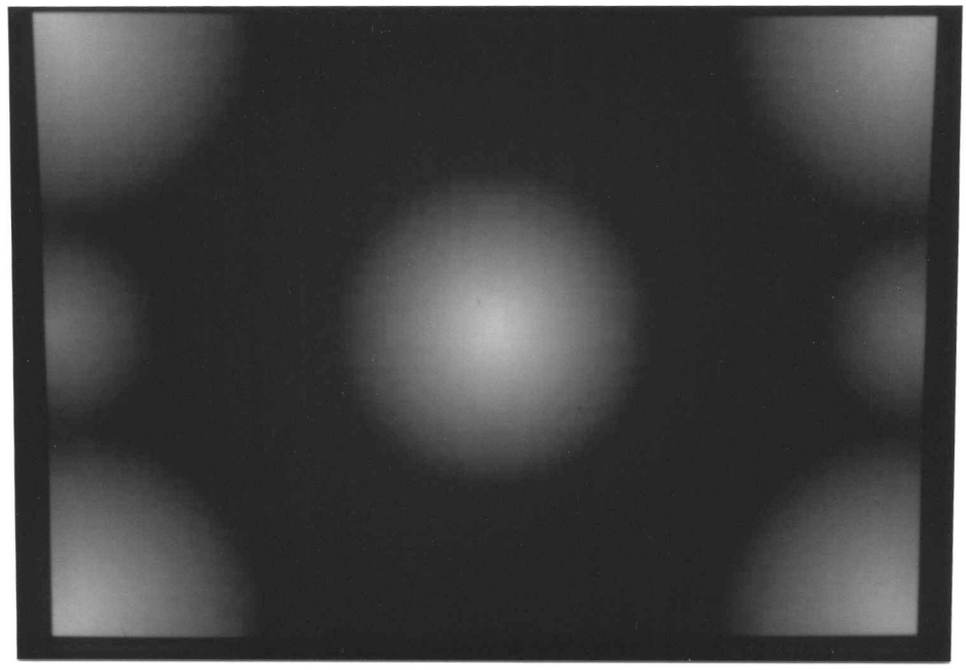

Figure 1.3 Photograph of the graphical output representing the surface topography of a unit mesh of the $\{110\}$ section of $CaTiO_3$

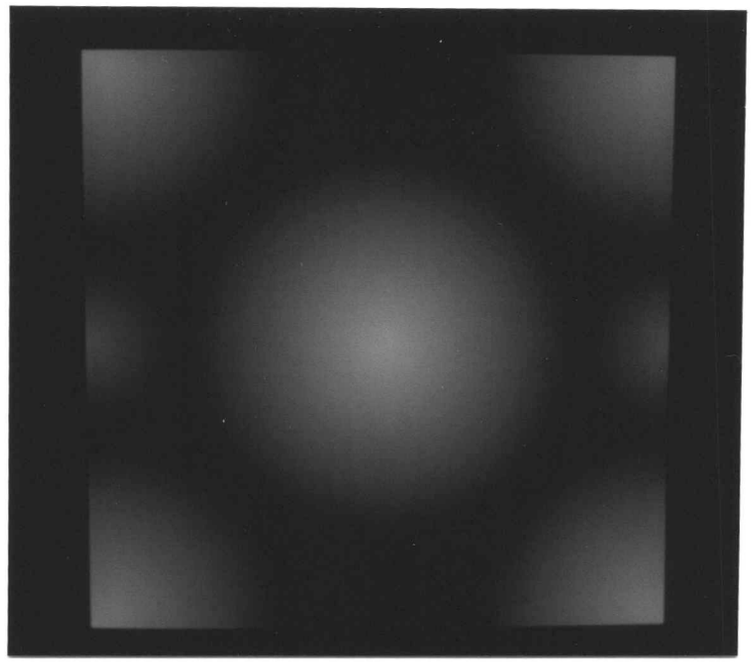

Figure 1.4 Graphical output of the modelled atomic relief of the $\{100\}$ section of WO_3

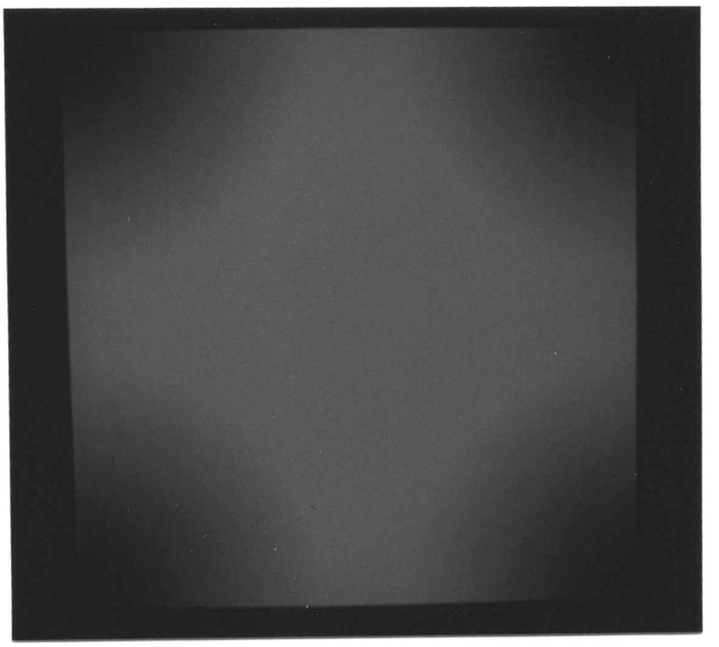

Figure 1.5 Photograph of the graphical output of the topography of the hollows in the atomic surface of a unit mesh of the $\{100\}$ section of ferrite

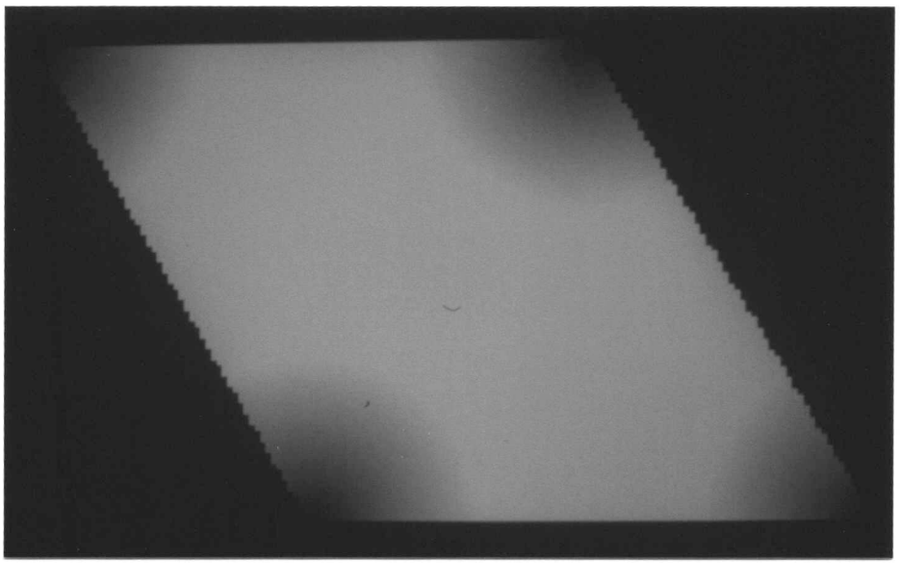

Figure 1.6 Graphical output showing the topography of the hollows of the unit mesh of the $\{111\}$ section of ferrite

1.4 Results of the Model and Conclusions

Some obvious limitations to this meshing program exist:

(i) That the relative rotation of the atomic surfaces is limited to 90°.

(ii) That the atom protrusion above the plane base is modelled as conical.

(iii) That the radii of the atoms are taken from ionic radius data, and will therefore be highly inaccurate for the more covalent minerals.

(iv) That the comparison between two atomic surfaces involving calculation of the difference function is slow even on the Sun minicomputer.

(v) That only the relief is considered in the meshing analysis. Properties such as charge distribution are ignored.

Such limitations were likely to seriously affect the reliability of the results produced. Therefore, it has been the main aim of this chapter to describe the method used, and the concept behind the model, rather than analyse results obtained. For more reliability of analysis the above program limitations must be addressed.

APPENDIX 2

Meshing Analysis Program

```
      INTEGER PIX1(50000), PIY1(50000)
      INTEGER PIX2(50000), PIY2(50000),RESY2,RESX2
      INTEGER PICAR1,PICAR2,RESY1,RESX1,ASISE2,PICSIZ,ASISE1
      INTEGER CSHY,CR,CSHX
      DOUBLE PRECISION REX2(1024), RWHY2(1024),RMIN,RWHY1(1024)
      DOUBLE PRECISION VALUE1(50000), VALUE2(50000),REX1(1024)
      OPEN (unit=3,file='data3.out')
      CALL FUNCTION1(PIX1,PIY1,VALUE1,PICAR1,RESY1,RESX1,PICSIZ,
     &  ASISE1,REX1,RWHY1)
      CALL FUNCTION2(PIX2,PIY2,VALUE2,PICAR2,ASISE2,VALUE2,
     &  REX2,RWHY2,RESY2,RESX2,PICSIZ)
* Want to store the shiftx, shifty and rotation that produces the minimum
* RMIN so that it may be redetermined using a fine resolution, and plotted
* on uniras.
      IF (PICAR1 .GT. PICAR2) THEN
          CALL RMESH(PICAR2,PICAR1,PIX2,PIY2,PIX1,PIY1,ASISE1,
     &       VALUE1,REX1,RWHY1,VALUE2,RESY2,RESX2,RMIN,PICSIZ,RESY1,
     &       CSHY,CR,CSHX)
      ELSE
          CALL RMESH(PICAR1,PICAR2,PIX1,PIY1,PIX2,PIY2,ASISE2,VALUE2,
     &       REX2,RWHY2,VALUE1,RESY1,RESX1,RMIN,PICSIZ,RESY2,CSHY,CR,CSHX)
      ENDIF
      STOP
      CALL ACCUR(CR,CSHX,CSHY,PIX1,PIY1,PICAR1,VALUE1,RESX1,
     &  RESY1,PICAR2,PIX2,PIY2,ASISE2,VALUE2,REX2,RWHY2,PICSIZ,RESY2)
      END

. . . . . .
      SUBROUTINE FUNCTION1(PICX1,PICY1,VAL1,PICARRAY1,RESLX1,
     &  RESLY1,PICSI,ASIZE1,RX1,RY1)
. . . . . .
      INTEGER X1(1024), Y1(1024), Z1(1024), LP1(1024),PICSI
      INTEGER H1, K1 ,L1, ASIZE1, LAT1, I, MOTIF1,PICARRAY1
      DOUBLE PRECISION A1, B1, C1, RAD1(1024)
      DOUBLE PRECISION RX1(1024), RY1(1024), RZ1(1024)
      CHARACTER*4 ELEMENTS(187),TYP1(1024)
      DOUBLE PRECISION IONICR(187)
      DOUBLE PRECISION VAL1(50000)
      INTEGER PICX1(50000),PICY1(50000),RESLX1,RESLY1
      COMMON /ATOM/ ELEMENTS
      COMMON /RADIUS/ IONICR
      OPEN (unit=1,file='data1.out')
      CALL DATAIN(X1,Y1,Z1,LP1,H1,K1,L1,
     &  ASIZE1,LAT1,MOTIF1,A1,B1,C1,TYP1)
      CALL PCELL(X1,Y1,Z1,TYP1,LAT1,ASIZE1,LP1)
      CALL MINICRYST(X1,Y1,Z1,TYP1,ASIZE1,LP1)
      CALL PLANE(X1, Y1, Z1, TYP1, ASIZE1, H1, K1, L1, LP1)
```

```
      CALL ORIGIN(X1,Y1,Z1,TYP1,LP1,ASIZE1,MOTIF1)
      CALL TRANS1(X1,Y1,Z1,TYP1,A1,B1,C1,H1,K1,L1,ASIZE1,RX1,RY1,LP1)
      CALL TRANS2(Z1,TYP1,A1,B1,C1,H1,K1,L1,ASIZE1,RX1,RY1,RZ1,LP1)
      CALL MESH(RX1,RY1,TYP1,LP1,ASIZE1)
      CALL RADIUSS(TYP1,ASIZE1,RAD1)
      CALL PIXEL(RAD1,RX1,RY1,PICX1,PICY1,VAL1,ASIZE1,
     &  A1,B1,PICARRAY1,RESLX1,RESLY1,PICSI)
* So picarray gives the size of the pixel array
      DO  21 I=1,PICARRAY1
          WRITE(1,*) PICX1(I),PICY1(I),VAL1(I)
21    CONTINUE
      END

. . . . . .
      SUBROUTINE FUNCTION2(PICX2,PICY2,VAL2,PICARRAY2,ASIZE2,
     &  VAL2,RX2,RY2,RESLY2,RESLX2,PICSI)
. . . . . .
      INTEGER X2(1024), Y2(1024), Z2(1024), LP2(1024),PICSI
      INTEGER H2, K2 ,L2, ASIZE2, LAT2, I, MOTIF2,PICARRAY2
      DOUBLE PRECISION A2, B2, C2, RAD2(1024)
      DOUBLE PRECISION RX2(1024), RY2(1024), RZ2(1024)
      CHARACTER*4 ELEMENTS(187),TYP2(1024)
      DOUBLE PRECISION IONICR(187)
      DOUBLE PRECISION VAL2(50000)
      INTEGER PICX2(50000),PICY2(50000),RESLX2,RESLY2
      COMMON /ATOM/ ELEMENTS
      COMMON /RADIUS/ IONICR
      OPEN (unit=2,file='data2.out')
      CALL DATAIN(X2,Y2,Z2,LP2,H2,K2,L2,
     &  ASIZE2,LAT2,MOTIF2,A2,B2,C2,TYP2)
      CALL PCELL(X2,Y2,Z2,TYP2,LAT2,ASIZE2,LP2)
      CALL MINICRYST(X2,Y2,Z2,TYP2,ASIZE2,LP2)
      CALL PLANE(X2, Y2, Z2, TYP2, ASIZE2, H2, K2, L2, LP2)
      CALL ORIGIN(X2,Y2,Z2,TYP2,LP2,ASIZE2,MOTIF2)
      CALL TRANS1(X2,Y2,Z2,TYP2,A2,B2,C2,H2,K2,L2,ASIZE2,RX2,RY2,LP2)
      CALL TRANS2(Z2,TYP2,A2,B2,C2,H2,K2,L2,ASIZE2,RX2,RY2,RZ2,LP2)
      CALL MESH(RX2,RY2,TYP2,LP2,ASIZE2)
      CALL RADIUSS(TYP2,ASIZE2,RAD2)
      CALL PIXEL(RAD2,RX2,RY2,PICX2,PICY2,VAL2,ASIZE2,
     &  A2,B2,PICARRAY2,RESLX2,RESLY2,PICSI)
* So picarray gives the size of the pixel array
      CALL INVPIXEL(VAL2,PICARRAY2)
      DO  21 I=1,PICARRAY2
          WRITE(2,*) PICX2(I),PICY2(I),VAL2(I)
21    CONTINUE
      END
```

```
. . . . . .
      SUBROUTINE DATAIN(EX,WHY,ZEE,LATP,ACH,KAY,EL,
     &  ASIZ,LAT,MOTIV,AY,BE,CE,TYP)
. . . . . .
      INTEGER EX(1024), WHY(1024), ZEE(1024), LATP(1024)
      INTEGER ACH, KAY ,EL, ASIZ, LAT, I, N, MOTIV
      DOUBLE PRECISION AY, BE, CE
      CHARACTER*4 TYP(1024)
      ASIZ=0
      WRITE(6,*) 'LATTICE TYPE ?'
      WRITE(6,*) '1=Primitive'
      WRITE(6,*) '2=Body centred'
      WRITE(6,*) '3=Face centred'
      WRITE(6,*) '4=A-centred'
      WRITE(6,*) '5=B-centred'
      WRITE(6,*) '6=C-centred'
      READ(5,*) LAT
      WRITE (6,*) 'Give me the lattice parameters then!'
      READ (5,*) AY, BE, CE
      WRITE(6,*) 'How many atoms are there in the motif ?'
      READ(5,*) N
      DO  9 I=1, N
          WRITE(6,*) 'Give me fractional co-ords in WRITE(6,*) 'placing an atom at the
origin'
          READ(5,*,END=8) EX(I), WHY(I), ZEE(I)
          LATP(I)=I
          ASIZ=ASIZ+1
          WRITE(6,*) 'And what is the atomic type?'
          WRITE(6,*) 'What we need is the chemical species and the'
          WRITE(6,*) 'ionic charge if the crystal were considered'
          WRITE(6,*) 'as ionic e.g FE+3'
          READ (5,*) TYP(I)
9     CONTINUE
8     MOTIV=ASIZ
      WRITE (6,*) 'Size of array of points',ASIZ
      WRITE (6,*) 'So, what plane are we considering here ?'
      WRITE (6,*) 'Give the Miller indices'
      READ (5,*) ACH, KAY, EL
      END


. . . . . .
* This subroutine takes the elements of the Primitive
* unit cell motif and creates a cuboid of unit cells
* from which to section the plane of atoms in which
* we are interested
      SUBROUTINE MINICRYST(X,Y,Z,T,ASIZE,LP)
. . . . . .
      INTEGER ASIZE, I, X(ASIZE), Y(ASIZE), Z(ASIZE)
      INTEGER LP(ASIZE)
      CHARACTER*4 T(ASIZE)
      DO  20 I=1, ASIZE
```

```
            X(ASIZE + I) = X(I) + 100
            Y(ASIZE + I) = Y(I)
            Z(ASIZE + I) = Z(I)
            T(ASIZE + I) = T(I)
            LP(ASIZE + I) = LP(I)
20      CONTINUE
        ASIZE=2*ASIZE
        DO  21 I=1, ASIZE
            X(ASIZE + I) = X(I)
            Y(ASIZE + I) = Y(I) + 100
            Z(ASIZE + I) = Z(I)
            T(ASIZE + I) = T(I)
            LP(ASIZE + I) = LP(I)
21      CONTINUE
        ASIZE=2*ASIZE
        DO  22 I=1, ASIZE
            X(ASIZE + I) = X(I)
            Y(ASIZE + I) = Y(I)
            Z(ASIZE + I) = Z(I) + 100
            T(ASIZE + I) = T(I)
            LP(ASIZE + I) = LP(I)
22      CONTINUE
        ASIZE=2*ASIZE
        DO  23 I=1, ASIZE
            X(ASIZE + I) = X(I) - 200
            Y(ASIZE + I) = Y(I)
            Z(ASIZE + I) = Z(I)
            T(ASIZE + I) = T(I)
            LP(ASIZE + I) = LP(I)
23      CONTINUE
        ASIZE=2*ASIZE
        DO  24 I=1, ASIZE
            X(ASIZE + I) = X(I)
            Y(ASIZE + I) = Y(I) - 200
            Z(ASIZE + I) = Z(I)
            T(ASIZE + I) = T(I)
            LP(ASIZE + I) = LP(I)
24      CONTINUE
        ASIZE=2*ASIZE
        DO  25 I=1, ASIZE
            X(ASIZE + I) = X(I)
            Y(ASIZE + I) = Y(I)
            Z(ASIZE + I) = Z(I) - 200
            T(ASIZE + I) = T(I)
            LP(ASIZE + I) = LP(I)
25      CONTINUE
        ASIZE=2*ASIZE
        END
```

```
. . . . . .
* This subroutine creates the primitive unit cell motif
. . . . . .
      SUBROUTINE PCELL(X,Y,Z,T,L,ASIZE,LP)
. . . . . .
      INTEGER ASIZE,X(ASIZE),Y(ASIZE),Z(ASIZE),LP(ASIZE),L,I
      CHARACTER*4 T(ASIZE)
* If L=1 the lattice is already Primitive
* IF (L .EQ. 1) RETURN
* If L=2 then the lattice is body centred and (LINE31)
* requires the following addition to make an
* effectively primitive lattice
          IF (L .EQ. 2) THEN
              DO  10 I=1, ASIZE
                  X(ASIZE + I) = X(I) + 50
                  Y(ASIZE + I) = Y(I) + 50
                  Z(ASIZE + I) = Z(I) + 50
                  T(ASIZE + I) = T(I)
                  LP(ASIZE + I) = LP(I)
10            CONTINUE
              ASIZE=2*ASIZE
          ENDIF
* If L=3 then the lattice is face centred
          IF (L .EQ. 3) THEN
              DO  11 I=1, ASIZE
                  X(ASIZE + I) = X(I) + 50
                  Y(ASIZE + I) = Y(I) + 50
                  Z(ASIZE + I) = Z(I)
                  T(ASIZE + I) = T(I)
                  LP(ASIZE + I) = LP(I)
                  X(2*ASIZE + I) = X(I) + 50
                  Y(2*ASIZE + I) = Y(I)
                  Z(2*ASIZE + I) = Z(I) + 50
                  T(2*ASIZE + I) = T(I)
                  LP(2*ASIZE + I) = LP(I)
                  X(3*ASIZE + I) = X(I)
                  Y(3*ASIZE + I) = Y(I) + 50
                  Z(3*ASIZE + I) = Z(I) + 50
                  T(3*ASIZE + I) = T(I)
                  LP(3*ASIZE + I) = LP(I)
11            CONTINUE
              ASIZE=4*ASIZE
          ENDIF
* If L=4 then the lattice is an A lattice
          IF (L .EQ. 4) THEN
              DO  12 I=1, ASIZE
                  X(ASIZE + I) = X(I)
                  Y(ASIZE + I) = Y(I) + 50
                  Z(ASIZE + I) = Z(I) + 50
                  T(ASIZE + I) = T(I)
                  LP(ASIZE + I) = LP(I)
```

```
12              CONTINUE
                ASIZE=2*ASIZE
            ENDIF
* If L=5 then the lattice is a B lattice
            IF (L .EQ. 5) THEN
                DO  13 I=1, ASIZE
                    X(ASIZE + I) = X(I) + 50
                    Y(ASIZE + I) = Y(I)
                    Z(ASIZE + I) = Z(I) + 50
                    T(ASIZE + I) = T(I)
                    LP(ASIZE + I) = LP(I)
13              CONTINUE
                ASIZE=2*ASIZE
            ENDIF
* If L=6 the the lattice is a C lattice
            IF (L .EQ. 6) THEN
                DO  14 I=1, ASIZE
                    X(ASIZE + I) = X(I) + 50
                    Y(ASIZE + I) = Y(I) + 50
                    Z(ASIZE + I) = Z(I)
                    T(ASIZE + I) = T(I)
                    LP(ASIZE + I) = LP(I)
14              CONTINUE
                ASIZE=2*ASIZE
            ENDIF
            END


. . . . . .
* This subroutine takes the co-ords generated
* by minicryst and selects those points which
* lie on a selected plane
. . . . . .
        SUBROUTINE PLANE(X,Y,Z,T,ASIZE,H,K,L,LP)
. . . . . .
        INTEGER ASIZE,H,K,L,COUNT,I
        INTEGER X(ASIZE), Y(ASIZE), Z(ASIZE), LP(ASIZE)
        INTEGER M(100), N(100), O(100), Q(100)
        CHARACTER*4 T(ASIZE),P(100)
        COUNT=0
        IF ((H .EQ. 0) .AND. (K .EQ. 0) .AND. (L .NE. 0)) THEN
            DO  30 I=1, ASIZE
                IF (Z(I) .EQ. INT(100/L)) THEN
                    COUNT = COUNT + 1
                    M(COUNT) = X(I)
                    N(COUNT) = Y(I)
                    O(COUNT) = Z(I)
                    P(COUNT) = T(I)
                    Q(COUNT) = LP(I)
                ENDIF
30          CONTINUE
        ENDIF
```

```
      IF ((H .EQ. 0 ) .AND. ( L .EQ. 0 ) .AND. ( K .NE. 0) ) THEN
          DO  31 I=1, ASIZE
              IF (Y(I) .EQ. INT(100/K)) THEN
                  COUNT = COUNT + 1
                  M(COUNT) = X(I)
                  N(COUNT) = Y(I)
                  O(COUNT) = Z(I)
                  P(COUNT) = T(I)
                  Q(COUNT) = LP(I)
              ENDIF
31        CONTINUE
      ENDIF
      IF ((K .EQ. 0 ) .AND. ( L .EQ. 0 ) .AND. ( H .NE. 0) ) THEN
          DO  32 I=1, ASIZE
              IF (X(I) .EQ. INT(100/H)) THEN
                  COUNT = COUNT + 1
                  M(COUNT) = X(I)
                  N(COUNT) = Y(I)
                  O(COUNT) = Z(I)
                  P(COUNT) = T(I)
                  Q(COUNT) = LP(I)
              ENDIF
32        CONTINUE
      ENDIF
      IF ((H .EQ. 0 ) .AND. ( K .NE. 0 ) .AND. ( L .NE. 0) ) THEN
          DO  33 I=1, ASIZE
              IF (INT((Y(I)/L) + (Z(I)/K)) .EQ. INT(100/(K*L))) THEN
                  COUNT = COUNT + 1
                  M(COUNT) = X(I)
                  N(COUNT) = Y(I)
                  O(COUNT) = Z(I)
                  P(COUNT) = T(I)
                  Q(COUNT) = LP(I)
              ENDIF
33        CONTINUE
      ENDIF
      IF ((H .NE. 0 ) .AND. ( K .EQ. 0 ) .AND. ( L .NE. 0) ) THEN
          DO  34 I=1, ASIZE
              IF (INT((X(I)/L) + (Z(I)/H)) .EQ. INT(100/(H*L))) THEN
                  COUNT = COUNT + 1
                  M(COUNT) = X(I)
                  N(COUNT) = Y(I)
                  O(COUNT) = Z(I)
                  P(COUNT) = T(I)
                  Q(COUNT) = LP(I)
              ENDIF
34        CONTINUE
      ENDIF
      IF ((H .NE. 0 ) .AND. ( K .NE. 0 ) .AND. ( L .EQ. 0) ) THEN
          DO  35 I=1, ASIZE
              IF (INT((X(I)/K) + (Y(I)/H)) .EQ. INT(100/(H*K))) THEN
```

```
                    COUNT = COUNT + 1
                    M(COUNT) = X(I)
                    N(COUNT) = Y(I)
                    O(COUNT) = Z(I)
                    P(COUNT) = T(I)
                    Q(COUNT) = LP(I)
                ENDIF
35          CONTINUE
        ENDIF
        IF ((H .NE. 0 ) .AND. ( K .NE. 0 ) .AND. ( L .NE. 0) ) THEN
            DO  36 I=1, ASIZE
                IF (INT(X(I)/(K*L) + Y(I)/(H*L) + Z(I)/(H*K))
    &                .EQ. INT(100/(H*K*L))) THEN
                    COUNT = COUNT + 1
                    M(COUNT) = X(I)
                    N(COUNT) = Y(I)
                    O(COUNT) = Z(I)
                    P(COUNT) = T(I)
                    Q(COUNT) = LP(I)
                ENDIF
36          CONTINUE
        ENDIF
        DO  37 I=1, COUNT
            M(I) = M(I)
            X(I) = M(I)
            N(I) = N(I)
            Y(I) = N(I)
            O(I) = O(I)
            Z(I) = O(I)
            T(I) = P(I)
            LP(I) = Q(I)
37      CONTINUE
        ASIZE = COUNT
        END

. . . . . .
* This subroutine takes the cartesian axes and
* shifts them relative to a plane of co-ordinates
* such that the y-axis, z-axis and plane-normal
* are co-planar
. . . . . .
        SUBROUTINE TRANS1(X,Y,Z,T,A,B,C,H,K,L,ASIZE,RX,RY,LP)
. . . . . .
        INTEGER ASIZE, H, K, L, I
        INTEGER X(ASIZE), Y(ASIZE), Z(ASIZE), LP(ASIZE)
        DOUBLE PRECISION J, A, B, C, ANG1, PI, DET, TEMP1, TEMP2
        DOUBLE PRECISION RX(ASIZE), RY(ASIZE)
        CHARACTER*4 T(ASIZE)
        PI = 3.1418
        IF ( (H .NE. 0) .AND. (K .EQ. 0) .AND. (L .EQ. 0)) THEN
            ANG1 = PI/2
```

```
      ENDIF
      IF ( (H .EQ. 0) .AND. (K .NE. 0) .AND. (L .EQ. 0)) THEN
          ANG1 = 0
      ENDIF
      IF ( (H .EQ. 0) .AND. (K .EQ. 0) .AND. (L .NE. 0)) THEN
          ANG1 = PI/2
      ENDIF
      IF ( (H .NE. 0) .AND. (K .NE. 0) .AND. (L .EQ. 0)) THEN
          J = (A/H)**2 + (B/K)**2
          DET = 1/(DSQRT(J))
          ANG1 = DACOS(DET*(A/H))
      ENDIF
      IF ( (H .NE. 0) .AND. (K .EQ. 0) .AND. (L .NE. 0)) THEN
          ANG1 = PI/2
      ENDIF
      IF ( (H .EQ. 0) .AND. (K .NE. 0) .AND. (L .NE. 0)) THEN
          ANG1 = 0
      ENDIF
      IF ( (H .NE. 0) .AND. (K .NE. 0) .AND. (L .NE. 0)) THEN
          J = (A/H)**2 + (B/K)**2
          DET = 1/(DSQRT(J))
          ANG1 = DACOS(DET*(A/H))
      ENDIF
      DO  40 I=1, ASIZE
          TEMP1 = (X(I)*DCOS(ANG1)) - (Y(I)*(B/A)*DSIN(ANG1))
          TEMP2 = (X(I)*(A/B)*DSIN(ANG1)) + (Y(I)*DCOS(ANG1))
          RX(I) = TEMP1
          RY(I) = TEMP2
          Z(I) = Z(I)
          T(I) = T(I)
          LP(I) = LP(I)
40    CONTINUE
      END

. . . . . .
* This subroutine transforms the axes such that
* the z axis will lie parallel to the plane normal
. . . . . .
      SUBROUTINE TRANS2(Z,T,A,B,C,H,K,L,ASIZE,RX,RY,RZ,LP)
. . . . . .
      INTEGER ASIZE, H, K, L, I
      INTEGER Z(ASIZE), LP(ASIZE)
      DOUBLE PRECISION J, A, B, C, ANG2, PI, DET, TEMP1, TEMP2
      DOUBLE PRECISION RX(ASIZE), RY(ASIZE), RZ(ASIZE)
      CHARACTER*4 T(ASIZE)
      PI = 3.1418
      IF ( (H .NE. 0) .AND. (K .EQ. 0) .AND. (L .EQ. 0)) THEN
          ANG2 = PI/2
      ENDIF
      IF ( (H .EQ. 0) .AND. (K .NE. 0) .AND. (L .EQ. 0)) THEN
          ANG2 = PI/2
```

```
      ENDIF
      IF ( (H .EQ. 0) .AND. (K .EQ. 0) .AND. (L .NE. 0)) THEN
          ANG2 = 0
      ENDIF
      IF ( (H .NE. 0) .AND. (K .NE. 0) .AND. (L .EQ. 0)) THEN
          ANG2 = PI/2
      ENDIF
      IF ( (H .NE. 0) .AND. (K .EQ. 0) .AND. (L .NE. 0)) THEN
          J = ((A/H)**2) + ((C/L)**2)
          DET = 1/(DSQRT(J))
          ANG2 = DACOS(DET*(A/H))
      ENDIF
      IF ( (H .EQ. 0) .AND. (K .NE. 0) .AND. (L .NE. 0)) THEN
          J = ((B/K)**2) + ((C/L)**2)
          DET = 1/(DSQRT(J))
          ANG2 = DACOS(DET*(B/K))
      ENDIF
      IF ( (H .NE. 0) .AND. (K .NE. 0) .AND. (L .NE. 0)) THEN
          J= (((B*C)/(K*L))**2) + (((A*C)/(H*L))**2)
     &     + (((A*B)/(H*K))**2)
          DET = 1/(DSQRT(J))
          ANG2 = DACOS( ((A*B)/(H*K))*DET )
      ENDIF
      DO  50 I=1, ASIZE
          RX(I) = RX(I)
          TEMP1 = (RY(I)*DCOS(ANG2)) - (Z(I)*(C/B)*DSIN(ANG2))
          TEMP2 = (RY(I)*(B/C)*DSIN(ANG2)) + (Z(I)*DCOS(ANG2))
          RY(I) = TEMP1
          RZ(I) = TEMP2
          T(I) = T(I)
          LP(I) = LP(I)
50    CONTINUE
      END

. . . . . .
* This subroutine will take the co-ordinates of the
* points on a chosen plane and transport them so that
* the plane lies on the origin - it moves a lattice
* point to the origin
. . . . . .
      SUBROUTINE ORIGIN(X,Y,Z,T,LP,ASIZE,MOTIF)
. . . . . .
      INTEGER ASIZE, I,J, COUNT, MOTIF
      INTEGER X(ASIZE), Y(ASIZE), Z(ASIZE)
      INTEGER LP(ASIZE)
      INTEGER M(1000), N(1000), O(1000), Q(1000)
      CHARACTER*4 T(ASIZE),P(1000)
      DO  63 J = 1, MOTIF
          COUNT = 0
          DO  60 I = 1, ASIZE
              IF ( LP(I) .EQ. 1) THEN
```

```
                    COUNT = COUNT + 1
                    M(COUNT) = X(I)
                    N(COUNT) = Y(I)
                    O(COUNT) = Z(I)
                    P(COUNT) = T(I)
                    Q(COUNT) = LP(I)
                ENDIF
60          CONTINUE
            IF (COUNT .LT. 3) THEN
                WRITE(6,*) 'There are not enough lattice point in this plane'
                WRITE(6,*) 'to define a unit mesh.'
                WRITE(6,*) 'We must change the lattice atom!'
                CALL SWAPLP(LP,MOTIF,ASIZE)
            ELSE
                GOTO 64
            ENDIF
63      CONTINUE
64      I=0
        DO  61 I = 1, ASIZE
            X(I) = X(I) - M(1)
            Y(I) = Y(I) - N(1)
            Z(I) = Z(I) - O(1)
            T(I) = T(I)
            LP(I) = LP(I)
61      CONTINUE
        END

. . . . . .
        SUBROUTINE MESH(X,Y,T,LP,ASIZE)
. . . . . .
        INTEGER ASIZE, LP(ASIZE), I, C1
        INTEGER LATTP(1000), COUNT2, COUNT3
        INTEGER NLATTP(1000)
        INTEGER KEEPP(1000)
        DOUBLE PRECISION X(ASIZE), Y(ASIZE), LATTX(1000), LATTY(1000),MAG
        DOUBLE PRECISION KEEPX(1000), KEEPY(1000), M, N
        DOUBLE PRECISION NLATTX(1000), NLATTY(1000)
        CHARACTER*4 T(ASIZE)
        CHARACTER*4 LATTT(1000),NLATTT(1000),KEEPT(1000)
* Want to select only those points on the plane
* which are lattice points
        WRITE(6,*)'THE ARRAYS OF X AND Y PASSED TO MESH ARE:'
        DO  59 I = 1,ASIZE
            WRITE(6,*) X(I), Y(I)
59      CONTINUE
        C1 = 0
        COUNT3 = 0
        DO  50 I = 1, ASIZE
            IF (LP(I) .EQ. 1) THEN
                C1 = C1 + 1
                LATTX(C1) = X(I)
```

```
                LATTY(C1) = Y(I)
                LATTT(C1) = T(I)
                LATTP(C1) = LP(I)
            ENDIF
50      CONTINUE
        WRITE(6,*)'Only looking at the lattice points at coords:'
        DO  58 I=1,C1
            WRITE(6,*) LATTX(I), LATTY(I)
58      CONTINUE
* Subroutine sort should list the magnitudes of
* the distances of all lattice vectors in ascending order
        CALL SORT(LATTX,LATTY,LATTT,LATTP,C1)
        WRITE (6,*) 'Sort gives the following distance order:'
        DO  57 I = 1,C1
            MAG = (LATTX(I)**2 + LATTY(I)**2)**(1.0/2.0)
            WRITE(6,*) MAG
57      CONTINUE
* Subroutine nonpar takes the arrays of lattice points
* in ascending order of distances from the origin and
* selects the two of lowest distance from the origin
* which are non-parallel. It then generates the co-ords
* of the 4 corners of the unit mesh .
        CALL NONPAR(LATTX,LATTY,LATTT,LATTP,C1)
* Now select only those points which are non-lattice points
        COUNT2 = 0
        DO  51 I = 1, ASIZE
            IF (LP(I) .NE. 1) THEN
                NLATTX(COUNT2+1) = X(I)
                NLATTY(COUNT2+1) = Y(I)
                NLATTT(COUNT2+1) = T(I)
                NLATTP(COUNT2+1) = LP(I)
                COUNT2 = COUNT2 + 1
            ENDIF
51      CONTINUE
        COUNT3 = 0
* Next keep only those non-lattice points which lie
* within the lattice motif
        IF (COUNT2 .GT. 0) THEN
            DO  52 I=1, COUNT2
                PART1 = (LATTY(2)*NLATTX(I)) - (LATTX(2)*NLATTY(I))
                PART2 = (LATTY(2)*LATTX(3)) - (LATTX(2)*LATTY(3))
                N = PART1/PART2
                PART3 = (LATTY(3)*NLATTX(I)) - (LATTX(3)*NLATTY(I))
                PART4 = (LATTY(3)*LATTX(2)) - (LATTX(3)*LATTY(2))
                M = PART3/PART4
                IF (M .GE. 0 .AND. M .LE. 1
    &                   .AND. N .GE. 0 .AND. N .LE. 1 .AND. NLATTT(I) .NE. 0) THEN
                    KEEPX(COUNT3+1) = NLATTX(I)
                    KEEPY(COUNT3+1) = NLATTY(I)
                    KEEPT(COUNT3+1) = NLATTT(I)
                    KEEPP(COUNT3+1) = NLATTP(I)
```

```
                    COUNT3 = COUNT3 + 1
                ENDIF
52          CONTINUE
        ENDIF
* Now need to reassign x,y,t,lp,asize, so that only the
* unit mesh is considered
        DO  53 I=1,C1
            X(I)=LATTX(I)
            Y(I)=LATTY(I)
            T(I)=LATTT(I)
            LP(I)=LATTP(I)
53      CONTINUE
        DO  54 I=1,COUNT3
            X(C1+ I)=KEEPX(I)
            Y(C1 + I)=KEEPY(I)
            T(C1 + I)=KEEPT(I)
            LP(C1 + I)=KEEPP(I)
54      CONTINUE
        ASIZE=C1 + COUNT3
        END

. . . . . .
        SUBROUTINE SORT(X,Y,T,LP,KOUNT)
. . . . . .
        INTEGER KOUNT, LP(KOUNT),I,K
        DOUBLE PRECISION X(KOUNT), Y(KOUNT),M,N
        DOUBLE PRECISION TEMP1, TEMP2, TEMP4
        CHARACTER*4 T(KOUNT),TEMP3
        DO  60 K=2, KOUNT
            I=K
            DO  WHILE (I .GT. 1)
                M = (X(I-1)**2) + (Y(I-1)**2)
                N = (X(I)**2) + (Y(I)**2)
                IF ( M .GT. N) THEN
                    TEMP1 = X(I-1)
                    TEMP2 = Y(I-1)
                    TEMP3 = T(I-1)
                    TEMP4 = LP(I-1)
                    X(I-1) = X(I)
                    Y(I-1) = Y(I)
                    T(I-1) = T(I)
                    LP(I-1) = LP(I)
                    X(I) = TEMP1
                    Y(I) = TEMP2
                    T(I) = TEMP3
                    LP(I) = TEMP4
                    I = I - 1
                ELSE
                    I = 1
                ENDIF
                END DO
```

```
60          CONTINUE
            KOUNT = KOUNT
            END

. . . . . .
* Subroutine nonpar takes the arrays of lattice points
* in ascending order of distances from the origin and
* selects the two of lowest distance from the origin
* which are non-parallel. It then generates the co-ords
* of the 4 corners of the unit mesh
. . . . . .
      SUBROUTINE NONPAR(X,Y,T,LP,KOUNT)
. . . . . .
      INTEGER KOUNT,LP(KOUNT),I, KEEP
      DOUBLE PRECISION X(KOUNT), Y(KOUNT),TEMP(100)
      CHARACTER*4 T(KOUNT)
* The DO  loop ignores the 0, 0 point i.e x(1), y(1)
            TEMP(2) = (X(2)/Y(2))**2
            DO  70 I=3, KOUNT
                TEMP(I) = (X(I)/Y(I))**2
                IF (TEMP(I) .NE. TEMP(2)) THEN
                    KEEP = I
                    GOTO 71
                ENDIF
70          CONTINUE
            WRITE (6,*)'Minicryst has not produced enough '
            WRITE (6,*)'non-parallel lattice vectors'
* Reassign values for the 4 corners of the unit mesh
71          X(1) = X(1)
            Y(1) = Y(1)
            T(1) = T(1)
            LP(1) = LP(1)
            X(2) = X(2)
            Y(2) = Y(2)
            T(2) = T(2)
            LP(2) = LP(2)
            X(3) = X(KEEP)
            Y(3) = Y(KEEP)
            T(3) = T(KEEP)
            LP(3) = LP(KEEP)
            X(4) = X(2) + X(3)
            Y(4) = Y(2) + Y(3)
            T(4) = T(1)
            LP(4) = LP(1)
            KOUNT = 4
            END
```

```
      SUBROUTINE SWAPLP(L,M,ASYZE)
      INTEGER ASYZE,I, J, L(ASYZE),M
      DO  70 I = 1, ASYZE
          DO  71 J = 2, M
              IF (L(I) .EQ. 1) THEN
                  L(I) = M + 1
              ENDIF
              IF (L(I) .EQ. J) THEN
                  L(I) = J - 1
              ENDIF
71        CONTINUE
          IF (L(I) .EQ. (M + 1)) THEN
              L(I) = M
          ENDIF
70    CONTINUE
      END

      BLOCK DATA
      INTEGER I
      CHARACTER*4 ELEMENTS(187)
      DOUBLE PRECISION IONICR(187)
      COMMON /ATOM/ ELEMENTS
      COMMON /RADIUS/ IONICR
      DATA (ELEMENTS(I), I=1,151)/'AC+3','AG+1','AG+2','AL+3','AM+3',
     &  'AM+4','AR+1','AS-3','AS+3','AS+5',
     &  'AT+7','AU+1','AU+3','B+1','B+3',
     &  'BA+1','BA+2','BE+1','BE+2','BI+1',
     &  'BI+3','BI+5','BR-1','BR+5','BR+7',
     &  'C-4','C+4','CA+1', 'CA+2','CD+1','CD+2','CE+1','CE+3','CE+4',
     &  'CL-1','CL+5','CL+7','CO+2','CO+3','CR+1','CR+2','CR+3','CR+6',
     &  'CS+1','CU+1','CU+2','DY+3','ER+3','EU+3','EU+2','F-1','F+7',
     &  'FE+2','FE+3','FR+1','GA+1','GA+3','GD+3','GE-4','GE+2','GE+4',
     &  'H-1','HF+4','HG+1','HG+2','HO+3','I-1','I+5', 'I+7','IN+3',
     &  'IR+4','K+1','LA+1','LA+3','LI+1','LU+3','MG+1','MG+2','MN+2',
     &  'MN+3','MN+4','MN+7','MO+1','MO+4','MO+6','N-3','N+1','N+3',
     &  'N+5','NA+1','NB+1','NB+4','NB+5','ND+3','NE+1','NI+2','NP+3',
     &  'NP+4','NP+7','O-2','O-1', 'O+1','O+6','OS+4','OS+6','P-3',
     &  'P+3','P+5','PA+3','PA+4','PA+5','PB+2','PB+4','PD+2','PD+4',
     &  'PM+3','PO+6','PR+3','PR+4','PT+2','PT+4','PU+3','PU+4','RA+2',
     &  'RB+1','RE+4','RE+7','RH+3','RU+4','S-2','S+2', 'S+4','S+6',
     &  'SB-3','SB+3','SB+5','SC+3','SE-2','SE-1','SE+1','SE+4','SE+6',
     &  'SI-4','SI-1','SI+1','SI+4','SM+3','SN-4','SN-1','SN+2','SN+4'/
      DATA (ELEMENTS(I), I=152,187)/'SR+2','TA+5','TB+3','TB+4','TC+7',
     &  'TE-2','TE-1','TE+1','TE+4','TE+6',
     &  'TH+4','TI+1','TI+2','TI+3','TI+4',
     &  'TL+1','TL+3','TM+3','U+4','U+6',
     &  'V+2','V+3','V+4','V+5','W+4',
```

```
     &    'W+6','Y+3','YB+2','YB+3','ZN+1',
     &    'ZN+2','ZR+1','ZR+4','AUST','FERR','XXX'/
          DATA (IONICR(I), I=1,187)/1.18,1.26,0.89,0.51,1.07,
     &    0.92,1.54,2.22,0.58,0.46,0.62,1.37,0.85,0.35,0.23,
     &    1.53,1.34,0.44,0.35,0.98,0.96,0.74,1.96,0.47,0.39,
     &    2.60,0.16,1.18,0.99,1.14,0.97,1.27,1.034,0.92,1.81,
     &    0.34,0.27,0.72,0.63,0.81,0.89,0.63,0.52,1.67,0.96,
     &    0.72,0.908,0.881,0.950,1.09,1.33,0.08,0.74,0.64,1.80,
     &    0.81,0.62,0.938,2.72,0.73,0.53,1.54,0.78,1.27,1.10,
     &    0.894,2.20,0.62,0.50,0.81,0.68,1.33,1.39,1.016,0.68,
     &    0.85,0.82,0.66,0.80,0.66,0.60,0.46,0.93,0.70,0.62,
     &    1.71,0.25,0.16,0.13,0.97,1.0,0.74,0.69,0.995,1.12,
     &    0.69,1.10,0.95,0.71,1.32,1.76,0.22,0.09,0.88,0.69,
     &    2.12,0.44,0.35,1.13,0.98,0.89,1.2,0.84,0.8,0.65,
     &    0.979,0.67,1.013,0.9,0.8,0.65,1.08,0.93,1.43,1.47,
     &    0.72,0.56,0.68,0.67,1.84,2.19,0.37,0.3,2.45,0.76,
     &    0.62,0.732,1.91,2.32,0.66,0.50,0.42,2.71,3.84,0.65,
     &    0.42,0.964,2.94,3.70,0.93,0.71,1.12,0.68,0.923,0.84,
     &    0.979,2.11,2.5,0.82,0.70,0.56,1.02,0.96,0.94,0.76,
     &    0.68,1.47,0.95,0.87,0.97,0.8,0.88,0.74,0.63,0.59,
     &    0.7,0.62,0.893,0.93,0.858,0.88,0.74,1.09,0.79,1.29,
     &    1.24,0.0/
          END

. . . . . .
* Subroutine rad takes the type of the atoms in the motif and
* assigns them their ionic radii in the array rad/radii. This
* array labels each atom during the various subroutines to follow,
* not only lattice no. but atomic radius for each atom.
. . . . . .
          SUBROUTINE RADIUSS(T,ASIZE,RAD)
. . . . . .
          INTEGER ASIZE,I, DONE, COUNT
          CHARACTER*4 T(ASIZE),ELEMENTS(187),TEMP1,TEMP2
          DOUBLE PRECISION RAD(ASIZE)
          DOUBLE PRECISION IONICR(187)
          COMMON /ATOM/ ELEMENTS
          COMMON /RADIUS/ IONICR
          COUNT = 1
          DO  80 J = 1, ASIZE
              DONE = 0
              I = 1
              DO  70 I=1,187
                  TEMP1=ELEMENTS(I)
                  TEMP2=T(J)
                  IF (ELEMENTS(I) .EQ. T(J)) THEN
                      RAD(COUNT) = IONICR(I)
                      DONE = 1
                      COUNT = COUNT +1
                  ENDIF
70            CONTINUE
```

```
            IF (DONE .EQ. 0) THEN
                WRITE(6,*) 'Error message: Element is not in data file!'
            ENDIF
80      CONTINUE
        END


. . . . . .
        SUBROUTINE PIXEL(RAD,X,Y,PICX,PICY,VAL,ASIZE,A,B,
     &   COUNT,RESOLX,RESOLY,PICSIZE)
. . . . . .
* This sub should take the information from the unit mesh
* and assign values of the matter function to pixels within the mesh
        INTEGER ASIZE, COUNT, XMAX,XMIN,YMAX,YMIN,I,J
        INTEGER PICX(50000), PICY(50000),TEMP,TEM,RESOLX,RESOLY,PICSIZE
        DOUBLE PRECISION X(ASIZE),Y(ASIZE),RAD(ASIZE),ROOT,ROOT1,ROOT2
        DOUBLE PRECISION VAL(50000),M,N,PART1,PART2,A,B
* HERE we make x and y of fractional atomic coords into real
* angstrom values(*100)
        DO  29 I = 1,ASIZE
            X(I)=A*X(I)
            Y(I)=B*Y(I)
            RAD(I)=100*RAD(I)
29      CONTINUE
        CALL EXTENT(X,Y,ASIZE,XMIN,XMAX,YMIN,YMAX)
* Now create array of pixels in Cartesian form
        COUNT = 0
* Resol are integers controlling the resolution of the
* description of the matter function of the unit mesh.
* The magnitude of resol = the number of pixels in the
* x or y direction
        PICSIZE=4
        RESOLX = (XMAX - XMIN)/PICSIZE
        RESOLY = (YMAX - YMIN)/PICSIZE
        DO  30 I = 1, RESOLX
            DO  31 J = 1, RESOLY
                TEM=((I-1)*PICSIZE)+XMIN
                TEMP=((J-1)*PICSIZE)+YMIN
                PICX(RESOLY*(I-1) + J)=TEM
                PICY(RESOLY*(I-1) + J)=TEMP
                COUNT = COUNT + 1
31          CONTINUE
30      CONTINUE
        TEMP=PICX(2)
        TEM=PICY(2)
* Now assign values to the pixels
        DO  32 J=1, COUNT
            VAL(J) = 0.0
            DO  33 I=1, ASIZE
                ROOT1=PICX(J)
                ROOT2=PICY(J)
                ROOT1=(PICX(J)-X(I))**2.0
```

```
                ROOT2=(PICY(J)-Y(I))**2.0
                ROOT=(ROOT1 + ROOT2)**0.5
                TEMP = RAD(I) - ROOT
                IF (TEMP .GE. 0) THEN
                    VAL(J) = VAL(J) + TEMP
                ELSE
                    VAL(J) = VAL(J)
                ENDIF
33          CONTINUE
32      CONTINUE
* Here we assign all pixels which lie outside the unit mesh the
* value of -1. This is really a labelso that such pixels may be
* ignored when calculating difference functions
        DO  34 I=1, COUNT
            PART1 = (Y(2)*PICX(I)) - (X(2)*PICY(I))
            PART2 = (Y(2)*X(3)) - (X(2)*Y(3))
            N = PART1/PART2
            PART3 = (Y(3)*PICX(I)) - (X(3)*PICY(I))
            PART4 = (Y(3)*X(2)) - (X(3)*Y(2))
            M = PART3/PART4
            IF (M .GE. 0 .AND. M .LE. 1
     &           .AND. N .GE. 0 .AND. N .LE. 1 ) THEN
                VAL(I) = VAL(I)
            ELSE
                VAL(I) = -1.0
            ENDIF
34      CONTINUE
* DO  35 I=1,COUNT
* WRITE(6,*)'SUB GIVES',PICX(I),PICY(I),VAL(I)
* 35 CONTINUE
            END


. . . . . .
        SUBROUTINE EXTENT(XX,YY,ASIZ,MINX,MAXX,MINY,MAXY)
. . . . . .
* This sub. finds extent of the unit mesh
* superimposed onto a cartesian reference frame
* in terms of min and max x and y
. . . . . .
        INTEGER MINX,MAXX,MINY,MAXY,I,ASIZ
        DOUBLE PRECISION XX(ASIZ),YY(ASIZ)
        MINX = INT(XX(1))
        MAXX = INT(XX(1))
        MINY = INT(YY(1))
        MAXY = INT(YY(1))
        DO  10 I = 1, ASIZ
            IF (INT(XX(I)) .LT. MINX) THEN
                MINX = INT(XX(I))
            ENDIF
            IF (INT(XX(I)) .GT. MAXX) THEN
                MAXX = INT(XX(I))
```

```
            ENDIF
            IF (INT(YY(I)) .GT. MAXY) THEN
                MAXY = INT(YY(I))
            ENDIF
            IF (INT(YY(I)) .LT. MINY) THEN
                MINY = INT(YY(I))
            ENDIF
10      CONTINUE
        END

. . . . . .
        SUBROUTINE INVPIXEL(VAL,COUNT)
. . . . . .
        INTEGER COUNT
        DOUBLE PRECISION VAL(COUNT),VALMAX,TEMP
        VALMAX=0.0
* First establish the maximum value of the matter
* function - valmax
        DO  10 I=1,COUNT
            TEMP = VAL(I)
            IF (TEMP .GT. VALMAX) THEN
                VALMAX = TEMP
            ELSE
                VALMAX = VALMAX
            ENDIF
10      CONTINUE
* Now produce the inverse values in the inv matter function
        DO  11 I = 1, COUNT
            TEMP = VALMAX - VAL(I)
            VAL(I) = TEMP
            IF (VAL(I) .GT. VALMAX) THEN
                VAL(I) = -1.0
            ENDIF
11      CONTINUE
* If in the original matter function the value was assigned as
* negative then the new value will be greater than valmax. This
* is therefore diagnostic of pixels outside the unit mesh. For
* the moment reassign such pixels with the value of -1.0
        END

. . . . . .
        SUBROUTINE RMESH(PICARR1,PICARR2,PICX1,PICY1,PICX2,PICY2,ASIZ2,
    &   VAL2,X2,Y2,VAL1,RESOLY1,RESOLX1,MINR,PICSI,RESOLY2,CTSHY,
    &   CTR,CTSHX)
. . . . . .
        INTEGER PICARR1,PICARR2,ASIZ2,RESOLY1,RESOLX1,I
        INTEGER PICX1(PICARR1),PICY1(PICARR1),RESOLY2
        INTEGER PICX2(PICARR2),PICY2(PICARR2),PICSI,J,COUNT
        INTEGER CTSHY,CTR,CTSHX
        DOUBLE PRECISION VAL1(PICARR1),VAL2(PICARR2),ROUGH
        DOUBLE PRECISION X2(ASIZ2),Y2(ASIZ2),MINR,MIN,RMEAN,RTOTA
```

```
      MINR=1.0D+10
      MIN =1.0D+10
      ROUGH=5.0
      COUNT=RESOLY1/ROUGH
      WRITE(6,*) 'Entering rmesh'
      RMEAN=0.0
      DO  10 I=1, (RESOLY1/ROUGH)
          CTSHX=0
          CALL RROW(PICARR1,PICARR2,PICX1,PICY1,PICX2,PICY2,
     &     ASIZ2,VAL2,X2,Y2,VAL1,RESOLY1,RESOLX1,MIN,PICSI,RESOLY2,
     &     ROUGH,RTOTA,CTSHX,CTR)
          IF (MIN .LT. MINR) THEN
              MINR=MIN
              CTSHY=(I-1)*ROUGH
          ENDIF
          RMEAN=RMEAN + (RTOTA/COUNT)
          DO  11 J=1,ROUGH
              CALL SHIFTY(RESOLX1,RESOLY1,VAL1,PICARR1)
11        CONTINUE
10    CONTINUE
      WRITE(6,*)'RMIN is :',MINR
      WRITE(6,*)'RMEAN is',RMEAN
      END

. . . . . .
      SUBROUTINE RROW(PICAR1,PICAR2,PIX1,PIY1,PIX2,PIY2,
     &  ASIZE2,VALUE2,EX2,WHY2,VALUE1,RESY1,RESX1,RRMIN,PICSIZE,RESOY2,
     &  RUGH,RTOTAL,CSHX,CR)
. . . . . .
      INTEGER PICAR1,PICAR2,ASIZE2,RESY1,RESX1,I,PICSIZE,RESOY2,J
      INTEGER PIX1(PICAR1),PIY1(PICAR1),PIX2(PICAR2),PIY2(PICAR2),COUNT
      INTEGER CSHX, CR, TEMPR
      DOUBLE PRECISION VALUE1(PICAR1),VALUE2(PICAR2),RPIC(50000)
      DOUBLE PRECISION EX2(ASIZE2),WHY2(ASIZE2),RRMIN,MIN,RUGH
      DOUBLE PRECISION RTOTAL,RTOTT
      MIN=1.0D+4
      CSHX=0
      WRITE(6,*) 'Entering rrow'
      RTOTAL=0.0
      COUNT=RESX1/RUGH
      DO  10 I=1,(RESX1/RUGH)
          CALL RUNIT(PICAR1,PICAR2,PIX1,PIY1,PIX2,PIY2,
     &     ASIZE2,VALUE2,EX2,WHY2,MIN,VALUE1,PICSIZE,RESOY2,RPIC,
     &     RUGH,RTOTT,CR)
          IF (MIN .LT. RRMIN) THEN
              RRMIN = MIN
              CSHX=INT((I-1)*RUGH)
              TEMPR=CR
          ENDIF
          RTOTAL = RTOTAL+(RTOTT/COUNT)
          DO  11 J=1,RUGH
```

```
                CALL SHIFTX(VALUE1,RESX1,RESY1,PICAR1)
11          CONTINUE
10      CONTINUE
        WRITE(6,*) 'After rrow, rmin is',RRMIN
        WRITE(6,*) 'After rrow, rmean is',RTOTAL
        CR = TEMPR
        END

. . . . . .
        SUBROUTINE RUNIT(PICARR1,PICARR2,PICX1,PICY1,PICX2,PICY2,
    &   ASIZ2,VAL2,X2,Y2,RMIN,VALU1,PICSI,RESY2,RP,RUFF,RTOT,
    &   CTROT)
. . . . . .
        INTEGER PICARR1,PICARR2,ASIZ2,I,RESY2
        INTEGER PICX1(PICARR1),PICY1(PICARR1),CTROT
        INTEGER PICX2(PICARR2),PICY2(PICARR2),PICSI
        DOUBLE PRECISION VAL2(PICARR2),X2(ASIZ2),Y2(ASIZ2),RTOT
        DOUBLE PRECISION VALU1(PICARR1),RMIN,RV,RP(50000),RUFF
        WRITE(6,*) 'Entering runit'
        RTOT=0.0
        RV =0.0
        DO  10 I=1,4
            CALL RVALUE(RV,PICARR1,PICARR2,PICX1,PICY1,PICX2,PICY2,
    &        ASIZ2,VAL2,X2,Y2,VALU1,PICSI,RESY2,RUFF)
* Only rv/4 because rotate takes array through 90 degrees
            RTOT=RTOT+(RV/4)
            IF (RV .LE. RMIN) THEN
                RMIN=RV
                CTROT=I-1
            ENDIF
            CALL ROTATE(PICX1,PICY1,PICARR1)
            WRITE(6,*)'The r-value pased to runit is',RV
10      CONTINUE
        WRITE(6,*) 'After runit, rmin is',RMIN
        WRITE(6,*) 'After runit, rmean is',RTOT
        END

. . . . . .
        SUBROUTINE RVALUE(R,PICAR1,PICAR2,PIX1,PIY1,PIX2,PIY2,
    &   ASIZE2,VALUE2,EX2,WHY2,VAL1,PICSIZE,RESOLY2,ROUGH)
. . . . . .
        INTEGER PICAR1,PICAR2,TEMPA,TEMPB,PIX1(PICAR1),PIY1(PICAR1)
        INTEGER ASIZE2, PIX2(PICAR2),PIY2(PICAR2),I,PICSIZE
        INTEGER RESOLY2,COUNT
        DOUBLE PRECISION VALUE2(PICAR2),EX2(ASIZE2),WHY2(ASIZE2),RR
        DOUBLE PRECISION V2, VAL1(PICAR1),FRAC,ROUGH,R
        WRITE(6,*) 'Entering rvalue'
        R=0.0
        COUNT=0
        DO  20 I=1,(PICAR1/ROUGH)
            COUNT = COUNT + 1
```

```
            FR = I
            A* = PICAR1/ROUGH
            FRAC=FR/AC
* WRITE(6,*)'Fraction through rval=',FRAC
            TEMPA=PIX1(I*ROUGH)
            TEMPB=PIY1(I*ROUGH)
            CALL VOUTMESH(TEMPA,TEMPB,VALUE2,EX2,WHY2,
     &       PICAR2,ASIZE2,PIX2,PIY2,V2,PICSIZE,RESOLY2,PICAR1)
            IF (VAL1(I*ROUGH) .LT. 0.0) THEN
                RR=0.0
            ELSE
                RR=((VAL1(I*ROUGH)-V2)**2.0)**0.5
            ENDIF
* WRITE(6,*) RR
            R =R+RR
            IF (ROUGH .EQ. 1) THEN
                WRITE(3,*) TEMPA,TEMPB,RR
            ENDIF
20      CONTINUE
        R = R*ROUGH/PICAR1
        END

. . . . . .
        SUBROUTINE VOUTMESH(PX1,PY1,V2,X2,Y2,PICARR2,ASIZE,PX2,
     &  PY2,VAL2,PICSI,RESY,PICARR1)
. . . . . .
* This subroutine takes a pixel from outside the unit mesh
* and assigns the value to it which the point would have if
* the mesh were continuous over all space
* px=pixel number along x of unassigned value
. . . . . .
        INTEGER PX1, PY1, REMX, REMY, ASIZE, PICARR2,RESY
        INTEGER PICARR1
        DOUBLE PRECISION VAL2, REM1, REM2, K, L,TEMP1,TEMP2
        DOUBLE PRECISION V2(PICARR2)
        INTEGER PX2(PICARR2), PY2(PICARR2),PICSI
        INTEGER YMIN,YMAX,XMIN,XMAX
        DOUBLE PRECISION X2(ASIZE),Y2(ASIZE)
* Next we take the value of px1 and py1 and find out what
* the value of function2 would be at that point.
* First step is to take point back to within one unit mesh
* vector of function2 from the origin
        TEMP1=(INT(Y2(2))*PX1) - (INT(X2(2))*PY1)
        TEMP2=(INT(Y2(2))*X2(3)) - (INT(X2(2))*Y2(3))
        L = TEMP1/TEMP2
        TEMP1=(INT(Y2(3))*PX1) - (INT(X2(3))*PY1)
        TEMP2=(INT(Y2(3))*X2(2)) - (INT(X2(3))*Y2(2))
        K = TEMP1/TEMP2
        REM1 = K - INT(K)
        REM2 = L - INT(L)
* Puts the pixel into the unit mesh already defined–problems if rem1,
```

```
* or rem2 are negative because, although scaled to within dimensions
* of the unit mesh, they may still lie outside the mesh
      IF ((REM1 .LT. 0) .AND. (REM2 .GE. 0)) THEN
          REM1 = REM1 + 1.0
      ENDIF
      IF ((REM1 .GE. 0) .AND. (REM2 .LT. 0)) THEN
          REM2 = REM2 + 1.0
      ENDIF
      IF ((REM1 .LT. 0) .AND. (REM2 .LT. 0)) THEN
          REM1 = REM1 + 1.0
          REM2 = REM2 + 1.0
      ENDIF
* Now the rem1, rem2 should give remx and remy within the mesh
* of function2
      REMX = INT((REM1*X2(2)) + (REM2*X2(3)))
      REMY = INT((REM1*Y2(2)) + (REM2*Y2(3)))
      CALL EXTENT(X2,Y2,ASIZE,XMIN,XMAX,YMIN,YMAX)
      REMX=(REMX-XMIN)/PICSI
      REMY=(REMY-YMIN)/PICSI
      A=((REMX)*RESY)+REMY+1
      IF (A .GT. PICARR2) THEN
          A=A-PICARR2
      ENDIF
      VAL2=V2(A)
      END


. . . . . .
      SUBROUTINE SHIFTX(VAL,RESX,RESY,PICARR)
. . . . . .
      INTEGER RESY, PICARR,ROW,RESX
      DOUBLE PRECISION VAL(PICARR), TEMP(10000)
      WRITE(6,*) 'Entering shiftx'
      ROW=RESX
      DO  20 I=1,ROW
          TEMP(I) = VAL(I)
20    CONTINUE
      DO  21 I=1, PICARR-RESY
          VAL(I) = VAL(ROW + I)
21    CONTINUE
      DO  22 I=1,ROW
          VAL((PICARR-ROW)+I)=TEMP(I)
22    CONTINUE
      END


. . . . . .
      SUBROUTINE SHIFTY(RESX,RESY,VAL,PICARR)
. . . . . .
      INTEGER RESX, RESY, PICARR,COLY,ROWX
      DOUBLE PRECISION VAL(PICARR)
      WRITE(6,*) 'Entering shifty'
      COLY=RESX
```

```
      ROWX=RESY
      DO  30 J=1,ROWX
          TEMP=VAL(((J-1)*COLY)+1)
          DO  31 I=1, COLY-1
              VAL(I+((J-1)*COLY))=VAL(I+1+((J-1)*COLY))
31        CONTINUE
          VAL(J*COLY)=TEMP
30    CONTINUE
      END

. . . . . .
      SUBROUTINE ROTATE(PICX,PICY,PICARR)
. . . . . .
      INTEGER PICARR, PICX(PICARR), PICY(PICARR)
      WRITE(6,*) 'Entering rotate'
      DO  40 I=1, PICARR
          TEMP=PICX(I)
          PICX(I)=-PICY(I)
          PICY(I)=TEMP
40    CONTINUE
      END

. . . . . .
      SUBROUTINE ACCUR(COUNTR,COUNTSHX,COUNTSHY,PICX1,PICY1,
     &  PICARR1,VALU1,RESOX1,RESOY1,PICARR2,PICX2,PICY2,ASIZ2,
     &  VALU2,X2,Y2,PICSI,RESOY2)
. . . . . .
      INTEGER COUNTR, COUNTSHX, COUNTSHY,PICARR1,PICARR2
      INTEGER ASIZ2,RESOX1,RESOY1,RESOY2,I
      INTEGER PICX1(PICARR1),PICY1(PICARR1)
      INTEGER PICX2(PICARR2),PICY2(PICARR2)
      DOUBLE PRECISION VALU1(PICARR1),VALU2(PICARR2)
      DOUBLE PRECISION X2(ASIZ2), Y2(ASIZ2),RV,RUFF
      RUFF=1.0
      DO  10 I = 1,COUNTR
          CALL ROTATE(PICX1,PICY1,PICARR1)
10    CONTINUE
      DO  11 I= 1, COUNTSHX
          CALL SHIFTX(VALU1,RESOX1,RESOY1,PICARR1)
11    CONTINUE
      DO  12 I= 1, COUNTSHY
          CALL SHIFTY(RESOX1,RESOY1,VALU1,PICARR1)
12    CONTINUE
      CALL RVALUE(RV,PICARR1,PICARR2,PICX1,PICY1,PICX2,PICY2,
     &  ASIZ2,VALU2,X2,Y2,VALU1,PICSI,RESOY2,RUFF)
      END
```

REFERENCES

Abson D. J., Dolby R. E., *Welding Institute Research Bulletin,* 1978, 202

Abson D. J., Dolby R. E., Hart P., *Welding Institute Research Report,* 1978, 67/1978/M 1–12

Bailey N., *Welding Institute Research Report,* 1983, 221/1983 1–4

Bailey N., *Welding Institute Research Report,* 1985, 291/1985

Bailey N., *Welding Institute Research Report,* 1986, 318/1986 1–12

Bailey N., Pargeter R. J., *Welding Institute Research Report,* 1979, 100/1979, Part 2, 1–21

Barantseva I. G., Paderno V. N., *Refractory Carbides,* Samsonov G. V. ed., Consultants Bureau, New York, 1974, 283–285

Barbaro F. J., Edwards R. H., Easterling K. E., 7^{th} *National Conference,* Aust. X–ray Anal. Association, 1988, AXAA–88

Barbaro F. J., Krauklis P., Easterling K. E., *Materials Science and Technology,* 1989, **5,** 1057–1068

Barrite G. S., *Svetsaren,* 1983, **1**

Barrite G. S., *Svetsaren,* 1983, **2**

Barrite G. S., Edmonds D. V., *Advances in the Physical Metallurgy and Application of Steels,* The Metals Society, London, 1981, 126–134

Barrite G. S., Ricks R. A., Howell P. R., *Quantitative Microanalysis with High Spatial Resolution,* The Metals Society, London, 1981, 112–118

Barrite G. S., Ricks R. A., Howell P. R., *ICSMA,* 1983, **6,** 121

Bhadeshia H. K. D. H., *Acta Metallurgica,* 1981, **29,** 1117–1130

Bhadeshia H. K. D. H., *Metals Science,* 1982, **16,** 159–165

Bhadeshia H. K. D. H., *Future Developments of Metals & Ceramics,* Charles J. A., Greenwood G. W., Smith G. S., eds., Institute of Materials, London, 1992, 61–63

Bhadeshia H. K. D. H., *Bainite in Steels,* Institute of Materials, London, 1992

Bhadeshia H. K. D. H., Svensson L. -E., *Mathematical Modelling of Weld Phenomena,* Cerjak H., Easterling K. E., eds., Institute of Materials, London, 1993, 109–212

Bhadeshia H. K. D. H., Svensson L. -E., Gretoft B., *Journal of Materials Science,* 1986, **21,** 3947–3951

Bhadeshia H. K. D. H., Svensson L. -E., Gretoft B., *Acta Metallurgica,* 1985, **33,** 1271–1283

Bonizewski T., *Advances in Joining & Cutting,* 1990, **36**

Bramfitt B. L., *Metallurgical Transactions,* 1970, **1,** 1987–1995

Brooksbank D., Andrews K., *Journal of the Iron & Steel Institute,* 1972, **210,** 246–253

Chen J., Xue S. B., *American Welding Journal,* 1991, **70,** 277-s–285-s

Christensen N., Grong Ø., *Scandanavian Journal of Metallurgy,* 1986, **15,** 30–40

Christian J. W., *Theory of Transformations in Metals and Alloys,* Pergamon Press, Oxford, 1965

Cissé J., Bolling G. F., *Journal of Crystal Growth,* 1971, **10,** 67–76

Cochrane R. C., Keville B. R., *Steels for Line Pipe and Pipeline Fittings,* The Metals Society, London, 1981, 51

Cochrane R. C., Kirkwood P. R., *Trends in Steels and Consumables for Welding,* The Welding Institute, London, 1978, 103–109

Cochrane R. C., Ward J. L., Keville B. R., *Residuals and Impurities in Steels,* The Welding Institute, London, 1986, 16-1–16-16

Court S. G., Pollard G., *Journal of Material Science Letters,* 1985, **4,** 427–430

Court S. G., Pollard G., *Metallography,* 1989, **22,** 219–243

Craig I., North T. H., Bell H. B., *Trends in Steel and Consumables for Welding,* The Welding Institute, London, 1978, 249–263

Dallum C. B., Olson D. L., *American Welding Journal,* 1989, 198-s–205-s

Davis M. L. E., Bailey N., *American Welding Journal,* 1991, **70,** 57-s–66-s

Devillers L., Kaplan D., Marander B., Ribes A., Riboud P. V., *The effect of Residual Impurity and Microalloying Elements on Weldability and Weld Properties,* The Welding Institute, London, 1983, 1-1–1-11

Deer W. A., Howie R. A., Zussman J., *An Introduction to the Rock Forming Minerals* Longman Scientific & Technical, Essex, England, 1966

Dowling J. M., Corbett J. M., Kerr H. W., *Metallurgical Transactions A,* 1986, **17A,** 1611–1623

Entrekin Jr. C. H., *Metallography,* 1979, **12,** 295–312

Es-Souni M., Beaven P. A., *Surface & Interface Analysis,* 1990, **16,** 504–509

Es-Souni M., Beaven P. A., Evans G. M., *International Institute of Welding Document,* 1991, II-A-847-91 1–18

Farrar R. A., Watson M. N., *Metal Construction,* 1979, **11,** 285–286

Ferrante M. , Farrar R. A., *Journal of Materials Science,* 1982, **17,** 3293–3298

Fleck N. A., Grong Ø., Edwards G. R., Matlock D. K., *American Welding Journal,* 1986, 113-s–121-s

Franklin A. G., *Journal of the Iron & Steel Institute,* 1969, **207,** 181–186

Gladman T., *Inclusions,* Institute of Metallurgists, The Chameleon Press Ltd., 5–25 Burr Road, London, 1979, 157–186

Goldsmith, Waterman, Hirschhorn, *Handbook of Thermophysical Properties of Solid Materials,* The Macmillan Company, New York, 1961

Grong Ø., Kluken A. O., Bjornbakk B., *Joining & Materials,* 1988, **1,** 164–169

Grong Ø., Kluken A. O., Nylund H. K., Hjelen J., Andersen I., *SINTEF Report,* 1992, STF34 A92014, 1–15

Harrison P. L., *Metal Construction,* 1987, **19,** 84R–91R

Harrison P. L., Farrar R. A., *Journal of Materials Science,* 1981, **16,** 2218–2226

Hart P. H. M., *American Welding Journal,* 1986, 14-s

Hirsch P., Howie A., Nicholson R., Pashley D. W., Whelan M. J., *Electron Microscopy of Thin Crystals,* Krieger Publishing Company, Malabar, Florida, 1965, 85

Homma H., Ohkita S., Matsuda S., Yamamoto K., *American Welding Journal,* Oct. 1987, 301-s–309-s

Horii Y., Ohkita S., Wakabayashi M., Namura M., *Nippon Steel Technical Report,* 1988, **37**

Hussen L. A., Hawkins D. N., *Microstructural Science,* DeHoff, Braun, M^{c}Call, eds., Elsevier, Holland, 1983

Indacochea J. E., Olson D. L., *Journal of Materials for Energy Systems,* 1983, **5,** 139–148

Irving Sax N., *Dangerous properties of industrial materials,* Van Nostrand Reinhold Company, New York, 1968, 1047

Ishikawa T., Haze T., *Materials Science and Engineering,* 1994, **A176,** 385–391

Ito Y., Nakanishi M., *The Sumitomo Search,* 1976, **15,** 42–62

Ito Y., Nakanishi M., Komizo Y., *International Institute of Welding Document,* 1981, IIW Doc IX-1194-81

Ito Y., Nakanishi M., Komizo Y., *Metal Construction,* 1982, **14,** 472–478

Jang J., Indacochea J. E., *Journal of Materials Science,* 1987, **22,** 689–700

Joint Committee for Powder Diffraction Studies, ed., *Powder Diffraction Files,* International Centre for Diffraction Data, Swarthmore, USA.

Kawabata F., Matsuyama J., Nakanishi N., Tanaka T., *Trans. ISIJ,* 1986, **26,** 395–402

Kayali E. S., Corbett J. M., Kerr H. W., *Journal of Materials Science Letters,* 1983, **2,** 123–128

Kluken A. O., Grong Ø., *Metallurgical Transactions A,* 1989, **20A,** 1335–1349

Kluken A. O., Grong Ø., Hjelen J., *Materials Science & Technology,* 1988, **4,** 649–654

Kluken A. O., Grong Ø., Hjelen J., *Metallurgical Transactions A,* 1991, **22A,** 657–663

Kluken A. O., Grong Ø., Rorvik G., *Metallurgical Transactions A,* 1990, **21A,** 2047–2058

Lathabai S., Stout R. D., *American Welding Journal,* Nov. 1985, 303-s–313-s

Liao F-C., Liu S., *American Welding Journal,* Mar. 1992, 94-s–103-s

Liu S., Olson D. L., *American Welding Journal,* 1986, 139-s–148-s

Maunder P., Charles J., *Journal of the Iron & Steel Institute,* 1968, **206,** 705–715

Massalki T. B., ed., *Binary Alloy Phase Diagrams,* American Society for Metals, Metals Park, Ohio 44073, 1986, 1118

Mills A. R., Thewlis G., Whiteman J. A., *Materials Science and Technology,* 1987, **3,** 1051–1061

Morgan–Warren E. J., *Arc Physics & Weldpool Behaviour,* 1980, **1**

Mori N., Homma H., Okita S., Wakabayashi M., *International Institute of Welding Document,* 1981, IIW Doc IX 1196 81 1–16

Narayan C., Goldstein J. I., *Metallurgical Transactions A,* 1983, **14A,** 2437–2439

North T. H., Mao X., Nakagawa H., Shinozaki K., *The Metallurgy, Welding, and Qualification of Microalloyed (HSLA) Steel Weldments Conf.,* AMS, Houston Texas, 1990, 219–248

Ochi T., Takahashi T., Takada H., *30th Mechanical Working & Steel Processing Conference, ISS,* 1988 1–8

Oh D. W., Olson D. L., Frost R. H., *Journal of Engineering for Industry,* 1991

Oldland R. B., M^{c}Pherson R., *Metals Forum,* 1984, **7,** 55–60

Pargeter R. J., *Welding Institute Research Report,* 1981, 151/1981 1–5

Pargeter R. J., *Welding Institute Research Report,* 1982, 189/1982

Pargeter R. J., *Welding Institute Research Bulletin,* 1983, 215–220

Pickering F. B., *Inclusions,* Institute of Metallurgists, The Chameleon Press Ltd., 5–25 Burr Road, London, 1979, 47–72

Rees G. I., Bhadeshia H. K. D. H., *Materials Science and Technology,* 1994, **10,** 353–358

Ribeiro de Avillez R., *Niobium Technical Report,* 1982, NbTR-01/82

Ricks R. A., Howell P. R., Barrite G. S., *Journal of Materials Science,* 1982, **17,** 732–740

Rooksby, *X-ray Identification and Crystal Structures of Clay Minerals,* London, 1951, 264

Saggese M. E., Bhatti A. R., Hawkins D. N., Whiteman J. A., *Welding Institute paper 15,* 1982 15-1–15-11

Samsonov G. V., ed., *The Oxide Handbook,* IFI/Plenum Data Corporation, New York, 1973

Schvezov C. E., Weinberg F., *Metallurgical Transactions B,* 1985, **16B,** 367

Sidgwick N. V., *Chemical elements & their compounds,* Oxford University Press, London, 1950, 700

St-Laurent S., L'Espérance G., *Materials Science and Engineering,* 1992, **A149,** 203–216

Strangwood M., Bhadeshia H. K. D. H., *Advances in Welding Technology and Science,* David S. A., ed., ASM, Met. Park, Ohio., 1987, 209–213

Strangwood M., Bhadeshia H. K. D. H., *Phase Transformations '87,* Lorimer G. W., ed., Institute of Metals, London., 1988, 466–470

Sugden A. A. B., Bhadeshia H. K. D. H., *Metallurgical Transactions A,* 1989, **20A,** 1811–1818

Suzuki M., Kunisada Y., Watanabe I., *International Institute of Welding Document,* 1985, IIW Doc II–1043–85 1–13

Terashima H., Hart P. H. M., *International Conference on the Effects of Residual Impurity and Microalloying Elements on Weldability and Weld Properties,* The Welding Institute, London, 1983, paper 27

Terlinde G., Müller L., Beaven P., Schwalbe K., *GKSS Report,* 1984, 84/E/33

Thewlis G., *Joining & Materials,* 1989, **1&2,** 25–31, 125–129

Thewlis G., *International Institute of Welding Document,* 1990, IXJ 165 90, 1–11

Thewlis G., *British Steel Technical Document,* 1993, SL/WE/1/93/C, 1–14

Thewlis G., Milner D. R., *American Welding Journal,* 1977, 281-s–288-s

Tsuboi J., Terashima H., *Welding in the World,* 1983, **21,** 304

Uhlmann D. R., Chalmers B., Jackson K. A., *Journal of Applied Physics,* 1964, **35,** 2986–2993

Watanabe I., Kojima T., *Journal of Japan Welding Society,* 1980, **49 (11) & 50 (7),** 772-780 & 702-709

Weast R. C., ed., *Handbook of Phys. & Chem., 57th edition,* CRC Press, Cleveland, Ohio, 1976

Wegrzyn J., *Metal Construction,* 1985, **17,** 759R–764R

Widgery D. J., *American Welding Journal,* 1976, 57-s–68-s

Willingham D. C., Bailey N., *Welding Institute Research Report,* 1975, M/83/75 1–10

Yamamoto K., Hasegawa T., Takamura J., *TISIJ,* 1993, **79,** 41–47

Yang J. R., Bhadeshia H. K. D. H., *Advances in Welding Technology and Science,* David S. A., ed., ASM, Met. Park, Ohio., 1987, 187–191